

2018

Detection of Buried Non-Metallic (Plastic and FRP Composite) Pipes Using GPR and IRT

Jonas Kavi

West Virginia University, jokavi@mix.wvu.edu

Follow this and additional works at: <https://researchrepository.wvu.edu/etd>



Part of the [Civil Engineering Commons](#), [Other Engineering Commons](#), and the [Structural Materials Commons](#)

Recommended Citation

Kavi, Jonas, "Detection of Buried Non-Metallic (Plastic and FRP Composite) Pipes Using GPR and IRT" (2018). *Graduate Theses, Dissertations, and Problem Reports*. 3724.

<https://researchrepository.wvu.edu/etd/3724>

This Dissertation is protected by copyright and/or related rights. It has been brought to you by the The Research Repository @ WVU with permission from the rights-holder(s). You are free to use this Dissertation in any way that is permitted by the copyright and related rights legislation that applies to your use. For other uses you must obtain permission from the rights-holder(s) directly, unless additional rights are indicated by a Creative Commons license in the record and/ or on the work itself. This Dissertation has been accepted for inclusion in WVU Graduate Theses, Dissertations, and Problem Reports collection by an authorized administrator of The Research Repository @ WVU. For more information, please contact researchrepository@mail.wvu.edu.

**DETECTION OF BURIED NON-METALLIC (PLASTIC AND FRP COMPOSITE)
PIPES USING GPR AND IRT**

Jonas Kavi

**Dissertation submitted to the
Benjamin M. Statler College of Engineering and Mineral Resources
at West Virginia University
in partial fulfillment of the requirements
for the degree of**

**Doctor of Philosophy
in
Civil Engineering**

**Udaya B. Halabe, Ph.D., P.E., Chair
Hota V. S. GangaRao, Ph.D., P.E.
Hema J. Siriwardane, Ph.D., P.E.
Radhey Sharma, Ph.D.
Benjamin Dawson-Andoh, Ph.D.**

Department of Civil and Environmental Engineering

**Morgantown, West Virginia
2018**

Keywords: Corrosion, Excavation Damage, Ground Penetrating Radar, GPR, Infrared Thermography, IRT, Pipelines, Oil and Gas, Fiber Reinforced Polymer, FRP, CFRP, GFRP, Composites

Copyright 2018 Jonas Kavi

ABSTRACT

DETECTION OF BURIED NON-METALLIC (PLASTIC AND FRP COMPOSITE) PIPES USING GPR AND IRT

Jonas Kavi

Pipelines are crucial in transporting petroleum products, natural gas, and water from production facilities to consumers under high pressure and long service life. In addition to being the primary means of transporting water from treatment facilities to consumers, pipelines also account for the transportation of more than half of the 100 quadrillions Btu of energy commodities consumed in the United States annually. The important role played by energy pipelines in the US economy and standard of living of citizens requires that these assets be safely maintained and appropriately expanded to meet growing demand. Pipelines remain the safest means of transporting natural gas and petroleum products, nonetheless, the pipeline infrastructure in the US is facing major challenges, especially, corrosion of steel/metallic pipes and excavation damage of onshore pipelines (leading to oil spills, explosions, and deaths). Problems associated with corrosion of metallic pipelines can be avoided by using non-corrosive materials such as PVC (Polyvinyl Chloride) or other plastics for water, sewer, or low pressure gas lines and Glass Fiber Reinforced Polymer composite (GFRP) for transporting high-pressure oil and natural gas. But buried non-metallic pipelines such as GFRP and PVC material are not easily detectable using the conventional techniques employed by construction crews to detect buried metallic pipes, which can lead to increased excavation damage during building/construction and rehabilitation works.

This research investigated alternative strategies for making buried non-metallic pipes (CFRP, GFRP, and PVC) easily locatable using Ground Penetrating Radar (GPR). Pipe diameters up to 12" and buried with up to 4 ft. of soil cover were investigated. The findings of this study will help address the detection problem of non-metallic pipelines and speed the adoption of composite pipes by the petroleum and natural gas industry. The research also investigated the possibility of locating buried pipes transporting hot fluids using Infrared Thermography (IRT).

Results from the study have shown that, using carbon fabric and aluminum foil/tape overlay on non-metallic pipes (GFRP or PVC for this study) before burying significantly increases the reflected GPR signal amplitude, thereby making it easier to locate such pipelines using GPR. The reflected GPR signal amplitude for pipe sections with carbon fabric or aluminum foil overlays was

found to have increased by a factor of up to 4.52 times, and 2.02 times on average across all the pipe sections tested, from the baseline (unwrapped) pipe sections. The research also highlights the importance of using the correct antenna frequency for detecting buried pipes in wet soil conditions. Wet soils with high electrical conductivity and dielectric constants have higher radar signal attenuations that significantly affect the penetration depth and returned signal amplitudes from buried objects. A 200 MHz frequency antenna was found in this study to be ideal for locating the buried pipes in all soil moisture conditions. The 200 MHz antenna was able to detect buried pipes up to the maximum 4 ft. depth of soil cover that was studied experimentally. Numerical estimation using the same soil from the experiment shows that this antenna can penetrate up to a depth of at least 5.5 ft. in very wet clay soils with volumetric water content of 0.473.

After evaluating the attenuation characteristics of different radar antennae, it was found that material/ohmic attenuation is constant across a range of antenna frequencies; the increase in GPR signal attenuation associated with higher antenna frequencies was found to be a result of scattering attenuation from subsurface inhomogeneity/clutter. Scattering attenuation is however usually ignored in literature, resulting in erroneous estimation of radar signal attenuation.

Finally, laboratory study proved that, heat from a buried pipeline transporting hot fluid can propagate through the soil to the surface and be detected using IRT. Additionally, a 6" diameter steam pipe with a 6" minimum insulation and buried with 2.5 – 3 ft. of soil cover was easily detected in varying soil moisture conditions during different seasons throughout the year using IRT in the field environment. The successful application of IRT in detecting this pipe proves the potential for using this technique in locating buried pipes transporting hot fluids such as steam or petroleum products from production wells or refinery plants.

ACKNOWLEDGEMENTS

I would like to express my sincere gratitude to my academic and research advisor, Dr. Udaya B. Halabe, for his guidance, support, and encouragement throughout my graduate studies. His extensive knowledge in the area of Nondestructive Evaluation of Civil Engineering infrastructure has been a great help for me during the M.S. and Ph.D. degree programs. I am thankful for the opportunity to work under Dr. Halabe, an experienced and knowledgeable faculty, and one of the best advisors in the department.

I would also like to thank Dr. Hota V. S. GangaRao, Dr. Hema J. Siriwardane, Dr. Radhey Sharma, and Dr. Benjamin Dawson-Andoh for serving as members on my Advisory and Examining Committee (AEC) and providing constructive feedback on my work. I am also grateful to Dr. Radhey Sharma for encouraging me to apply for the Chancellor's Scholarship; Dr. Hota V. S. GangaRao for making his extensive knowledge in fiber composite materials and manufacturing accessible during this study; Dr. Siriwardane for allowing me to use the heating oven available in the Geotechnical laboratory for determining soil moisture content; and Dr. Benjamin Dawson-Andoh for his valuable advice on making the most out of graduate school and preparing for life after graduation.

I would like to express my appreciation to WVU-CFC Technician, Mr. Jerry Nestor, for helping me during the sample preparation and experimental setup stage of this research. I am also grateful to fellow graduate students, for their immense help during this journey; I am especially appreciative to Andrew Wheeler, Ruben Joshi, Praveen Majjigapu, Amir Houshmandyar, Piyush Soti, and Shabnam Khanal for providing assistance during this research.

Funding for this study was provided through the Competitive Academic Agreement Program from the Pipeline and Hazardous Materials Safety Administration (PHMSA) of US Department of Transportation (USDOT) under contract numbers DTPH5615HCAP09 and DTPH5616HCAP02. Support for the study was also provided by Creative Pultrusions, Inc. (CP) in providing the composite pipe materials for the study. I would like to thank USDOT-PHMSA and CP for providing the resources and the opportunity for me to work on this study. I would also like to thank West Virginia University Division of Diversity, Equity and Inclusion; the Department of Civil and Environmental Engineering; and NACE International/Appalachian Underground Corrosion Short Course (AUCSC) for awarding me the Chancellor's Scholarship; Dianne D. Anderson Graduate Fellowship; and the AUCSC Scholarship respectively that enabled me to focus exclusively on my studies and research.

Finally, I am very grateful for my family and friends; their endless support, guidance and encouragement throughout this study made it a worthwhile journey.

TABLE OF CONTENTS

Abstract.....	ii
Acknowledgements	iv
Table of Contents	v
List of Figures.....	x
List of Tables.	xviii
Nomenclature	xix
Chapter 1: Introduction..	1
1.1 Background/Overview	1
1.2 Research Problem and Focus	5
1.3 Fiber Reinforced Polymer (FRP) Materials and why GFRP.....	5
1.4 Research Objectives and Scope.....	6
1.5 Research Significance	7
1.6 Research Collaboration	8
1.7 Organization.....	8
Chapter 2: State of the Pipeline Infrastructure	10
2.1 Introduction	10
2.2 PHMSA Pipeline Incidents Causes	10
2.2.1 Corrosion.....	11
2.2.2 Excavation Damage	13
2.2.3 Material/Weld/Equipment Failure	16
2.2.4 PHMSA Pipeline Incident Summary	18
2.3 Water and Sewage Pipelines	25

2.4	Conclusions	26
Chapter 3: Recent Advances in Non-Metallic Pipeline Detection		27
3.1	Introduction	27
3.2	Buried Object Detection Techniques	27
3.2.1	Dowsing	27
3.2.2	Geomagnetic Surveying.....	28
3.2.3	Electromagnetic Induction (EMI).....	29
3.2.4	Electrical/Surface Resistivity.....	29
3.2.5	Tracer Wires.....	32
3.2.6	Infrared Thermography (IRT).....	32
3.2.7	Ground Penetrating Radar (GPR).....	33
3.2.8	Advantages and Limitations, and why GPR.....	34
3.3	Use of GPR in Buried Non-Metallic Object Detection.....	35
3.4	Challenges in Detecting Non-Metallic Objects.....	36
3.5	Conclusions	37
Chapter 4: Ground Penetrating Radar (GPR) Theory		38
4.1	Introduction	38
4.2	Propagation Velocity.....	39
4.3	Signal Amplitude.....	42
4.4	Loss Factor and Skin Depth	44
4.5	Transmission and Reflection.....	45
4.6	Dielectric Characteristics of Common Soil Materials.....	47
4.6.1	Dielectric Models.....	47
4.6.2	Inverse Models.....	52
4.7	Conclusions	53

Chapter 5: GPR Equipment, Sensors, and Data Processing	54
5.1 Introduction	54
5.2 GPR Equipment.....	54
5.3 Soil Moisture and Electrical Conductivity Sensor	56
5.4 GPR Data Processing Techniques.....	57
5.4.1 Background Removal.....	57
5.4.2 Peaks Extraction.....	57
5.4.3 Horizontal Scaling	58
5.4.4 Amplitude Extraction.....	58
5.5 Conclusions	58
Chapter 6: Experimental Set Up for GPR Testing	59
6.1 Introduction	59
6.2 Research Procedure	59
6.3 Pipe Preparation	60
6.3.1 PVC Pipes	60
6.3.2 GFRP Pipes.....	62
6.3.3 CFRP Pipes	64
6.3.4 Creating Dielectric Contrast Between Non-Metallic Pipes and Surrounding Soil .	65
6.4 Pipe Burying.....	68
6.5 Conclusions	75
Chapter 7: GPR Test Results and Data Analysis.....	76
7.1 Introduction	76
7.2 GPR Test Results	76
7.2.1 900 MHz Antenna Data	77
7.2.2 Dataset I	77

7.2.3	Dataset II.....	93
7.2.4	Dataset III.....	100
7.2.5	Performance of Surface Configurations.....	107
7.3	Determination of Depth.....	111
7.3.1	Depth Estimation Using Soil Dielectric Constant	111
7.3.2	Depth Estimation Using GPR Hyperbolic Fitting	112
7.3.3	Depth Estimation Using Common Mid-Point (CMP) Method.....	114
7.4	Conclusions	116
Chapter 8: Numerical Computations.....		118
8.1	Introduction	118
8.2	Soil Dielectric Modelling.....	118
8.3	Inverse Dielectric Modelling.....	123
8.4	Signal Amplitude and Attenuation.....	127
8.5	Antenna Performance and Penetration Depth	133
8.6	Wave Velocity and Wavelength.....	137
8.7	Conclusions	138
Chapter 9: Infrared Thermography Testing and Results.....		139
9.1	Introduction	139
9.2	IRT Test Equipment (Camera and Thermocouples)	139
9.3	Experimental Set-Up for IRT Testing	140
9.4	IRT Test Results.....	142
9.4.1	Pipe Operating /Heating Cycle	142
9.4.2	Pipe Cooling Cycle	148
9.5	Testing of Field Pipes.....	150
9.6	Conclusions	156

Chapter 10: Conclusions and Recommendations	158
10.1 Research Summary	158
10.2 Conclusions	159
10.3 Recommendations for Field Implementation and Future Study.....	162
10.3.1 Recommendations for Field Implementation.....	162
10.3.2 Recommendations for Future Study	163
References.....	164
Appendix A: PHMSA Incident Definition and Criteria History	174
Appendix B: Supplementary GPR Data	176
B.1 Details of Pipes Identified in the 36 ft. Long Trench Using 400 MHz Antenna	177
B.2 Detailed Radar Profile for Features Marked in Figure 7-29(b) for Dataset II	180
B.3 Transverse GPR Scans over 36 ft. Long Trench Using 200 MHz Antenna.....	183
B.4 Transverse GPR Scans over 36 ft. Long Trench Using 400 MHz Antenna.....	185
Appendix C: Supplementary IRT Plots.....	187

LIST OF FIGURES

Figure 1-1: (a) 2014 U.S. Primary energy consumption by source (EIA n.d.) and (b) crude oil and petroleum product by transportation by mode in 2009 (USDOT 2017).....	2
Figure 1-2: U.S. refinery receipts of crude oil by method of transportation (EIA n.d.)	2
Figure 1-3: U.S. Primary energy consumption by source (EIA n.d.).....	3
Figure 1-4: Primary energy consumption by type, 1980-2040 (EIA 2015)	4
Figure 2-1: 20 year reported incident cause breakdown (1996-2015).....	11
Figure 2-2: External surface of the failed pipeline section (PHMSA 2016e and 2016f)	12
Figure 2-3: Spilled crude oil from the rupture being cleaned (Nicholson 2015)	12
Figure 2-4: Corrosion products deposited on the pipe surface (PHMSA 2016f)	13
Figure 2-5: Laser scanning rendering of the failure location showing the remaining wall thickness (PHMSA 2016f).....	13
Figure 2-6: Excavation damage explosion (DOT 2011).....	15
Figure 2-7: Natural gas pipeline explosion from excavation damage (NTSB 2013).....	16
Figure 2-8: Aftermath of natural gas pipeline explosion in San Bruno, CA (SacBee 2010)	17
Figure 2-9: Details of the aftermath of natural gas pipeline explosion in San Bruno, CA	17
Figure 2-10: Category summary of PHMSA pipeline incidents	18
Figure 2-11: Number of reported incidents for each category by year	19
Figure 2-12: Number of fatalities reported for each category by year	20
Figure 2-13: Number of injuries reported for each category by year	20
Figure 2-14: Total cost reported for each category by year	21
Figure 2-15: Percentage of pipeline incidents caused by different categories	21

<i>Figure 2-16: Casualties associated with different causes of pipeline failure</i>	22
<i>Figure 2-17: Total cost reported for each failure category over the last 20 years.....</i>	23
<i>Figure 2-18: Total cost reported for each failure category by year</i>	23
<i>Figure 2-19: Total barrels of hazardous liquid spilled per failure category.....</i>	24
<i>Figure 2-20: Net barrels of hazardous liquid lost per failure category.....</i>	24
<i>Figure 2-21: Break rates of different pipe materials (Folkman 2018)</i>	26
<i>Figure 3-1: Electrical resistivity result for an underground mine (Sheets 2002)</i>	30
<i>Figure 3-2: GPR printout showing hyperbolic features from steel drums.....</i>	35
<i>Figure 3-3: GPR data from agricultural drainage pipes (Allred et al. 2004)</i>	36
<i>Figure 4-1: Propagation path of electromagnetic wave from transmitter to receiver.....</i>	38
<i>Figure 4-2: Conditions under which the loss tangent $\ll 1$.....</i>	45
<i>Figure 4-3: Reflection and transmission of incident electromagnetic wave at an interface.....</i>	46
<i>Figure 4-4: Refraction of incident electromagnetic wave at the interface between two media..</i>	47
<i>Figure 4-5: Organic soil model by Roth et al. showing original and corrected fitted lines</i>	50
<i>Figure 5-1: SIR-20 GPR system and antennae used for testing.....</i>	55
<i>Figure 5-2: 200 MHz GPR antenna with survey wheel</i>	55
<i>Figure 5-3: Sensor for measuring soil moisture, conductivity, and dielectric.....</i>	56
<i>Figure 6-1: The 14' long 12" diameter PVC pipe being cut</i>	61
<i>Figure 6-2: The 12" diameter PVC pipe (a) after cutting, and (b) after capping.....</i>	61
<i>Figure 6-3: The 3" diameter PVC pipes.....</i>	62
<i>Figure 6-4: The 12" diameter GFRP pipes</i>	63

Figure 6-5: Manufacturing a 3" diameter GFRP pipe.....	64
Figure 6-6: 12" diameter CFRP pipe.....	65
Figure 6-7: The 3" diameter CFRP pipes	65
Figure 6-8: Pipe configurations: (a) 6" diameter PVC with carbon fabric rings, (b) 12" diameter PVC with carbon fabric strip, (c) 12" diameter GFRP with aluminum rings, and (d) 12" diameter GFRP with aluminum strip	67
Figure 6-9: 12" diameter GFRP pipe with carbon nanoparticle overlay	68
Figure 6-10: The site for pipe burying and monitoring (source: Google Maps).....	69
Figure 6-11: The located site on WVU campus for pipe burying, with utility lines marked.....	70
Figure 6-12: Pipe layout for GPR testing	71
Figure 6-13: Pipe layout for GPR testing (short trench).....	72
Figure 6-14: (a) Arrangement of pipes in the trench, (b) soil moisture and resistivity sensor ...	72
Figure 6-15: (a) Soil sensors with data wires running through conduits to protect the wires, (b) 3" diameter pipes and sensors in the 27" deep trench.....	73
Figure 6-16: Pipe samples being buried	74
Figure 6-17: (a) The site being seeded, (b) the field restored to initial condition.....	74
Figure 7-1: Longitudinal scan over 3" diameter pipes at 2 ft. depth using 900 MHz antenna ...	77
Figure 7-2: Dataset I - Longitudinal scans over the pipe trenches using 200 MHz antenna	78
Figure 7-3: Longitudinal scan over the 3 ft. deep trench for Dataset I using 200 MHz antenna	79
Figure 7-4: Longitudinal scan over the 4 ft. deep trench for Dataset I using 200 MHz antenna	79
Figure 7-5: Longitudinal scan over the 2 ft. deep trench for Dataset I using 200 MHz antenna	80
Figure 7-6: Longitudinal scan over the 2 ft. deep trench for Dataset I using 200 MHz antenna	80

Figure 7-7: Longitudinal scan over the 2 ft. deep trench for Dataset I using 400 MHz antenna 81

Figure 7-8: Longitudinal GPR scan (left) and A-Scan (right) over Unwrapped 12" GFRP pipe 83

Figure 7-9: Longitudinal GPR scan (left) and A-Scan (right) over 12" CFRP Ring GFRP pipe 83

Figure 7-10: Longitudinal GPR scan (left) and A-Scan (right) over 12" CFRP Strip GFRP pipe 84

Figure 7-11: Longitudinal GPR scan (left) and A-Scan (right) over 12" Unwrapped PVC pipe 84

Figure 7-12: Longitudinal GPR scan (left) and A-Scan (right) over 12" Al. Foil Ring PVC pipe 85

Figure 7-13: Longitudinal GPR scan (left) and A-Scan (right) over 12" Al. Foil Strip PVC pipe 85

Figure 7-14: Longitudinal GPR scan (left) and A-Scan (right) over 6" Unwrapped PVC pipe .. 86

Figure 7-15: Longitudinal GPR scan (left) and A-Scan (right) over 6" Al. Foil Ring PVC pipe 86

Figure 7-16: Longitudinal GPR scan (left) and A-Scan (right) over 6" Al. Foil Strip PVC pipe 87

Figure 7-17: Longitudinal GPR scan (left) and A-Scan (right) over 6" CFRP Ring PVC pipe .. 87

Figure 7-18: Longitudinal GPR scan (left) and A-Scan (right) over 6" CFRP Strip PVC pipe .. 88

Figure 7-19: Longitudinal GPR scan (left) and A-Scan (right) over 12" CFRP Strip GFRP pipe 90

Figure 7-20: Longitudinal GPR scan (left) and A-Scan (right) over Unwrapped 12" GFRP pipe 90

Figure 7-21: Longitudinal GPR scan (left) and A-Scan (right) over C. Nano p. 12" GFRP pipe 91

Figure 7-22: Longitudinal GPR scan (left) and A-Scan (right) over Al. Foil Strip 12" PVC pipe 91

Figure 7-23: Longitudinal GPR scan (left) and A-Scan (right) over Unwrapped 10" GFRP pipe	92
Figure 7-24: Longitudinal GPR scan (left) and A-Scan (right) over 12" Steel pipe	92
Figure 7-25: Dataset II - Longitudinal scans over the pipe trenches using 200 MHz antenna ...	95
Figure 7-26: Longitudinal scans over 3" diameter pipes at 2 ft. deep using 200 MHz antenna .	96
Figure 7-27: Longitudinal scan over 3" diameter pipes at 2 ft. deep using 400 MHz antenna ...	97
Figure 7-28: Longitudinal scans over 12" and 10" diameter pipes at 2 ft. deep using 400 MHz antenna	98
Figure 7-29: Reflection details marked on 12" and 10" diameter pipes with 2 ft. of soil cover.	99
Figure 7-30: Dataset III - Longitudinal scans over the pipe trenches using 200 MHz antenna	101
Figure 7-31: Transverse scans over the pipes in 65 ft. long trenches using 200 MHz antenna for Dataset III	105
Figure 7-32: Transverse scans over the pipes in 36 ft. long trench using 200 MHz antenna for Dataset III	106
Figure 7-33: Comparison of returned radar signal amplitude from different pipe configurations	109
Figure 7-34: Comparison of returned radar signal amplitude from GFRP pipe configurations	110
Figure 7-35: Comparison of returned radar signal amplitude from PVC pipe configurations.	110
Figure 7-36: Circular reflector and associated hyperbolic feature	112
Figure 7-37: Velocity estimation using hyperbolic feature in GPR data (pipe 6"@3')	113
Figure 7-38: Common Mid-Point (CMP) technique	114
Figure 7-39: Plot for estimating velocity from CMP survey	115

<i>Figure 7-40: The simplified Common Mid-Point (CMP) technique</i>	115
<i>Figure 8-1: Experimental dielectric constant versus VWC.....</i>	121
<i>Figure 8-2: Comparison between dielectric models and experimental data</i>	121
<i>Figure 8-3: Comparison between the three dielectric models and experimental data</i>	123
<i>Figure 8-4: Experimental VWC versus dielectric constant.....</i>	124
<i>Figure 8-5: Comparison between inverse dielectric models and experimental data.....</i>	124
<i>Figure 8-6: Comparison between the three inverse dielectric models and experimental data..</i>	126
<i>Figure 8-7: Comparison between experimental data/model and secondary data and models..</i>	127
<i>Figure 8-8: Variation of material attenuation coefficient with antenna frequency</i>	129
<i>Figure 8-9: Variation of material attenuation coefficient with lower antenna frequencies</i>	129
<i>Figure 8-10: Variation of components of attenuation with antenna frequency</i>	132
<i>Figure 8-11: Decay of signal amplitude with travel distance</i>	133
<i>Figure 8-12: Variation of attenuation coefficient for different soil types</i>	134
<i>Figure 8-13: Variation of skin depth with antenna frequency for different soil types</i>	135
<i>Figure 8-14: Estimated penetration depths for antennae in different soil types.....</i>	136
<i>Figure 9-1: FLIR InfraCAM SD camera and type-T thermocouple.....</i>	139
<i>Figure 9-2: (a) Automated thermocouple reader and (b) Thermo Recorder.....</i>	141
<i>Figure 9-3: Insulated wooden box used for IRT testing.....</i>	141
<i>Figure 9-4: CFRP pipe for IRT testing (top), sketch showing thermocouple locations (bottom)</i> <i>.....</i>	141
<i>Figure 9-5: IRT test set-up</i>	142

Figure 9-6: Infrared thermography data at the soil surface at various stages of testing	144
Figure 9-7: Variation of soil surface (TSC, IRT) and room (Amb) temperatures with time.....	145
Figure 9-8: Soil surface temperature difference with time	145
Figure 9-9: Difference between soil surface temperature and room temperature with depth...	148
Figure 9-10: Variation of soil surface (TSC, IRT) and room (Amb) temperatures during cooling	149
Figure 9-11: Soil surface temperature difference with time during cooling.....	149
Figure 9-12: Location of field IRT test pipe.....	150
Figure 9-13: Field IRT test pipe installation details (CJD 2015).....	151
Figure 9-14: Comparison of IRT and visible image results.....	153
Figure 9-15: Infrared thermography data at the soil surface in different seasons.....	154
Figure 9-16: IRT data at the soil surface taken from close range in different seasons	155
Figure 9-17: Temperature distribution across each IRT data in Figure 9-16.....	156
Figure B-1: Longitudinal scan over 12" CFRP Strip GFRP pipe: raw data (top), data with background noise removed (middle), and reflection peaks extracted from the data (bottom) ...	177
Figure B-2: Longitudinal scan over 12" Unwrapped GFRP pipe: raw data (top), data with background noise removed (middle), and reflection peaks extracted from the data (bottom) ...	178
Figure B-3: Longitudinal scan over 12" Al. Foil Strip PVC pipe: raw data (top), data with background noise removed (middle), and reflection peaks extracted from the data (bottom) ...	179
Figure B-4: Features A and A1	180
Figure B-5: Features B and B1	180
Figure B-6: Features C and C1	181

Figure B-7: Feature D	181
Figure B-8: Feature E	182
Figure B-9: Feature F	182
Figure B-10: Transverse scan over some of the pipes in 36 ft. long trench using 200 MHz GPR antenna for Dataset I	183
Figure B-11: Transverse scan over some of the pipes in 36 ft. long trench using 200 MHz GPR antenna for Dataset II	184
Figure B-12: Transverse scan over some of the pipes in 36 ft. long trench using 400 MHz GPR antenna for Dataset II (raw data)	185
Figure B-13: Transverse scan over some of the pipes in 36 ft. long trench using 400 MHz GPR antenna for Dataset II (data with background noise removed)	186
Figure C-1: Variation of test temperature with time of heating and cooling	188
Figure C-2: Top and bottom temperature difference of the pipe during heating and cooling ..	189
Figure C-3: Inlet and outlet temperature difference of the pipe during heating and cooling ...	190
Figure C-4: Soil surface temperature difference during heating and cooling	191

LIST OF TABLES

<i>Table 2-1: Corrosion, excavation damage and material failure contribution to pipe incidents..</i>	25
<i>Table 3-1 Drillers' descriptions of borings along resistivity survey line (Sheets 2002).....</i>	31
<i>Table 4-1: Relative dielectric constants and conductivity of common subsurface materials.....</i>	48
<i>Table 5-1: GPR antenna specifications</i>	56
<i>Table 5-2: GS3 sensor specifications</i>	57
<i>Table 6-1: Material and section properties of CFRP and GFRP pipes/fabrics.....</i>	63
<i>Table 6-2: Summary of pipe samples and configurations</i>	75
<i>Table 7-1: Average soil dielectric properties during data collection</i>	76
<i>Table 7-2: Description of features marked in Figure 7-29</i>	99
<i>Table 7-3: Target depth estimated using hyperbolic fitting</i>	113
<i>Table 8-1: Measured soil dielectric properties</i>	120
<i>Table 8-2: Dielectric models derived from experimental data.....</i>	122
<i>Table 8-3: Inverse dielectric models derived from experimental data.....</i>	126
<i>Table 8-4: Material attenuation values for the GPR datasets.....</i>	128
<i>Table 8-5: Material properties for scattering attenuation computation</i>	130
<i>Table 8-6: Components of total signal attenuation</i>	130
<i>Table 8-7: Remaining signal amplitude after two way travel to 4 ft. depth</i>	133
<i>Table 8-8: Phase coefficient and wavelength of the antennae used for GPR test.....</i>	138
<i>Table 9-1: Estimated variation of soil surface temperature with depth.....</i>	147
<i>Table 9-2: Field IRT test pipe parameters</i>	152

NOMENCLATURE

A number of labels, terms, and acronyms are frequently used in this document for brevity. These terms and acronyms may be ambiguous, or they may not be familiar to all readers. The definitions of terms and acronyms given below apply throughout this document.

- **AC:** Alternating Current
- **AC:** Asbestos Cement
- **AEC:** Advisory and Examining Committee
- **Amb:** Ambient/room temperature
- **ASCE:** American Society of Civil Engineers
- **BI:** Bottom Inlet temperature (inlet temperature measured at the bottom of the pipe)
- **BO:** Bottom Outlet temperature (outlet temperature measured at the bottom of the pipe)
- **CFRP:** Carbon Fiber Reinforced Polymer
- **CI:** Cast Iron
- **CIA:** Central Intelligence Agency
- **CMP:** Common Mid-Point
- **CP:** Condensate Pumped pipeline or Creative Pultrusions Inc.
- **CRIM:** Complex Refractive Index Model
- **CSC:** Concrete Steel Cylinder
- **DC:** Direct Current
- **DDB:** Dortmund Data Bank
- **DI:** Ductile Iron
- **DOT:** US Department of Transportation
- **EIA:** US Energy Information Administration
- **EM:** Electromagnetic
- **EMIS:** Electromagnetic Induction Spectroscopy
- **ERT:** Electrical Resistivity Tomography
- **ESB:** Engineering Sciences Building
- **FHWA:** Federal Highway Administration
- **FRP:** Fiber Reinforced Polymer
- **GFRP:** Grass Fiber Reinforced Polymer

- **GPR:** Ground Penetrating Radar
- **GSSI:** Geophysical Survey Systems, Inc.
- **HPS:** High Pressure Steam
- **IRT:** Infrared Thermography
- **MRB:** Mineral Resources Building
- **NACE:** NACE International
- **NaCl:** Sodium Chloride
- **NTSB:** National Transportation Safety Board
- **PRT:** Personal Rapid Transit
- **PST:** Pipeline Safety Trust
- **PVC:** Polyvinyl Chloride
- **R-Value:** Relative insulating value (unit of $\text{ft}^2 \cdot ^\circ\text{F} \cdot \text{h}/\text{BTU}$)
- **SCH:** Schedule
- **SDR:** Standard Dimension Ratio
- **TC:** Temperature measured at the top of the pipe, midway between the inlet and the outlet
- **TI:** Top Inlet temperature (inlet temperature measured at the top of the pipe)
- **TO:** Top Outlet temperature (outlet temperature measured at the top of the pipe)
- **TSC:** Temperature at top of the soil over mid portion of the pipe
- **USDOT:** US Department of Transportation
- **USDOT-PHMSA/ PHMSA:** Pipeline and Hazardous Materials Safety Administration
- **UAV:** Unmanned Aerial Vehicle
- **VWC:** Volumetric Water Content
- **WT:** Water Temperature
- **WVU-CFC:** West Virginia University Constructed Facilities Center

CHAPTER 1

INTRODUCTION

1.1 BACKGROUND/OVERVIEW

The pipeline industry in the United States (U.S.) is an important component of the nation's economy, and essential in the standard of living of its citizens. Energy pipelines (pipelines used in transporting fuel/energy products) also play an important role in ensuring the security of the nation. The pipeline infrastructure is the primary means of transporting water, sewage, natural gas, petroleum products, and the majority of hazardous liquids from production basins, points of generation, and the ports to areas of consumption, storage, or disposal.

Best available data in 2015 indicates that, energy pipelines in the United States alone accounted for about 65% of the world's energy pipeline network (CIA n.d.). The role played by pipelines in the United States cannot be overestimated; almost all natural gas in the United States and a greater portion of crude oil and petroleum products are transported by pipelines.

According to data available from the U.S. Energy Information Administration (EIA), the US consumes about 100 quadrillions Btu of energy annually. Natural gas accounts for 28% of the energy commodities consumed in the United States while petroleum products account for 35% (Figure 1-1a). Thus natural gas and petroleum products account for about 63% of the total energy consumption in the United States. Natural gas is almost entirely transported by pipelines while over 70% of crude oil and petroleum products are transported by pipelines (Figure 1-1b). It can therefore be concluded that, 53% of all energy commodities consumed in the United States are transported by pipelines. In addition, the percentage of crude oil/petroleum products transported by pipelines in the United States has been increasing since 2005, while the percentage transported by other modes of petroleum transport have decreased over the same period as shown in Figure 1-2 (EIA n.d., USDOT 2017).

Natural gas consumption in the U.S. has been on the ascendancy since 2005, while coal and petroleum product consumption has been decreasing over the same period, with total energy consumption remaining almost constant (Figure 1-3). The U.S. Energy Information

Administration’s projection of primary energy consumption by fuel type predicts the percentage of natural gas consumption to increase over the coming years (Figure 1-4). Energy pipelines are therefore going to play an increasingly important role in the U.S. energy commodity sector

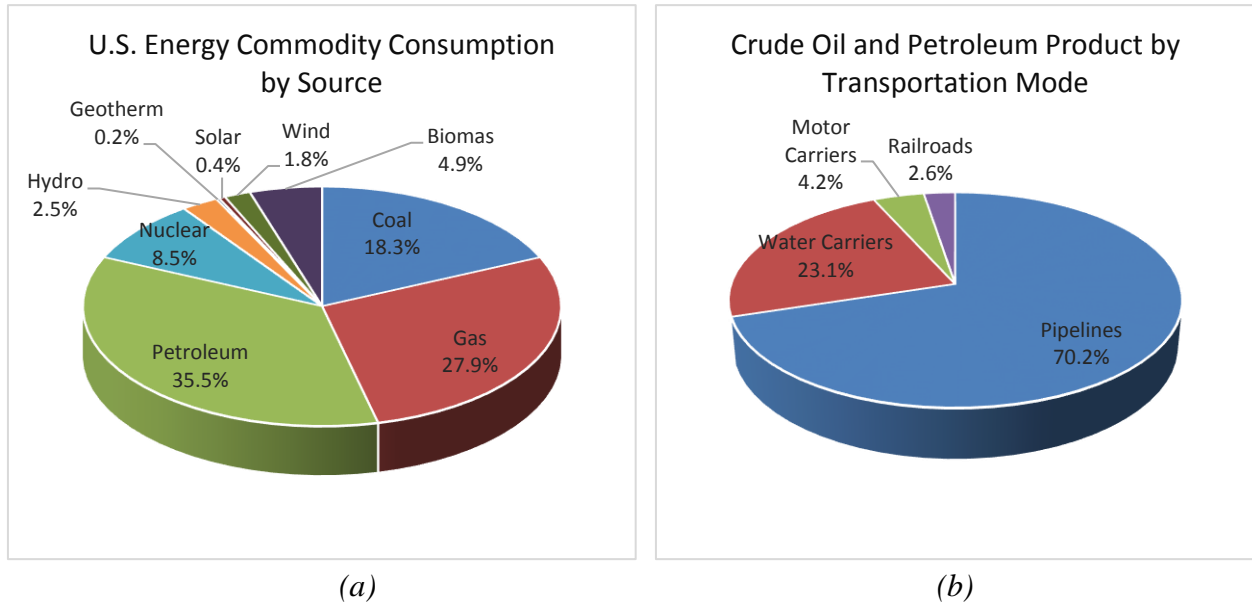


Figure 1-1: (a) 2014 U.S. Primary energy consumption by source (EIA n.d.) and (b) crude oil and petroleum product by transportation by mode in 2009 (USDOT 2017)

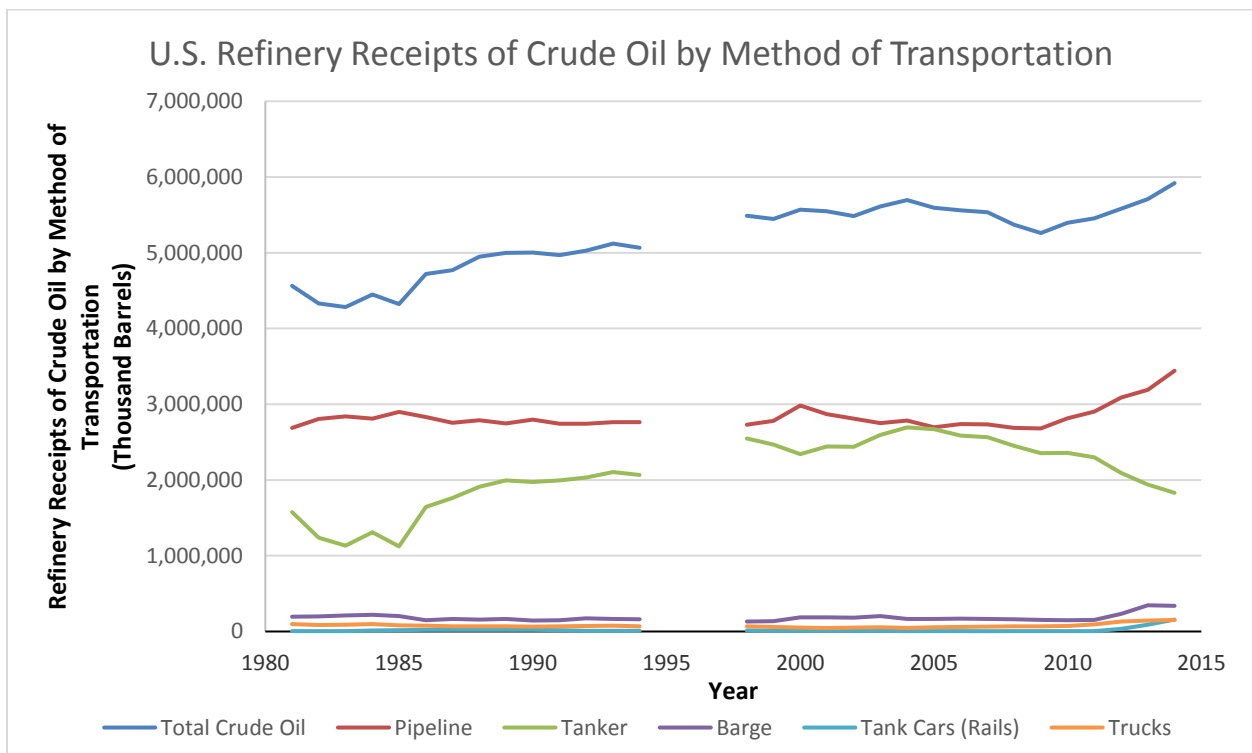


Figure 1-2: U.S. refinery receipts of crude oil by method of transportation (EIA n.d.)

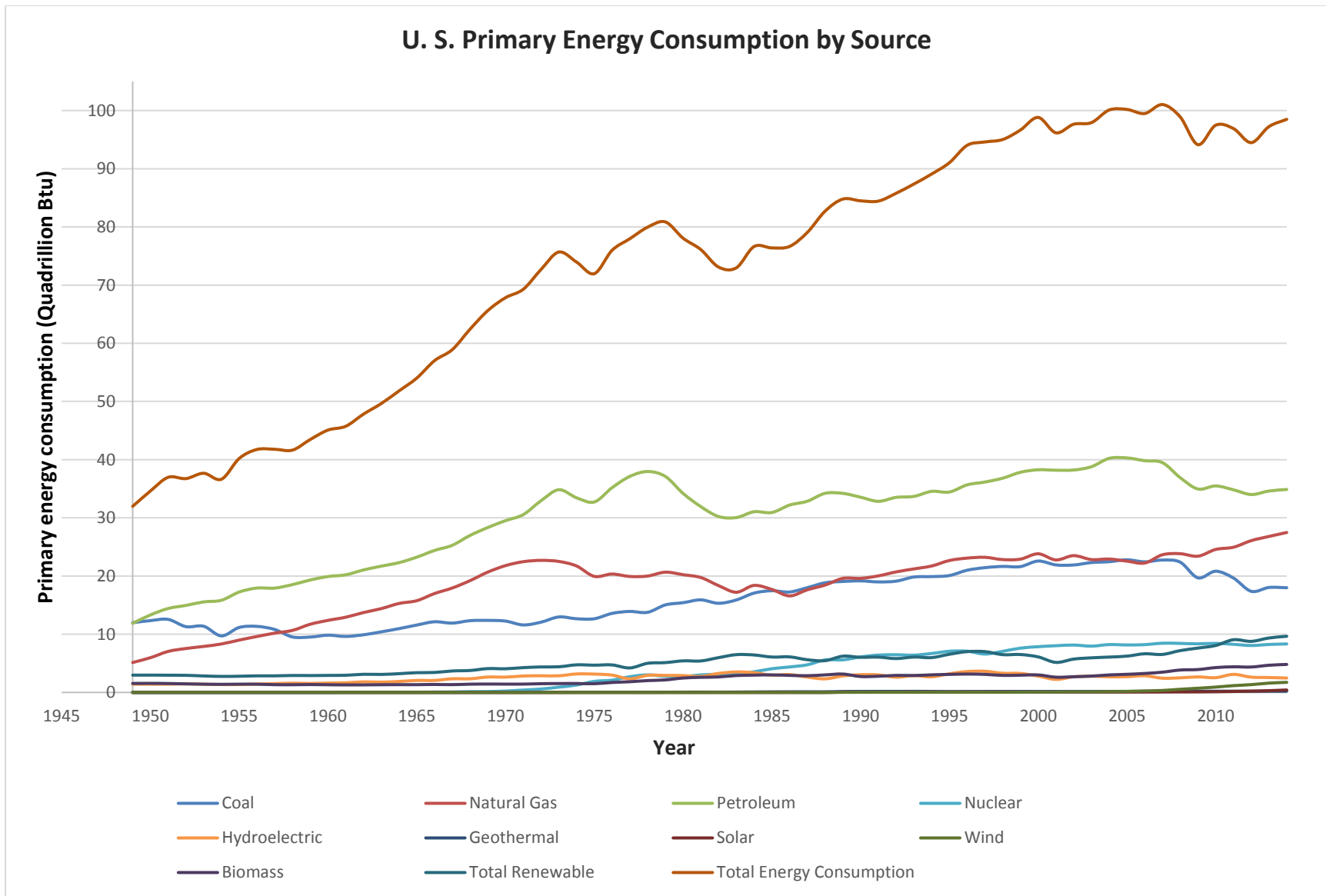


Figure 1-3: U.S. Primary energy consumption by source (EIA n.d.)

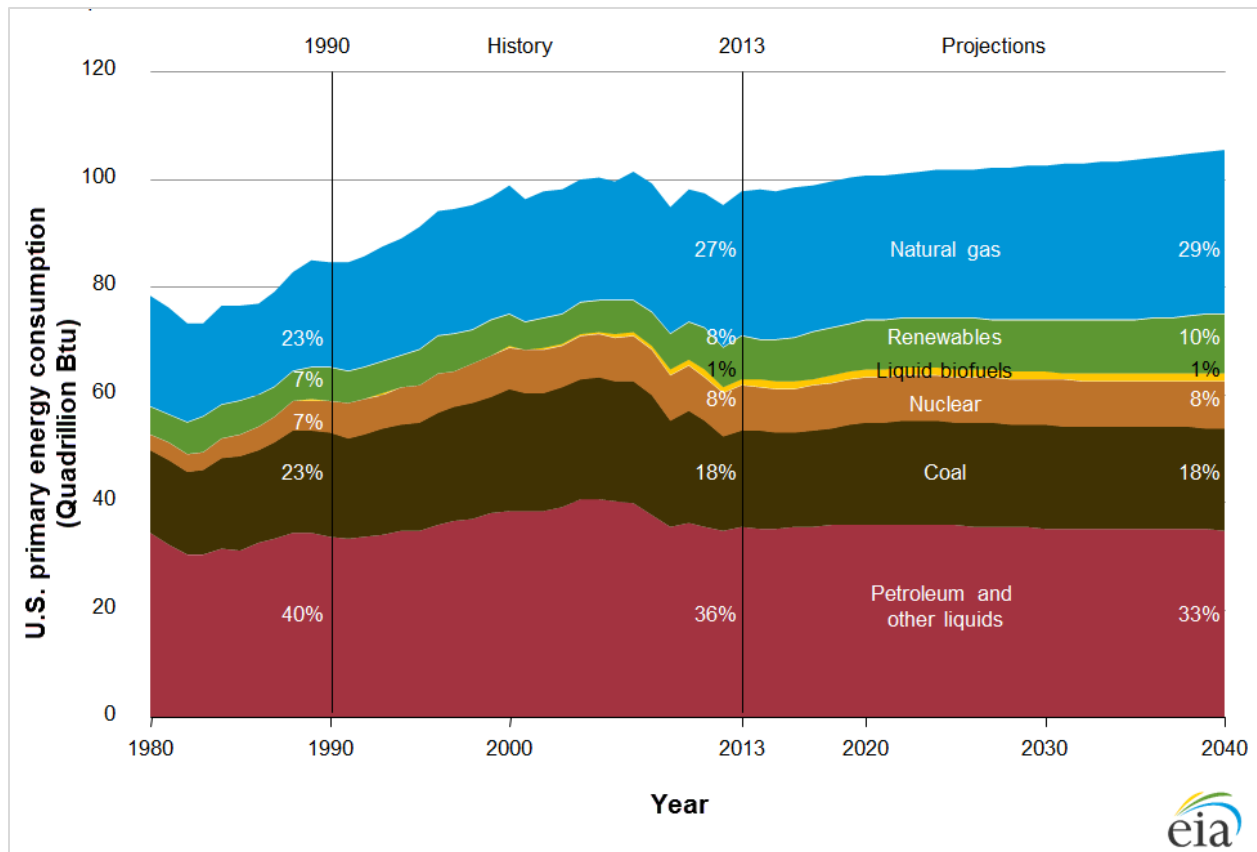


Figure 1-4: Primary energy consumption by type, 1980-2040 (EIA 2015)

The importance of pipelines (particularly energy pipelines) “to the U.S. economy, [security,] and our standard of living requires that these assets be safely maintained and appropriately expanded to sustain demand.” (PHMSA 2015).

Pipelines remain the safest means of transporting natural gas, crude oil, and petroleum products, nonetheless, the pipeline industry is having major challenges; including corrosion of steel/metallic pipes (leading to oil spills, explosions, and deaths), excavation damage (damage to existing pipelines during excavation work), and pipeline material/weld/equipment failure as discussed in Chapter 2 of this document. These pipeline incidents often result in catastrophic failures, with associated fatalities, injuries, property loss, and environmental contamination. The Pipeline and Hazardous Materials Safety Administration (PHMSA), under U.S. Department of Transportation (USDOT), has identified corrosion as the leading cause of failure in metallic pipelines, and excavation damage as the leading cause of on shore pipeline incidents (PHMSA 2015).

1.2 RESEARCH PROBLEM AND FOCUS

The focus of this research is to work on a solution that can prevent excavation damage and pipe material failure for non-corrosive (non-metallic) pipes by making them detectable in-situ.

The problems associated with corrosion of steel/metallic pipelines, and to some extent pipe material failure, can be addressed by using non-corrosive materials such as the commonly available and widely used PVC (Polyvinyl Chloride) or other plastics for water, sewer, or low pressure gas lines and advanced composite materials such as Glass Fiber Reinforced Polymer (GFRP) for transporting high-pressure oil and natural gas products. However, buried PVC and GFRP materials are not easily detectable using the available ground sensory technologies, which can lead to increased excavation damage of pipelines during building/construction and rehabilitation works. Tracer wires are employed in some applications to make non-metallic pipelines locatable, but these wires can break over time and render the pipeline difficult to locate. The inability to easily locate buried GFRP and other non-metallic pipes has limited the adoption of such pipe materials in the oil and gas industry. Making these pipe materials detectable when buried will therefore help accelerate their adoption, and hence provide solutions to the corrosion related pipeline failure incidents as well.

1.3 FIBER REINFORCED POLYMER (FRP) MATERIALS AND WHY GFRP

Fiber Reinforced Polymer (FRP) composite has emerged as alternative material in many industries due to its better engineering properties that are desirable to manufacturers and infrastructure developers. FRPs generally have high specific strength, high specific modulus, low specific weight, high resistance to corrosion, high fatigue strength, and low coefficient of thermal expansion compared to conventional materials like steel. FRPs (particularly Carbon Fiber Reinforced Polymers – CFRP and Glass Fiber Reinforced Polymers – GFRP) are increasingly being used in infrastructure development applications – both for new constructions and rehabilitation of aging infrastructure (Kavi 2015, GangaRao et al. 2007, Mallick 2007) – with tremendous benefits. There is therefore a great potential for fiber composite material application in the pipeline transportation industry (Rawls 2015). GFRP is less expensive compared to CFRP, hence GFRP is used more in infrastructure development application.

1.4 RESEARCH OBJECTIVES AND SCOPE

To help address some of the major challenges associated with transportation by pipelines, this research is focused on investigating alternative strategies for making buried non-metallic pipelines easily detectable using available ground sensory technologies – Ground Penetrating Radar (GPR) and Infrared Thermography (IRT). The primary objectives of this research are as follows:

1. Develop, investigate, and compare alternative strategies for locating buried pipelines created with Fiber Reinforced Polymer (FRP) materials – particularly Carbon and Glass fibers (CFRP and GFRP).
2. Investigate the potential and feasibility for using CFRP fabric, carbon nanoparticle, or aluminum overlay to increase the detectability of GFRP and PVC (plastic) pipes with Ground Penetrating Radar (GPR).
3. Investigate and compare the detectability of the above pipes using GPR with antennas of different frequencies.
4. Investigate the possibility of detecting buried pipe transporting hot liquid, using Infrared Thermography (IRT).
5. Evaluate the above strategies for making non-metallic pipelines detectable using ground sensory technologies, and recommend the most appropriate configuration to be used in the pipeline industry in order to increase the detectability of buried non-metallic pipes in the field.

The above research objectives were achieved by:

1. Producing sample CFRP pipes by wrapping carbon fabric around cardboard tubes.
2. Using CFRP fabric, carbon nanoparticle, or aluminum overlay for GFRP and PVC (plastic) pipes to increase detectability by GPR. This setup includes the following pipe configurations:
 - i. Use CFRP fabric overlay in the form of strips or rings on GFRP and PVC pipes.
 - ii. Use aluminum foil/tape overlay in the form of strips or rings on GFRP and PVC pipes.
 - iii. Use multiple pipe diameters for both pipe materials (GFRP and PVC).
 - iv. Use carbon nanoparticle overly on a GFRP pipe.

3. Burying variations of the above pipes (including different pipe materials, diameters, pipe surface configurations, and different depth of soil cover over the buried pipes) for GPR investigation.
4. Using GPR with different antenna frequencies to investigate and compare the detectability of the buried pipes.
5. Burying a CFRP pipe in a wooden box filled with soil and pumping hot water through it over a 10 day period, while the soil surface temperature variation is recorded using Infrared Thermography (IRT) and thermocouples.
6. Finally, results obtained from the above strategies were compared and the most promising configuration and test setting/parameters for making non-metallic pipelines detectable in the field using ground sensory technologies has been recommended for possible future implementation in the pipeline industry.

1.5 RESEARCH SIGNIFICANCE

Advanced non-metallic composite pipe materials such as Glass Fiber Reinforced Polymer (GFRP) have desirable engineering and mechanical properties that can help address some of the challenges encountered in the pipeline transportation industry. However, limitations such as difficulty in locating buried GFRP pipes are preventing the adoption of such materials in the pipeline industry.

This research has the potential of having a significant impact on the pipeline industry. First, it will prevent corrosion related pipeline failures by aiding the adoption of alternative non-corrosive material for pipeline fabrication. In the case of GFRP pipes with carbon fabric, carbon nanoparticle, or aluminum foil overlays, this will provide an advanced material with better engineering and desirable properties such as low density, high specific strength and high specific modulus. Additionally, these alternative and advanced materials will be detectable in buried state using GPR and/or IRT, thereby preventing excavation damage of pipelines. Finally, the advanced materials with better engineering properties will significantly reduce the pipeline failure incidents caused by material damage.

Since corrosion, excavation damage, and material failure are the major causes of all pipeline incidents reported to PHMSA (see Section 2-2), this research – and its subsequent implementation by industry stakeholders – will significantly reduce pipeline failures, and minimize the associated

negative impact of such failures. This research focusing on detection of buried non-metallic pipes will therefore play a crucial role in making the pipeline transportation infrastructure sound, durable, environmentally friendlier, safer, and more cost effective while minimizing leakage over its service life.

1.6 RESEARCH COLLABORATION

This research involves collaboration with other institutions, including the funding and feedback on industry needs from U.S. Department of Transportation – Pipeline and Hazardous Materials Safety Administration (USDOT-PHMSA), and supply of composite pipes from a composite manufacturer (Creative Pultrusions, Inc.) to enhance the implementation of the proposed research. This collaboration also includes public debriefing of the research findings to industry stakeholders which can help in future implementation of the findings of this research project in the pipeline industry.

1.7 ORGANIZATION

A brief overview of the organization of this dissertation is as follows:

- **Chapter 1**
 - This chapter gives the background and outlines the objectives of this research.
- **Chapter 2**
 - This chapter provides a review of the current state of the pipeline infrastructure in the US. It provides summary of major challenges facing the pipeline industry, as well as some of the major pipeline incidents in recent times. Pipeline incident issues such as cause of failure, cost, injuries, fatalities, and environmental impact are discussed.
- **Chapter 3**
 - This chapter reviews the most commonly used buried object detection techniques, and also discusses recent advances in buried non-metallic pipeline detection. Particularly, the use of ground penetrating radar, its advantages and limitations are discussed.
- **Chapter 4**
 - The theory of ground penetrating radar and the specific concepts and parameters that apply to the current study are presented in this chapter.

- **Chapter 5**
 - Ground penetrating radar equipment, sensors, and data processing techniques used in this study are presented/discussed in this chapter
- **Chapter 6**
 - This chapter presents the experimental set up for GPR testing. Materials used for the research, sample preparation steps, and the various test samples are discussed in detail.
- **Chapter 7**
 - Ground penetrating radar testing of the buried pipe samples, test data, data processing, detailed result interpretation are provided in this chapter.
- **Chapter 8**
 - Numerical models that help estimate soil dielectric properties from the volumetric water content or dielectric constant are presented. Also, computations that help explain the performance and penetration depths of different GPR antennae used in the study is presented in this chapter.
- **Chapter 9**
 - This chapter investigates the potential for detecting buried pipelines transporting hot fluids by using infrared thermography. Infrared thermography test set up, tests, results, and data interpretation are presented in this chapter.
- **Chapter 10**
 - A summary of the scope of work conducted to fulfill the proposed research objectives, and the key findings are highlighted in this chapter. Finally, the chapter provides recommendations for field implementation of the research results as well as recommendations for future work in this area.

CHAPTER 2

STATE OF THE PIPELINE INFRASTRUCTURE

2.1 INTRODUCTION

While pipelines remain the safest means of transporting hazardous materials, there still exists significant room for improvement. In addition, increasing demand for these materials in homes and industries coupled with increasing production output require that the necessary transportation infrastructure be expanded and appropriately maintained to serve the need (Vealey 2016, PHMSA 2015). This chapter reviews some of the recent pipeline incidents that call for more efforts and resources to be put in making the pipeline infrastructure safer than it has been.

2.2 PHMSA PIPELINE INCIDENTS CAUSES

Over the past 20 years (1996-2015), there have been a total of 11,192 pipeline incidents reported to the PHMSA¹. Out of this total, 5,663 fall under significant² incidents, while 862 fall under the serious³ incidents category. PHMSA broadly groups pipeline incidents under seven (7) main categories (corrosion, excavation damage, incorrect operation, material/weld/equipment failure, natural force damage, other outside force damage, and all other causes) based on the reported cause of the incident. These failure causes are further broken down into different sub-categories, with material/weld/equipment failure having the highest number of sub-categories.

Corrosion, excavation damage and material/weld/equipment failure are the three main leading causes of pipeline incidents in the United States, contributing to 66% of all energy pipeline failures (Figure 2-1). The following sub-sections look at these three causes of pipeline failure.

¹ Data for all the charts/plots and tables in this chapter are obtained from the PHMSA Pipeline Incident 20 Year Trends, unless otherwise referenced. Links to these data are provided in the reference section as PHMSA 2016a, PHMSA 2016b, PHMSA 2016c, and PHMSA 2016d.

² PHMSA defines Serious Incidents as those including a fatality or injury requiring in-patient hospitalization.

³ PHMSA defines Significant Incident as those including any of the following conditions: (1) Fatality or injury requiring in-patient hospitalization; (2) \$50,000 or more in total costs, measured in 1984 dollars; (3) Liquid releases resulting in an unintentional fire or explosion (PHMSA 2016a). Details of PHMSA incident definitions are in Appendix A.

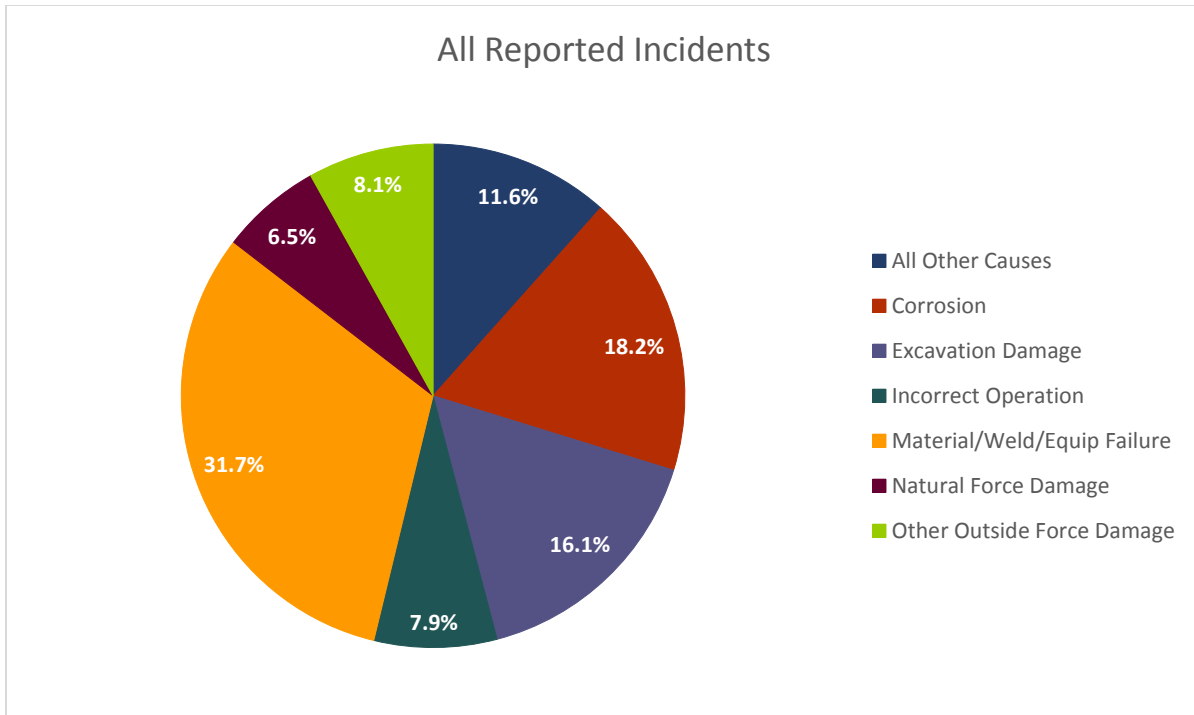


Figure 2-1: 20 year reported incident cause breakdown (1996-2015)

2.2.1 Corrosion

Corrosion is one of the leading causes of failures in oil, gas, and hazardous liquid transportation pipelines (both onshore and offshore) in the United States. It is also a threat to oil and gas gathering systems, as well as water and sewage transportation/distribution pipelines and systems.

NACE International (NACE) and the U.S. Federal Highway Administration (FHWA) currently estimate the total direct cost associated with corrosion in the U.S. to be \$276 billion (in 1998 dollars). Corrosion of gas and liquid transmission pipelines represents \$7 billion of this total. Gas distribution accounts for \$5 billion, while drinking water and sewage systems represents \$36 billion. This results in a total direct corrosion cost of \$48 billion associated with transportation pipelines. If indirect costs associated with corrosion are added, the above amount doubles to \$96 billion per year – in 1998 dollars (Koch et al. 2002, Baker 2008).

Corrosion of pipelines has directly resulted in major pipeline incidents/failures in recent history, resulting in fatalities and injuries to industry personnel and the general public, as well as financial losses. These pipeline failures also result in environmental contamination, with significant impact on terrestrial and aquatic life.

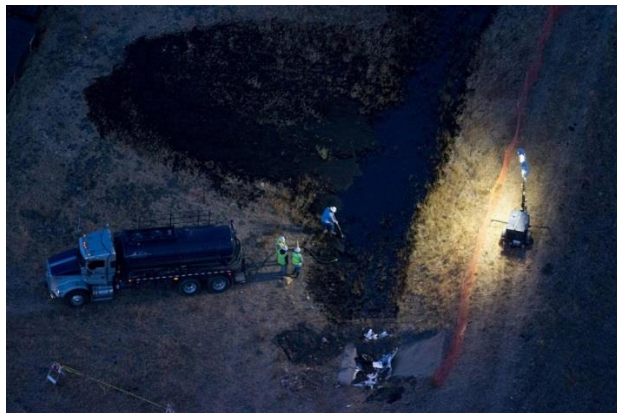
On May 19 2015, a 24-inch diameter pipeline operated by Plains Pipeline, LP ruptured in Santa Barbara County, California. This incident, which is as a result of external corrosion of a pipeline section (Figure 2-2), resulted in the release of about 2,934 barrels of heavy crude oil that contaminated the surrounding areas and beaches. An estimated 500 barrels of crude oil entered the Pacific Ocean. (Figure 2-3). A total cost of \$143 million was reported for the incident (PHMSA 2016e and 2016f). Figures 2-4 and 2-5 show corrosion products deposited on the pipe surface and laser scan rendering of the failure surface respectively.



(b) The failed pipe with surrounding insulation and coating

(b) The failed with surrounding insulation and coating removed

Figure 2-2: External surface of the failed pipeline section (PHMSA 2016e and 2016f)



(b) Clean-up at the rupture site

(b) Clean-up at a contaminated beach

Figure 2-3: Spilled crude oil from the rupture being cleaned (Nicholson 2015)

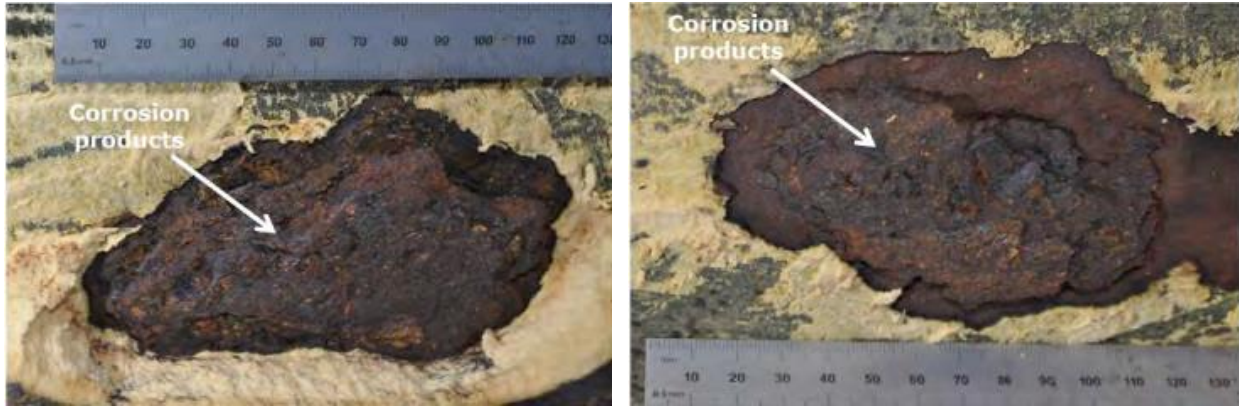


Figure 2-4: Corrosion products deposited on the pipe surface (PHMSA 2016f)

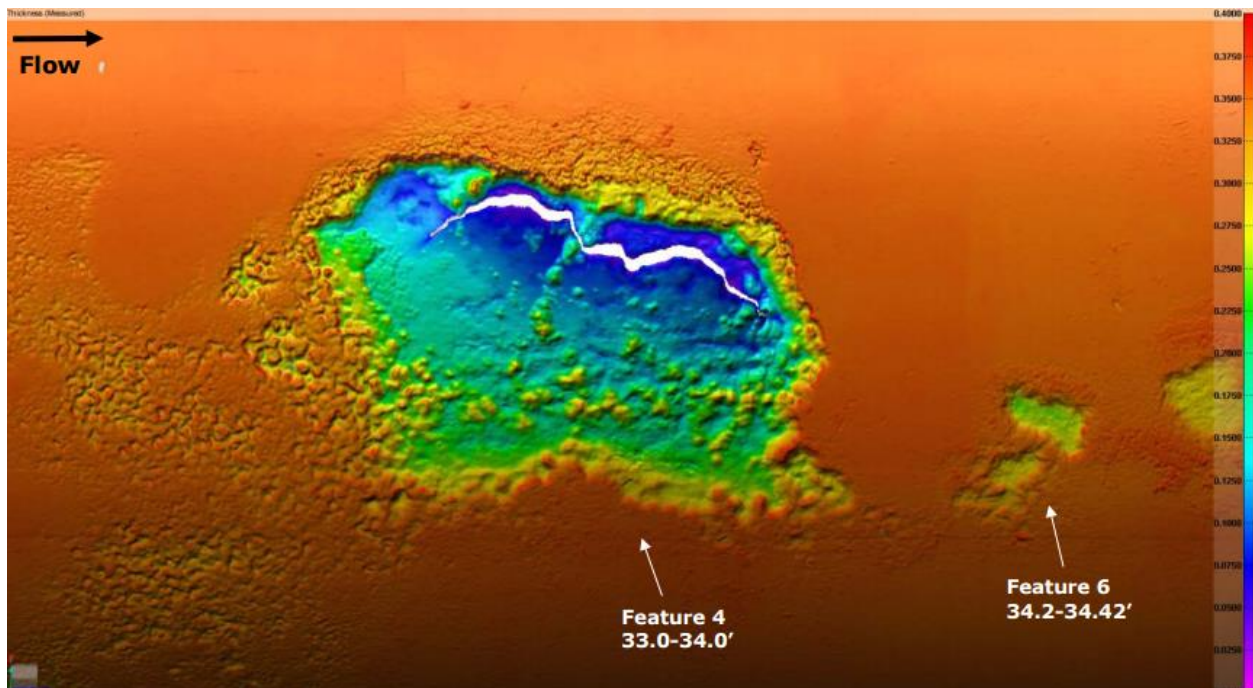


Figure 2-5: Laser scanning rendering of the failure location showing the remaining wall thickness (PHMSA 2016f)

2.2.2 Excavation Damage

According to the U.S. Department of Transportation’s Pipeline and Hazardous Materials Safety Administration (PHMSA), “One of the greatest challenges to safe pipeline operations is accidental damage to the pipe or its coating that is caused by someone inadvertently digging into a buried pipeline.” (PHMSA 2014a) Data available from PHMSA indicates that, excavation damage has

accounted for over 20% of all significant natural gas and hazardous liquid pipeline incidents over the past 20 years. About one-third (33%) of all serious pipeline incidents were caused by excavation damage over the same time period. On gas distribution systems, excavation damage is the leading cause of failure; it accounted for more than 36% of all significant pipeline incidents and more than 34% of all serious pipeline incidents, this is substantially greater than any other cause of pipeline failure. Excavation damage also accounted for over 32% of all serious incidents in both gas transmission and hazardous liquid pipelines since 1996, making it the number one cause of failure on those pipeline systems. Of all causes of pipeline failure, fatalities and injuries are most likely to occur with excavation damage (see Figure 2-16 in Section 2.2.4). Thus excavation damage is a major cause (second leading cause) in significant pipeline incidents and the leading cause of serious pipeline incidents, resulting in many deaths and injuries, as well as substantial property damage.

In addition to fatalities, injuries, and property damage, pipeline incidents caused by excavation damage also result in significant costs, environmental damages/contaminations, and unintentional fire or explosions (PHMSA 2017, PST 2015). Excavation damage mostly results in immediate pipeline failure due to line hits with excavation equipment; however, there have been failures that resulted from mechanical damage inflicted on the pipeline from previous excavation damage (Baker 2009). In the delayed failure mode, damage to pipeline coating can allow accelerated corrosion to occur; a combination of the resulting corrosion and the physical damage to the pipe material from any accompanying dents or scrapes can result in increased potential for future failure. “Unreported mechanical damage can have serious consequences” (Baker 2009), as was the case of the Edison, New Jersey, and Bellingham, Washington natural gas and gasoline explosions respectively (Baker 2009). According to the Pipeline Safety Trust (PST), “The threat from excavation damage is larger than [*sic*] the PHMSA data implies” (PST 2015).

Excavation/mechanical damage of pipelines can be caused by any of the typical forms of excavation including digging, grading, trenching, boring, etc. These activities are usually undertaken during highway maintenance, general construction, and many farming activities, as well as new home construction and routine homeowner activities (PHMSA 2014a). For this reason, PHMSA, pipeline industry stakeholders, regulators and safety advocates/organizations encourage anyone planning an excavation work to make the required “One-Call” (call 811) before digging.

This enables pipeline/utility owners and operators to locate and mark all buried facilities (including pipelines) around the site before the excavation activity to prevent accidents related to excavation damage. Figures 2-6 and 2-7 show some of the recent pipeline incidents that resulted from excavation damage in Thomson, GA and Cleburne, TX respectively in 2010.



Figure 2-6: Excavation damage explosion (DOT 2011)



(a) Natural gas burning from 36" diameter pipeline (b) Ruptured section of the pipeline

Figure 2-7: Natural gas pipeline explosion from excavation damage (NTSB 2013)

2.2.3 Material/Weld/Equipment Failure

Pipeline incidents attributed to material, weld, or equipment failure tend to be broad, with many sub-categories of cause of failure. Some of these sub-categories are attributed to defective material manufacturing and/or fabrication process, inadequate construction and installation methods and technologies used. Majorities of pipeline incidents in this category are as a result of fitting/equipment failure and joints/welds failure.

Of all failures in the PHMSA pipeline incident database, failures caused by material/weld/equipment failure are the most common. Failures under this category have the highest total reported cost of all pipeline incidents between 1996 and 2015 (the cost is particularly influenced by the San Bruno explosion in 2010, which resulted in over \$558 million in reported cost). The devastating impact of the San Bruno natural gas pipeline incident is illustrated by Figures 2-8 and 2-9.



Figure 2-8: Aftermath of natural gas pipeline explosion in San Bruno, CA (SacBee 2010)



*(a) A massive fire in San Bruno, CA
(SacBee 2010)*



*(b) Picture of a burned car in front of several
destroyed houses (NTSB 2011)*

Figure 2-9: Details of the aftermath of natural gas pipeline explosion in San Bruno, CA

2.2.4 PHMSA Pipeline Incident Summary

An analysis of the pipeline incidents reported to the PHMSA between 1996 and 2015 indicates that, out of the total 11,192 incidents, 51% (5,663) fell under significant incidents while only 8% (862) fell under serious incidents (Figure 2-10). However, serious incidents (and hence significant incidents) accounted for almost all of the fatalities and injuries reported – 96% and 98% respectively. When it comes to the total reported cost associated with these incidents, significant incidents accounted for 97% even though it was only about half of the number of reported incidents, while serious incidents contributed a smaller share of 11% as shown in Figure 2-10.

Figures 2-11 through 2-14 show details of these parameters according to the year of report. In 2002, PHMSA changed the definition for a reportable hazardous liquid incident from “Loss of 50 or more barrels (8 or more cubic meters) of hazardous liquid or carbon dioxide” to “Release of 5 gallons (19 liters) or more of hazardous liquid or carbon dioxide” (PHMSA 2014b). This resulted in sharp increase in “All Incidents” shown in Figure 2-11. This change however did not affect the significant and serious incidents reported. It is further observed from Figures 2-12 and 2-13 that, serious incidents (and hence significant incidents) accounted for 100% of fatalities and injuries in most years, while significant incidents accounted for almost all of the reported cost (Figure 2-14).

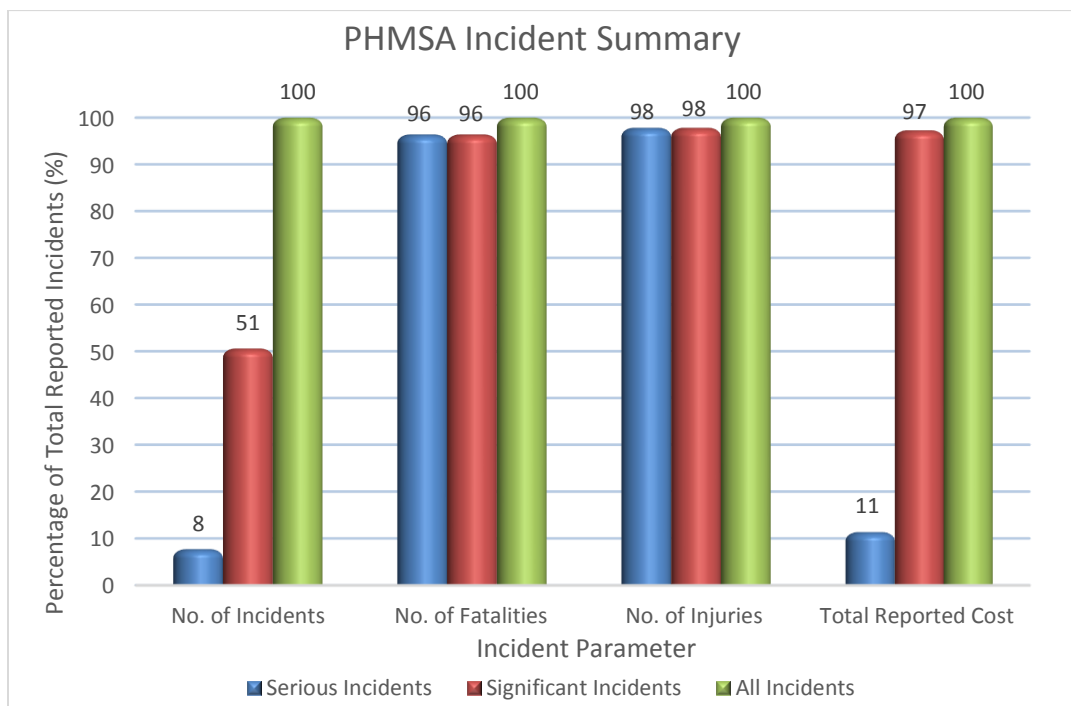
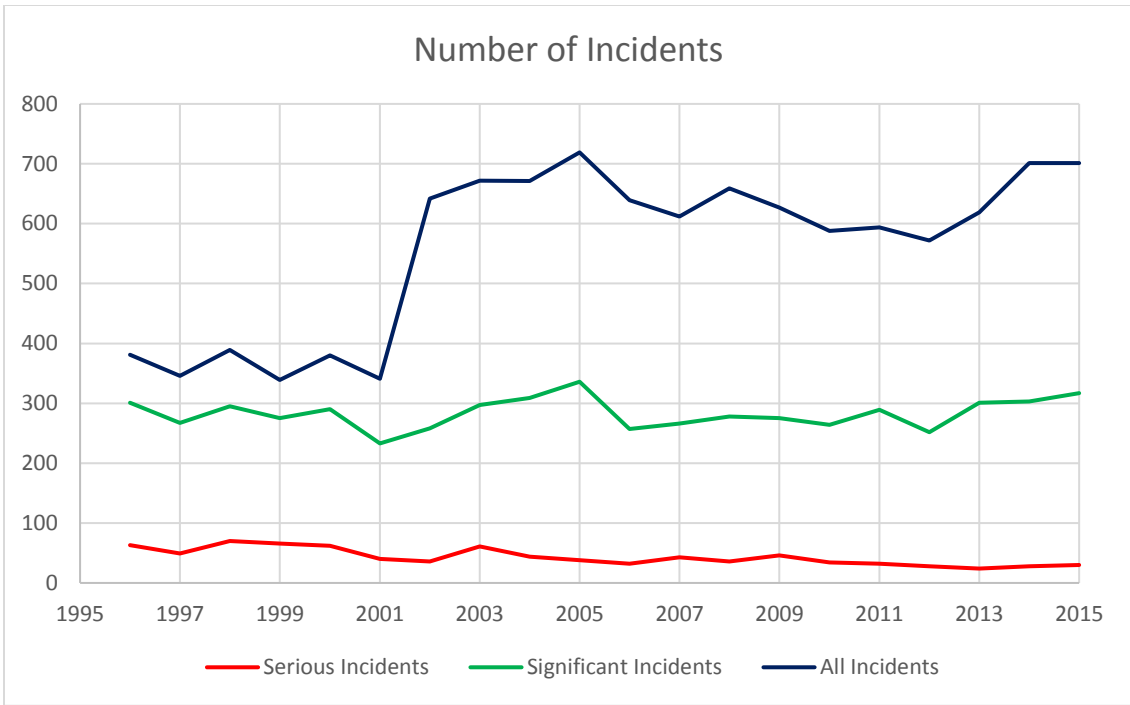
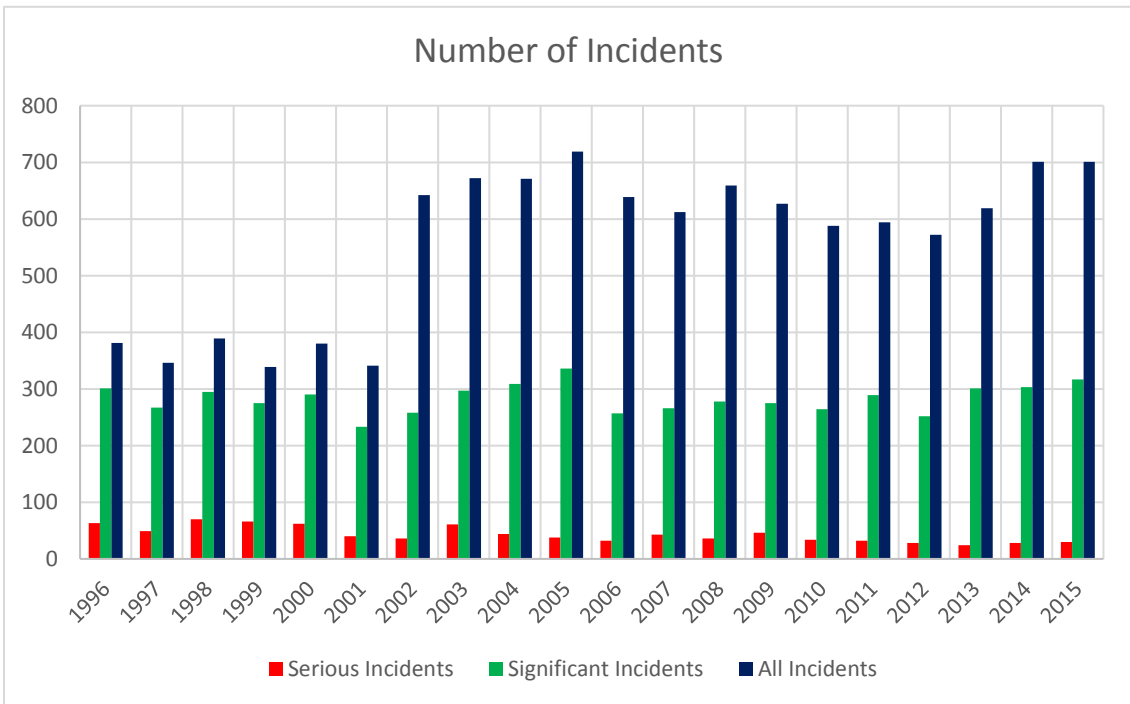


Figure 2-10: Category summary of PHMSA pipeline incidents



(a) Line plot of reported incidents



(b) Bar plot of reported incidents

Figure 2-11: Number of reported incidents for each category by year

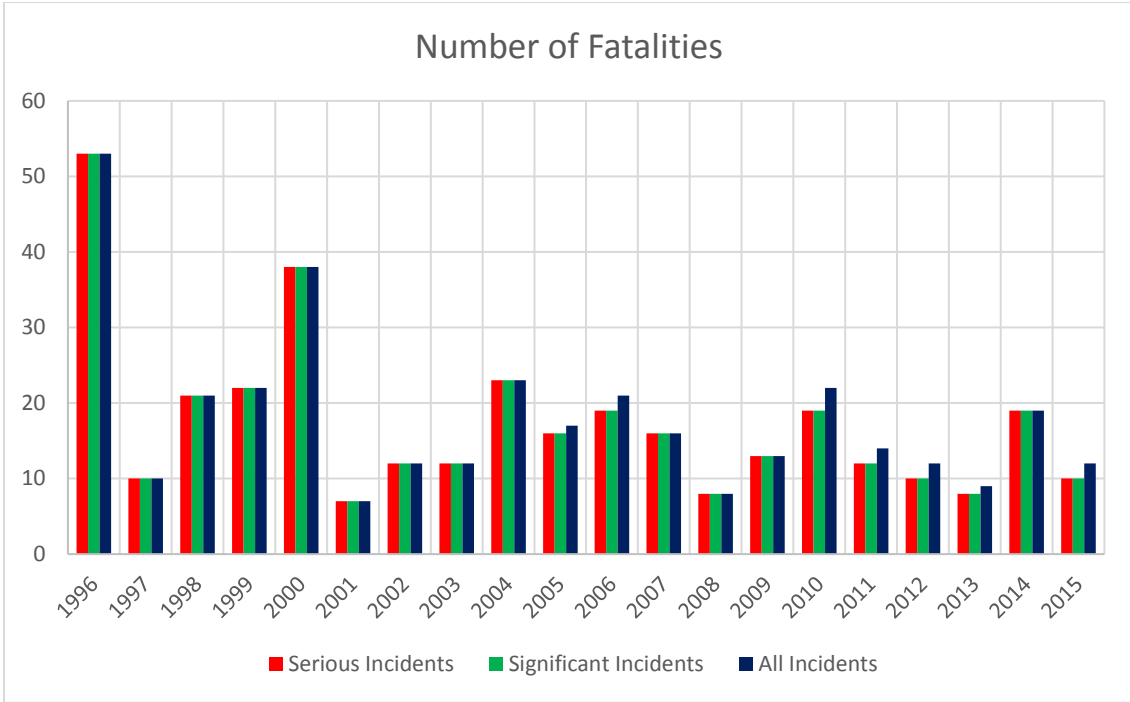


Figure 2-12: Number of fatalities reported for each category by year

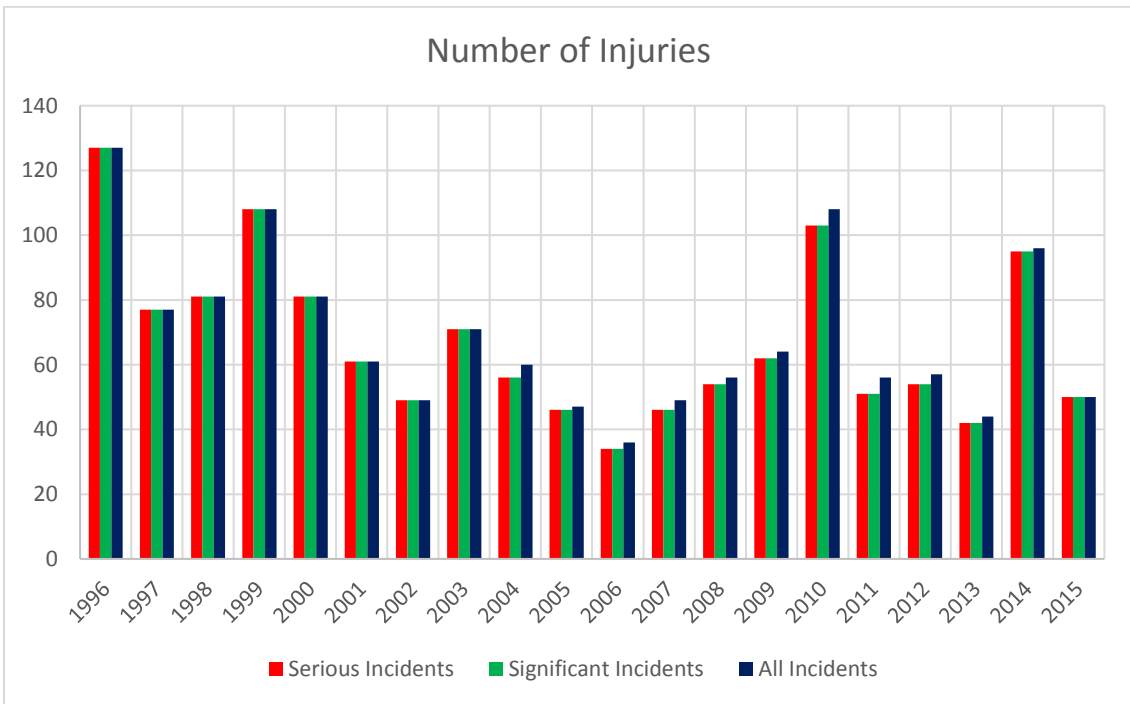


Figure 2-13: Number of injuries reported for each category by year

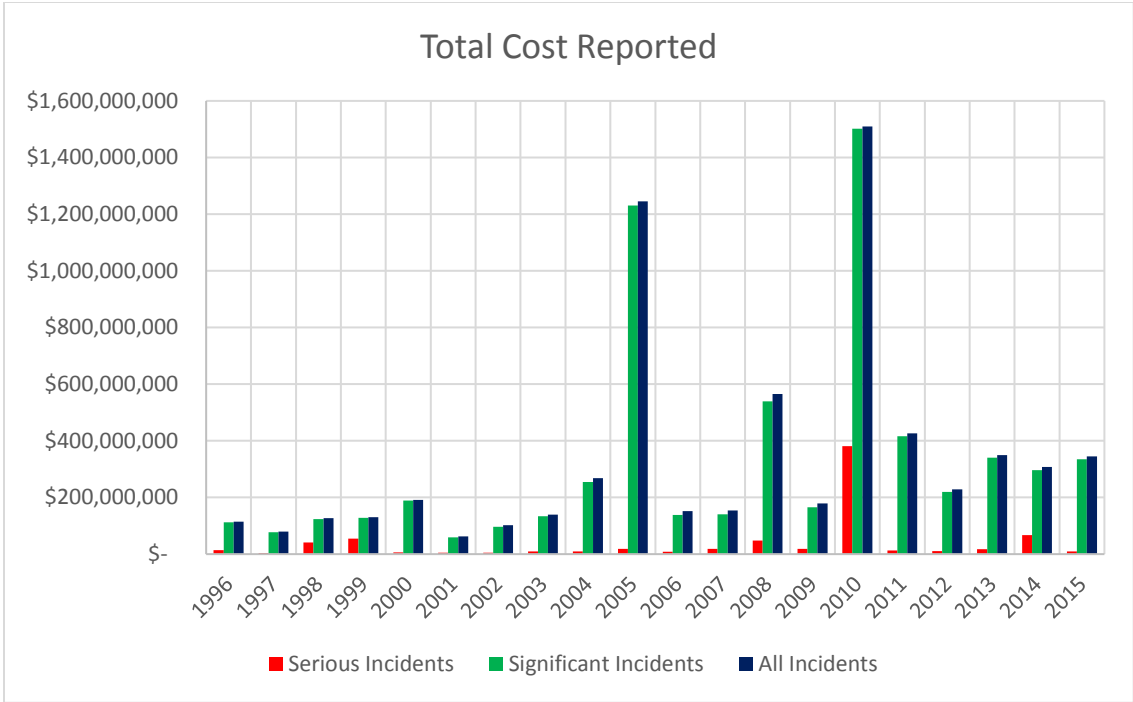


Figure 2-14: Total cost reported for each category by year

As has already been shown in Figure 2-1 and reproduced here (in Figures 2-15) for easy reference, and in Figure 2-16 below, the reported pipeline incidents are mostly dominated by corrosion, excavation damage, and material/weld/equipment failure: while excavation damage is the leading cause of injuries and fatalities in pipeline incidents.

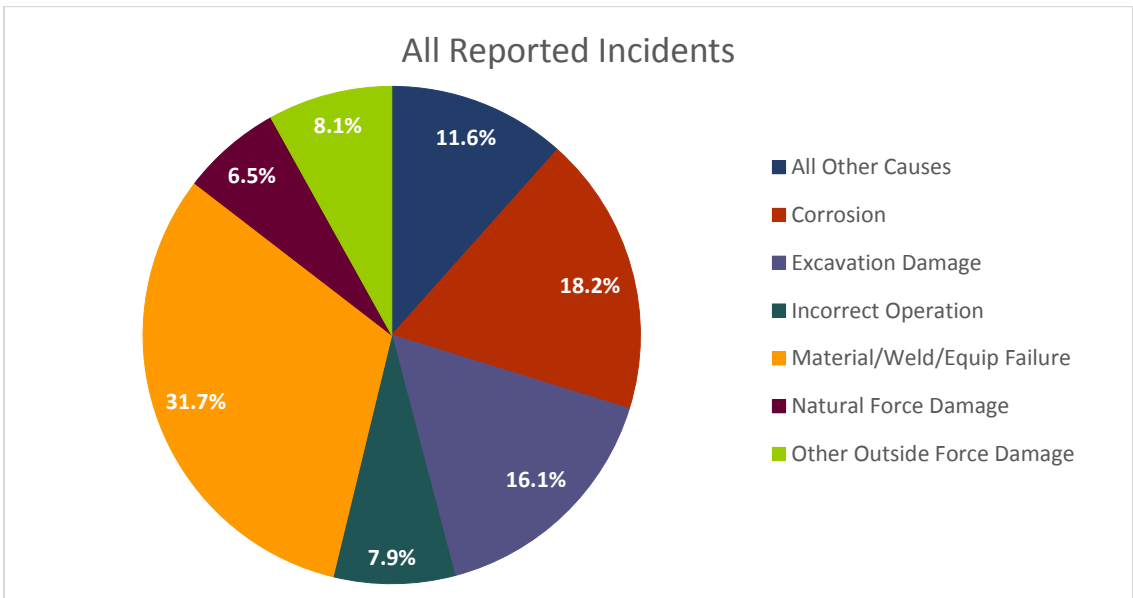


Figure 2-15: Percentage of pipeline incidents caused by different categories

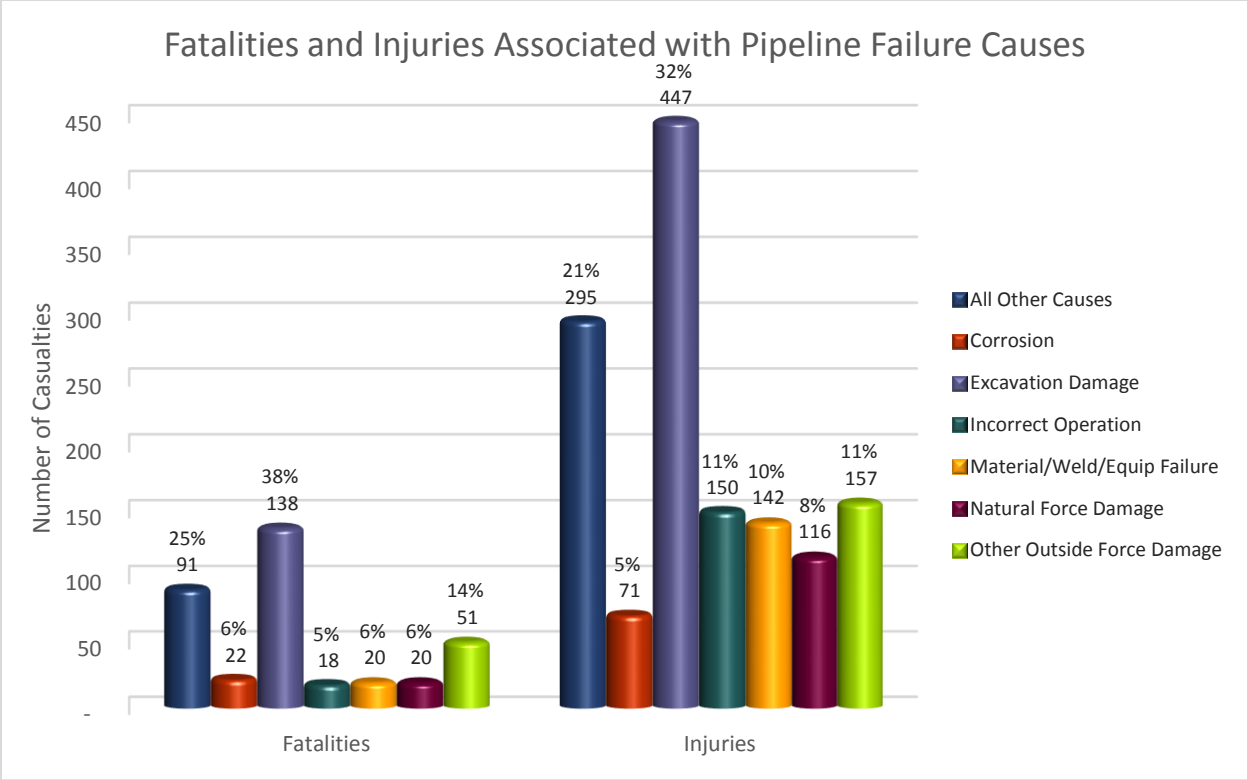


Figure 2-16: Casualties associated with different causes of pipeline failure

Pipeline incidents caused by material/weld/equipment failures are the most expensive, accounting for 34.4% of total reported cost over the past 20 years (Figure 2-17). This is closely followed by natural force damage, which accounted for 27.0% of the total reported cost. As shown in Figure 2-18, these two leading categories were greatly influenced by the pipeline incidents in 2005 and 2010 for natural force damage and material/weld/equipment failures respectively. The high cost reported for material/weld/equipment failure in 2010 was predominantly caused by two major incidents - the Pacific Gas and Electric Company natural gas transmission pipeline explosion in San Bruno, California (NTSB 2011); and the Enbridge Incorporated hazardous liquid pipeline rupture in Marshall, Michigan (NTSB 2012). These two incidents resulted in 84% of the total reported cost for 2010, and 21% of the 20 year total cost. On the other hand, the cost reported for natural force damage in 2005 was from a series of pipeline failures caused by heavy rains/floods, high winds, and earth movements – mostly in the outer continental shelf – which made up 81% of total reported cost for 2005 and 15% of the 20 year total cost shown in Figure 2-17. Corrosion of pipelines also contributed significantly to the total cost, accounting for 13.9% over the same 20 year period.

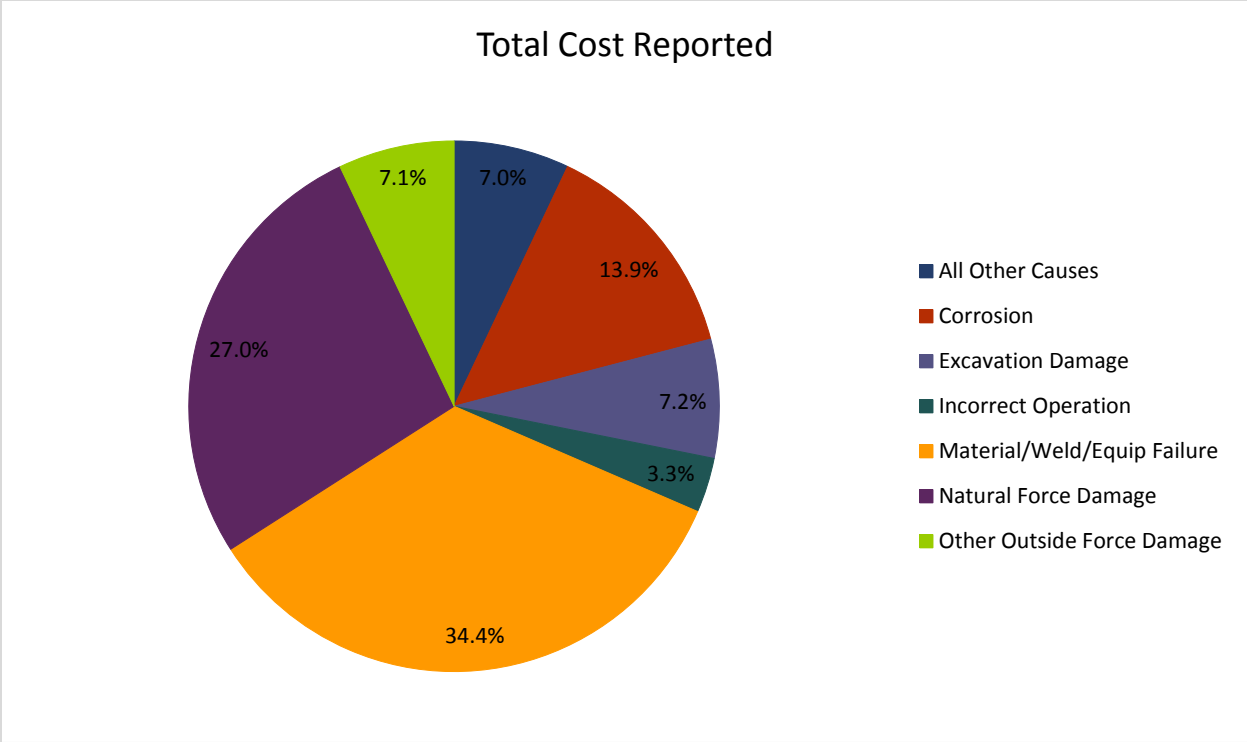


Figure 2-17: Total cost reported for each failure category over the last 20 years

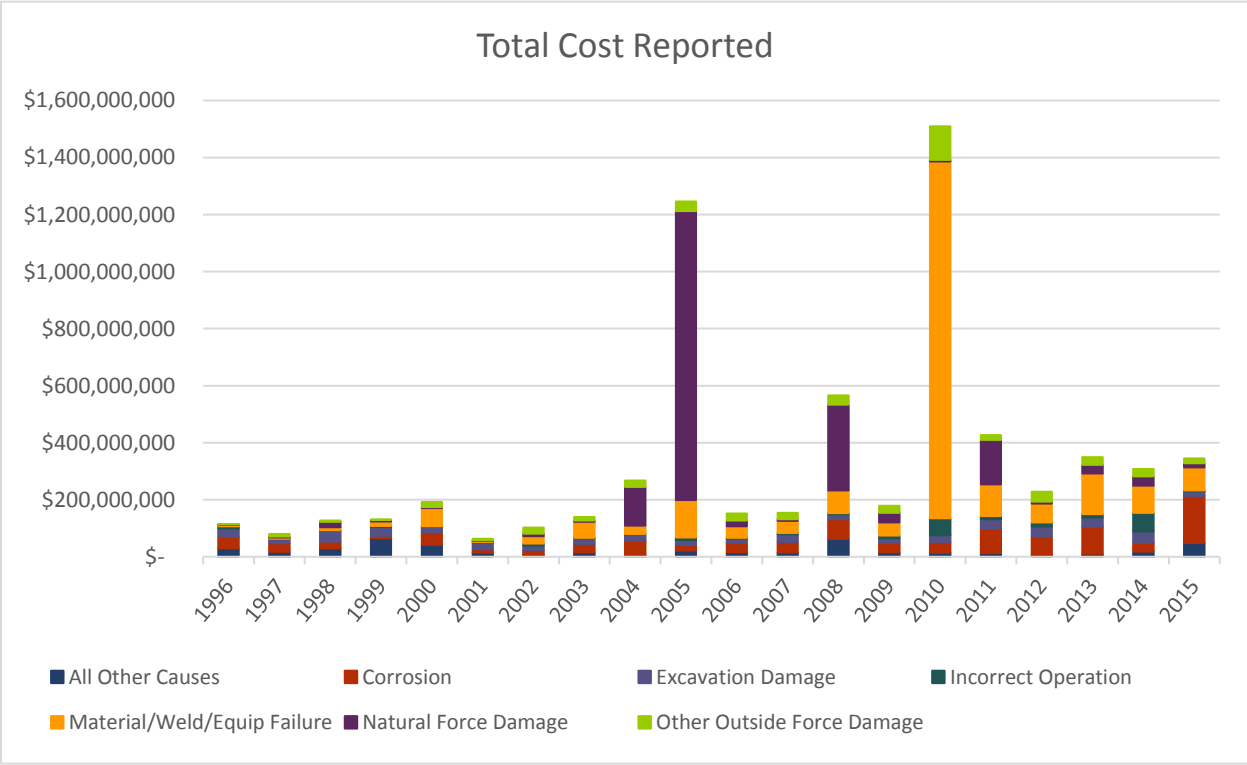


Figure 2-18: Total cost reported for each failure category by year

Similarly, corrosion, excavation damage and material/weld/equipment failure accounted for the top three highest percentages of total barrels of hazardous liquid⁴ spilled and net barrels lost (Figures 2-19 and 2-20).

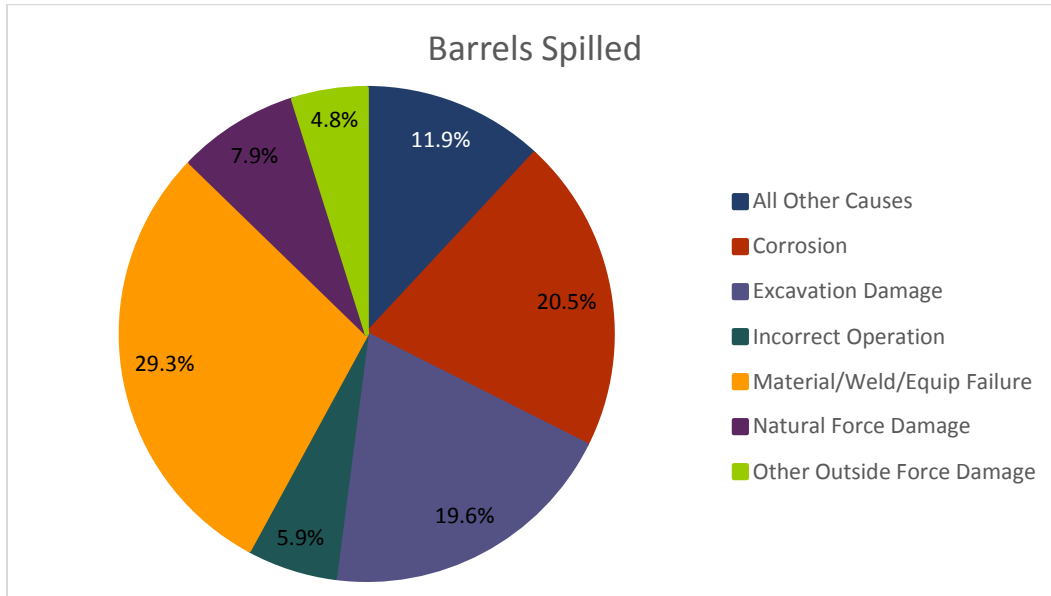


Figure 2-19: Total barrels of hazardous liquid spilled per failure category

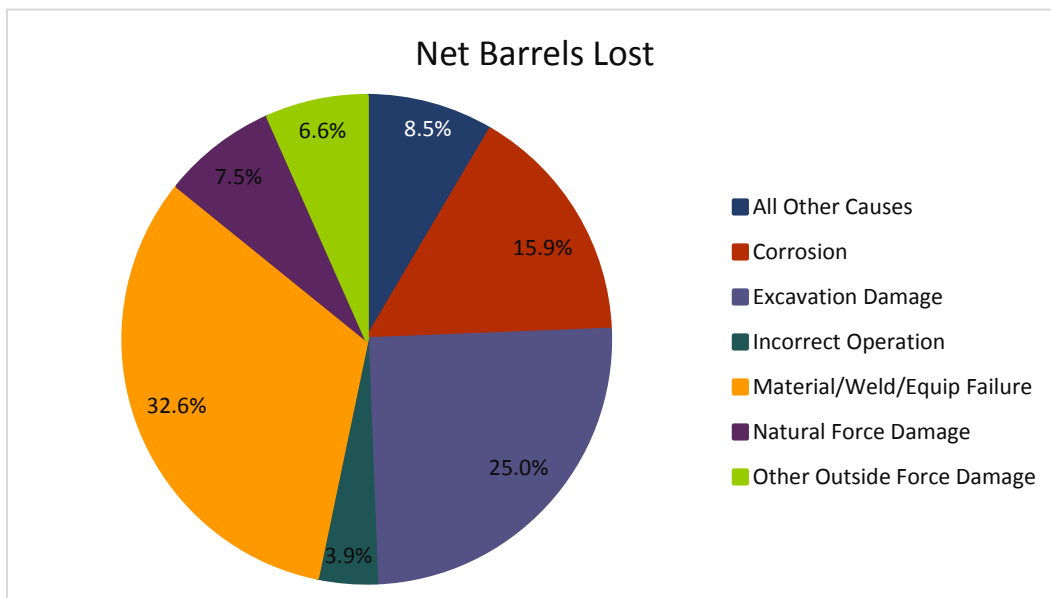


Figure 2-20: Net barrels of hazardous liquid lost per failure category

⁴ “Barrel data appears only for Hazardous Liquid incidents. Net Barrels Lost is the difference between Total Barrels Released and Barrels Recovered” (PHMSA 2016b, 2016c, 2016d).

Since this study seeks to make significant impact in preventing pipeline incidents caused by corrosion, excavation damage and pipe material failure (these have also been identified as the top three leading causes of pipeline failure), a summary of how the above categories affect the overall pipeline industry in terms of failure losses is given in Table 2-1.

Table 2-1: Corrosion, excavation damage and material failure contribution to pipe incidents

Cause of Failure	No. of Incidents	Fatalities	Injuries	Cost	Barrels Spilled	Barrels Lost
Corrosion	18.2 %	6.1 %	5.2 %	13.9 %	20.5 %	15.9 %
Excavation Damage	16.1 %	38.2 %	32.4 %	7.2 %	19.6 %	25.0 %
Material/Weld/Equip Failure	31.7 %	5.5 %	10.3 %	34.4 %	29.3 %	32.6 %
Total	66.0 %	49.8 %	47.9 %	55.5 %	69.4 %	73.5 %

2.3 WATER AND SEWAGE PIPELINES

Though water and sewage pipeline incidents do not frequently result in immediate fatalities and injuries as hazardous or energy pipelines, these incidents have serious consequences on the lives of people. Some of the recent water and sewage pipeline incidents resulted from corrosion of metallic pipelines and aging infrastructure. This leads to water main breaks resulting in loss of treated water and/or contamination of water delivered to consumers. The America Society of Civil Engineers graded the aging water infrastructure a D, with an estimated 240,000 water main breaks per year and loss of about “six billion gallons of treated drinking water” (ASCE 2017) each day. A study on water main breaks found corrosion to be a major cause of these breaks. In the same study, PVC pipes were found to have the lowest break rate of all pipe materials evaluated (Folkman 2018). Figure 2-21 shows comparison of failure rate of the different pipe materials. Making buried PVC pipes easily locatable and increasing their adoption rate in the water and sewage infrastructure will help reduce water main breaks.

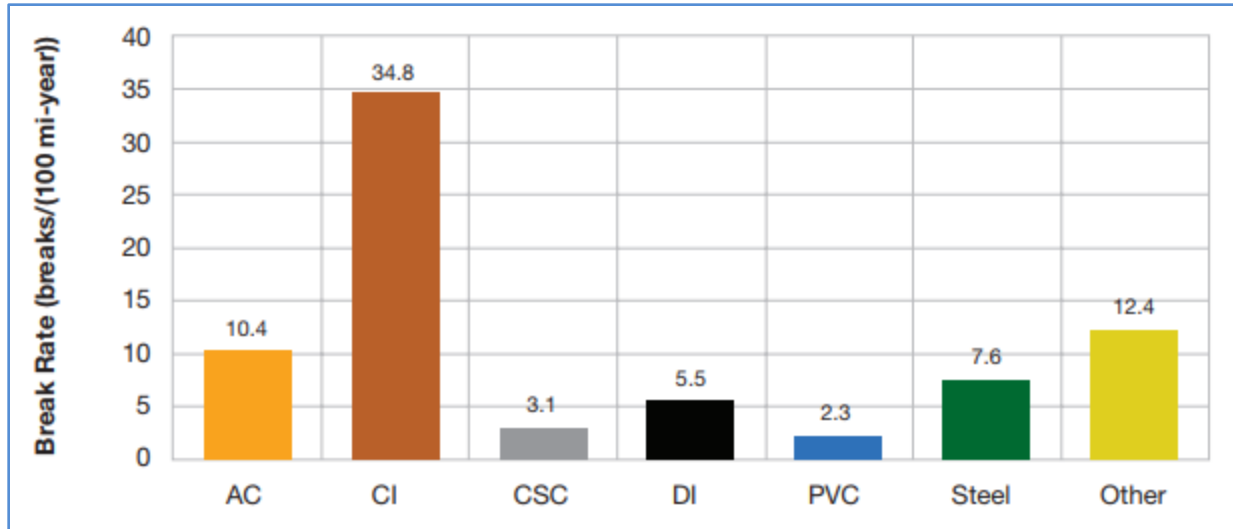


Figure 2-21: Break rates of different pipe materials (Folkman 2018)

2.4 CONCLUSIONS

This chapter reviewed the current state of the pipeline infrastructure in the US. The challenges discussed and the necessity for a sound infrastructure to serve pipeline transportation needs require significant investment into infrastructure development, monitoring and maintenance. The remainder of this dissertation will explore ways to aid in this process by making advanced materials for building resilient pipelines locatable in-situ.

CHAPTER 3

RECENT ADVANCES IN NON-METALLIC PIPELINE DETECTION

3.1 INTRODUCTION

Subsurface object/feature detection has been a subject of interest in many fields of study for several centuries now. From the use of dowsing rods in the early ~1400s (Hansen 1982) for locating underground water, to the utilization of more advanced techniques such as ground penetrating radar, x-ray, and acoustic/seismic systems for detecting pavement thickness and moisture variations in a medium among many others in current applications, subsurface profiling has come a long way; both in the scope of the technologies employed and the fields/areas of application. This chapter reviews the commonly used subsurface object detection techniques, and their application and performance for non-metallic pipeline detection.

3.2 BURIED OBJECT DETECTION TECHNIQUES

As mentioned earlier, several techniques have been employed over the years for detecting buried/subsurface objects. Some of these techniques, including Ground Penetrating Radar, Infrared Thermography/Systems, X-Ray Backscatter, Dowsing, Acoustic/Seismic Systems, Electromagnetic Induction/Conductivity (Buried Metal Detection), Magnetometer Surveys, and Electrical Resistivity Tomography or Surface Resistivity are still widely used in industry today.

3.2.1 Dowsing

Dowsing (also called witching) is the oldest of the subsurface object location techniques still in use today. Dowsing is generally regarded as a problem solving technique which utilizes “motor automatism in conjunction with a mechanical instrument to obtain information otherwise unknown to the dowser” (Hansen 1982). Dowsers (a term used for people using the dowsing technique) use dowsing rods or witching sticks to identify hidden objects; the rods move in response to the presence of buried/hidden objects that the dowser wishes to locate. In recent applications to buried utility locating, the L-shaped diving rods are used. One L-shaped rod is held in each hand by the dowser while moving around to locate buried objects, the two rods move inwards to cross each

other when the dowser walks over a buried utility line. Though recent literature on this technique is scarce, multiple practitioners have confirmed they have been using it to successfully locate buried pipes.

One of the major limitations with this techniques is its inability to determine the depth at which objects are buried. It can also not be used to determine the diameter of buried objects.

3.2.2 Geomagnetic Surveying

Geomagnetic Surveying is a geophysical method that uses an instrument called magnetometers to measure changes in the earth's magnetic field (measurement of magnetic field direction, gradient, or intensity) that are caused by the magnetic properties of underlying material or changes in the subsurface structure. This technique is also sometimes referred to as *magnetometer surveys*. Magnetometers are sensitive instruments, allowing subtle variations in the local magnetic field to be detected – which may indicate the presence of buried objects (Allred et al. 2004, Mariita 2007) or other subsurface anomalies. There are different types of commercial magnetometers available. Gradiometer magnetometers employ two magnetometers, mounted a short distant apart, to measure magnetic field gradient between the two magnetometers. This allows for the removal of background noise and diurnal magnetic fluctuations since they measure magnetic field gradient rather than total magnetic field. Geomagnetic surveying can be used in a variety of geophysical survey applications, including investigation of archaeological sites, mapping of geologic structures such as rock formations, locating steel well casings, buried steel tanks, steel pipes, and other metallic debris (Allred et al. 2004, Mariita 2007).

An investigation by Allred et al. (2004) found that, magnetometer survey was not able to locate buried agricultural drainage pipes located at depths between 0.5 and 1 m (1.5 – 3 ft.). Portable one-hand operated magnetic locaters, suitable for locating utility lines and other ferrous objects, are available in several models. However, these are only able to locate ferrous/magnetic objects. Geomagnetic surveying/magnetic locaters are therefore not suitable for locating buried non-metallic pipelines.

3.2.3 Electromagnetic Induction (EMI)

Electromagnetic induction (and Electromagnetic Induction Spectroscopy, EMIS) works on the principle that, an electrically conductive or magnetically permeable object exposed to a low-frequency electromagnetic field produces a secondary electromagnetic field. The secondary field can be measured and used to classify the object. During EMIS surveys, an electromagnetic (EM) field (called the primary field) is transmitted into the ground by a transmitter coil, this generates a secondary EM field in the ground. The secondary EM field then propagates through the ground back to the surface. A receiver coil on the EM sensor detects and measures both the primary and secondary fields, which are then used to determine the presence or absence of a subsurface object. The electromagnetic induction principle forms the basis of metal detectors commonly used for locating metallic utility lines (Won et al. 2001, Allred et al. 2004).

EMI/metal detectors has been successfully used in various metallic target application, including unexploded ordnance characterization (Huang and Won 2003, Won et al. 2001) and detection of metallic natural gas pipelines.

This technique however has little success when it comes to detection of non-metallic targets. EMI has been explored by Allred et al. (2004) for detecting non-metallic agricultural drainage lines and found to be ineffective.

3.2.4 Electrical/Surface Resistivity

The electrical resistivity (also known as Electrical Resistivity Tomography, ERT) method for subsurface profiling typically employs four electrodes, placed in contact with the ground/medium being evaluated. A known direct current (DC) is applied to the medium through two of the electrodes, while the resulting potential is measured between the remaining two electrodes. The value of the applied current, the measured potential, and the spacing between the electrodes is combined to obtain the electrical resistivity of the medium. This technique can be used to measure both lateral and vertical changes in electrical resistivity of the ground. This electrical resistivity distribution of the ground can then be used to determine physical conditions of the subsurface, such as the presence of voids, depth of bedrock, degree of saturation, salty water, geologic formations, buried objects, among many other features (Johnson 2003, Munk and Sheets 1997).

The electrical resistivity technique has been employed in locating underground mine voids (Johnson 2003, Sheets 2002), groundwater exploration (Mohamaden and Ehab 2017, Asry et al. 2012, Zhu et al. 2011), and study of geological structures (Carrière et al. 2013).

ERT is however a low resolution technique, it works well in estimating the large geologic features but has little success in locating small features. It was not able to locate agricultural drainage pipes buried between 0.5 and 1 m (1.5 – 3 ft.) depths when investigate by Allred et al. (2004). Because of its low resolution output, it is difficult to characterize the exact location, size, and depth of a feature of interest using ERT. This is evident when the resistivity result of an underground mine in Figure 3-1 is compared with the boring result of the same mine in Table 3-1 showing the location of voids.

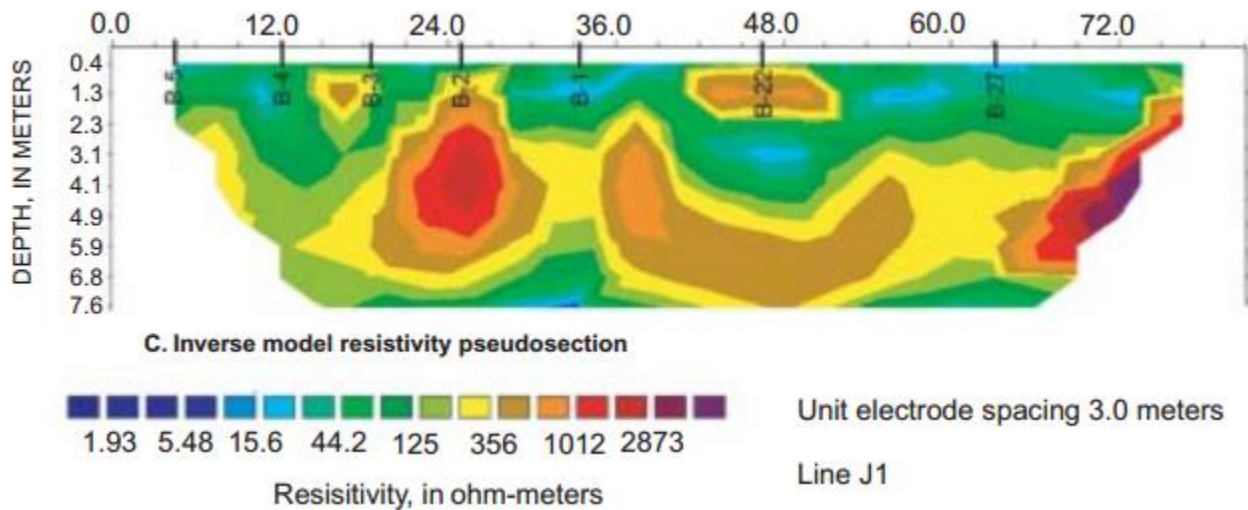


Figure 3-1: *Electrical resistivity result for an underground mine (Sheets 2002)*

Table 3-1 Drillers' descriptions of borings along resistivity survey line (Sheets 2002)

Depth below land surface (meters)	BORING NAME AND DISTANCE (METERS) ALONG RESISTIVITY SURVEY LINE						
	B-5 4.8	B-4 12.5	B-3 18.9	B-2 25.0	B-1 33.8	B-22 46.9	B-27 63.4
0.00	TOPSOIL	TOPSOIL	TOPSOIL	TOPSOIL	TOPSOIL	OVERBURDEN	SOD
0.15	CLAY*	SILTY CLAY*	SILT*	TOPSOIL	TOPSOIL	OVERBURDEN	SILT/CLAY*
0.30	CLAY*	SILTY CLAY*	SILT*	BOULDERS	SILTY CLAY*	LIMESTONE	SILT/CLAY*
0.46	CLAY*	SILTY CLAY*	SILT*	BOULDERS	SILTY CLAY*	LIMESTONE	SILT/CLAY*
0.61	CLAY*	SILTY CLAY*	LIMESTONE	BOULDERS	SILTY CLAY*	LIMESTONE	SILT/CLAY*
0.76	LIMESTONE	SILTY CLAY*	LIMESTONE	BOULDERS	SILTY CLAY*	LIMESTONE	SILT/CLAY*
0.91	LIMESTONE	SILTY CLAY*	LIMESTONE	LIMESTONE	SILTY CLAY*	LIMESTONE	SILT/CLAY*
1.07	LIMESTONE	SILTY CLAY*	LIMESTONE	LIMESTONE	SILTY CLAY*	LIMESTONE	SILT/CLAY*
1.22	LIMESTONE	SANDY SILT*	LIMESTONE	LIMESTONE	SILTY CLAY*	LIMESTONE	LIMESTONE
1.37	LIMESTONE	SANDY SILT*	LIMESTONE	LIMESTONE	SILTY CLAY*	LIMESTONE	LIMESTONE
1.52	LIMESTONE	SHALE	SHALE	SHALE	SILTY CLAY*	LIMESTONE	LIMESTONE
1.68	LIMESTONE	COAL	SHALE	SHALE	SHALE	LIMESTONE	LIMESTONE
1.83	LIMESTONE	COAL	SHALE	SHALE	SHALE	LIMESTONE	LIMESTONE
1.98	LIMESTONE	COAL	SHALE	SHALE	SHALE	SHALE	LIMESTONE
2.13	VOID	COAL	VOID	SHALE	VOID	SHALE	LIMESTONE
2.29	VOID	COAL	VOID	VOID	VOID	SHALE	SHALE
2.44	SHALE	COAL	VOID	VOID	VOID	SHALE	SHALE
2.59	SHALE	COAL	VOID	VOID	VOID	COAL	SHALE
2.74	SHALE	COAL	VOID	VOID	VOID	COAL	VOID
2.90	SHALE	COAL	VOID	VOID	VOID	COAL	VOID
3.05	SHALE	CLAY-SHALE	SHALE	COAL	VOID	VOID	VOID
3.20	CLAY-SHALE	CLAY-SHALE	SHALE	COAL	VOID	COAL	VOID
3.35	CLAY-SHALE	CLAY-SHALE	SHALE	SHALE	SHALE	COAL	VOID
3.51	SILTSTONE	CLAY-SHALE	SHALE	SHALE	SHALE	COAL	VOID
3.66	SILTSTONE	SILTSTONE	SHALE	SHALE	SHALE	COAL	VOID
3.81	SANDSTONE	SILTSTONE	SHALE	SANDSTONE	SHALE	COAL	VOID
3.96	SANDSTONE	SILTSTONE	SHALE	SANDSTONE	SHALE	SHALE	
4.11	SANDSTONE	SANDSTONE	SHALE	SANDSTONE	SHALE	SHALE	
4.27	SANDSTONE	SANDSTONE	SHALE	SANDSTONE	SHALE	SHALE	
4.42	SANDSTONE	SANDSTONE	SHALE	SANDSTONE	SANDSTONE	SHALE	
4.57	SANDSTONE	SANDSTONE	SHALE	SANDSTONE	SANDSTONE	SHALE	
4.72					SANDSTONE		
4.88					SILTSTONE		
5.03					SILTSTONE		
5.18					SANDSTONE (continues to 10.7 meters)		

3.2.5 Tracer Wires

Tracer wires have been employed over the years to make detecting buried utilities easier. Conductive tracer wires are laid alongside (either above or below) a utility line to make this technique work. An electrical contact is made with one end of the tracer wire so an electric signal can be transmitted through it, a handheld receiver is then moved along the ground to detect the resulting magnetic field generated by the buried tracer wire. The received magnetic field is then interpreted to provide pipe location information. Moving the receiver along the tracer wire helps to map it out, and hence detect the utility line (Costello et al. 2007, Satterfield 2006, Cist and Schutz 2001)

Major weakness of this technique is that, tracer wires may break over time due to corrosion, or they may get torn during back-fill of pipe trenches. When breaks occur, the transmitted electrical current will stop at the break point, and the ability to locate pipelines beyond the break will be adversely affected. In some instances, the tracer wires completely disappeared in the soil due to decades of corrosion activity. In addition, the tracer wire technique cannot determine the depth at which pipes are buried.

3.2.6 Infrared Thermography (IRT)

Infrared thermography operates on the principle of energy/heat transfer from hotter to colder regions within an object. Object and feature detection using this technique is based on the variation of electromagnetic radiations reflected or emitted by the object of interest and its surroundings. Different materials have different thermal characteristics, and this affects the rate of energy flow through and from the material. An infrared sensor/camera is used to measure the variations in energy emitted from an object, which is converted into a thermographic image, representing thermal characteristics of the object. This helps to locate subsurface objects such as missing/poor insulation, delaminations, voids, and pipelines. Infrared thermography is one of the widely used nondestructive testing techniques for infrastructure monitoring (Dalrymple 2014, Sakagami et al. 2014, Mitani and Matsumoto 2012, Taillade et al. 2012, Spring et al. 2011, Ghosh and Karbhari 2011, Halabe and Dutta. 2010, Costello et al. 2007).

Most infrastructure applications of IRT (such as bridge deck monitoring, testing fiber reinforced polymer wraps, and locating underground voids) rely on solar heating of the object of interest. In other cases where solar heating is insufficient, other active heat source is required.

Literature on the use of IRT for buried pipeline detection is scarce, however, it is anticipated that the technique can be applied in detecting buried pipelines transporting hot fluids. Other pipelines not transporting hot fluids may also be detected if their content has significant difference in thermal properties relative to the surrounding soil, and there is enough solar heating to produce a radiation contrast (limited to very shallow depths). As with the tracer wire technique, IRT cannot detect the depth at which objects are buried. However, IRT is a non-contact technique, hence direct access to the pipeline may not be required for mapping. In addition, IR cameras also come in portable form factors, which offer a great potential for it to be mounted on UAVs (Unmanned Aerial Vehicles) or to be integrated into UAV inspection systems. This study investigates the use of IRT for detecting buried pipelines carrying hot fluids in a later chapter.

3.2.7 Ground Penetrating Radar (GPR)

Ground penetrating radar is one of the geophysical survey methods with a long history of application in a wide variety of fields. GPR is an electromagnetic method, and hence relies on the electromagnetic properties of the test medium for object detection. A transmitting antenna sends radar pulse into the test medium during a GPR application, the pulse signal propagates through the medium and is partly reflected by subsurface boundaries having different electromagnetic properties. Part of the incident signal which was not reflected is transmitted deeper into the medium or attenuated. The reflected signal propagates back to the surface and is detected by a receiving antenna. Characteristics of the received signal (including signal strength, phase, and time of flight) are interpreted to detect subsurface objects.

GPR is a very versatile technique which has been successfully employed in many infrastructure monitoring and geophysical survey applications, including buried pipe/utility and container detection (Prego 2017, Sagnard et al. 2016, Porsani et al. 2012, Bowders 1982), defect detection (Alani et al. 2013, Hing and Halabe 2010), measuring pavement thickness (AL-Qadi and Lahoouar 2005), locating reinforcing steel in concrete (Razinger 2017, Dalrymple 2014), archaeological investigation (Barone et al. 2011 and 2010), detection of landmines (Metwaly 2007), snow

thickness measurement and/or subglacial topography detailing (Lamsters et al. 2016, Paolo et al. 2015), tree root detection (Hirano et al 2009, Butnor et al. 2001 & 2003), irrigation and soil water content monitoring (Takahashi et al. 2012, Wijewardana and Galagedara 2010), cracks in concrete or pipe wall, (Najafi 2010, Ékes et al. 2011), and underground/concrete void detection (Trela et al. 2015, Munk and Sheets 1997). Some of these applications of GPR are reviewed further in Section 3.3 of this chapter.

GPR surveys offer several advantages over the other subsurface object locating methods reviewed. A GPR survey provides high resolution continuous profile of the subsurface. This makes it possible to find the exact location of buried objects, together with accurate determination of buried depth and object size. GPR data can also be collected and viewed in a variety of forms, including single trace waveforms, cross section of the subsurface, and 3D views.

3.2.8 Advantages and Limitations, and why GPR

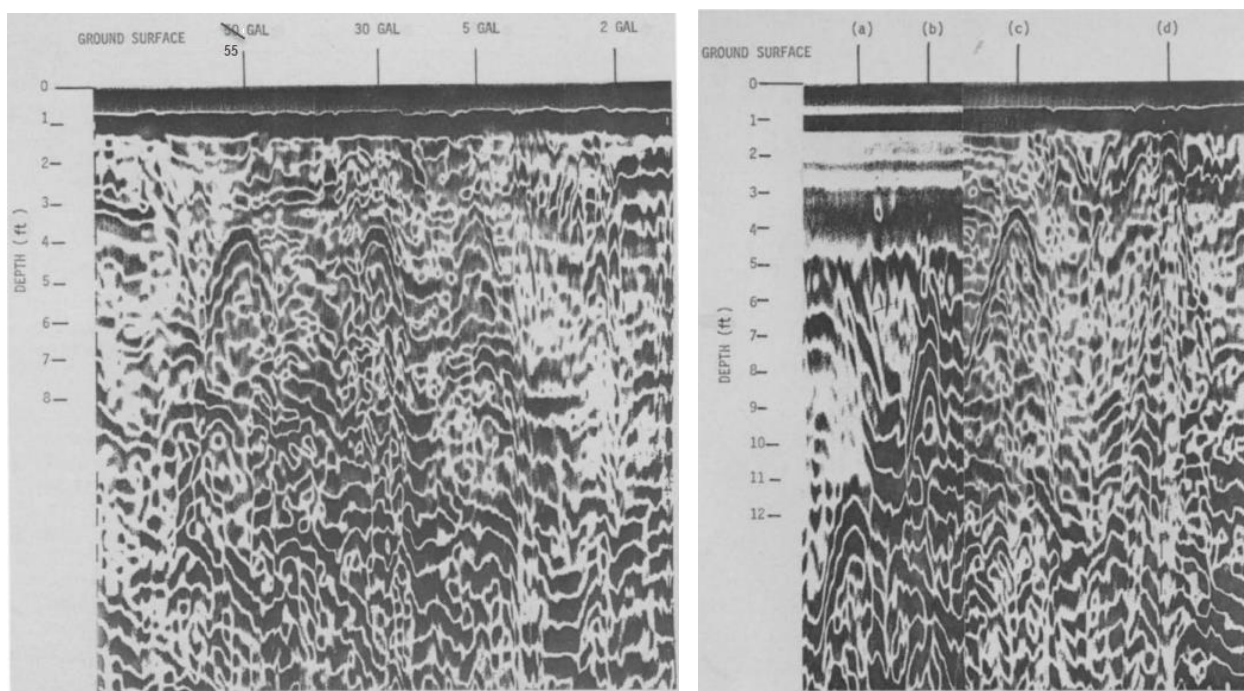
From the reviews above, it is evident that GPR offers the best nondestructive testing option for buried utility detection. In addition to its versatility, it produces data with the highest resolution, making it possible to detect exact location and depth of buried objects. GPR also offers the option to collect and view data in a variety of forms, which aids in data interpretation and subsurface object detection.

Electrical resistivity method is a slow process that produces low resolution data, making it difficult to deduce the depth, location, and extent of the subsurface object. While a tracer wire technique can be accurate if it works (that is, if the wire is not broken due to corrosion), the location might be off if there is a differential lateral displacement between the wire and the pipe. Techniques like dowsing, tracer wire, infrared thermography, acoustic systems, geomagnetic surveys, and electromagnetic induction do not provide depth information.

Finally, some of the above methods only work on ferrous or metallic objects, while GPR can work on any material provided there is sufficient dielectric contrast between the object of interest and its surrounding material.

3.3 USE OF GPR IN BURIED NON-METALLIC OBJECT DETECTION

While GPR is a versatile technique that is widely successful in locating underground objects and features, locating buried non-metallic materials continue to be a challenge in most soil conditions. Bowders (1982) investigated the use of GPR for locating buried containers of various material types and sizes. The author was able to locate 55, 30, 5, and 2 gallon steel drums (diameters of about 23, 18, 13, and 9 inches respectively) buried with 3.5 feet of soil cover using a 120 MHz antenna. The steel drums are represented by the hyperbolic features around a depth of 3.5 feet in the GPR printout in Figure 3-2(a). The author was also able to detect 30 gallon steel drums buried with 11, 6, 3, and 1 feet depth of soil cover Figure 3-2(b).



(a) Different diameter steel drums at 3.5 ft. (b) 30 gallon steel drums at different depths

Figure 3-2: GPR printout showing hyperbolic features from steel drums

Buried 40 gallon plastic drums at 11, 6, 3, and 1 feet depths could not be detected since plastic is transparent to radar waves. Two plastic drums, one filled with fresh water and the other filled with salt water (in the ratio of 1 lb. of salt in 4 gallons of water) and buried at 2 ft. depth were however detected by GPR due to the water having very high dielectric constant and being conductive compared to the surround sand medium. The pipe content was therefore reflective to radar waves, thereby making it detectable (the plastic drum material could not be detected, but their content was detected using GPR).

It should be noted that, Bowders' test was carried out in a nearly ideal conditions for GPR testing (the test site was level, with no vegetation and miscellaneous debris, and “consisted of a relatively uniform sandy soil of low water content” (Bowders 1982). The sand was almost dry, with in-situ water content of 2% and an 8% degree of saturation. In addition, there were no buried utilities (pipelines and cables) or overhead wires within 1000 feet of the test area; this helped in limiting background noise from nearby objects in the GPR survey data. GPR was able to penetrate up to a depth of 11 feet (3.5m) in this soil, when 80 MHz and 120 MHz frequency antennae were used Bowders (1982).

Allred et al. (2004) researched on detecting buried agricultural drainage lines (made of clay tile or corrugated plastic tubing), and were able to detected the pipes down to about 1 m (3 ft.) depth, achieving an average success rate of 81%. Some of this test result is shown in Figure 3-3.

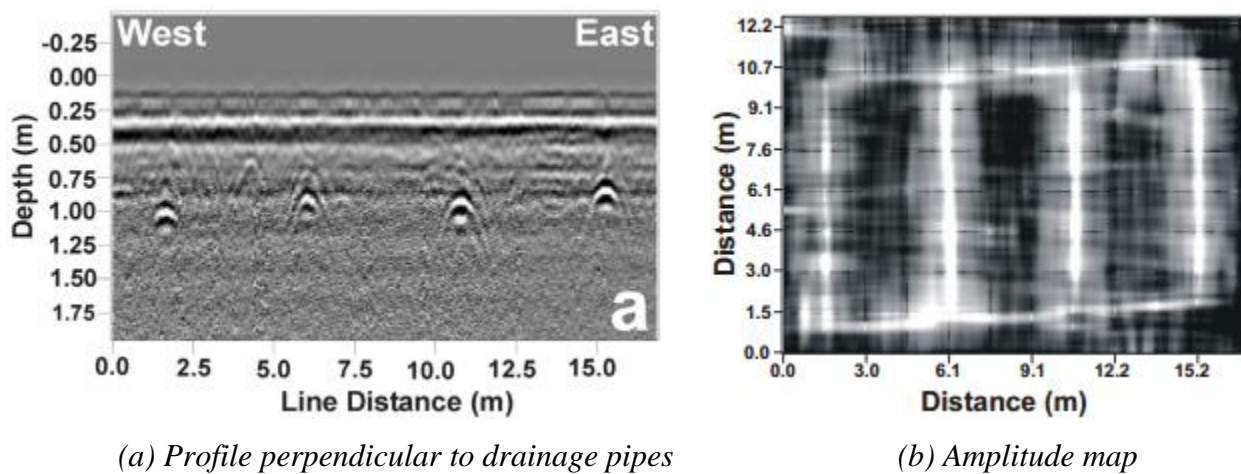


Figure 3-3: GPR data from agricultural drainage pipes (Allred et al. 2004)

3.4 CHALLENGES IN DETECTING NON-METALLIC OBJECTS

It can be inferred from the previous section that, locating buried non-metallic object is a challenge; even in the most favorable soil conditions. Buried non-metallic pipelines may be detectable if their content makes it possible. However, this cannot be relied on since the content might not always make this possible. For instance, fresh water in its natural state has a dielectric constant of about

80, while that of natural gas is less than 2 (two⁵). Also, 1 lb. of salt in 4 gallons of water gives a concentration of about 0.5M (assuming NaCl) which has a dielectric constant of about 75 at 20°C (Gavish and Promislow 2016). This means that the high dielectric constants of fresh water and salt water reflect radar waves and make it possible to locate buried pipes with such contents. However, the low dielectric constant of natural gas will not reflect much radar waves, and hence will be undetectable. In addition, changes in soil properties such as increase in silt and clay content, as well as higher soil water and electrical conductivity makes it more difficult to locate buried materials using GPR.

3.5 CONCLUSIONS

From the review of the buried object location techniques commonly used in field applications today, GPR has been found to be the most promising technique to be used in this research. In addition to locating buried objects, GPR can also be used to determine the depth at which the object is buried.

However, detection of buried non-metallic objects in most soil conditions is still a problem when using GPR. As presented in the review, 22" diameter plastic drums (40 gallon drums) could not be detected at 1 ft. depth in dry sand (which is an ideal condition for GPR application). Thus, this research will investigate strategies for making non-metallic pipelines easily locatable using GPR. The study will involve detection of 3" diameter non-metallic pipes buried at 2 ft. depth and 12" diameter non-metallic pipe at 4 ft. depth in wet clay soil using GPR.

⁵ Methane, which is the primary component of natural gas – typically about 94% – has a dielectric constant less than 2, while that of the remaining components; ethane, propane, butane, pentane, hexane, nitrogen, and carbon dioxide carbon dioxide all fall under 1.8 (sources: Enbridge Gas, Dortmund Data Bank - DDB, The Engineering ToolBox).

CHAPTER 4

GROUND PENETRATING RADAR (GPR) THEORY

4.1 INTRODUCTION

The ground penetrating radar method operates by transmitting electromagnetic energy from an antenna into a material, and measuring the reflected signal response from subsurface features. Reflected signal amplitude, phase, and elapsed time of the received signal are all recorded by the receiving antenna. Record of reflections from different depths into a material produces a signal trace, which helps in locating subsurface features. As a GPR signal travels through a material, it undergoes attenuation (losses – which results in reduction in signal amplitude), refraction (when signal travels through different materials), and reflection from interfaces among other changes. Figure 4-1 illustrates the simplified path of a GPR signal from the transmitting antenna through a media and back to the receiving antenna. The theory behind the application of GPR is summarized in this chapter.

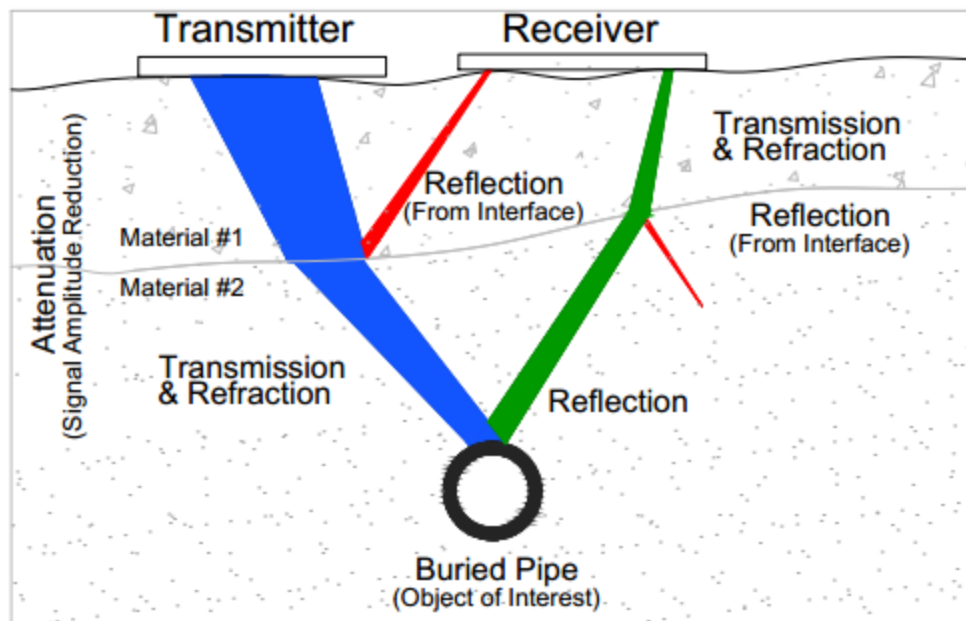


Figure 4-1: Propagation path of electromagnetic wave from transmitter to receiver

4.2 PROPAGATION VELOCITY

Propagation of electromagnetic waves through a medium such as soil is characterized by the electromagnetic properties of the medium; such as the dielectric permittivity ϵ , the magnetic permeability μ , and the electrical conductivity σ . The dielectric permittivity is in turn affected by several material properties, including “electromagnetic properties of solid particles, porosity, moisture content, and salt/ionic content” (Halabe et al. 1995). The electromagnetic wave velocity, v , through a non-conductive/slightly conducting medium is given by;

$$v = \frac{1}{\sqrt{\epsilon'_m \mu_m}} = \frac{1}{\sqrt{\epsilon_o \epsilon'_r \mu_o \mu_r}} \quad (4-1)$$

where ϵ'_m and μ_m are the dielectric permittivity and magnetic permeability (absolute) of the medium/material, $\epsilon_o = 8.854 \times 10^{-12}$ F/m is the dielectric permittivity of vacuum/free space, $\epsilon'_r = \epsilon_m/\epsilon_o$ is the relative dielectric permittivity (sometimes referred to as *dielectric constant*) of the medium, $\mu_o = 4\pi \times 10^{-7}$ H/m is the magnetic permeability of vacuum/free space, and $\mu_r = \mu_m/\mu_o$ is the relative magnetic permeability of the medium.

Magnetic properties for slightly conducting mediums, that is, non-magnetic materials such as most soils, are taken as being equal to that for vacuum, resulting in $\mu_m = \mu_o$ and $\mu_r = 1$ (Takahashi et al. 2012, Reynolds 2011, Halabe et al. 1995, Halabe et al. 1993). For such mediums, Equation 4-1 becomes;

$$v = \frac{c}{\sqrt{\epsilon'_r}} \quad (4-2)$$

$$c = \frac{1}{\sqrt{\epsilon_o \mu_o}} \quad (4-3)$$

where $c \approx 3 \times 10^8$ m/s is the velocity of electromagnetic waves in vacuum (speed of light).

The electromagnetic properties of materials (ϵ , μ , and σ), - both absolute and relative for ϵ and μ - are complex in general, and can be expressed as (*Most of the theory from hence forward will involve the relative form of dielectric permittivity and magnetic permeability, hence the subscript “r” in relative dielectric permittivity and relative magnetic permeability will be dropped from hence forward for brevity. Other subscripts will be used to denote quantities that are not relative*):

$$\varepsilon = \varepsilon' + i\varepsilon'' \quad (4-4)$$

$$\mu = \mu' + i\mu'' \quad (4-5)$$

$$\sigma = \sigma' + i\sigma'' \quad (4-6)$$

where ε , μ , and σ are the complex relative dielectric permittivity, complex relative magnetic permeability, and complex conductivity respectively. ε' and ε'' are the real and imaginary parts of the complex relative dielectric permittivity. The real part of dielectric (ε'), called the polarization term, reflects material polarization property while the imaginary part (ε''), called polarization loss, “reflects energy loss in the dielectric material caused by delay in material’s response to the applied field” (Pal 2015) or polarization lag.

Similarly, μ' and μ'' are the real and imaginary parts of the complex relative magnetic permeability. The real part (μ') reflects polarization property of the material by measuring the “amount of magnetic moments that become aligned with the applied magnetic field” (Pal 2015). Additionally, it reflects the amount of energy stored by the magnetic moments when an external magnetic field is applied. The imaginary part (μ''), called polarization loss, “reflects energy loss in the magnetic material caused by delay in material’s response to the applied field” (Pal 2015). For dispersive materials, the values of ε' , ε'' , μ' and μ'' are frequency dependent.

The conductivity terms, σ' and σ'' are related to ohmic conduction and faradaic diffusion respectively (Takahashi et al. 2012).

In general, the propagating velocity of electromagnetic wave through an electrically conducting, frequency independent, dielectrically lossless medium with uniform magnetic properties is given by (Cassidy 2009, Goodman and Piro, 2013):

$$v = \frac{c}{\left(\frac{\varepsilon'\mu'}{2} \left[\sqrt{1 + \left(\frac{\sigma'}{\omega\varepsilon_0\varepsilon'} \right)^2} + 1 \right] \right)^{1/2}} \quad (4-7)$$

Where,

$\omega = 2\pi f$ is the angular frequency (rad/s)

f is the signal frequency (Hz)

The propagating velocity for a dielectrically lossy material, having complex conductivity and complex permittivity but non-complex magnetic permeability, can be obtained by using a real effective permittivity ($\varepsilon_m^{e'}$) and real effective conductivity ($\sigma^{e'}$) in place of σ' and ε'_m (and $\varepsilon_m^{e'}/\varepsilon_o$ for ε') in Equation 4-7 (Cassidy 2009, Pal 2015, Takahashi et al. 2012).

$$\varepsilon_m^{e'} = \varepsilon'_m + \frac{\sigma''}{\omega} \quad (4-8)$$

$$\sigma^{e'} = \sigma' + \omega\varepsilon_m'' \quad (4-9)$$

The effective parameters in Equations 4-8 and 4-9 account for the combined electromagnetic energy loss and storage mechanisms of conductivity and permittivity relaxation, “and represent currents that are either in phase ($\sigma^{e'}$) or out of phase ($\varepsilon_m^{e'}$) with the electric field during the polarization and relaxation processes” (Cassidy 2009).

The complex relative permittivity, ε , defined in Equation 4-4 assumed that the static electrical conductivity of a material is negligible, thus it considered only displacement charges. Thus, the effective complex relative permittivity (ε^e), which considers both free and displacement charges can be defined as:

$$\begin{aligned} \varepsilon^e &= \left(\varepsilon' + \frac{\sigma''}{\omega\varepsilon_o} \right) + i\varepsilon'' + i \left(\frac{\sigma'}{\omega\varepsilon_o} \right) \\ &= \left(\varepsilon' + \frac{\sigma''}{\omega\varepsilon_o} \right) + i \left(\varepsilon'' + \frac{\sigma'}{\omega\varepsilon_o} \right) \end{aligned} \quad (4-10)$$

The conductivity component of effective permittivity (Equations 4-8 and 4-10) is considered frequency independent, and having only real value in most applications.

Hence the effective relative permittivity becomes (Cassidy 2009, Pal 2015, Takahashi et al. 2012):

$$\begin{aligned} \varepsilon^e &= \varepsilon' + i \left(\varepsilon'' + \frac{\sigma'}{\omega\varepsilon_o} \right) \\ \text{or} \quad \varepsilon^e &= \varepsilon + i \left(\frac{\sigma'}{\omega\varepsilon_o} \right) \end{aligned} \quad (4-11)$$

The loss term (imaginary part) in equation 4-11 accounts for both polarization loss and energy loss due to static electric conductivity. The effective loss factor, ε''_{eff} , can be defined by expressing ε^e as:

$$\varepsilon^e = \varepsilon' + i\varepsilon''_{eff} \quad (4-12)$$

where

$$\varepsilon''_{eff} = \left(\varepsilon'' + \frac{\sigma'}{\omega\varepsilon_0} \right) \quad (4-13)$$

Complex effective electrical conductivity can also be alternatively expressed to define the effective loss factor, σ'_{eff} , accounting for energy losses due to both polarization and static conductivity (Pal 2015):

$$\sigma_e = i\omega\varepsilon_m = \sigma'_{eff} + i\sigma'' \quad (4-14)$$

where

$$\sigma'_{eff} = \sigma' + \omega\varepsilon''_m \quad (4-15)$$

$$\sigma'' = \omega\varepsilon'_m \quad (4-16)$$

$$\varepsilon'_m = \varepsilon_0\varepsilon' \quad (4-17)$$

4.3 SIGNAL AMPLITUDE

GPR signals undergo transformations such as attenuation (absorption of energy), scattering, reflection, and refraction as the signal travels through a dielectric medium. As such, the signal amplitude decreases with increase in travel distance. The amplitude of a one dimensional electromagnetic wave propagation is given by (Halabe et al. 1993):

$$A(x, t) = A_0 e^{i(kx - \omega t)} = A_0 e^{-k_I x} e^{i(k_{R x} - \omega t)} \quad (4-18)$$

where;

A_0 is the initial signal amplitude

$A(x, t)$ is the signal amplitude at a distance x and time t

k is the wave number - complex if the medium is conductive, and is related to ε as follows:

$$k = k_R + ik_I = \omega\sqrt{\varepsilon_m\mu_m} = \omega\sqrt{(\varepsilon'_m + i\varepsilon''_m)\mu_m} \quad (4-19)$$

where;

k_R is the real part of complex wave number, also called phase coefficient (rad/m)

k_I is the imaginary part of complex wave number, also called attenuation coefficient (Np/m)

$$\mu_m = \mu_o = 4\pi \times 10^{-7} \text{ H/m}$$

$$\varepsilon''_m = \sigma' / \omega$$

k_R and k_I are expressed as (Cassidy 2009, Halabe et al. 1993):

$$k_R = \omega \sqrt{\frac{\varepsilon'_m\mu_m}{2} \left(\sqrt{1 + \left(\frac{\sigma'}{\omega\varepsilon'_m}\right)^2} + 1 \right)} = \frac{\omega}{v} = \frac{2\pi}{\lambda} \quad (4-20)$$

$$k_I = \omega \sqrt{\frac{\varepsilon'_m\mu_m}{2} \left(\sqrt{1 + \left(\frac{\sigma'}{\omega\varepsilon'_m}\right)^2} - 1 \right)} \quad (4-21)$$

where λ is the wavelength of the radar wave.

In a highly conducting medium (i.e., $\varepsilon_m'' / \varepsilon_m' \gg 1$), Equations 4-20 and 4-21 become (Halabe et al. 1993):

$$k_R = k_I = \sqrt{\frac{\omega\mu_m\sigma'}{2}} \quad (4-22)$$

In a slightly conducting medium (i.e., $\varepsilon_m'' / \varepsilon_m' \ll 1$), Equations 4-20 and 4-21 become (Halabe et al. 1993):

$$k_R = \omega\sqrt{\varepsilon'_m\mu_m} \quad (4-23)$$

$$k_I = \frac{\sigma}{2} \sqrt{\frac{\mu_m}{\varepsilon'_m}} \quad (4-24)$$

4.4 LOSS FACTOR AND SKIN DEPTH

The loss components of a dielectric material are described by parameters such as the loss tangent ($\tan \delta$) and skin depth (d_p). The skin depth is the depth/distance that a plane wave has to travel for its amplitude to reduce to $1/e$, or 37% of its original value. The skin depth is inversely proportional to the attenuation coefficient/factor, $d_p = 1/k_I$ (Reynolds 2011). This is useful in estimating the penetration depth and the likely amplitude of any GPR signal reflections (Cassidy 2009). When round-trip wave propagation is considered, the wave amplitude reduces to 13.5% of the original signal amplitude ($0.37^2 = 0.135$). The loss tangent describes the ratio of the imaginary and real parts of the complex effective permittivity. It also relates electromagnetic energy loss factor ($\sigma' + \omega\epsilon_m''$) to energy storage ($\omega\epsilon_m' + \sigma''$). The parameters help in assessing how ‘lossy’ a dielectric material is, and its attenuation effects on an electromagnetic wave (Cassidy 2009, Takahashi et al. 2012).

$$\tan \delta = \frac{\epsilon_m''}{\epsilon_m'} = \frac{\epsilon''}{\epsilon'} = \frac{\sigma' + \omega\epsilon''\epsilon_0}{\omega\epsilon'\epsilon_0 + \sigma''} = \frac{\sigma' + \omega\epsilon_m''}{\omega\epsilon_m' + \sigma''} \quad (4-25)$$

For a material that is relatively dry and low in conductivity (ϵ'' and σ'' are small), the loss tangent is approximated as (Cassidy 2009, Takahashi et al. 2012):

$$\tan \delta = \frac{\sigma'}{\omega\epsilon_m'} = \frac{\sigma'}{\omega\epsilon_0\epsilon'} \quad (4-26)$$

And the electromagnetic wave velocity for such a medium is given previously by equation 4-1.

The skin depth (also known as penetration depth), d_p , is given by:

$$d_p = \frac{1}{k_I} = \frac{1}{\omega \sqrt{\frac{\epsilon_m'\mu_m}{2} \left(\sqrt{1 + \left(\frac{\sigma'}{\omega\epsilon_m'}\right)^2} - 1 \right)}} \quad (4-27)$$

which can be approximated as given in Equation 4-28 provided the loss tangent is considerably less than one:

$$d_p = \frac{2\sqrt{\epsilon_r'}}{377\sigma} \quad (4-28)$$

Equation 4-28 is only valid when the loss tangent is ‘considerably’ less than one. The value of skin depth will be overestimated if the simplified equation is used while the condition is not satisfied. Reynolds (2011) provides a graph to help determine when this condition is met. The graph is modified to include other antenna frequencies of interest, and shown in Figure 4-2. The theoretical conductivity values (mS/m) for when the factor is equal to one is shown on the left side of the vertical axis. “The observed conductivity for the condition of being much less than unity to apply should be of the order of 0.05 of the theoretical conductivity” (Reynolds 2011) as shown on the right side of the vertical axis. Thus, if for example, the observed true conductivity is 15 mS/m and a 900 MHz radar antenna is being used for a test, then the full form of the skin depth must be considered, unless the relative dielectric permittivity is greater than or equal to 6.

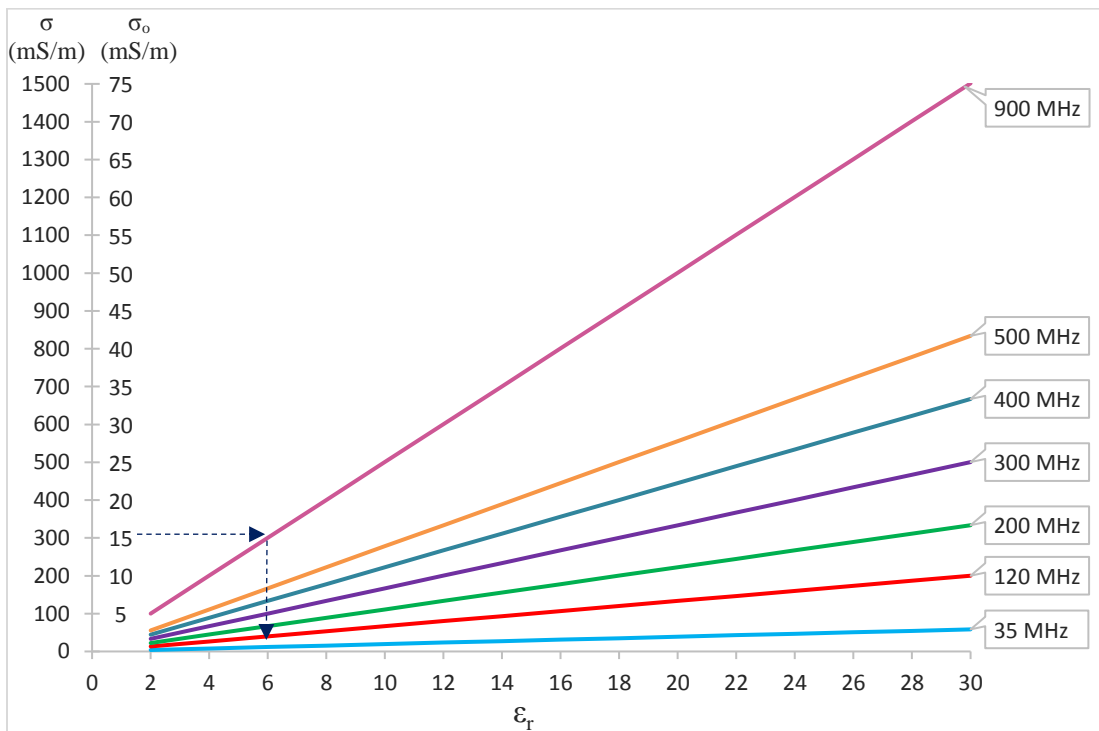


Figure 4-2: Conditions under which the loss tangent $\ll 1$

4.5 TRANSMISSION AND REFLECTION

Ground penetrating radar methods depend on detection of reflected signal from objects or interfaces. The amplitude of reflected signal depends on the reflection coefficient and the incident signal amplitude. In the case of subsurface objects/features, the incident signal amplitude is

controlled by the reflection, transmission, and attenuation properties of the overlaying material. For an electromagnetic wave travelling in slightly conducting media, (from medium 1 to medium 2 as shown in Figure 4-3), the reflection and transmission coefficients $-R_{1,2}$ and $T_{1,2}$ – for signal amplitude between the media can be expressed as (Takahashi et al. 2012, Halabe et al. 1993):

$$R_{1,2} = \frac{\sqrt{\epsilon'_1} - \sqrt{\epsilon'_2}}{\sqrt{\epsilon'_1} + \sqrt{\epsilon'_2}} \quad (4-29)$$

$$T_{1,2} = 1 + R_{1,2} = \frac{2\sqrt{\epsilon'_1}}{\sqrt{\epsilon'_1} + \sqrt{\epsilon'_2}} \quad (4-30)$$

Where the subscripts 1 and 2 denote the first and second medium at the interface.

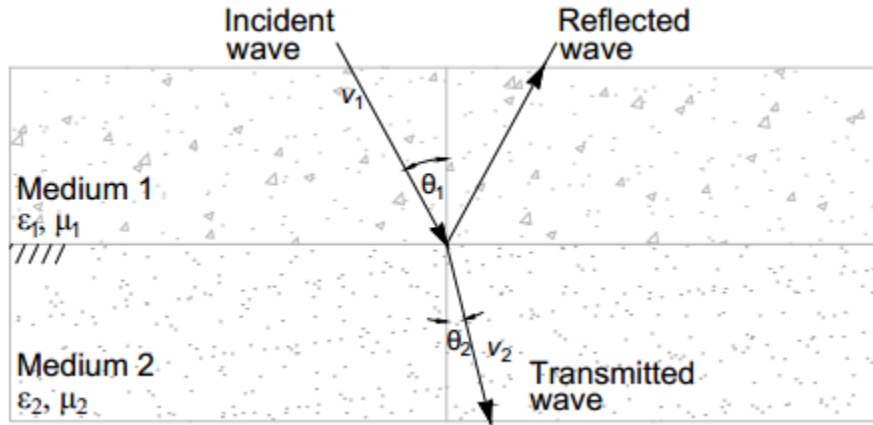


Figure 4-3: Reflection and transmission of incident electromagnetic wave at an interface

As illustrated in Figure 4-3, the direction of wave travel changes at the media interface (i.e., the wave is refracted) in accordance with Snell's law – Equation 4-31).

$$\frac{\sin \theta_1}{v_1} = \frac{\sin \theta_2}{v_2} \quad (4-31)$$

If v_2 is greater than v_1 , then there is a maximum angle called the *critical angle* for medium 1 beyond which the electromagnetic wave cannot propagate from medium 1 to medium 2. In this case, the incident signal is completely reflected - a condition referred to as *total internal reflection*. When the incident wave is at the critical angle, the refracted wave travels along the boundary between

the two media, and forms an angle of 90° with the normal (Figure 4-4) (Reynolds 2011, Annan 2009).

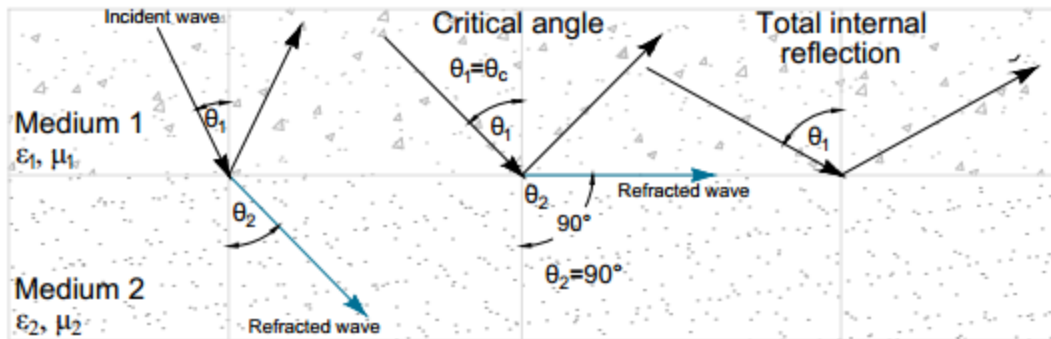


Figure 4-4: Refraction of incident electromagnetic wave at the interface between two media

4.6 DIELECTRIC CHARACTERISTICS OF COMMON SOIL MATERIALS

For certain GPR applications, material properties provided in Table 4-1 (adapted from Cassidy 2009, Goodman and Piro 2013, Davis and Annan 1989, and Daniels 2004) and the assumption of low-loss condition can be combined to appropriately estimate the GPR wave velocity, attenuation, and wave length in a material (Cassidy 2009). For a more accurate and/or detailed characterization of most porous material (e.g. soils), the material is considered as a mixture of its various components (mixture of solid particles/grains, air, and water/pore fluid). An appropriate mixing model is then selected to estimate the effective dielectric permittivity of the mixture.

4.6.1 Dielectric Models

There are a number of empirical relations for estimating the effective dielectric permittivity of mixtures; most of these relations rely on water content and porosity of the mixture to calculate the dielectric constant. This is because the dielectric permittivity of water is significantly higher than that of most dry soils, as such the dielectric permittivity of soils is primarily controlled by the presence of water in the pore space.

One of the widely used basic dielectric models (ϵ - θ relationships) is the Topp equation (Topp et al. 1980), which requires selection of appropriate polynomial coefficients for accurate results. A general form of the formula for mineral soils is provided below.

Table 4-1: Relative dielectric constants and conductivity of common subsurface materials

Material	Relative permittivity, ϵ				Conductivity(mS/m)			
	Cassidy 2009	Goodman & Daniels Piro 2013	Daniels 2004	Davis & Annan '89	Cassidy 2009	Goodman & Daniels Piro 2013	Daniels 2004	Davis & Annan '89
Air	1	1	1	1	0	0	0	0
Clay – dry	2 – 20		2 – 6	5 – 40	1 – 100	1	100 – 1E3	2 – 1000
Clay – wet	15 – 40	12	5 – 40		100 – 1000	100	100 – 1E3	
Concrete – dry	4 – 10	7	4-10		1 – 10	0.1	1 – 10	
Concrete – wet	10 – 20		10 – 20		10 – 100		10 – 100	
Freshwater /Distilled	78 – 88	81	81	80	0.1 – 10	0.1 – 10	0.001 – 10	0.01 – 0.5
Seawater	81 – 88	81	81	80	4000	4000	100000	30000
Freshwater ice	3	4	4	3 – 4	1 – 1E-6	1	0.1 – 1	0.01
Seawater ice	4 – 8		4 – 8		10 – 100		10 – 100	
Permafrost	2 – 8	8	4 – 8		0.1 – 10	1	0.01 – 10	
Granite – dry	5 – 8	5	5	4 – 6	5	1E-5	3	0.01 – 1
Granite – wet	5 – 15		7		1 – 10		1 – 10	
Limestone – dry	4 – 8		7	4 – 8	7		3	0.5 – 2
Limestone – wet	6 – 15		8		10 – 100		10 – 100	
Sandstone – dry	4 – 7		2 – 5		1E-3 – 1E-7		1E-3 – 0.01	
Sandstone – wet	5 – 15	6	5 – 10		0.01 – 0.001	40	0.1 – 10	
Shale – dry			4 – 9				1 – 10	
Shale – saturated	6 – 9		9 – 16		10 – 100		1 – 100	
Sand – dry	3 – 6	9	2 – 6	3 – 5	0.0001 – 1	1	1E-4 – 1	0.01
Sand – wet	10 – 30		10 – 30	20 – 30	0.1 – 10		1 – 10	0.1 – 1.0
Sand – coastal, dry	5 – 10				0.01 – 1			
Soil – sandy, dry	4 – 6	2.5	4 – 10		0.1 – 100	0.14	0.1 – 10	
Soil – sandy, wet	15 – 30	25	10 – 30		10 – 100	7	10 – 100	
Soil – loamy, dry	4 – 6	2.5	4 – 10		0.1 – 1	0.11	0.1 – 1	
Soil – loamy, wet	10 – 20	19	10 – 30		10 – 100	21	10 – 100	
Soil – clayey, dry	4 – 6	2.4	4 – 10		0.1 – 100	0.3	10 – 100	
Soil – clayey, wet	10 – 15	15	10 – 30		100 – 1000	50	1 – 1E3	
Soil – average	16				5			
Asphalt		6	2 – 12			1	1 – 100	
Basalt		8				10		
Copper		1				5800		
Silicon		12				1		
Snow		1.4	6 – 12			1E-4	1E-3 – 0.01	
Iron		1				1E9		
Wood (dry)		3				3		
Sand		8				3		
Shales				5 – 15				1 – 100
Silts				5 – 30				1 – 100
Coal, dry			3.5				1 – 10	
Coal, wet			8				1 – 100	
Salt, dry			4 – 7	5 – 6			0.1 – 10	0.01 – 1

$$\varepsilon'_r = 3.03 + 9.3\theta + 146\theta^2 - 76.7\theta^3 \quad (4-32)$$

where θ is the volumetric water content of the soil.

For clay or organic rich soils, Equation 4-32 is considered inappropriate, and a site specific calibration may be required (Friedman 1998, Cassidy 2009, Zegelin et al. 1992). Topp et al. (1980) also provided a calibration of Equation 4-32 and selection of polynomial coefficients for organic soils as given by:

$$\varepsilon'_r = 1.74 - 0.34\theta + 135\theta^2 - 55.3\theta^3 \quad (4-33)$$

Equation 4-33 is considered to be applicable “for soils with higher water content or organic matter” (Porretta and Bianchi 2016):

Many other ε - θ relationship models have been developed by various researchers, some of which are reviewed by Porretta and Bianchi (2016), and Mukhlism and Saputra (2013). Some of the ε - θ models are presented in Equations 4-34 through 4-41

Roth et al. (1992) developed the following model from experiment conducted on mineral soils:

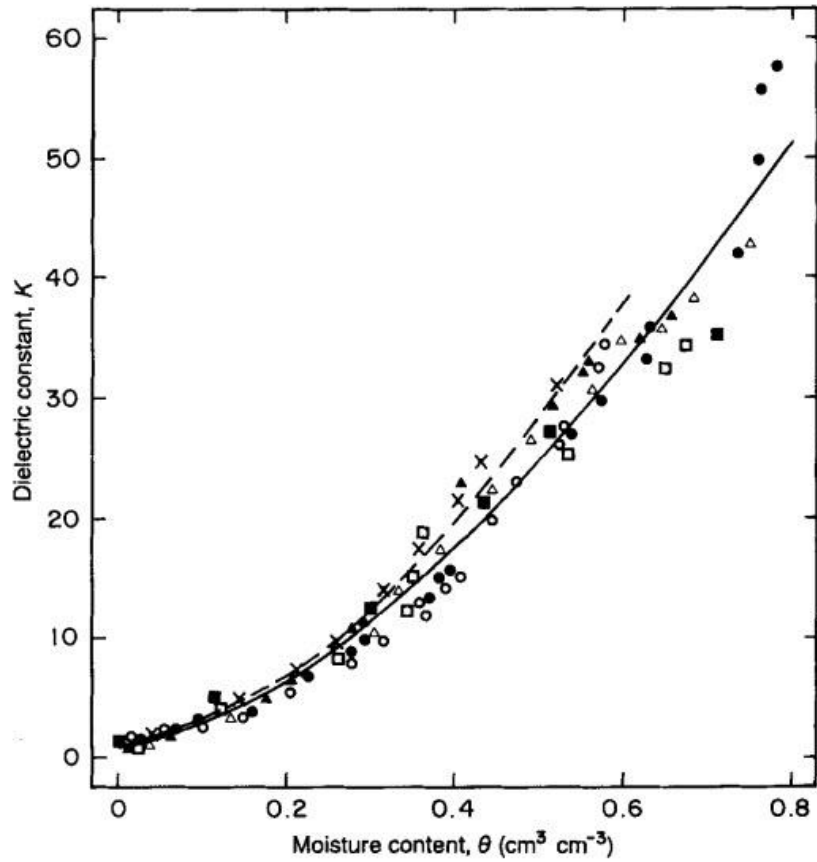
$$\varepsilon'_r = 2.87 - 11.1\theta + 276\theta^2 - 272\theta^3 \quad (4-34)$$

And for organic soils:

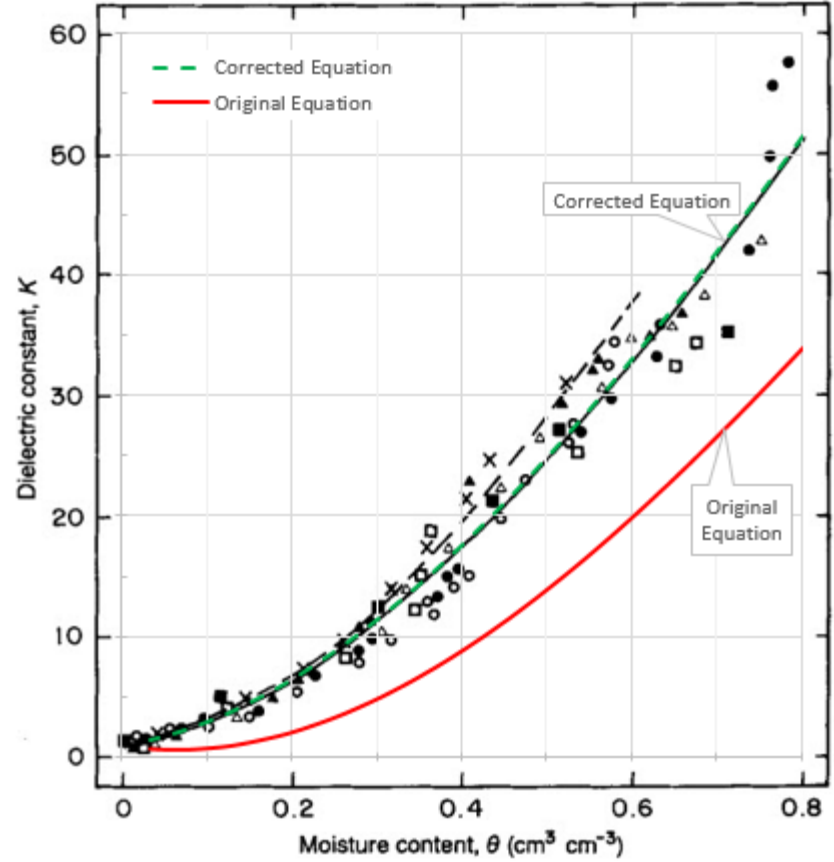
$$\varepsilon'_r = 0.97 + 10.9\theta + 87.4\theta^2 - 28.0\theta^3 \quad (4-35)$$

The original equation for organic soils in the literature by Roth et al. had coefficient of the second term to be negative (-10.90), this however did not conform to the data and plots presented in the same paper. It was realized after investigation that, changing the coefficient to positive (+10.90) as presented in Equation 4-35 made the equation conform to the plot presented in the original literature. Detailed comparison between the original (erroneous) equation and the corrected equation (Equation 4-35) are shown in Figure 4-5.

Ferré et al. (1996) developed a simple square root averaging model for ε - θ relationship as presented in Equation 4-36. The author also showed that this relation (Equation 4-36) conforms to the Topp equation for mineral soils.



(a) Original plot showing the fitted line (Roth et al. 1992)



(b) Plot overlaid with the original and corrected equations

Figure 4-5: Organic soil model by Roth et al. showing original and corrected fitted lines

$$\theta = 0.1181\sqrt{\varepsilon'_r} - 0.1841 \quad (4-36)$$

$$\therefore \varepsilon'_r = \left(\frac{\theta + 0.1841}{0.1181} \right)^2 \quad (4-37)$$

Schaap et al. (1996) also developed a ε - θ relationship model from experiments conducted on organic soil floor samples. This model similar to Equation 4-36:

$$\theta = 0.136\sqrt{\varepsilon'_r} - 0.119 \quad (4-38)$$

$$\therefore \varepsilon'_r = \left(\frac{\theta + 0.119}{0.136} \right)^2 \quad (4-39)$$

Ledieu et al. (1986) proposed another form of this ε - θ relationship as provided by Porretta and Bianchi (2016):

$$\theta = 0.1138\sqrt{\varepsilon'_r} - 0.1758 \quad (4-40)$$

$$\therefore \varepsilon'_r = \left(\frac{\theta + 0.1758}{0.1138} \right)^2 \quad (4-41)$$

The most popular mixing model formulation for GPR applications is the Complex Refractive Index Model (CRIM). This estimates the effective dielectric permittivity of a mixture by taking into account the properties of its constituents. This model is simple, and has been found to be robust and accurate (Cassidy 2009). The general form of the CRIM formula is written as:

$$\varepsilon_{mix}^e = \left(\sum_{i=1}^n f_i \sqrt{\varepsilon_i} \right)^2 \quad (4-42)$$

where:

ε_{mix}^e = relative complex effective permittivity of the mixture

f_i = volume fraction of the i th component

ε_i = relative complex effective permittivity of the i th component

A three component model is appropriate for soils in most cases, which results in formula given below:

$$\varepsilon_{mix}^e = \left[(\phi S \sqrt{\varepsilon_w}) + ((1 - \phi) \sqrt{\varepsilon_s}) + (\phi(1 - S) \sqrt{\varepsilon_g}) \right]^2 \quad (4-43)$$

where:

ε_{mix}^e = complex relative effective permittivity of the mixture

ϕ = porosity of the mixture

S = degree of saturation

$\varepsilon_s, \varepsilon_w, \varepsilon_g$ = relative permittivities of solids, water, and gas/air components respectively

Thus, using Equation 4-43 and known properties of a given soil, the relative dielectric permittivity can be computed. This can greatly help in analyzing and interpreting GPR data.

4.6.2 Inverse Models

Similar to the models used to estimate dielectric constant from volumetric water content measurements, a number of inverse models exist for computing volumetric water content from dielectric data. These relations are useful in estimating the water content of the soil from GPR survey data if the depth to target or dielectric constant of the soil is known.

Topp et al. (1980) provided a model for the inverse ε - θ relation for mineral soils, based on the same experimental data used to derive Equation 4-32:

$$\theta = -5.3 \times 10^{-2} + 2.92 \times 10^{-2} \varepsilon_r' - 5.5 \times 10^{-4} \varepsilon_r'^2 + 4.3 \times 10^{-6} \varepsilon_r'^3 \quad (4-44)$$

Roth et al. (1992) proposed another inverse ε - θ relation from experimental data. The relationship proposed by Roth et al. for mineral soils is given by:

$$\theta = -0.0728 + 0.0448 \varepsilon_r' - 0.00195 \varepsilon_r'^2 + 0.0000361 \varepsilon_r'^3 \quad (4-45)$$

And for organic soil material, they proposed:

$$\theta = -0.0233 + 0.0285 \varepsilon_r' - 0.000431 \varepsilon_r'^2 + 0.00000304 \varepsilon_r'^3 \quad (4-46)$$

Yet another model is provided by Curtis (2001), based on experiment conducted on a wide range of soil textures as:

$$\theta = -0.0286 + 0.02435 \varepsilon_r' - 0.0003421 \varepsilon_r'^2 + 0.00000237 \varepsilon_r'^3 \quad (4-47)$$

Other models are provided by Ferré et al. (1996), Schaap et al. (1996), and Ledieu et al. (1986); these have already been presented in Equations 4-36, 4-38, and 4-40 respectively. Equations 4-36, 4-38, and 4-40 are simpler, and therefore could also be used to calculate dielectric constant from soil volumetric water content without resorting to complicated solvers or trial-and-error approach as shown in Equations 4-37, 4-39, and 4-41.

4.7 CONCLUSIONS

The theory behind the application of GPR, and how to estimate the various parameters has been evaluated in this chapter. Some of the equations presented will be used later in Chapter 8 to calculate parameters for the experimental work done in this study.

CHAPTER 5

GPR EQUIPMENT, SENSORS, AND DATA PROCESSING

5.1 INTRODUCTION

A versatile GPR equipment with changeable antenna set-up, and capable of operating with different antenna frequencies was used in this research in order to evaluate the appropriate choice of antenna for buried non-metallic pipe detection. This chapter describes the GPR equipment and the antenna frequencies used, soil moisture sensors used, as well as the data processing techniques employed to enhance the obtained GPR data for easier interpretation and buried pipe identification.

5.2 GPR EQUIPMENT

The GPR system used in this study was the SIR-20 model manufactured by Geophysical Survey Systems, Inc. (GSSI). SIR-20 is a versatile, high-performance dual channel GPR data acquisition system, with operating temperature of -10°C to 40°C . The system can operate with either 120V AC or 12V DC power supply, and can be mounted on a cart, a vehicle, or used without any mount. A cart mounted set-up was used during this study. A 200 MHz antenna with a specified penetration depth of up to 9 m or 30 ft. (in dry sand) and a 400 MHz antenna with a specified penetration depth of up to 4 m or 12 ft. (in dry sand) were evaluated with this system. In addition to these antenna frequencies, a 900 MHz antenna with a specified penetration depth of up to 1 m or 3 ft. was also evaluated at the beginning of the study and found to be inadequate in achieving the expected penetration depth in the wet soil medium in the study. The quoted penetration depths depend on the complex dielectric permittivity of the soil medium, and therefore can be significantly lower in soils with high moisture contents and high clay content. The GPR system and antennae used in this study are shown in Figure 5-1.

The GPR system has survey wheels with optical encoder for tracking horizontal distance along the ground surface. A survey wheel attached to the GPR cart is used to track distance when the 400 MHz antenna is used, while the 200 MHz antenna has a survey wheel attached to the antenna for horizontal distance measurement as shown in Figure 5-2. Physical dimensions and depth specifications of the GPR antennae used are summarized in Table 5-1.

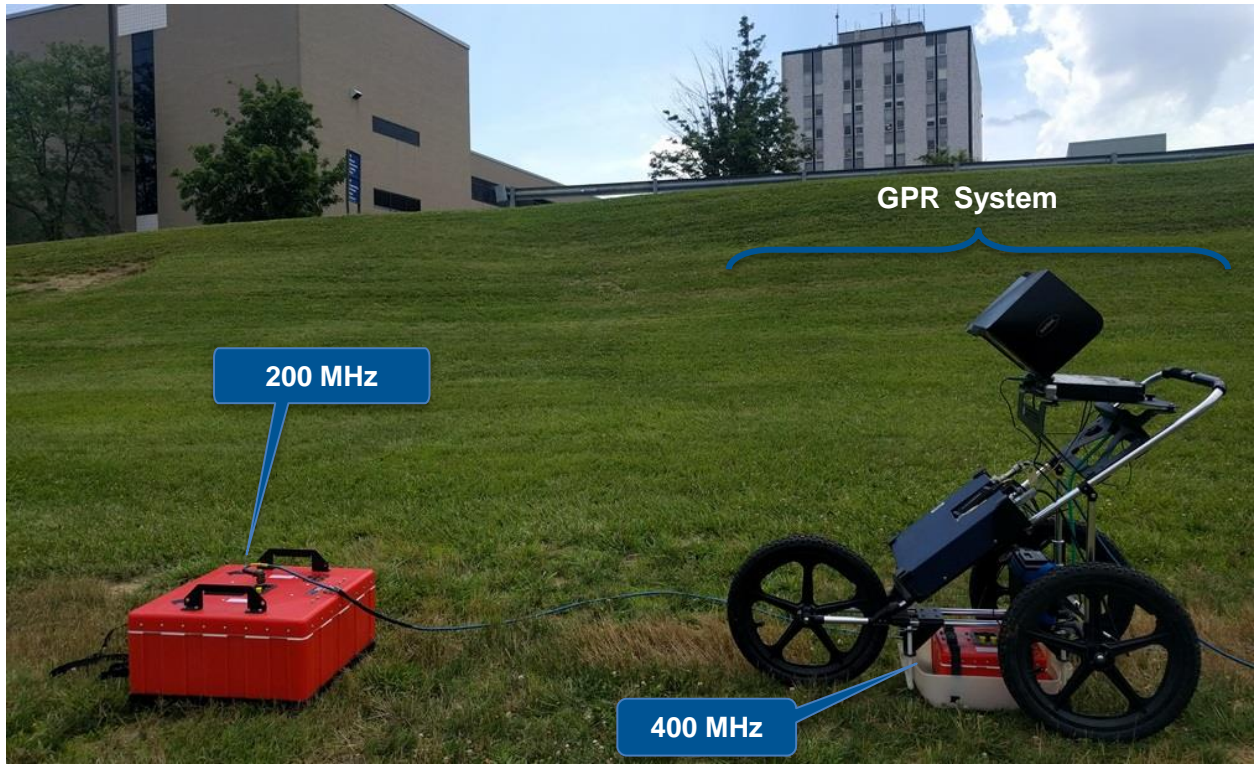


Figure 5-1: SIR-20 GPR system and antennae used for testing



Figure 5-2: 200 MHz GPR antenna with survey wheel

*Table 5-1: GPR antenna specifications**

Antenna Frequency	Dimensions (L x W x D)		Weight		Depth Range	
	cm	inches	kg	lb.	m	ft.
200 MHz	60 x 60 x 30	24 x 24 x 12	20.5	45	0-9	0-30
400 MHz	30 x 30 x 17	12 x 12 x 6.5	5	11	0-4	0-12
900 MHz	33 x 20 x 8	13 x 7.5 x 3.5	2.3	5	0-1	0-3

*From antenna brochure provided by GSSI, Inc.

5.3 SOIL MOISTURE AND ELECTRICAL CONDUCTIVITY SENSOR

Soil moisture content, electrical conductivity, and dielectric constant affects the penetration depth of GPR signals, as well as the amplitude of any returned signals from subsurface objects. GS3 sensors manufactured by Decagon Devices, Inc. were used to measure soil volumetric moisture content, electrical conductivity, and temperature. These parameters enable dielectric constant of the soil medium to be computed, which is very useful in accurate determination of the depth at which objects are buried from GPR data. Figure 5-3 shows one of the GS3 sensors used in this study, and the data logger for recording the sensor data. Specifications of the GS3 sensor, including accuracy and resolution are given in Table 5-2. Details on the sensor arrangement and measurements can be found in Section 6.4 in Chapter 6 and Section 7.2 in Chapter 7 respectively.



(a) Soil moisture and conductivity sensor



(b) Data logger

Figure 5-3: Sensor for measuring soil moisture, conductivity, and dielectric

Table 5-2: GS3 sensor specifications*

Parameter	Volumetric Water Content, VWC or θ (m^3/m^3)	Dielectric Constant, ϵ	Electrical Conductivity (mS/m)	Temperature ($^{\circ}C$)
Range	0.0 to 1.0	1 to 80	0 to 2500	-40 to +60
Accuracy	± 0.03	± 1 from 1 to 40 $\pm 15\%$ from 40 to 80	$\pm 5\%$ from 0 to 500 $\pm 10\%$ from 500 to 2500	± 1
Resolution	0.002 from 0.0 to 0.4 0.001 from 0.4 to 1.0	0.1 from 1 to 20 <0.75 from 20 to 80	0.1	0.1

*From soil moisture sensor specifications provided by Decagon Devices, Inc.

5.4 GPR DATA PROCESSING TECHNIQUES

A number of data processing operations were undertaken to improve the GPR data and make it easier for interpretation and identification of buried non-metallic pipes. All data processing methods discussed here were accomplished using RADAN™ 7⁶. Some of these data processing techniques are briefly explained below.

5.4.1 Background Removal

System noise from the GPR equipment or reflections from smaller subsurface objects such as soil particles, air voids, gravels, etc. can appear in a radargram as background noise. These can sometimes make it difficult to see reflections from the target being investigated. These noises are usually uniform throughout the GPR data and can therefore be removed to improve the visibility of subsurface objects. In some of the data presented in this study, it was necessary to perform background noise removal on the GPR data to improve visibility of the buried pipes.

5.4.2 Peaks Extraction

Reflections from buried objects in a GPR surveys result in higher amplitude signal traces that are recorded by the receiving antenna. However, signals from buried objects are sometimes difficult to interpret because of noise in the medium (reflections from other unwanted objects, signal interference from nearby objects such as cell phones and overhead electric lines among many

⁶ RADAN™ 7 is a GPR data post-processing software developed by Geophysical Survey Systems, Inc. (GSSI)

others). Peaks extraction enables a specified number of peaks/maximum amplitudes to be extracted along the entire depth of the GPR scan data while “muting” all other received data along the depth. Performing this procedure over the entire length of the GPR data may reveal patterns that make it easier to identify buried non-metallic pipes in an otherwise difficult to interpret data.

5.4.3 Horizontal Scaling

This study involves scanning 65 ft. long trenches to locate buried non-metallic pipe samples, and up to 5 ft. depth of penetration. This usually results in data that is very long, requiring continuous scrolling, thus making it difficult to see the overall picture along the entire length of the trenches. The long data are also difficult to fit into a report without losing the vertical resolution/depth information or distorting the data. Horizontal scaling (by stacking) enables a number of successive scans to be averaged and the results stacked together to reduce the file size/length and makes it easier to evaluate the entire data.

5.4.4 Amplitude Extraction

Amplitude extraction makes it possible to obtain amplitudes of reflected signals from buried objects in a GPR data for comparative analysis. This technique was employed to analyze the amplitudes of reflected signals from the different pipe samples evaluated in this study. The obtained amplitude values were then analyzed to identify the best performing pipe samples that could be implemented in industry.

5.5 CONCLUSIONS

A brief description of the GPR equipment, antennae, and some of the data processing techniques used in this study has been present in this chapter. The following chapter will discuss the experimental set up for the study.

CHAPTER 6

EXPERIMENTAL SET UP FOR GPR TESTING

6.1 INTRODUCTION

This research involved investigating the detectability of buried PVC, GFRP, and CFRP pipes with different external surface finishes using GPR in different soil moisture conditions. This chapter provides a brief description of the research procedure, together with the specimen types and configuration, preparation of sample pipe sections, and a description of the pipe layout and site conditions for GPR testing.

6.2 RESEARCH PROCEDURE

In order to determine the detectability of different pipeline materials buried at various depths using Ground Penetrating Radar (GPR), thirty-nine (39) pipe samples with different external surface configurations were prepared and buried in the field. Pipeline materials investigated in this research include Polyvinyl Chloride (PVC), Glass Fiber Reinforced Polymer (GFRP), and Carbon Fiber Reinforced Polymer (CFRP). A 12" diameter steel pipe was also buried to serve as a control specimen. The pipe samples were all 5 ft. long, and capped at both ends to prevent ground water from filling them when buried since the objective is to locate the pipe material without the assistance of the pipe content.

All pipe caps were made of plastic; caps for 12" diameter steel, CFRP, and GFRP pipes with carbon fabric, nanoparticle, or aluminum foil overlays had metal straps around them. Plastic straps were used for the pipe caps in case of the GFRP control pipes (12" and 10" diameter) to ensure that these control pipes did not have any metallic content. It should be noted that the metal straps are very small (~ 0.5" wide by 1/16" thick) and are not expected to interfere with GPR signals at 2 ft. of burial depth or deeper. Caps for the PVC pipes and smaller diameter GFRP and CFRP pipes did not need any straps because the caps were tight fitting.

The pipe segments were buried in four separate trenches, with soil cover of 2 ft., 3 ft., and 4 ft. above the pipes. These buried pipe segments were scanned with GPR in different soil moisture

conditions and the results compared to determine the most promising pipe surface configuration to improve GPR detection.

6.3 PIPE PREPARATION

Pipe samples used in this research are of 12", 6", and 3" diameters and made from PVC, GFRP, and CFRP materials. A 10" diameter GFRP pipe which was used for high pressure testing was also used in this study. Sample preparation of the various pipe segments for GPR testing is elaborated below.

6.3.1 PVC Pipes

The 12" diameter PVC pipes for testing were obtained by cutting 14 ft. long SDR-35 pipes into 5 ft. long segments. The pipes were then capped to prevent ground water from filling them after burying since the objective was to establish the pipe detectability without the help of GPR reflections from any water inside the pipes. Finally, the surfaces of two of the pipes were sanded to enable adequate bonding with CFRP fabric wrap as will be discussed later in Section 6.3.4.1. The 12" diameter PVC pipes are shown in Figures 6-1 and 6-2.

Similar to the 12" diameter PVC pipes, 14 ft. long SDR-35 and 10 ft. long schedule 40 (SCH 40) pipes were cut to obtain the 5 ft. long 6" and 3" diameter pipe samples respectively. The 6" and 3" diameter pipes were also capped, and the surfaces of some of them were sanded to enable adequate bonding with GFRP and CFRP fabric (Figure 6-3).



Figure 6-1: The 14' long 12" diameter PVC pipe being cut



(a)



(b)

Figure 6-2: The 12" diameter PVC pipe (a) after cutting, and (b) after capping



(a) Surface of 3" diameter PVC pipe being sanded

(b) Some of the capped pipes

Figure 6-3: The 3" diameter PVC pipes

6.3.2 GFRP Pipes

The 12" diameter GFRP pipes used in this study were supplied by the manufacturer in 5 ft. long segments (Figure 6-4). The pipes were capped to keep ground water out of the pipes after burying. The external surfaces of some of the pipes were sanded to ensure adequate bonding with CFRP fabric wrap. Fiber and section properties of the GFRP pipes are given in Table 6-1.

The 10" diameter GFRP pipes used in this study were supplied by the manufacturer in 48 inch long segments - these set of pipes were being used for high burst pressure testing. One of the 10" diameter pipes was capped and buried for GPR testing.

The 3" diameter GFRP pipes for the study were manufactured in the WVU Constructed Facilities Center (WVU-CFC) by wrapping two layers of 24 oz. biaxial (0/90) stitched GFRP fabric around 3" diameter PVC pipes (the PVC pipes serving as molds in this process). This increased the outside diameter of the GFRP pipes above the standard 3" PVC pipe dimension. Details of the GFRP fabric and the resin (matrix) system used in manufacturing the 3" GFRP pipe is shown in Table 6-1. The manufacturing process and a completed GFRP pipe are illustrated in Figure 6-5.



(a) GFRP pipes from the manufacturer



(b) Capped pipes

Figure 6-4: The 12" diameter GFRP pipes

Table 6-1: Material and section properties of CFRP and GFRP pipes/fabrics

Pipe Section	Wall Thickness (in)	Fiber Material	Fiber Mat	Fiber Weight (oz. /sq. yd.)	Matrix Material
12" GFRP	3/8	E-Glass	45/90/-45	-	Polyurethane
10" GFRP	3/8	E-Glass	Filament wound	-	Vinyl Ester
3" GFRP	**	E-Glass	0/90	24	Vinyl Ester
12" CFRP	**	Carbon	0/90/±45	28	Vinyl Ester
CFRP Strip/Ring	*	Carbon	0/90/±45	28	Vinyl Ester
3" CFRP	5/16	Carbon	-	-	-

* One layer of fabric was used.

** Two layers of fabric were used.



(a) Manufacturing process



(b) Manufacturing process



(c) Completed pipe

Figure 6-5: Manufacturing a 3" diameter GFRP pipe

6.3.3 CFRP Pipes

The 12" diameter CFRP pipe used in this study was also fabricated in the WVU Constructed Facilities Center (WVU-CFC) by wrapping two layers of quad-axial (0/90/±45) stitched CFRP fabric around a 12" diameter cardboard tube (the cardboard tube served as a mold in this process). Details of the CFRP fabric and the resin system used in manufacturing the 12" CFRP pipe is shown in Table 6-1. The pipe was finally capped to keep ground water out of it after burying. Figures-6-6(a) and 6-6(b) show the CFRP fabric and the completed 12" diameter CFRP pipe respectively

The 3" diameter CFRP pipes used in this study were supplied by the manufacturer in 6 ft. long segments (Figure 6-7). The pipes were first cut into 5 ft. long segments to keep the lengths consistent with the other pipes, they were then capped to keep ground water out of them after burying.



(a) Roll of CFRP fabric



(b) The completed pipe

Figure 6-6: 12" diameter CFRP pipe



Figure 6-7: The 3" diameter CFRP pipes

6.3.4 Creating Dielectric Contrast Between Non-Metallic Pipes and Surrounding Soil

Non-metallic pipe materials (such as PVC and GFRP) buried underground are generally not detectable using GPR in most soil conditions. This is because PVC and GFRP pipe materials have similar dielectric constant as most soils, and are generally transparent to radar waves and hence do not reflect the incident waves in most soil conditions. In order to make these pipe materials detectable using GPR after burying, we have to create a contrast between the dielectric constants of the pipes and the surrounding soil. Three different approaches were adopted to create dielectric

contrast between the pipe materials and the sounding soil – using CFRP rings and strips, aluminum rings and strips, and carbon nanoparticle overlay.

6.3.4.1 Creating Dielectric Contrast Using CFRP Rings and Strips

Carbon fiber, like steel, is an electrical conductor and as such does not allow transmission of radio waves like GPR signal. GPR signal incident on carbon fiber material is reflected back to a receiver (unlike the surrounding soil, which absorbs and/or allows the signal to travel through it), thereby making the material detectable underground.

Dielectric contrast between both the PVC and GFRP pipes, and the surrounding soil was created by wrapping the pipes with CFRP fabric in two different configurations. The first configuration involved wrapping 3" wide CFRP fabric around three of the PVC pipe samples (one each of 12", 6", and 3" diameters) and two of the GFRP pipe samples (12" and 3" diameter) in the form of rings, at a clear spacing of 3". The second configuration involved wrapping CFRP fabric strip along the full lengths (excluding pipe caps in most cases) of three PVC and two GFRP pipe samples. For the 12" diameter pipes, the widths of the strips were up to half the circumference of the pipes. The width of the CFRP strips were up to $\frac{3}{4}$ of the circumference of the 6" diameter pipes, and the strips covered almost the entire circumference in the case of the 3" diameter pipes. This was to ensure part of the CFRP strip remains at the top of the pipe after burying even if the pipe rotates during backfilling. Figure 6-8(a) and (b) show the 6" diameter PVC pipe with the 3" wide CFRP rings and the 12" diameter PVC pipe with the CFRP strip respectively.

6.3.4.2 Creating Dielectric Contrast Using Aluminum Rings and Strips

Aluminum is also an electrical conductor, and hence prevents the transmission and attenuation of radio waves like GPR signal. GPR signal incident on an aluminum material is reflected, thereby making the material distinctive from the surrounding soil, resulting in aluminum being detectable underground.

Similar to the CFRP fabric, aluminum foil was wrapped around some of the PVC and GFRP pipes (in strips and rings) to create a dielectric contrast between the pipes and the surrounding soil when buried. The first configuration involved wrapping 2.83" wide aluminum foil rings around three PVC pipe samples (12", 6", and 3" diameters) and two GFRP pipe samples (12" and 3" diameters),

at a clear spacing of 3". The second configuration involved wrapping aluminum foil strip along the lengths of three PVC pipes and two GFRP pipe samples similar to the CFRP fabric strips. Figure 6-8(c) and (d) show a 12" diameter GFRP pipe with aluminum rings, and a 12" diameter GFRP pipe with aluminum strip along the length respectively. The aluminum foil overlays will be especially useful for PVC pipes since these foils are readily available in hardware stores and can be bonded to already manufactured PVC pipes (which are also readily available in hardware stores).

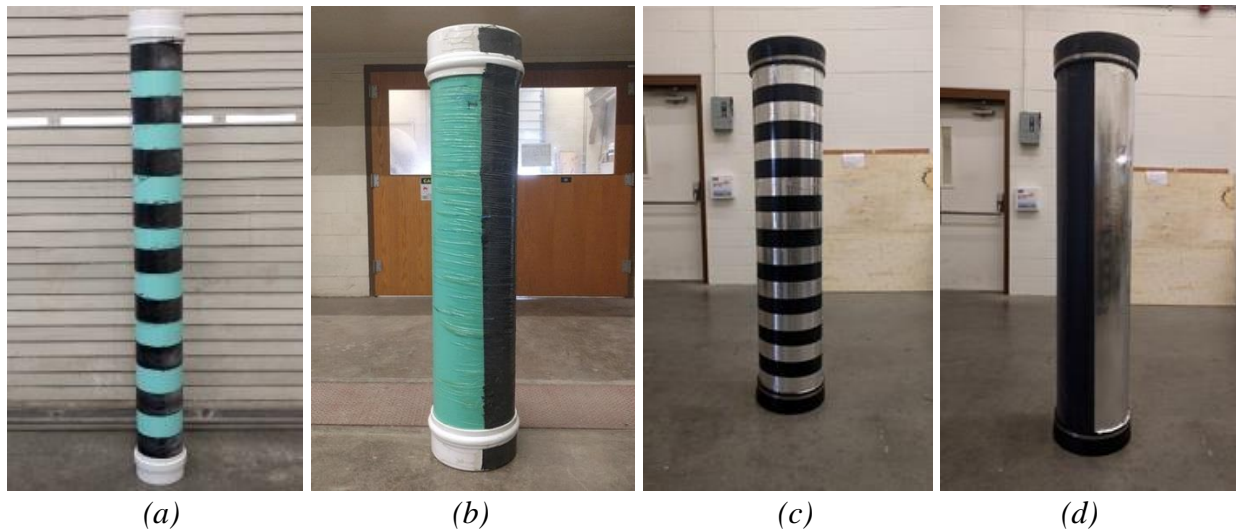


Figure 6-8: Pipe configurations: (a) 6" diameter PVC with carbon fabric rings, (b) 12" diameter PVC with carbon fabric strip, (c) 12" diameter GFRP with aluminum rings, and (d) 12" diameter GFRP with aluminum strip

6.3.4.3 Creating Dielectric Contrast Using Carbon Nanoparticle Overlay

Just like carbon fabric, carbon nanoparticles are also good electrical conductors, and therefore do not allow the transmission and attenuation of radio waves like GPR signal. It is anticipated that, interconnection between carbon nanoparticles in an overlay will be able to reflect incident GPR signal, and make the buried material detectable as a result.

A 12" diameter GFRP pipe was coated with a mixture of carbon nanoparticle and Vinyl Ester matrix up to a quarter of the pipe circumference, and through the entire length of the pipe (excluding caps) as shown in Figure 6-9. This is expected to create a dielectric contrast between the pipe and the surrounding soil when buried.



Figure 6-9: 12" diameter GFRP pipe with carbon nanoparticle overlay

Some of the PVC and GFRP pipes were not wrapped (these are labelled as “Unwrapped” in Figure 6-12), and were used as control specimens during GPR detectability testing of the samples.

As stated earlier, a total of thirty-nine, 5 ft. long pipe segments were prepared using different pipe materials (CFRP, GFRP, and PVC), different pipe diameters (12", 6", and 3"), different surface finishes (CFRP ring, CFRP strip, aluminum ring, aluminum strip, carbon nanoparticles, and unwrapped/control), and buried at different depths (2 ft., 3 ft., and 4 ft. of soil cover above the top of the pipe). Pipes with CFRP, aluminum, or carbon nanoparticles overlays are expected to be easier to detect using GPR (compared to the control samples) because of their higher dielectric permittivity leading to higher reflection coefficient. In addition, the bigger diameter pipes buried with less depth of soil cover should be easier to detect compared to smaller diameter pipes and pipes at deeper depths.

6.4 PIPE BURYING

Pipe specimens prepared for GPR testing were buried at a site located on the WVU campus. The site, which was selected by WVU-CFC in consultation with the Facilities Management at WVU, is near the Engineering Sciences Building (ESB) and is marked with the red polygon on Figure 6-10. Utility lines close to the allocated site were first marked to prevent excavation damage of the lines during pipe burying. The site and the marked utility lines are shown in Figure 6-11.

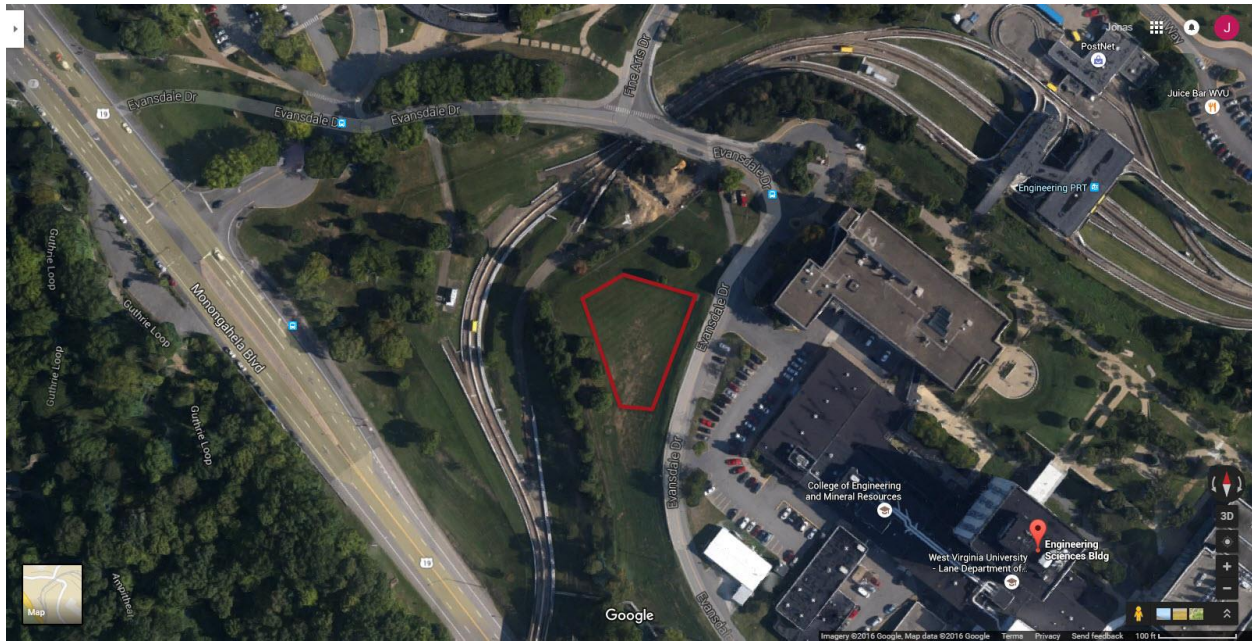


Figure 6-10: The site for pipe burying and monitoring (source: Google Maps)

The pipe samples were buried in 4 separate 65 ft. and 36 ft. long trenches, spaced at 12 ft. apart. 12" diameter and 5 ft. long PVC, CFRP, and GFRP pipes were buried at a depth of 4 ft. in one of the trenches (total trench depth of 5 ft.). The second trench had 3" diameter pipes buried at a depth of 2 ft. (total trench depth of 27"). Two different diameter pipes, 12" and 6", were buried in the third trench, both diameters buried at a depth of 3 ft. to the top of the pipe. The fourth trench is 36 ft. long, and contains 12" diameter GFRP, PVC, Steel, and 10" diameter GFRP pipes buried with 2 ft. of soil cover. Eleven pipes were buried in each of the first three trenches, with 1 ft. spacing between each subsequent pipe as shown in Figure 6-12 and 6-14(a). Six pipes were buried in the final trench, with 1 ft. spacing between subsequent pipes and 2 ft. spacing between pipes at the middle of the trench. The layout of the pipes, including the pipe material, diameter, pipe surface configuration and depth of burial are shown in Figures 6-12 and 6-13.

Additionally, five GS3 soil sensors (Figure 6-14b) manufactured by Decagon Devices, Inc. were buried along the trenches at different depths to measure soil properties throughout the testing period. Two of the sensors were buried at 4 ft. depth along the 12" diameter pipes, two were buried at 2 ft. depth along the 3" diameter pipes and one was used to measure soil properties at various locations on the ground surface. Wires connecting the soil sensors to a data logger were run through 1" diameter PVC conduits before burying to prevent the wires from getting damaged

during compaction of backfill (Figure 6-15). These sensors enabled quantitative determination of volumetric water content, electrical conductivity, temperature, and dielectric constant of the soil during the testing period. The above parameters from the GS3 sensor enabled accurate estimation of the depth of soil cover over the pipes using GPR. These soil parameters are also used in numerical computations in order to make comparison between the GPR field results and the theoretical estimations as presented in Chapter 8.

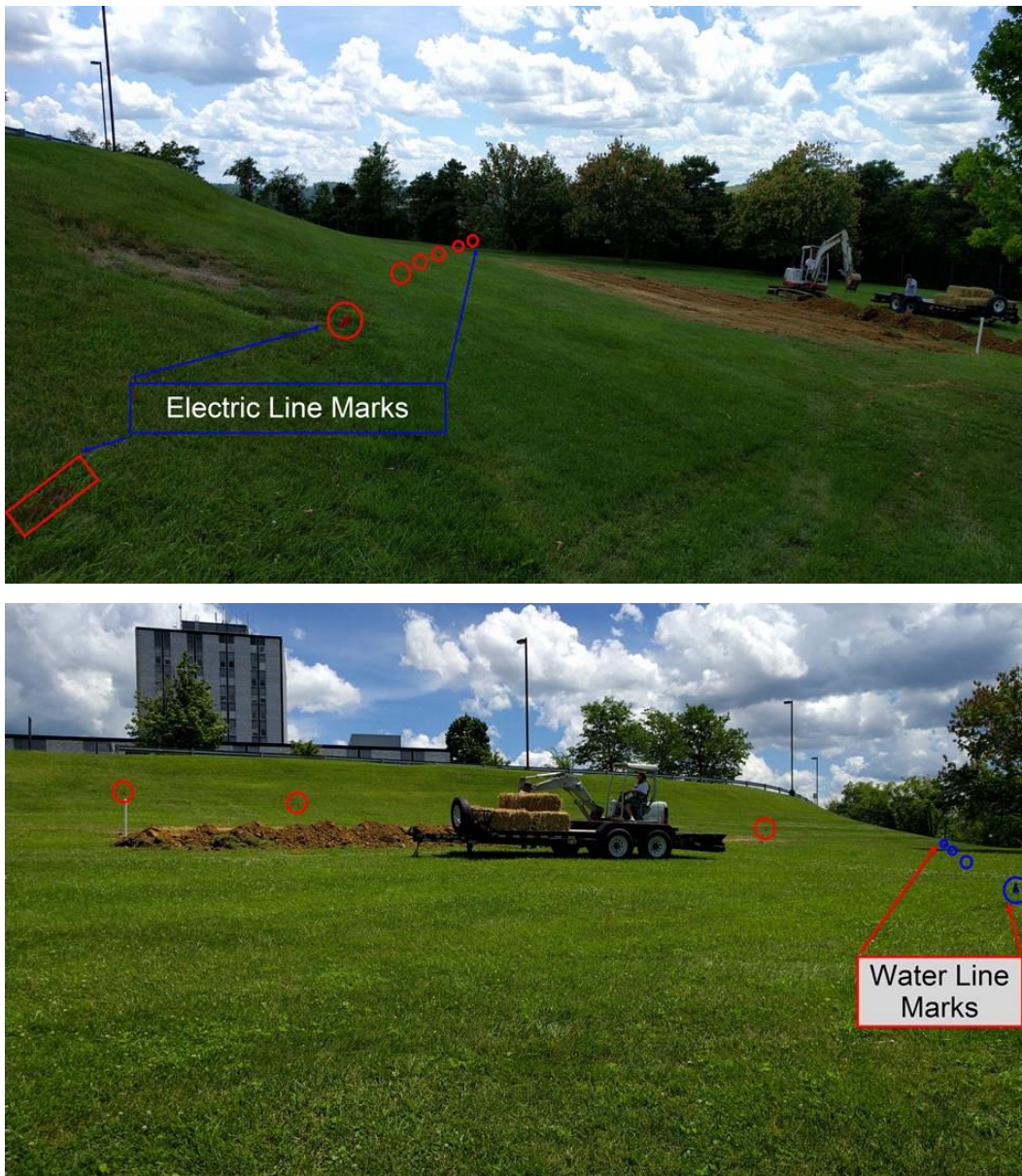
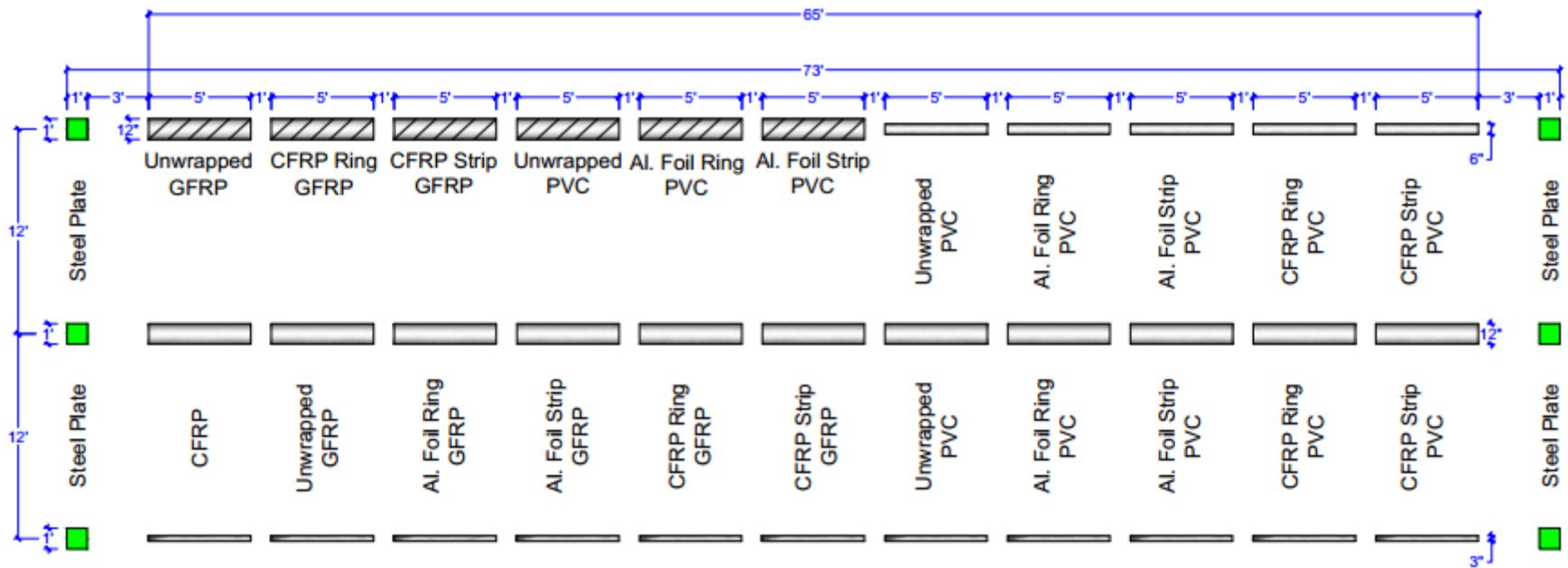


Figure 6-11: The located site on WVU campus for pipe burying, with utility lines marked








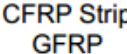
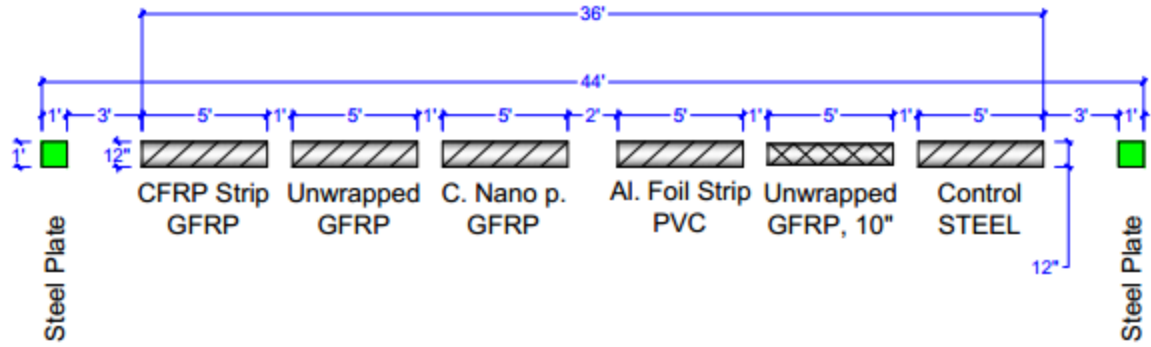
-  Steel plates buried at a depth of 3"
-  12" diameter pipes buried at a depth of 48" (Total trench depth of 60")
-  12" diameter pipes buried at a depth of 36" (Total trench depth of 48")
-  6" diameter pipes buried at a depth of 36" (Total trench depth of 42")
-  3" diameter pipes buried at a depth of 24" (Total trench depth of 27")
-  CFRP Strip GFRP GFRP pipe with CFRP fabric strip over half of the pipe circumference. Similar naming scheme applies to the other pipes in the layout

Figure 6-12: Pipe layout for GPR testing



■ Steel plates buried at a depth of 3"

▨ 12" diameter pipes buried at a depth of 24" (Total trench depth of 36")

▩ 10" diameter pipes buried at a depth of 24" (Total trench depth of 34")

Trench placed at 12' spacing away from the 3' deep pipe trench.

Figure 6-13: Pipe layout for GPR testing (short trench)



Figure 6-14: (a) Arrangement of pipes in the trench, (b) soil moisture and resistivity sensor

Figure 6-16 (a) shows trenching for the 12" and 10" diameter pipes buried with 2 ft. depth of soil cover, while Figure 6-16 (b and c) show the 12" and 6" diameter pipes placed at 3 ft. depth (to the top of the pipe) in the trench and the pipes being covered with backfill. Figure 6-16(d) shows some of the 12" diameter pipes placed in the trench at 4 ft. depth (to the top of the pipe). Two 1 ft. wide

steel plates were buried at about 3" depth (one at each end of the trench) to mark the beginning and end of each trench for GPR testing. The steel plates were buried at a distance of 3 ft. away from the nearest pipe segments at each end of the trench to avoid interference with GPR signal from the buried pipes.

Finally, the trenches were backfilled and compacted, the ground surface was levelled and then seeded with grass (Figure 6-17) to restore the initial field condition before GPR testing. Levelling the ground and seeding with grass was done to ensure the site mirrors actual field conditions for buried pipes that need to be detected in the pipeline industry using GPR. Thus the results obtained from GPR testing will give an indication of the applicability of the developed techniques in the pipeline industry. Levelling and seeding the ground also helps to ensure lawn keeping operations at the site are not interrupted by this study.

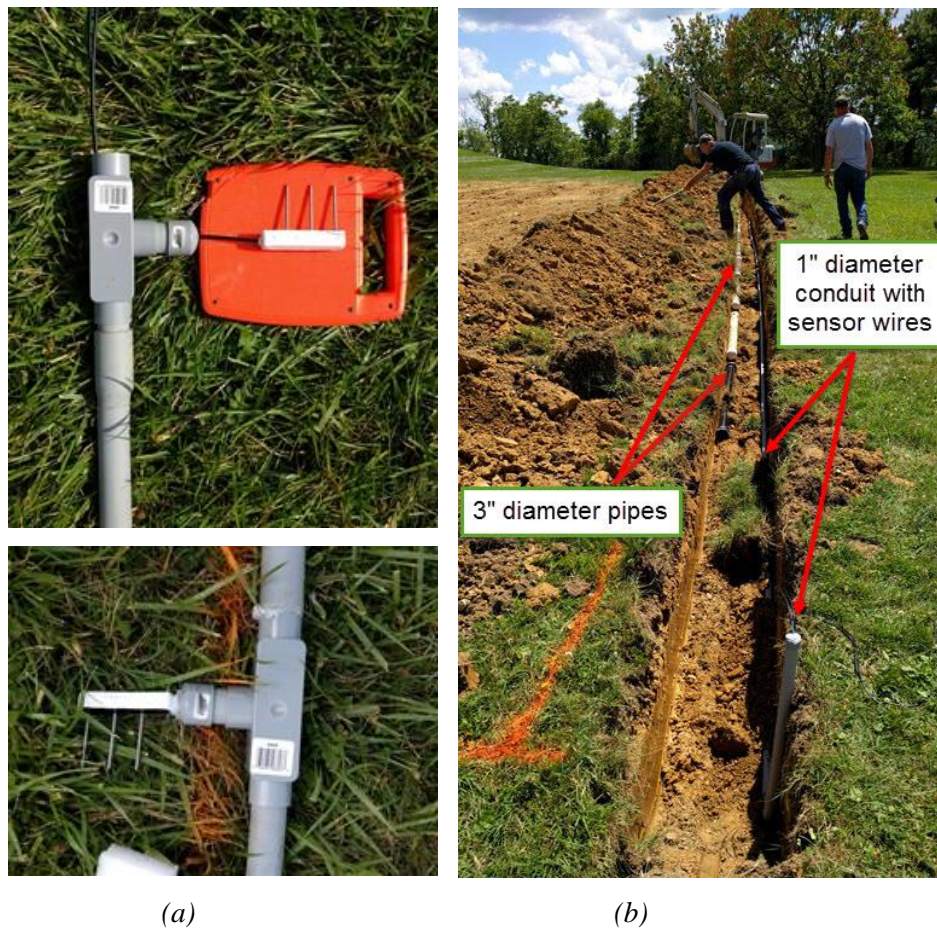


Figure 6-15: (a) Soil sensors with data wires running through conduits to protect the wires, (b) 3" diameter pipes and sensors in the 27" deep trench



(a) (b) (c) (d)

Figure 6-16: Pipe samples being buried



(a) (b)

Figure 6-17: (a) The site being seeded, (b) the field restored to initial condition

A summary of the pipe samples, materials, surface configuration, pipe diameter, and depth of soil cover over buried pipes is presented in Table 6-2. Several GPR field tests of the buried pipes were conducted under varying weather and soil moisture conditions, after the grass was allowed to grow to restore the field to its initial condition. These GPR test results are discussed in the next chapter. Comparison of the results for the various buried pipes serves to determine the suitable pipe surface configurations for easier detection of buried non-metallic pipes.

Table 6-2: Summary of pipe samples and configurations

Pipe Materials	Soil Cover Depth (ft.)	Pipe Diameters with Each Surface Configuration					Carbon Nano-particle	Total
		Control	CFRP		Aluminum			
			Strip	Ring	Strip	Ring		
CFRP	4	12"						1
	2	3"						1
GFRP	4	12"	12"	12"	12"	12"		5
	3	12"	12"	12"				3
	2	12", 10", 3"	12", 3"	3"	3"	3"	12"	9
PVC	4	12"	12"	12"	12"	12"		5
	3	12", 6"	6"	6"	12", 6"	12", 6"		8
	2	3"	3"	3"	12", 3"	3"		6
Steel	2	12"						1
Total		12	7	6	7	6	1	39

6.5 CONCLUSIONS

This chapter summarized the sample preparation and material properties of the pipe specimens used in the GPR detectability testing. The following chapter presents the field testing results and analysis of the obtained data.

CHAPTER 7

GPR TEST RESULTS AND DATA ANALYSIS

7.1 INTRODUCTION

Different pipe material samples (CFRP, GFRP, and PVC) with different external surface finishes were buried at a test site as explained in Chapter 6. Multiple GPR surveys were carried out during this study to evaluate the detectability of the different pipe configurations. The results of these tests and analyses conducted on the data are presented in the following sections.

7.2 GPR TEST RESULTS

GPR tests were conducted under different soil moisture conditions (indicated by the changing soil volumetric water content and dielectric constant for each test), and using different antennae frequencies (200 MHz and 400 MHz). A 900 MHz antenna was also evaluated at the beginning of the study and found to be inadequate in achieving the expected penetration depth in the wet soil medium in this study. Scans were carried out in both the longitudinal direction along the pipe trenches, and transverse direction across the trenches/pipes. Some of the test data, labelled as Dataset I through Dataset III are presented below. GPR survey for Dataset I was conducted in a relatively dry soil in the summer months, with average volumetric water content up to 2 ft. depth of $0.290 \text{ m}^3/\text{m}^3$; survey for Dataset II was conducted in a relatively wet soil in the winter months, with average volumetric water content up to 2 ft. depth of $0.473 \text{ m}^3/\text{m}^3$; while survey for Dataset III was conducted in spring months, with average volumetric water content up to 2 ft. depth of $0.343 \text{ m}^3/\text{m}^3$. Detailed average soil properties for the dataset presented are given in Table 7-1.

Table 7-1: Average soil dielectric properties during data collection

Depth Up to	Dataset I			Dataset II			Dataset III		
	<i>VWC, θ</i> (m^3/m^3)	<i>Diel.</i> ϵ	<i>Cond.</i> (mS/m)	<i>VWC, θ</i> (m^3/m^3)	<i>Diel.</i> ϵ	<i>Cond.</i> (mS/m)	<i>VWC, θ</i> (m^3/m^3)	<i>Diel.</i> ϵ	<i>Cond.</i> (mS/m)
2'	0.290	13.42	10.94	0.473	26.77	17.08	0.343	16.60	12.47
3'	0.315	15.09	11.43	0.473	26.75	16.97	0.363	18.12	12.86
4'	0.341	16.76	11.92	0.473	26.73	16.85	0.383	19.65	13.25

7.2.1 900 MHz Antenna Data

Figure 7-1 shows a longitudinal GPR scan over the full length of the trench with 3" diameter pipes buried at 2 ft. depth of soil cover using the 900 MHz antenna. Average soil dielectric constant and electrical conductivity (up to 2 ft. depth) for this data were 19.76 and 14.13 mS/m respectively. As can be seen in the figure, none of the buried pipes could be identified in the GPR scan. Further tests were conducted and it was concluded that the 900 MHz antenna is inadequate for this study. The remainder of this chapter will focus on data obtained from the deeper penetrating 200 MHz and 400 MHz antennae.

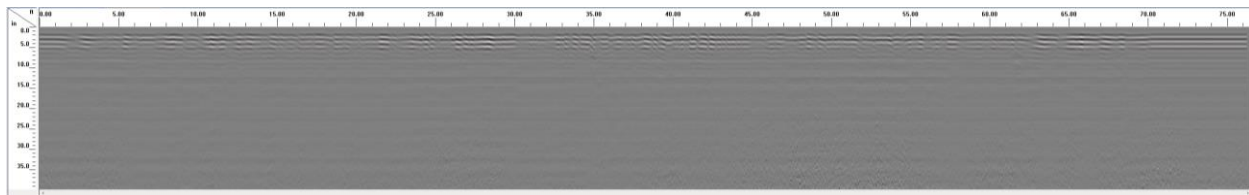
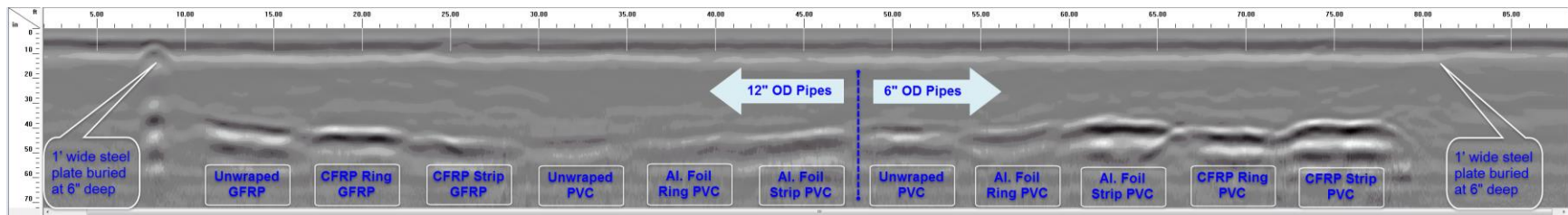


Figure 7-1: Longitudinal scan over 3" diameter pipes at 2 ft. depth using 900 MHz antenna

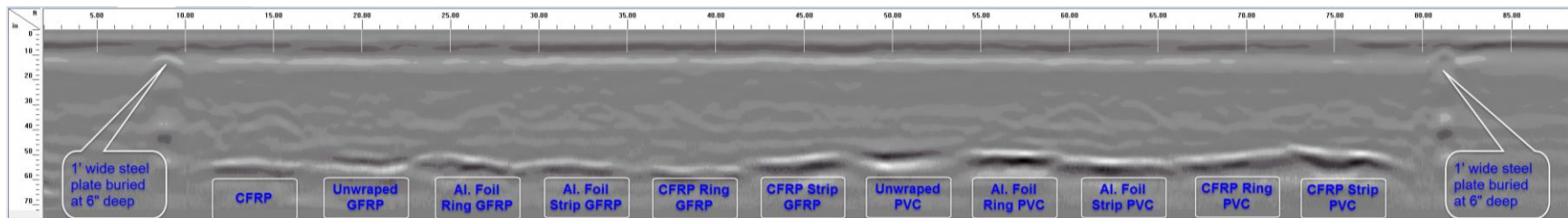
7.2.2 Dataset I

Raw data from longitudinal scans over the four trenches for Dataset I using 200 MHz antenna are shown in Figure 7-2(a) through (d) for comparison. Figures 7-3 through 7-6 show comparisons between the raw and the processed scans from each trench using “Peaks extraction” data processing technique in RADAN™ 7. Extracting reflected signal peaks in the GPR data makes it easier to see the buried pipes. Data from radar scan using the 400 MHz antenna over the 12" and 10" diameter pipes buried with 2 ft. of soil cover is shown in Figure 7-7.

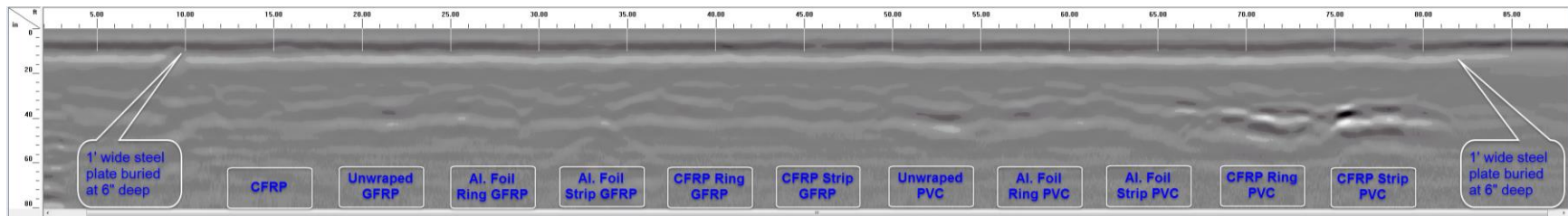
With the exception of the 3" diameter pipes buried with 2 ft. of soil cover, good GPR signal reflections were recorded from pipes buried in all the other trenches as shown in Figure 7-2. Good signal reflection from the buried pipes in this dataset can be attributed to the relatively dry soil under which the data was collected (compared to the other datasets). These reflected signals made it possible to detect the buried pipes with varying levels of clarity and signal strengths. It is observed from Dataset I (Figures 7-2 through 7-6) that, carbon fabric and aluminum foil wraps/overlays on the pipe sections improve detectability with GPR. It is also observed that, carbon fabric strips and aluminum strips along the full length of the pipe sections generally produce better results compared to aluminum rings and carbon fabric rings; this will be explained further



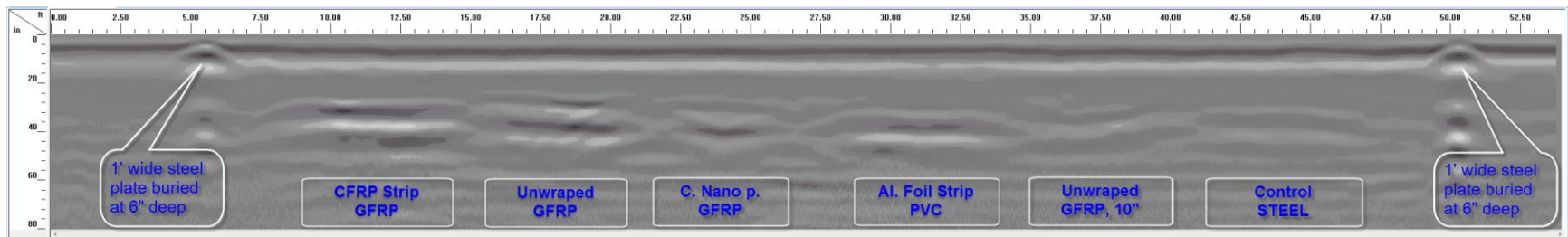
(a) Longitudinal scan along the full length of 12" and 6" diameter pipes with 3 ft. of soil cover



(b) Longitudinal scan along the full length of 12" diameter pipes with 4 ft. of soil cover

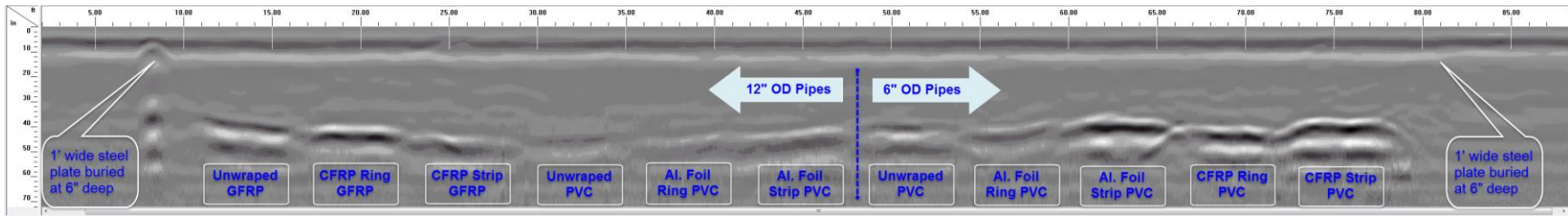


(c) Longitudinal scan along the full length of 3" diameter pipes with 2 ft. of soil cover

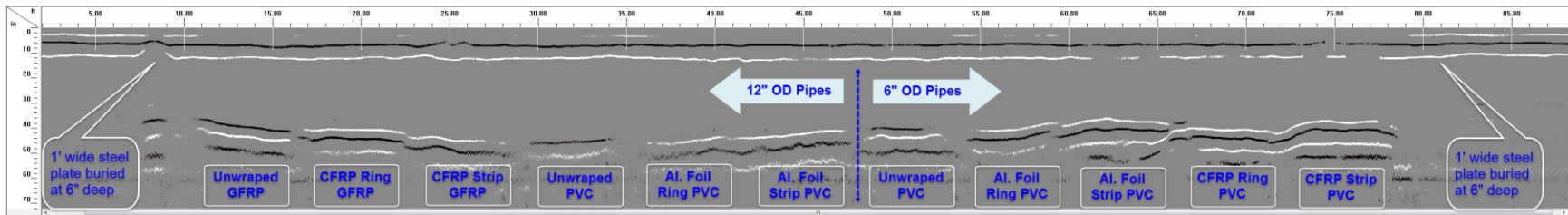


(d) Longitudinal scan along the full length of 12" and 10" diameter pipes with 2 ft. of soil cover

Figure 7-2: Dataset I - Longitudinal scans over the pipe trenches using 200 MHz antenna

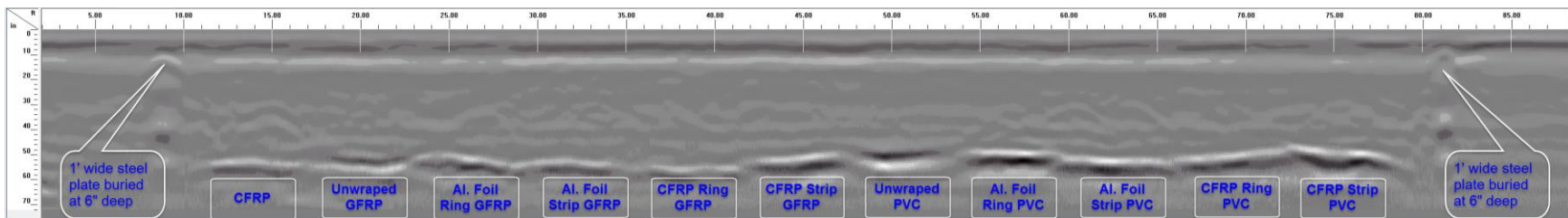


(a) Longitudinal scan along the full length of 12" and 6" diameter pipes with 3 ft. of soil cover

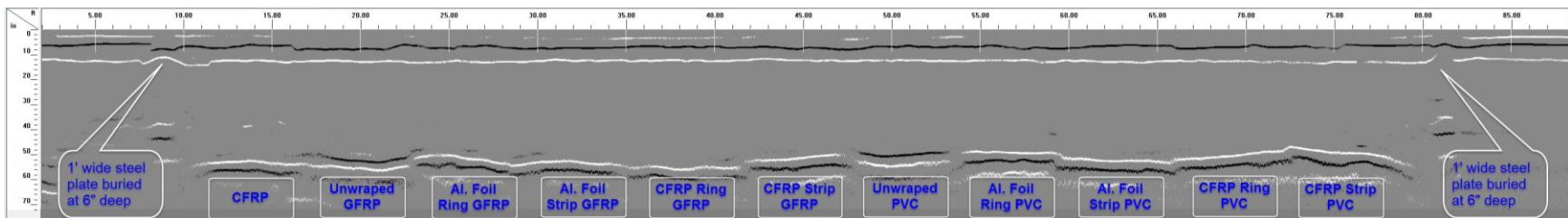


(b) Peaks extraction processing used to make buried pipes in scan (a) more visible

Figure 7-3: Longitudinal scan over the 3 ft. deep trench for Dataset I using 200 MHz antenna

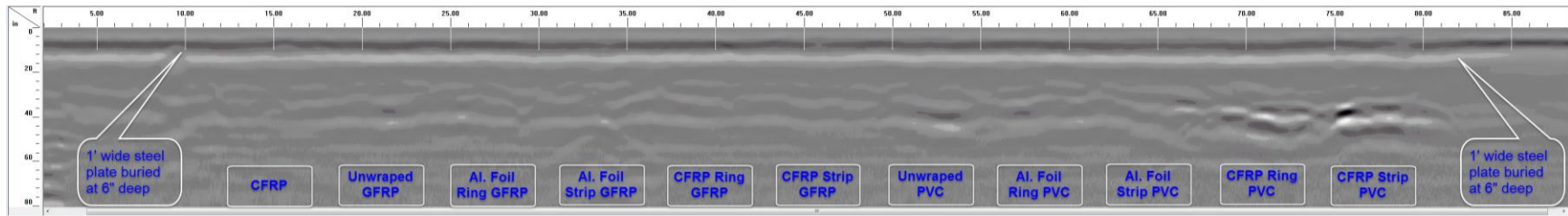


(a) Longitudinal scan along the full length of 12" diameter pipes with 4 ft. of soil cover

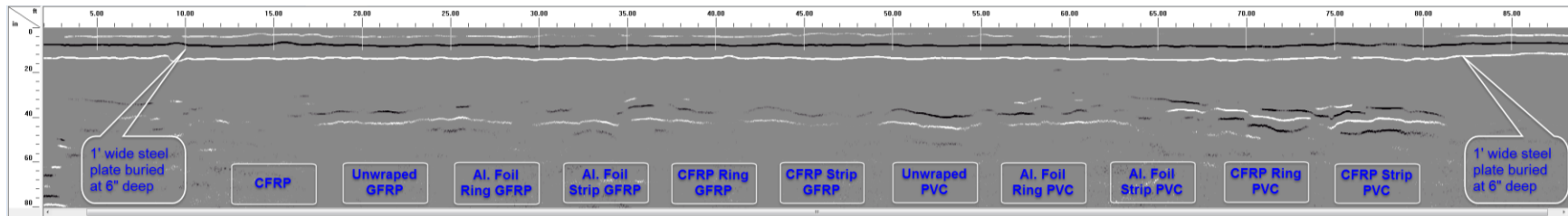


(b) Peaks extraction processing used to make buried pipes in scan (a) more visible

Figure 7-4: Longitudinal scan over the 4 ft. deep trench for Dataset I using 200 MHz antenna

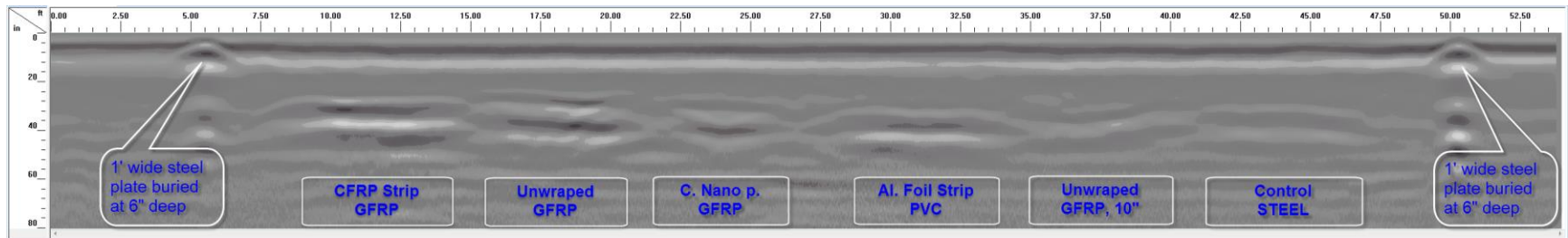


(a) Longitudinal scan along the full length of 3" diameter pipes with 2 ft. of soil cover

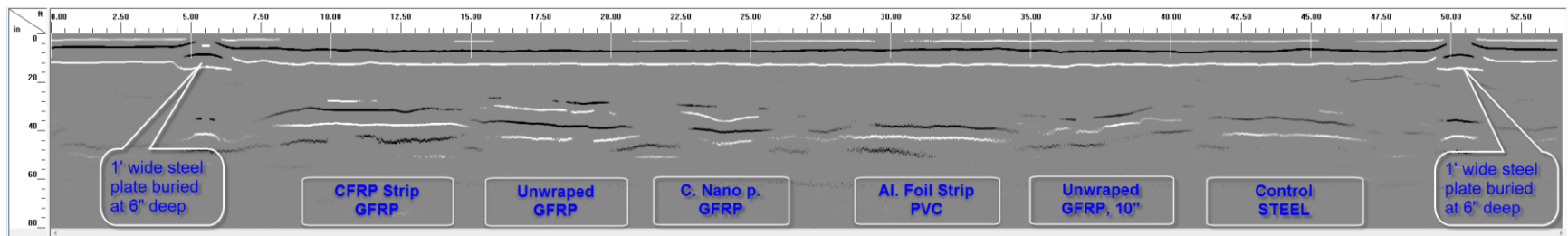


(b) Peaks extraction processing used to make buried pipes in scan (a) more visible

Figure 7-5: Longitudinal scan over the 2 ft. deep trench for Dataset I using 200 MHz antenna

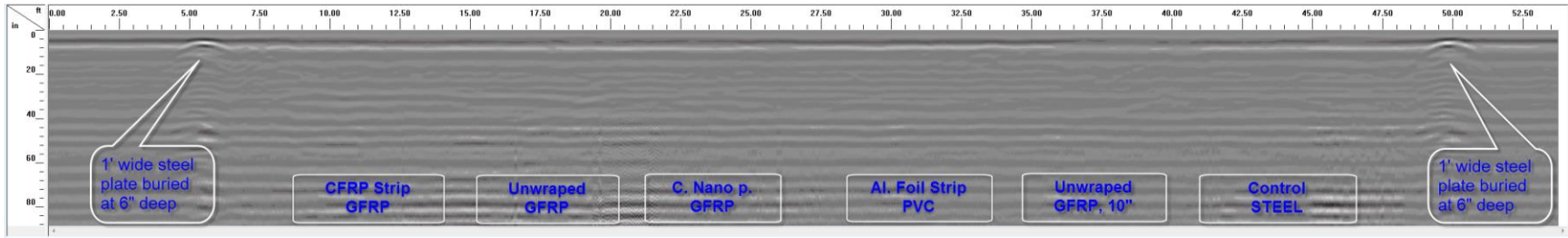


(a) Longitudinal scan along the full length of 12" and 10" diameter pipes with 2 ft. of soil cover

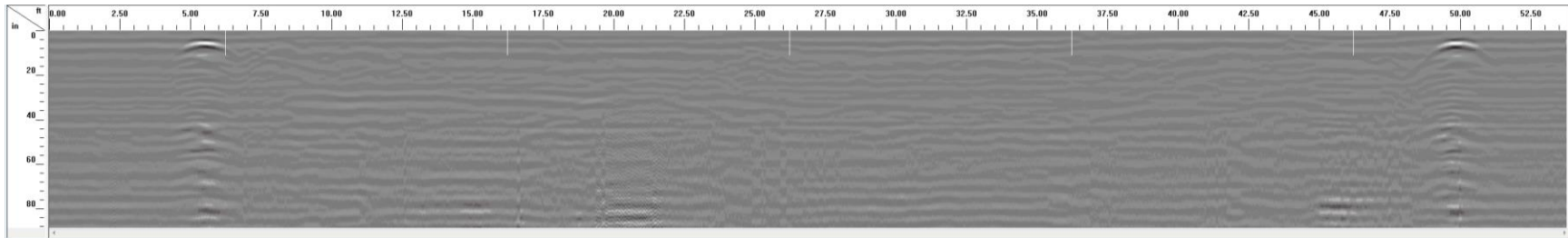


(b) Peaks extraction processing used to make buried pipes in scan (a) more visible

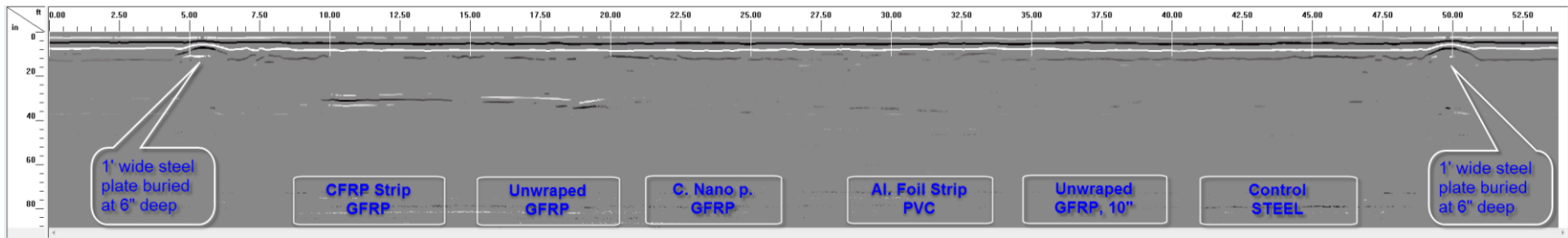
Figure 7-6: Longitudinal scan over the 2 ft. deep trench for Dataset I using 200 MHz antenna



(a) Longitudinal scan along the full length of 12" and 10" diameter pipes with 2 ft. of soil cover



(b) Background noise removal applied to the scan in (a)



(c) Peaks extraction processing used to make buried pipes in scan (a) visible

Figure 7-7: Longitudinal scan over the 2 ft. deep trench for Dataset I using 400 MHz antenna

in Section 7.2.5. GPR signal reflections from some of the pipe sections will also be evaluated individually for better clarity. Only data from the 12" and 6" diameter pipes buried with 3 ft. of soil cover, and 12" and 10" diameter pipes buried with 2 ft. of soil cover will be evaluated for brevity. However, conclusions drawn from this detailed evaluation applies to pipes in the other trenches.

As shown in Figure 7-2(a) and 7-3 for Dataset I, all the buried pipes with 3 ft. of soil cover (with the exception of 12" diameter PVC pipe without any overlay and 12" diameter PVC pipe with aluminum foil rings) can be detected with varying levels of clarity in the raw data when scanned with the 200 MHz radar antenna. Particularly, pipe sections with CFRP and aluminum foil overlays appear prominently, and with higher signal strengths. These are easily detected compared to pipes without any overlay. Among the pipes with CFRP or aluminum foil overlays, CFRP and aluminum foil strips along the full length of the pipes are generally easier to detect compared to CFRP and aluminum foil rings around the pipes. Extracting reflected signal peaks during post processing makes it easier to locate the buried pipes as shown in Figure 7-3(b). Peak extraction also makes it possible to locate pipes that were otherwise not visible in the raw GPR scan.

Figures 7-8 through 7-18 show details of each pipe in Figure 7-2(a), including the B-Scan to the left and A-Scan to the right of each figure. The depth of soil cover over the pipes was also accurately estimated from the GPR data as shown in Figures 7-8 and 7-9, where the measured pipe depth of 37.00" and 37.10" using GPR signal correlates very well with the actual pipe depth of 3 ft. (36"). Measurement of soil dielectric constant using buried sensors during GPR surveys enabled these depths to be estimated. Reflections from both the top and bottom of some of the pipes make it possible to estimate the diameters of such pipes as shown in Figure 7-8. However, since the diameter of the pipe is estimated from the electromagnetic wave velocity, which is based on the average soil dielectric constant, there is the possibility for the estimated diameter to be less than the actual diameter. This is because, the dielectric constant of the overlying soil medium is significantly more than the dielectric constant of air in the pipe. The above statements apply even more to Dataset II (presented later) where the dielectric constant of the soil is much higher than that of air (26.75 for the soil up to 2 ft. and 1 for air). Furthermore, the wavelength (and pulse width) of the radar wave for this test is higher than the actual pipe diameter, hence reflection from the bottom of the pipe overlaps with reflection from the top of the pipe. This results in the signal

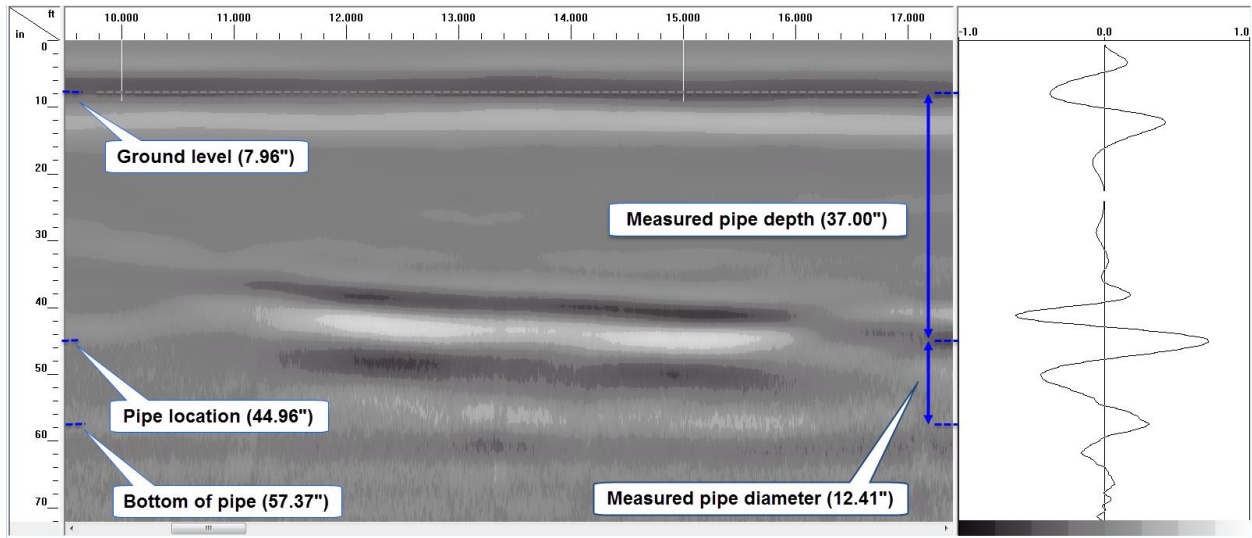


Figure 7-8: Longitudinal GPR scan (left) and A-Scan (right) over Unwrapped 12" GFRP pipe

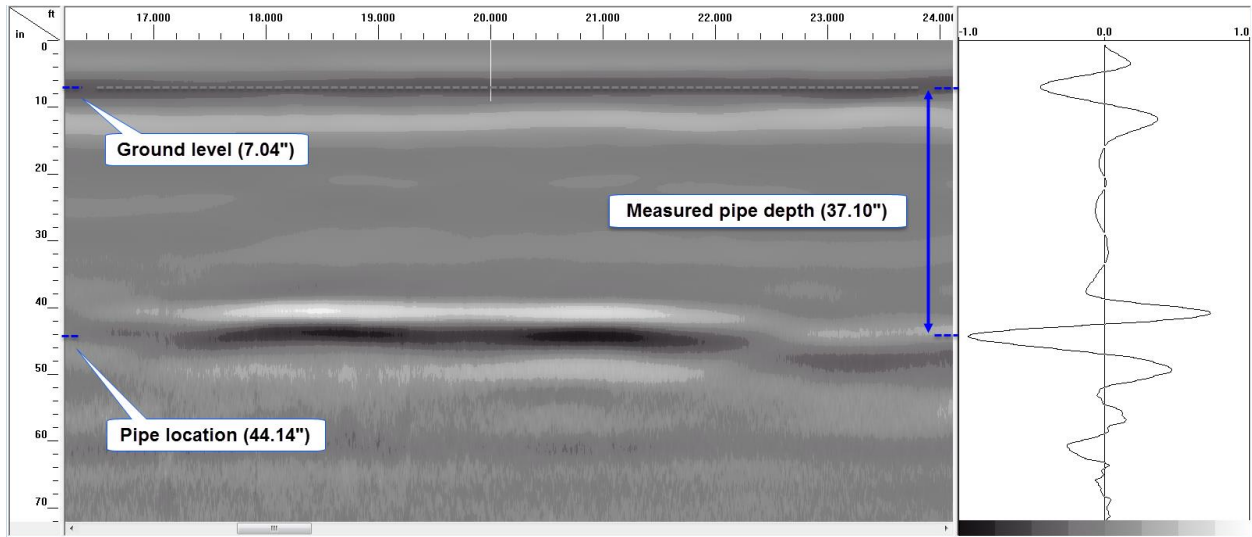


Figure 7-9: Longitudinal GPR scan (left) and A-Scan (right) over 12" CFRP Ring GFRP pipe

peak of the bottom reflection being shifted, and hence affecting the estimated diameter.

The unwrapped 12" diameter GFRP shows up well in the GPR scan at 3 ft. depth (Figure 7-8) and is detected with clean reflected signal from the top and bottom of the pipe.

Figure 7-9 shows the GPR scan at 3 ft. depth over 12" diameter GFRP pipe with CFRP Ring. This pipe shows up prominently in the GPR scan and is detected with clean reflected signal from the top of the pipe. Good/prominent reflection from the top of the pipe will make it possible to locate the pipe with GPR irrespective of the content of the pipe.

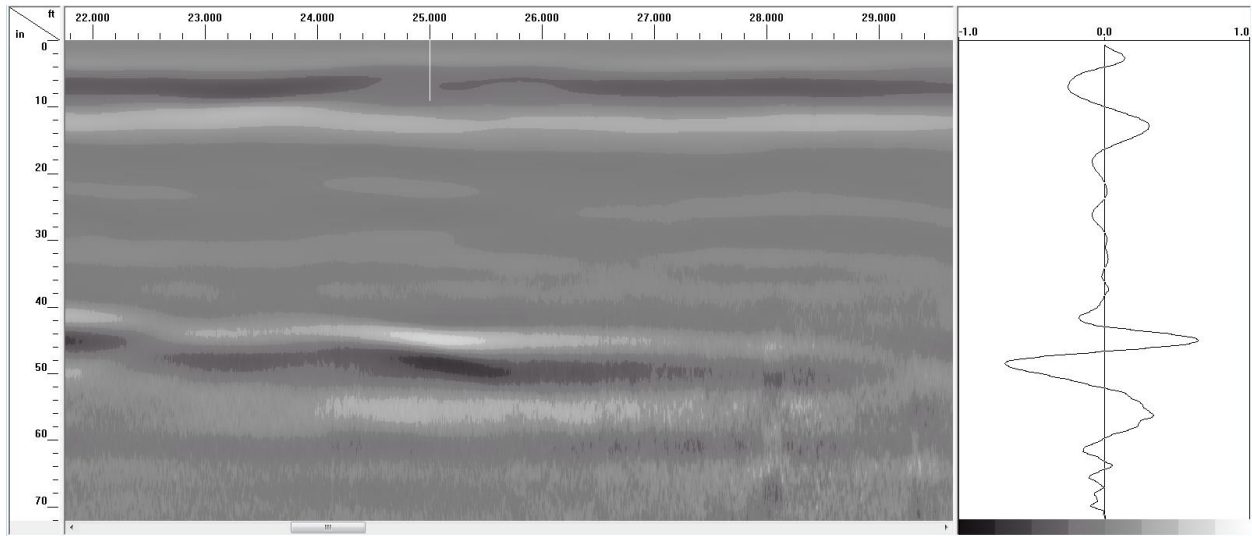


Figure 7-10: Longitudinal GPR scan (left) and A-Scan (right) over 12" CFRP Strip GFRP pipe

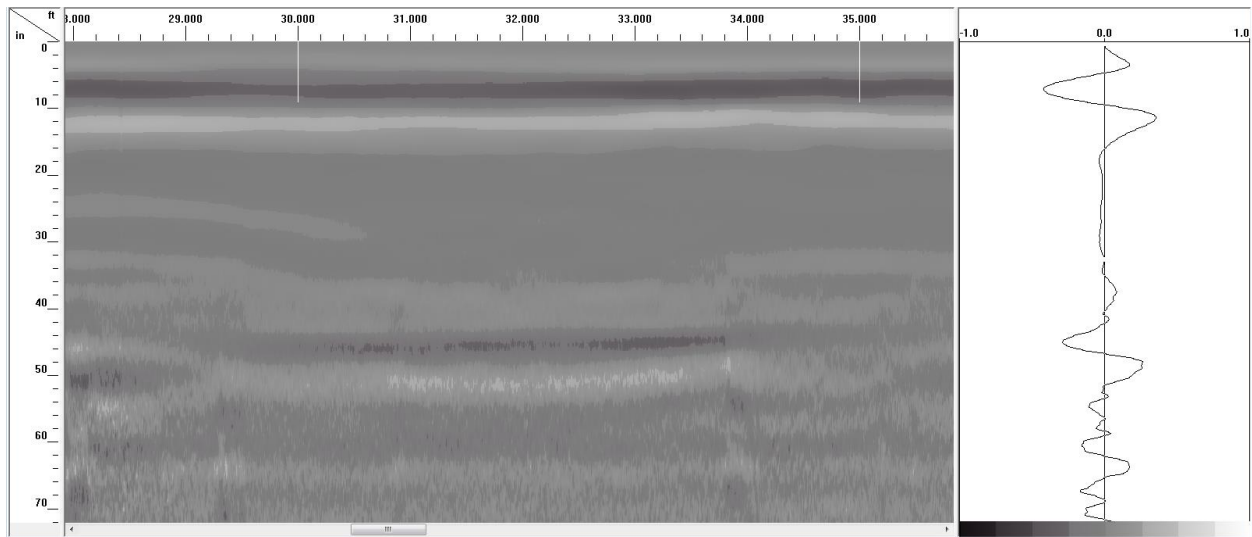


Figure 7-11: Longitudinal GPR scan (left) and A-Scan (right) over 12" Unwrapped PVC pipe

Figure 7-10 shows the GPR scan at 3 ft. depth over 12" diameter GFRP pipe with CFRP Strip at the top. This pipe also shows up very well in the GPR scan and is detected with clean reflected signal from the top of the pipe.

GPR scan over the unwrapped 12" diameter PVC pipe is shown in Figure 7-11; this pipe produced a very poor GPR signal reflection which makes it very difficult to detect the pipe in the raw GPR data.

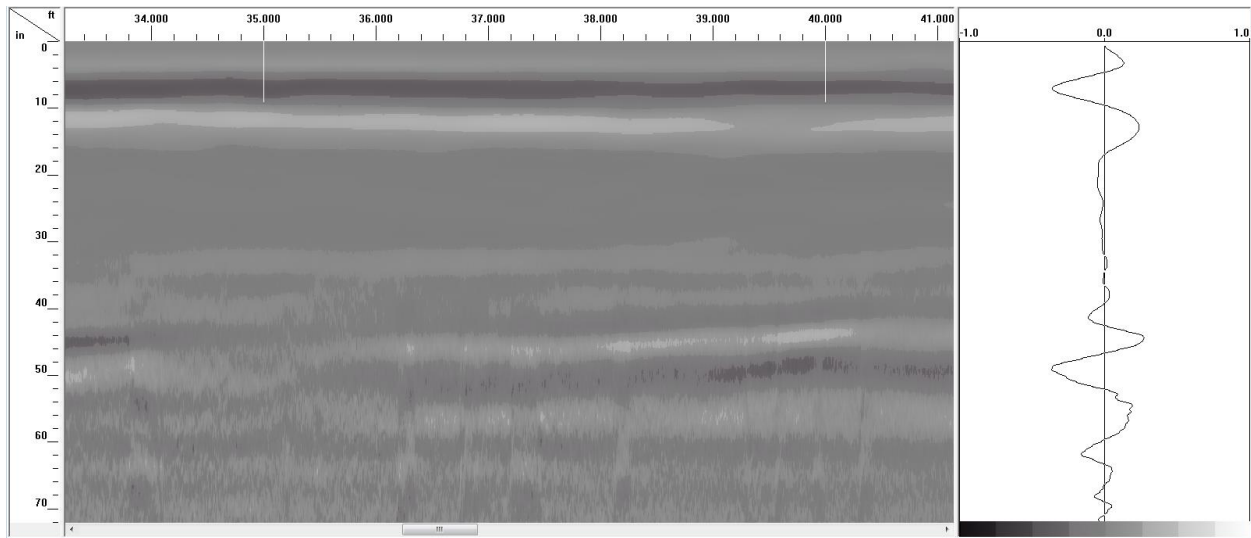


Figure 7-12: Longitudinal GPR scan (left) and A-Scan (right) over 12" Al. Foil Ring PVC pipe

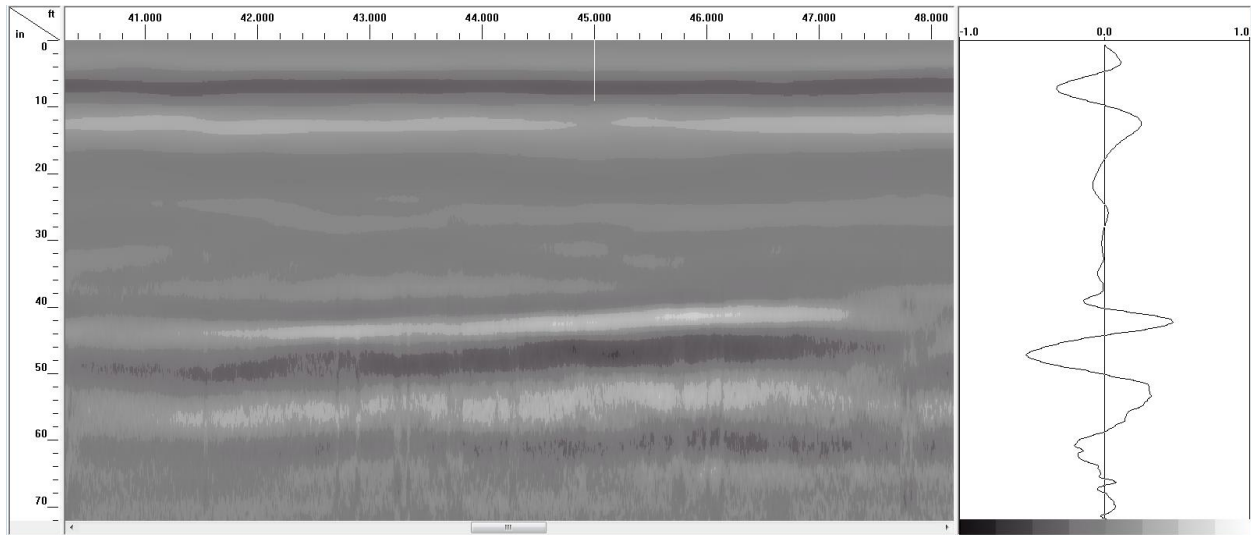


Figure 7-13: Longitudinal GPR scan (left) and A-Scan (right) over 12" Al. Foil Strip PVC pipe

Figures 7-12 and 7-13 show the GPR scan over the 12" diameter PVC pipe with aluminum foil rings and aluminum foil strip respectively. The PVC pipe with aluminum foil rings produced a better reflected signal in the radar scan compared to the unwrapped pipe shown in Figure 7-11. The PVC pipe with aluminum foil strip at the top produced the best reflected radar signal (clean signal with highest amplitude) among the three PVC pipes in Figures 7-11 through 7-13. This makes it a lot easier to identify the pipe in the GPR scan.

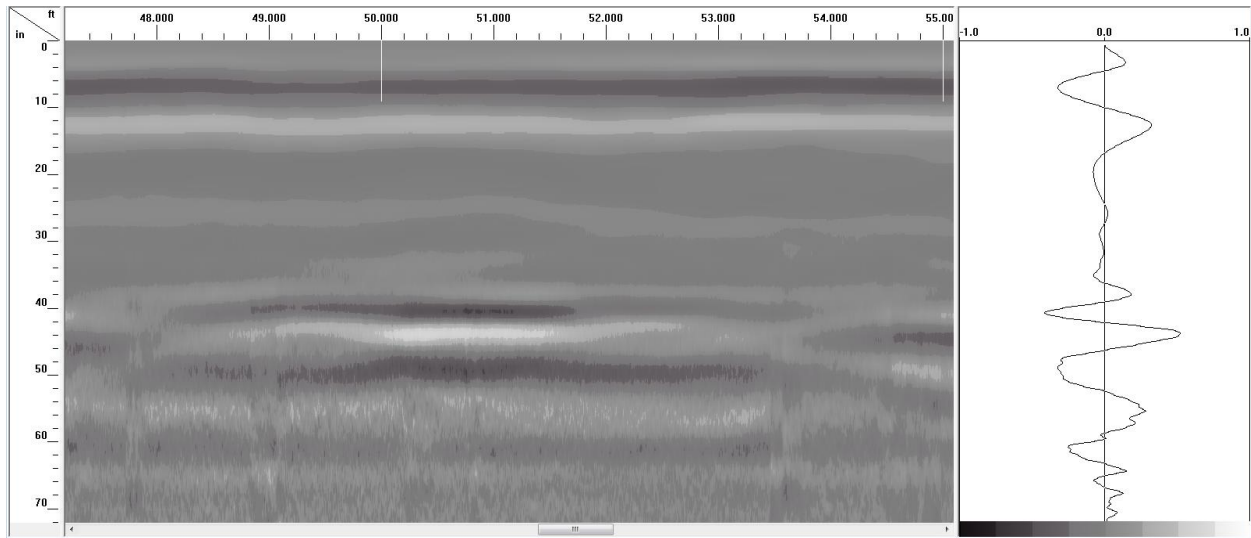


Figure 7-14: Longitudinal GPR scan (left) and A-Scan (right) over 6" Unwrapped PVC pipe

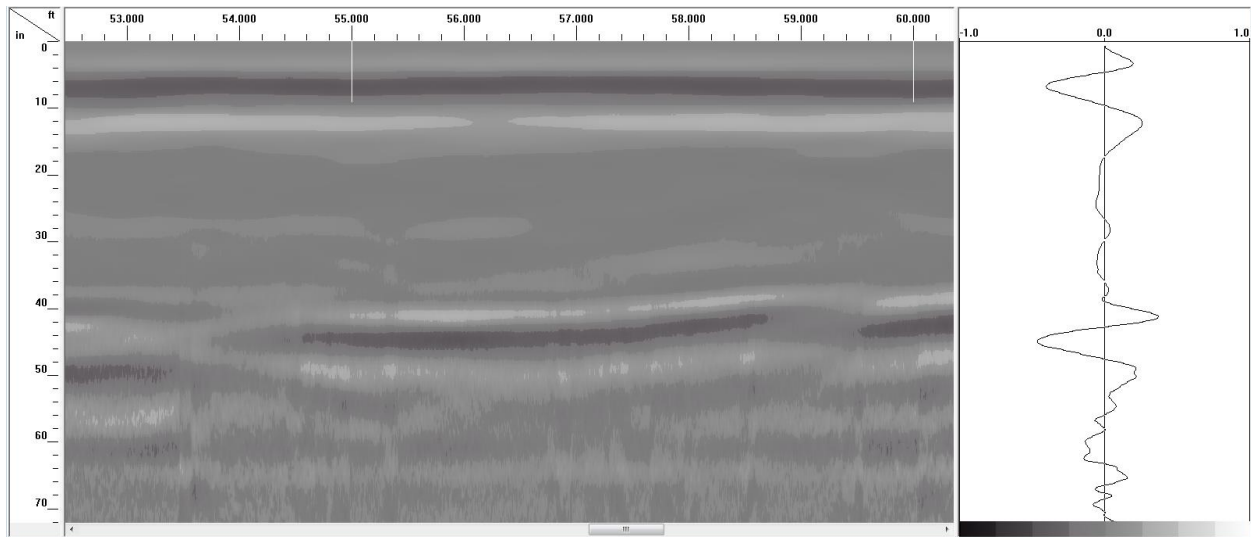


Figure 7-15: Longitudinal GPR scan (left) and A-Scan (right) over 6" Al. Foil Ring PVC pipe

Figure 7-14 shows the GPR scan at 3 ft. depth over 6" diameter unwrapped PVC pipe. This pipe produced a fairly good radar reflection that covers only a short section of the pipe. Thus the pipe is only visible over the short span that produced GPR reflection.

The 6" diameter PVC pipe with aluminum foil rings also produced a fairly good reflection, but this reflection is recorded over the entire length of the pipe (Figure 7-15). Thus, it will be easier to locate this pipe using GPR than the one without any wrap.

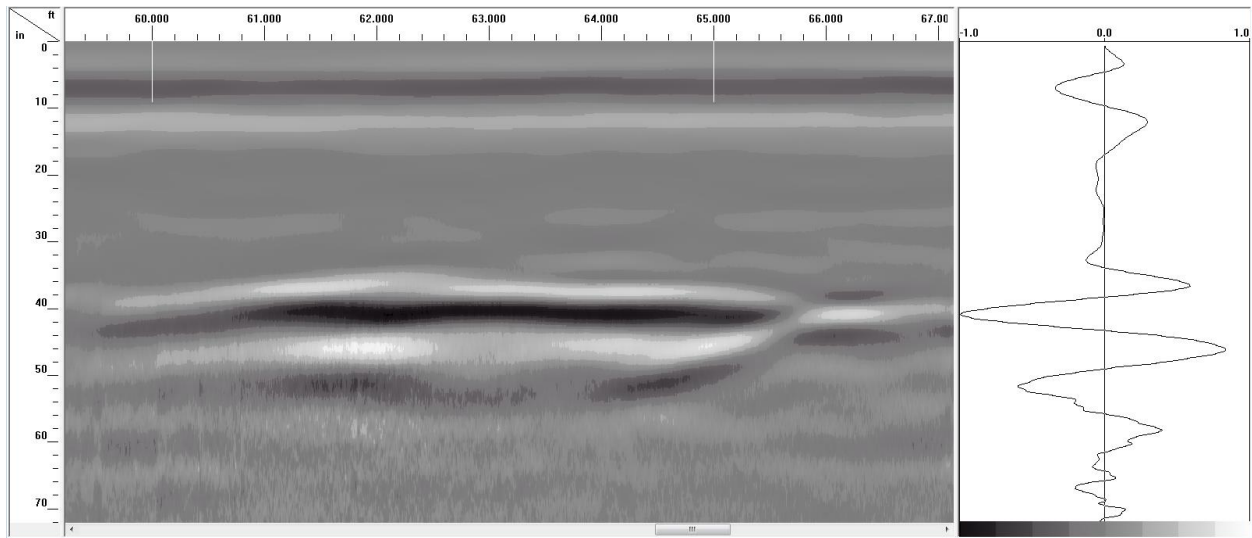


Figure 7-16: Longitudinal GPR scan (left) and A-Scan (right) over 6" Al. Foil Strip PVC pipe

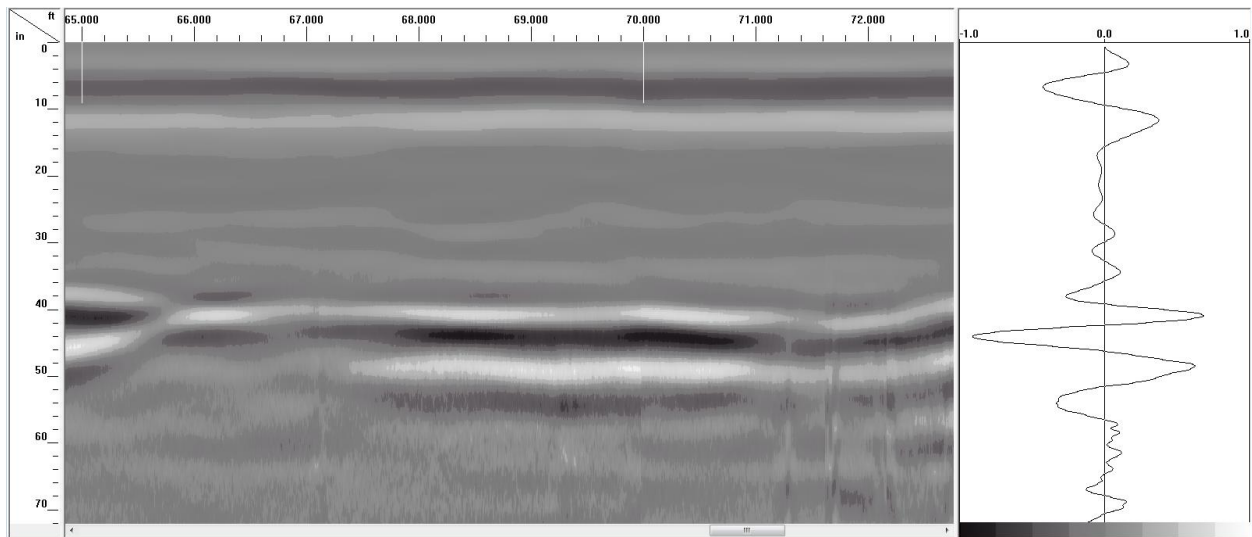


Figure 7-17: Longitudinal GPR scan (left) and A-Scan (right) over 6" CFRP Ring PVC pipe

Figures 7-16 shows the GPR scan over the 6" diameter PVC pipe with aluminum foil strip at the top; this pipe shows up prominently in the GPR scan due to the very strong radar reflection produced. This pipe, with aluminum foil strip, produced the best reflected radar signal (clean signal with highest amplitude) among the three 6" diameter PVC pipes in Figures 7-14 through 7-16.

Figures 7-17 shows the GPR scan over the 6" diameter PVC pipe with CFRP rings; this pipe also shows up prominently in the GPR scan with very strong reflected radar signals. This pipe can also be easily located in the GPR scan.

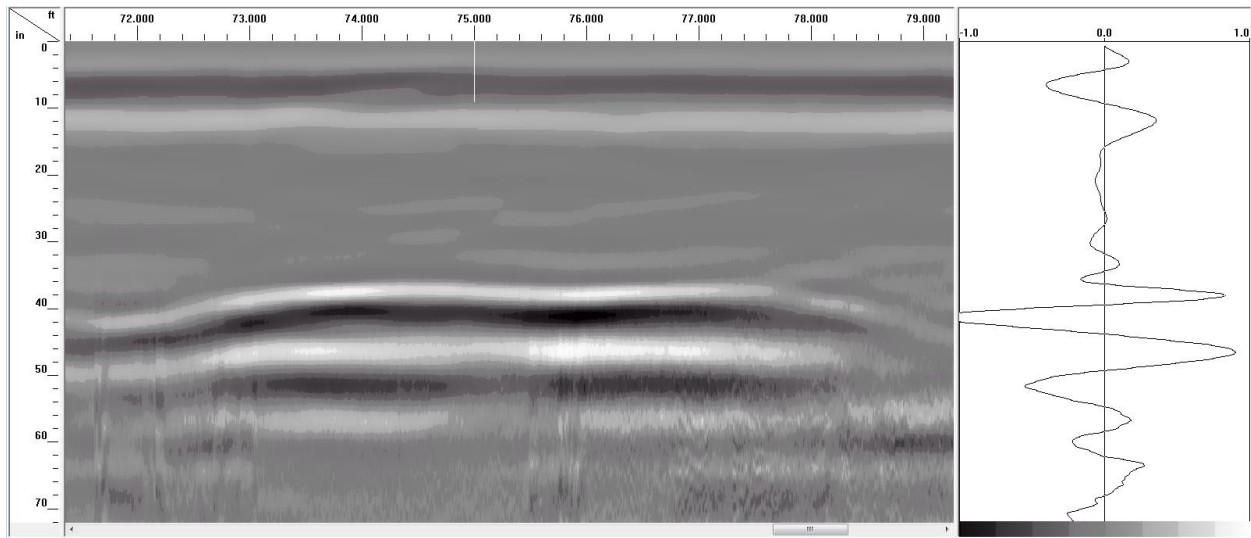


Figure 7-18: Longitudinal GPR scan (left) and A-Scan (right) over 6" CFRP Strip PVC pipe

Finally, GPR scan over the 6" diameter PVC pipe with CFRP strip at the top is shown in Figure 7-18. This pipe produced radar reflection with the highest amplitude among all the 6" diameter PVC pipes buried at 3 ft. depth (it also produced highest amplitude reflection among all pipes buried at 3 ft. depth in this dataset). The amplitude of the reflected radar wave for this pipe was higher than what the radar system could record, resulting in the clipped signal as shown in the A-Scan to the right of Figure 7-18.

Thus, by focusing on the GPR scan over the 6" diameter PVC pipes shown in Figures 7-14 through 7-18, it can be seen that pipe sections with CFRP and aluminum foil overlays appear prominently, with higher signal strengths. These are easily detected in the GPR scans compared to pipes without any overlay. Among the pipes with CFRP or aluminum foil overlays, CFRP and aluminum foil strips along the full length of the pipes produced higher amplitude reflections, making the pipes easier to detect compared to CFRP and aluminum foil rings around the pipes. In addition, CFRP rings/strips produced higher reflected signal amplitudes compared to aluminum foil rings/strips.

As shown in Figures 7-2(d) and 7-6, for Dataset I, all the 12" and 10" diameter pipes with 2 ft. of soil cover are detectable in the raw data with varying levels of clarity when scanned with the 200 MHz radar antenna. Similar to the previous discussions, the GFRP pipe with CFRP strip at the top and the PVC pipe with aluminum foil strip at the top are prominently visible. Returned signal from the 12 inch diameter GFRP pipe with no external wrap is also very good, however, reflection from top of the pipe is very short, or not continuous over the entire length of the pipe (only signal

reflection from the bottom of the pipe is continuous through the length of the pipe). The GFRP pipe with carbon nanoparticle overlay produced a good but very short (or discontinues) reflection from the top of the pipe as shown in Figure 7-2(d). The 10 inch diameter GFRP and the steel produced weak reflections, with the steel pipe being a bit more visible in the GPR B-Scan shown in Figure 7-2(d).

Figures 7-19 through 7-24 show details of each of the 12" and 10" diameter pipes buried with 2 ft. of soil cover. The depth of soil cover over the pipes was also accurately estimated from the GPR data as shown in Figures 7-19 and 7-20, where the measured pipe depth of 24.6" and 25.00" using GPR signal correlates very well with the actual pipe depth of 2 ft. (24"). Reflections from both the top and bottom of some of the pipes in this trench also make it possible to estimate the diameter of such pipes as shown in Figures 7-19 and 7-20. The limitations of using this method to estimate pipe diameter as discussed previously (including different dielectric constant for the content of the pipe and the overlaying soil, and wavelength and pulse width of the radar wave being bigger than the actual pipe diameter) still applies.

Figure 7-19 shows the GFRP pipe with CFRP strip at the top; the pipe is detected with clean reflected signal from the top and bottom of the pipe. Prominent reflection from the top of the pipe will make it possible to locate the pipe with GPR irrespective of the content of the pipe. It was also possible to estimate the pipe diameter because of reflections from both the top and bottom of the pipe.

Figure 7-20 shows the GFRP pipe without any surface wrap; the pipe is detected with short and weaker signal from the top (compared to the pipe bottom reflection) and continuous, stronger reflection from the bottom. Though the pipe is detected using the combination of top and bottom reflections in this case, it will be difficult to locate the pipe if its content absorbs the radar signal and makes it impossible to obtain reflections from the bottom of the pipe. It was also possible to estimate the pipe diameter from the recorded GPR signal reflections for this pipe.

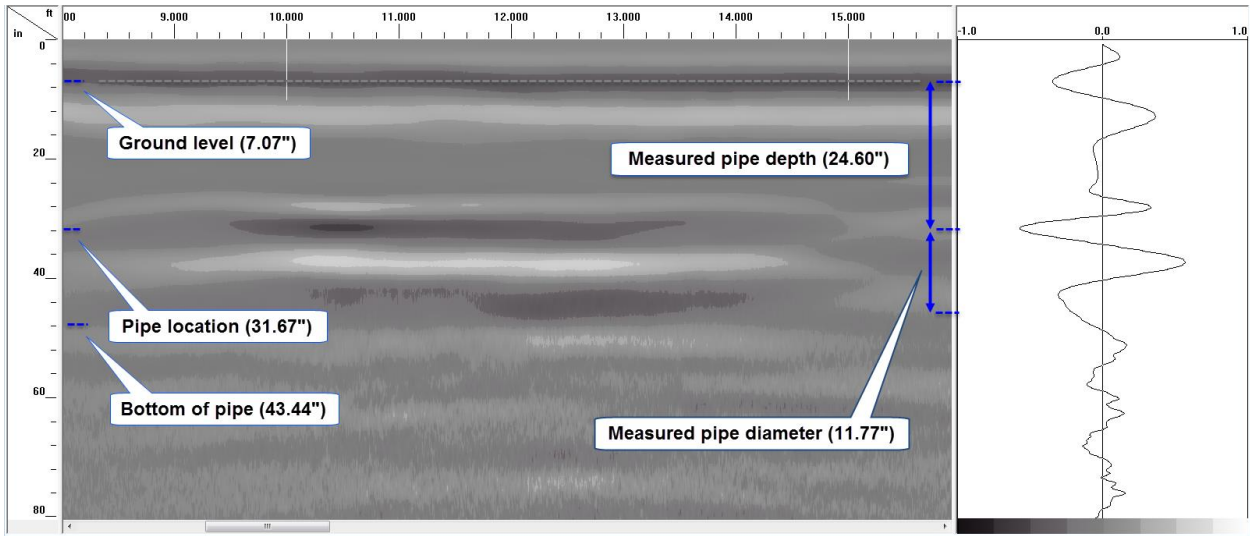


Figure 7-19: Longitudinal GPR scan (left) and A-Scan (right) over 12" CFRP Strip GFRP pipe

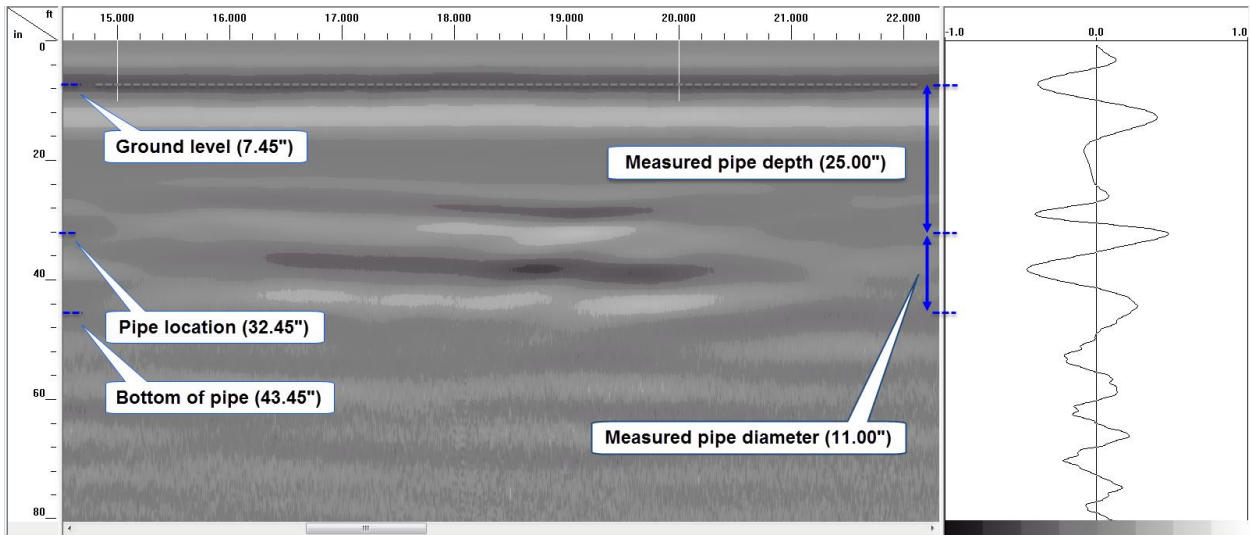


Figure 7-20: Longitudinal GPR scan (left) and A-Scan (right) over Unwrapped 12" GFRP pipe

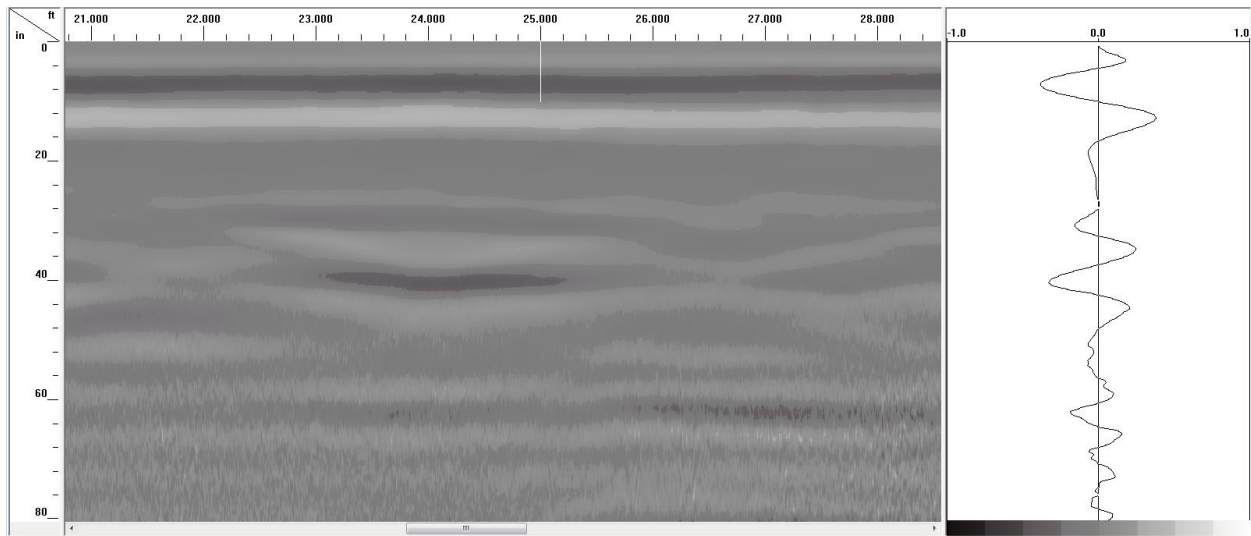


Figure 7-21: Longitudinal GPR scan (left) and A-Scan (right) over C. Nano p. 12" GFRP pipe

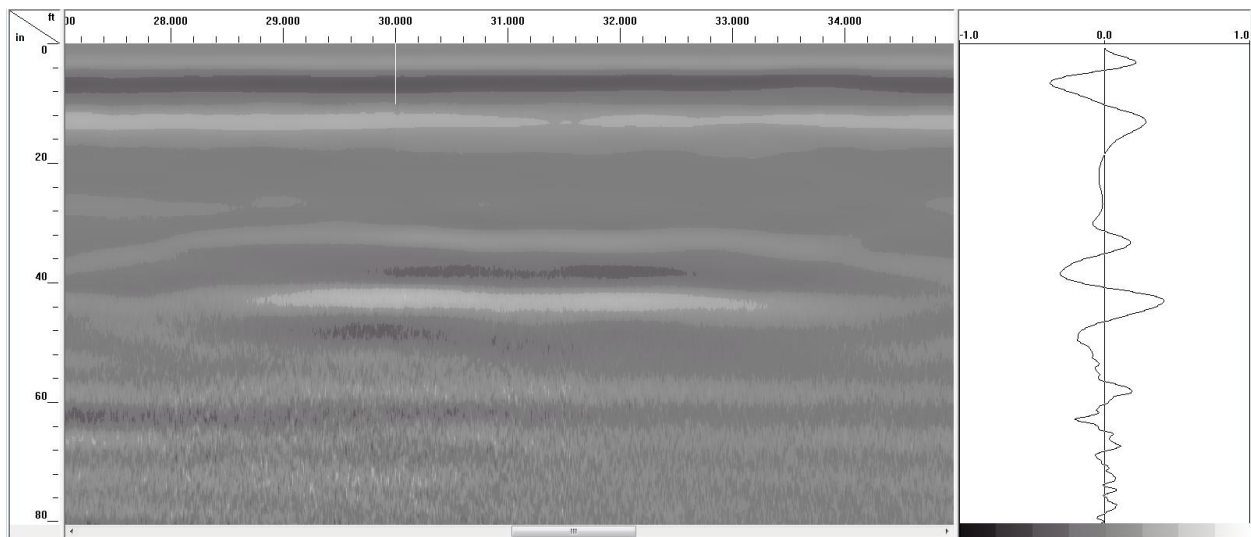


Figure 7-22: Longitudinal GPR scan (left) and A-Scan (right) over Al. Foil Strip 12" PVC pipe

Figure 7-21 shows the GFRP pipe with carbon nanoparticle overlay; this pipe produced a good but very short reflection (reflection not continuous over the pipe length) from the top of the pipe. This signal is weaker than the one produced by the GFRP pipe without any surface wrap in Figure 7-20. Thus the carbon nanoparticle overlay did not improve the detectability of the buried GFRP pipe.

Figure 7-22 shows the PVC pipe with aluminum foil strip at the top; this pipe produced a very good reflection from the top of the pipe, thus making it possible to locate the pipe. The prominent reflection from the top of this pipe will also make it possible to locate the pipe with GPR irrespective of the content of the pipe.

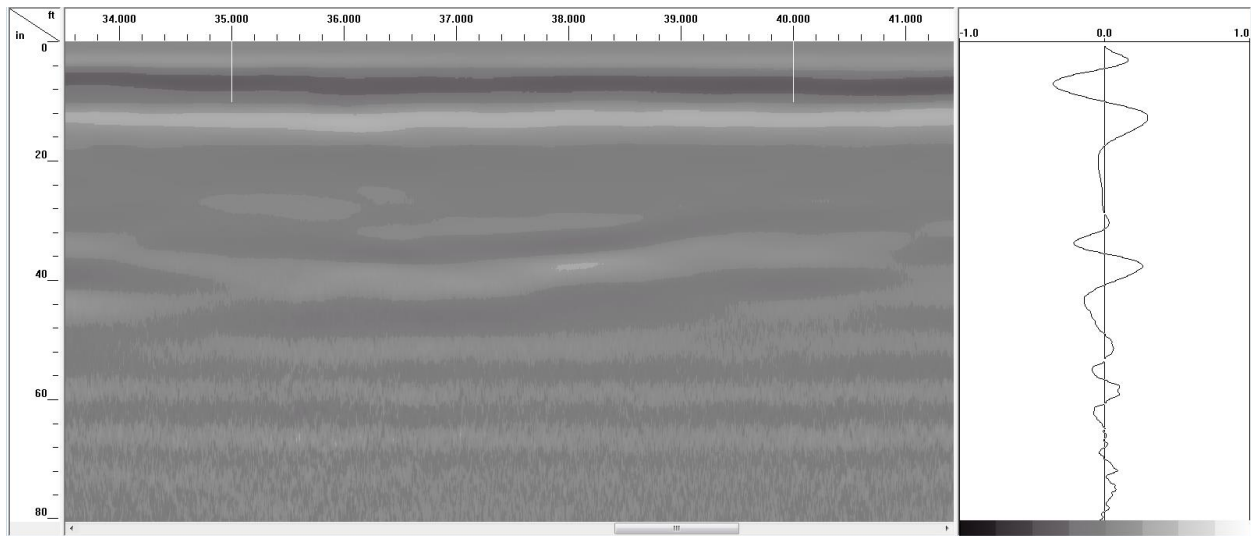


Figure 7-23: Longitudinal GPR scan (left) and A-Scan (right) over Unwrapped 10" GFRP pipe

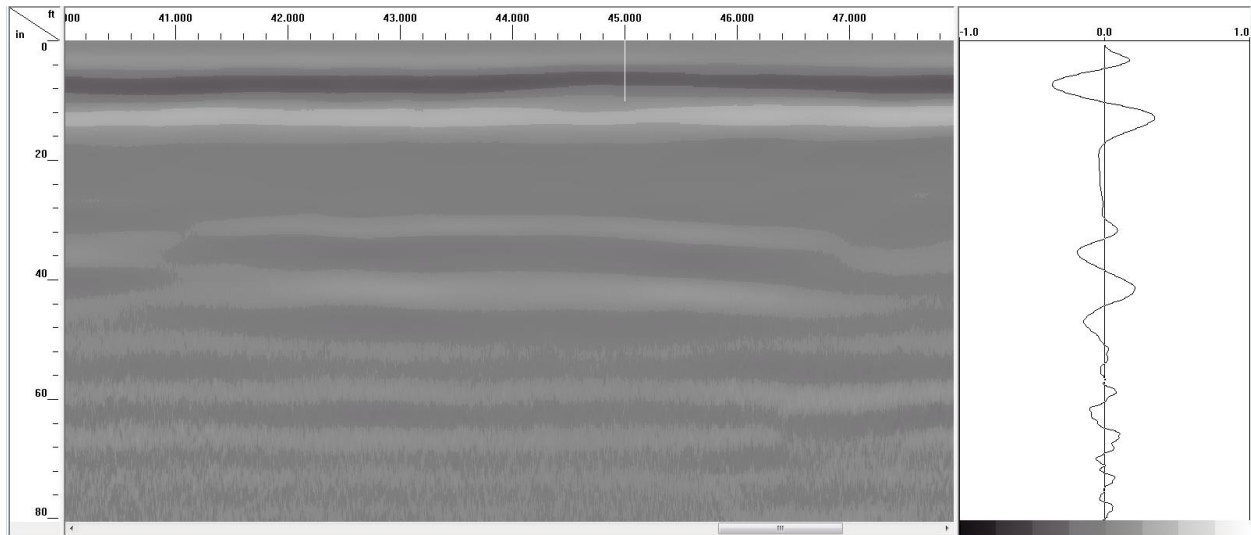


Figure 7-24: Longitudinal GPR scan (left) and A-Scan (right) over 12" Steel pipe

Figure 7-23 shows the 10" GFRP pipe with no external surface wrap; this pipe produced a weak but continuous reflection from the top of the pipe. The continuous reflection made it possible to locate the pipe in this test. However, the weak reflection means the pipe might not be detected at depths beyond the 2 ft. investigated in this test. At deeper depths, the weak reflected signal from this pipe will attenuate and completely dissipate in the overlaying soil and therefore will not be detected by the receiving radar antenna.

Figure 7-24 shows the steel pipe used as control specimen; this also produced a weak but continuous reflection from the top of the pipe, and hence made it possible to locate the pipe in this

test. Reflections from the steel pipe are more defined compared to the 10 inch diameter GFRP pipe (Figure 23), with the ends of the steel pipe clearly visible in the GPR B-Scan (left side of Figure 7-24).

Figure 7-7(a) shows the raw GPR scan from all the 12" and 10" diameter pipes buried with 2 ft. of soil cover scanned using the 400 MHz antenna (for Dataset I), and Figures 7-7(b) and 7-7(c) show the data in Figure 7-7(a) processed using background noise removal and peaks extraction respectively. It is difficult to identify any pipe in Figures 7-7(a) and 7-7(b), but extracting the reflected signal peaks makes it possible to see the GFRP pipe wrapped with CFRP strip and the GFRP pipe with no external surface wrap. The PVC pipe with aluminum foil strip at the top is also faintly visible in the processed data in Figure 7-7(c). Thus, the 400 MHz antenna is less effective in locating the buried pipes at 2 ft. depth or deeper when scanned in the longitudinal direction along the pipes. Conducting scans in the transverse direction across the pipes however makes it possible to detect the buried pipes at 2 ft. depth using the 400 MHz antenna, though with less clarity compared to results from the 200 MHz antenna. This is because, the 400 MHz radar antenna has higher signal attenuation compared to the 200 MHz antenna. Thus greater portion of the transmitted signal is lost; signal attenuation for the different antennae will be explained later in Section 8.4 of Chapter 8. Details of the three pipes identified in the Figure 7-7(c) are provided in Appendix B.1; this includes the raw data, data with background noise removed, and the data with signal peaks extracted respectively in each figure. Appendix B.4 also includes results for transverse scans over the buried pipes using 400 MHz antenna.

7.2.3 Dataset II

Figure 7-25 shows the GPR scan data over the four trenches for Dataset II using the 200 MHz antenna. GPR survey for this data was conducted in a relatively wet soil in the winter months, with the ground surface covered with snow up to a depth of 3.75". Soil properties measured during this survey were higher than that for Dataset I as already shown in Table 1-1.

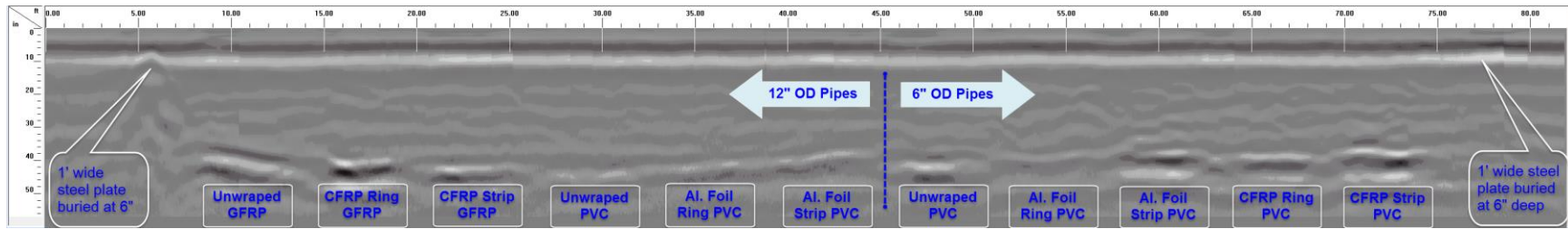
Similar to Dataset I, the addition of CFRP and aluminum foil overlays in the form of strips at the top of the pipes and rings around the pipes significantly improved the detectability of these pipes using GPR. The application of carbon nanoparticle coating on a pipe did not improve on the detectability of such pipes in this dataset. In the case of 3" diameter pipes buried with 2 ft. of soil

cover, most of the pipe sections are not visible in the raw data shown in Figure 7-25(c). The data was thus processed by extracting reflected signal peaks to make it easier to identify buried pipes in the scan. After the peaks extraction process, all the pipe sections with CFRP or aluminum foil overlays are visible in the radar data as shown in Figure 7-26(b). The pipe sections without any CFRP/aluminum foil overlay (Unwrapped GFRP and Unwrapped PVC) remained invisible even after the peaks extraction process. A combination of background noise removal and peaks extraction did not make these unwrapped pipe sections visible. It should be noted that the 3" diameter pipes buried with 2 ft. of soil cover did show very well even in the raw GPR data when scanned in the transverse direction across the pipes as will be shown later in Dataset III.

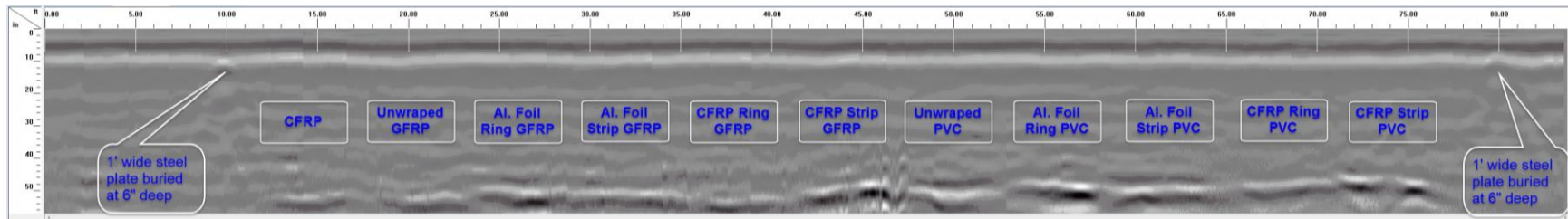
Figure 7-27 shows results from the 3" diameter pipes buried with 2 ft. of soil cover scanned in the longitudinal direction using the 400 MHz antenna. In Figure 7-27, (a), (b), and (c) show the raw GPR scan data, data with background noise removal applied, and data with background noise removal and peaks extraction applied respectively. None of the buried pipes are visible in Figure 7-27(a through c) even after different data processing techniques, including background noise removal, peaks extraction, and combination of both have been applied.

GPR results from the 12" and 10" diameter pipes buried at 2 ft. depth and scanned using the 400 MHz are shown in Figure 7-28. Similar to Figure 7-27, (a), (b), and (c) in Figure 7-28 show the raw GPR scan data, data with background noise removal applied, and data with background noise removal and peaks extraction applied respectively. It is difficult to identify the buried pipes in the raw data as shown in Figure 7-28(a). However, performing background noise removal on the raw data (Figure 7-28b) makes it possible to identify three of the pipes; the GFRP pipe with carbon fabric strip, the 12" diameter GFRP pipe with no wrap/overlay, and the steel control pipe. All the buried pipes were visible (as shown in Figure 7-28c) after extracting reflected signal peaks from the GPR data in Figure 7-28(b).

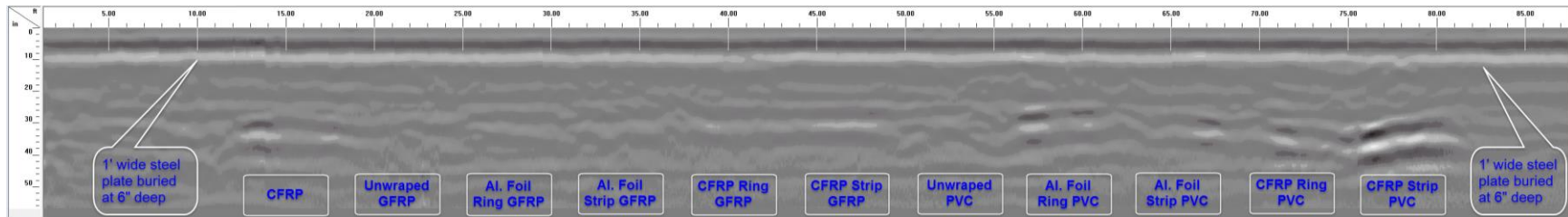
This result reinforces the fact that, the 400 MHz antenna is less effective in locating the buried pipes at 2 ft. depth and deeper because of the higher signal attenuation compared to the 200 MHz antenna. Scanning the pipes in the transverse direction using the 400 MHz antenna however produces a better result as shown in Appendix B.4.



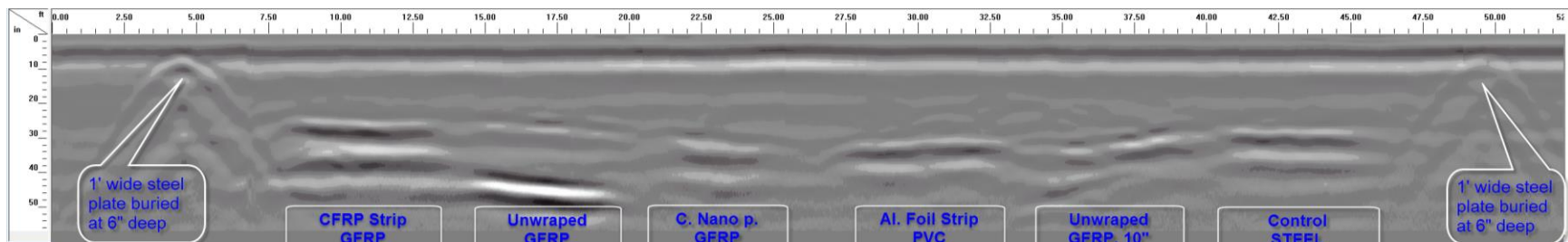
(a) Longitudinal scan along the full length of 12" and 6" diameter pipes with 3 ft. of soil cover



(b) Longitudinal scan along the full length of 12" diameter pipes with 4 ft. of soil cover

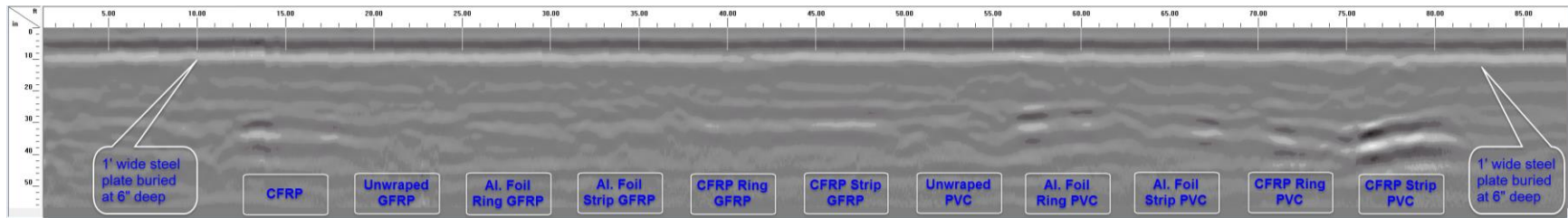


(c) Longitudinal scan along the full length of 3" diameter pipes with 2 ft. of soil cover

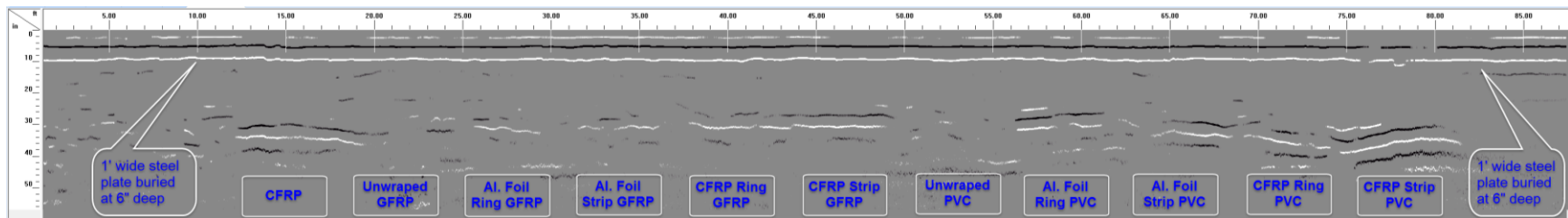


(d) Longitudinal scan along the full length of 12" and 10" diameter pipes with 2 ft. of soil cover

Figure 7-25: Dataset II - Longitudinal scans over the pipe trenches using 200 MHz antenna

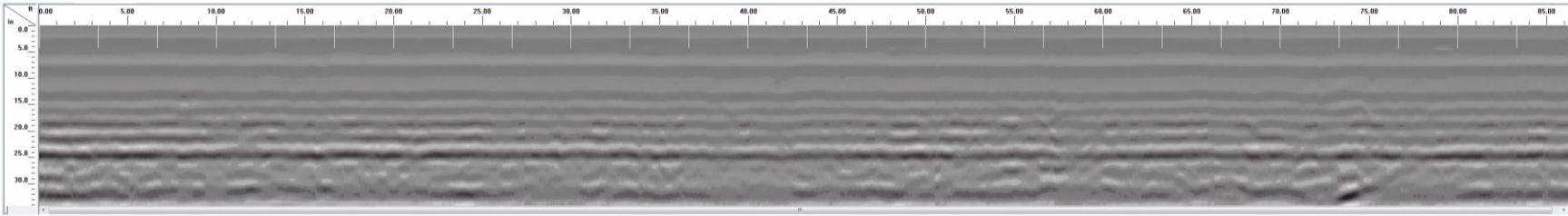


(a) Longitudinal scan along the full length of 3" diameter pipes with 2 ft. of soil cover

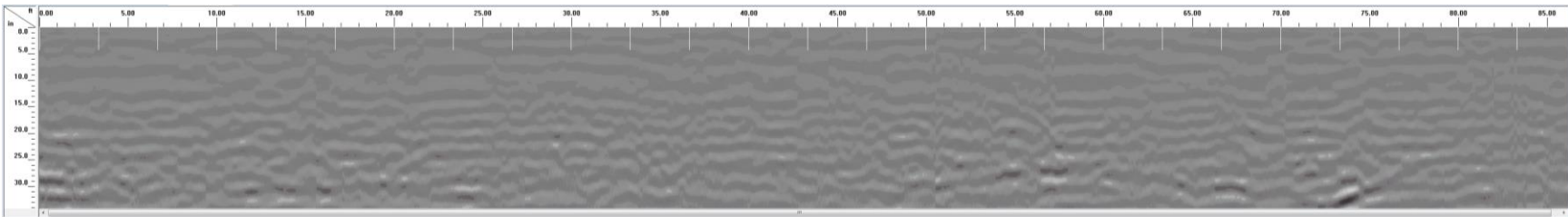


(b) Peaks extraction processing used to make buried pipes in scan (a) more visible

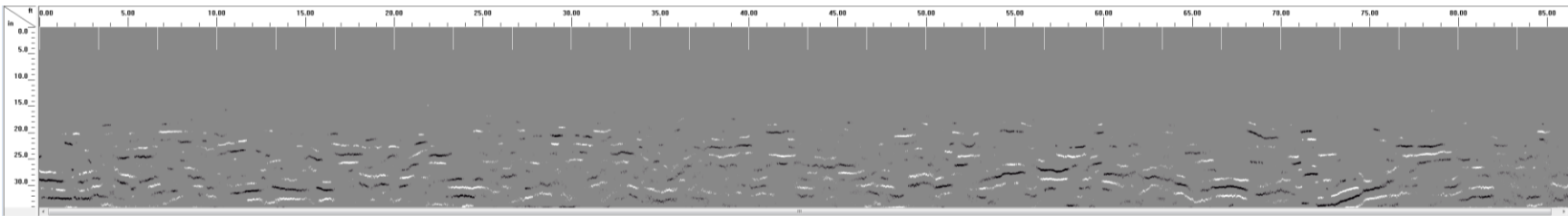
Figure 7-26: Longitudinal scans over 3" diameter pipes at 2 ft. deep using 200 MHz antenna



(a) Longitudinal scan along the full length of 3" diameter pipes with 2 ft. of soil cover

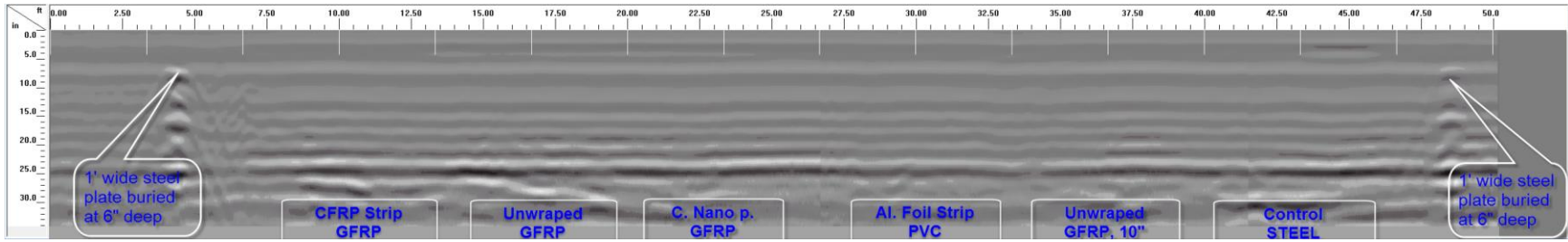


(b) Background noise removal applied to the scan in (a)

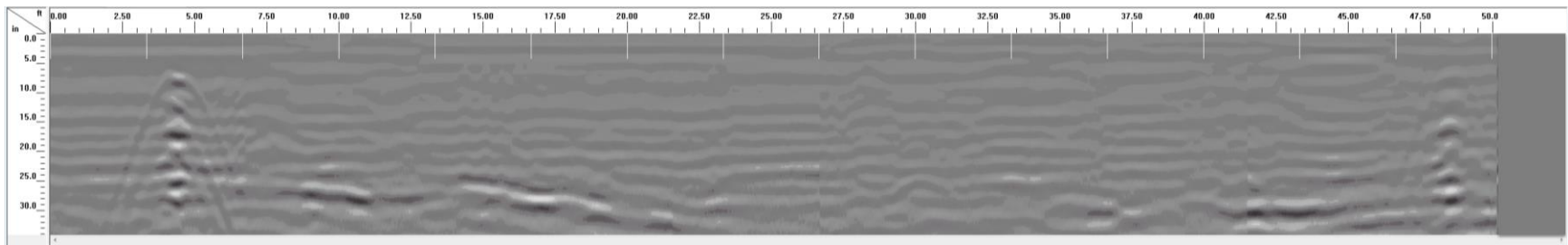


(c) Peaks extraction processing applied to data in (b)

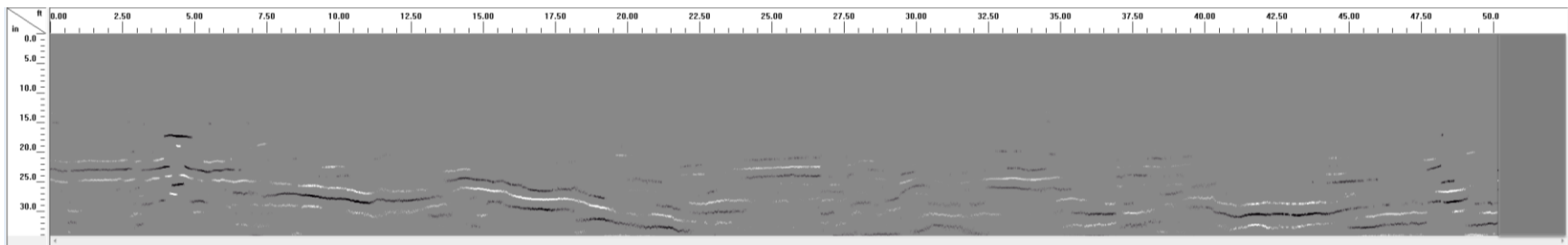
Figure 7-27: Longitudinal scan over 3" diameter pipes at 2 ft. deep using 400 MHz antenna



(a) Longitudinal scan along the full length of 12" and 10" diameter pipes with 2 ft. of soil cover

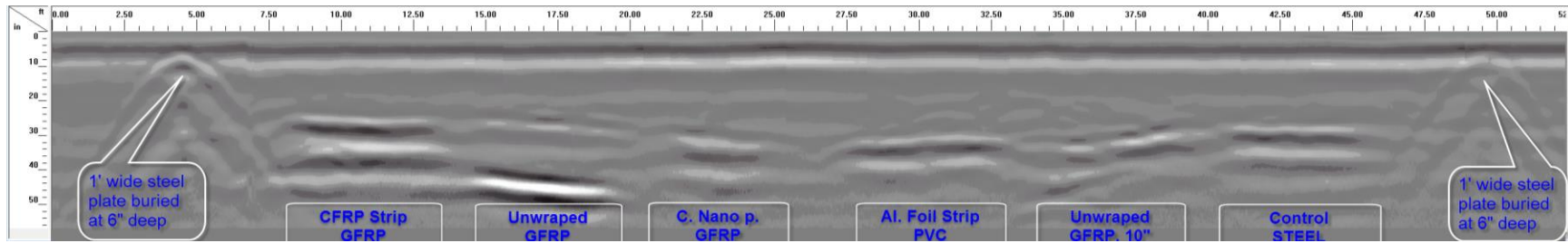


(b) Background noise removed from figure in (a)

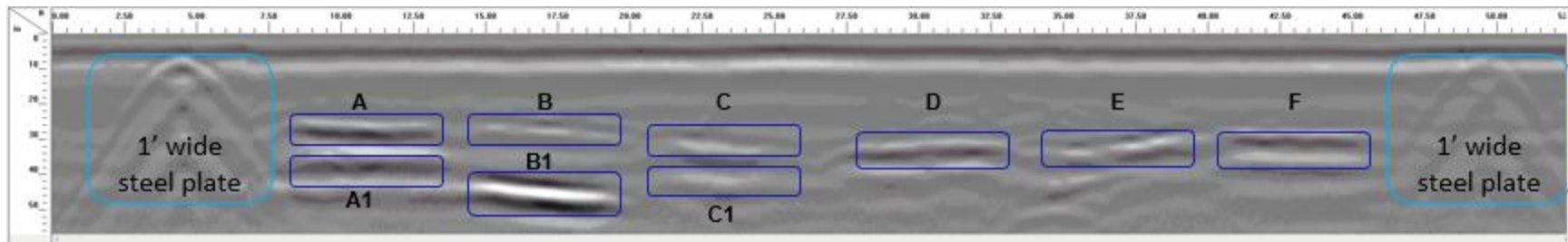


(c) Signal reflection peaks extracted from (b)

Figure 7-28: Longitudinal scans over 12" and 10" diameter pipes at 2 ft. deep using 400 MHz antenna



(a) Longitudinal scan along the full length of 12" and 10" diameter pipes with 2 ft. of soil cover



(a) Reflection details marked in the longitudinal scan from (a)

Figure 7-29: Reflection details marked on 12" and 10" diameter pipes with 2 ft. of soil cover

Table 7-2: Description of features marked in Figure 7-29

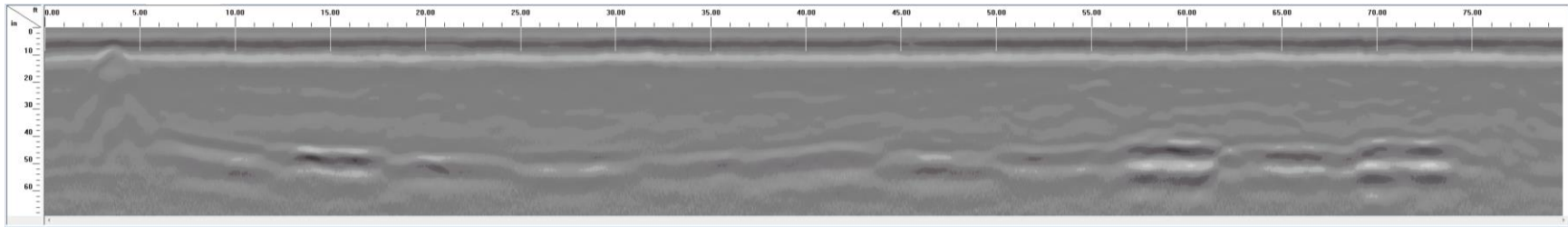
Feature/Label	Object/Pipe Type	Result Description
Steel plates	1 ft. wide steel plates	Appear prominently in the GPR scans
A	GFRP pipe with CFRP strip	Produced very strong reflection from both the top (A) and bottom (A1) of the pipe, pipe was clearly detected
A1	Reflection from bottom of pipe	
B	GFRP pipe with no wrap (12" diameter)	The pipe produced very weak reflection over sections of the pipe (B). Very strong reflection recorded from the bottom of the trench (B1)
B1	Reflection from bottom of trench	
C	GFRP pipe with carbon nanoparticle coating	Produced weaker reflection than D (over short section of pipe), from both the top (C) and bottom (C1) of the pipe. Portion of pipe detected
C1	Reflection from bottom of pipe	
D	PVC pipe with aluminum strip	Produced strong, continuous reflection, pipe was detected
E	GFRP pipe with no wrap (10" diameter)	Produced strong reflection over sections of the pipe, pipe was detected
F	Steel pipe	Produced strong continuous reflection, pipe was detected

Figure 7-29 shows details of the pipes and other features identified in this scan from the 12" and 10" diameter pipes with 2 ft. of soil cover. Description of the features marked A through F in Figures 7-29(b) are summarized in Table 7-2. Detailed radar data for these features are provided in Appendix B.2.

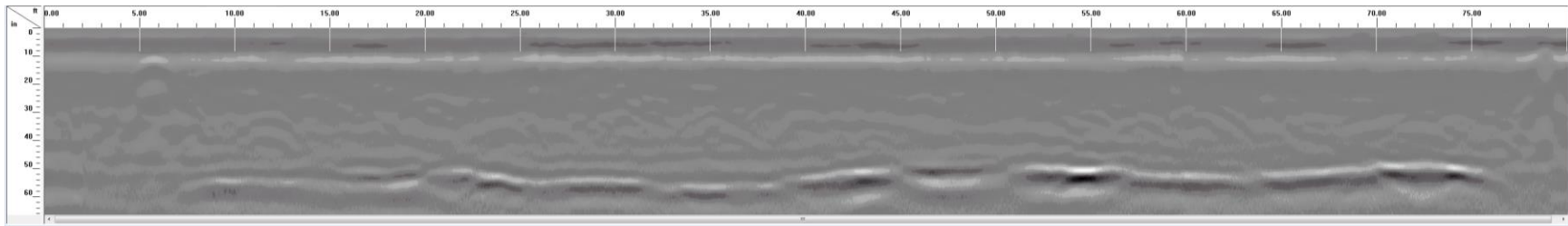
The GPR result presented in Dataset II indicates that snow cover on the ground surface does not hinder the detection of buried pipes using GPR. The results obtained in the GPR survey for this dataset (with the ground covered with snow up to 3.75") is similar to what was obtained for Dataset I which did not have any snow cover on the ground surface.

7.2.4 Dataset III

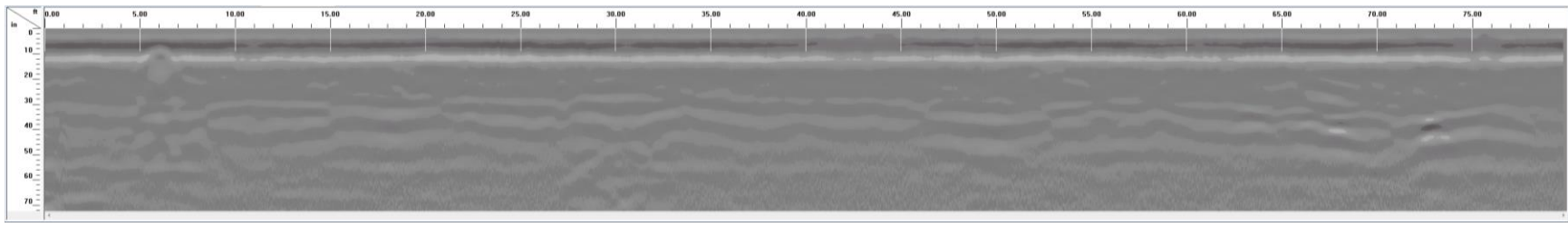
GPR survey results over the four trenches using the 200 MHz antenna for Dataset III are shown in Figure 7-30. This survey was carried out in the spring, with the measured soil properties during the survey already shown in Table 1-1. Results in this dataset correlates well with the two datasets discussed previously, with CFRP and aluminum foil overlays improving the detectability of buried non-metallic pipes while carbon nanoparticle coating did not provide any noticeable benefit in pipe detectability using GPR.



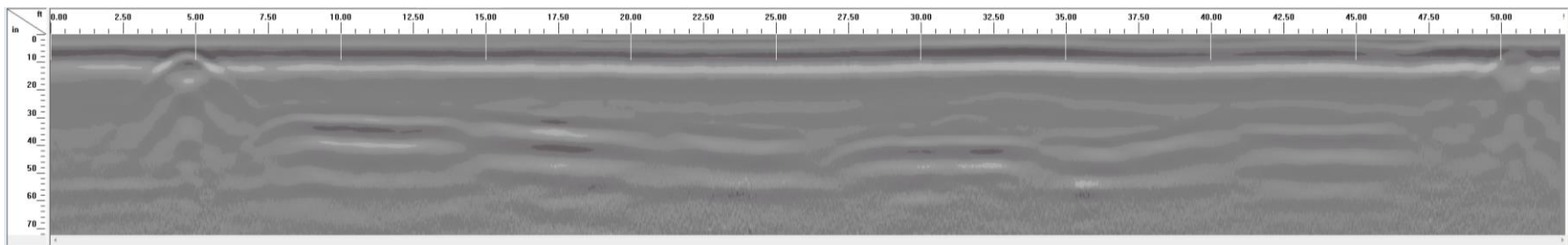
(a) Longitudinal scan along the full length of 12" and 6" diameter pipes with 3 ft. of soil cover



(b) Longitudinal scan along the full length of 12" diameter pipes with 4 ft. of soil cover



(c) Longitudinal scan along the full length of 3" diameter pipes with 2 ft. of soil cover



(d) Longitudinal scan along the full length of 12" and 10" diameter pipes with 2 ft. of soil cover

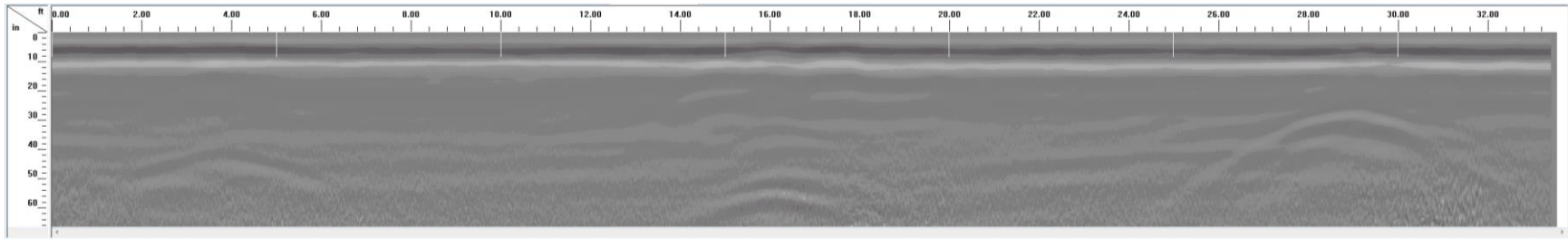
Figure 7-30: Dataset III - Longitudinal scans over the pipe trenches using 200 MHz antenna

For most GPR applications in locating buried utility lines, scans are performed perpendicular to the expected direction of the utility line. Thus, for Dataset III, scans were also performed perpendicular to the direction of the pipes for comparison. Figure 7-31 (a through k) shows GPR scans over the buried pipes in the first three trenches (65 ft. long trenches), while scans over the fourth trench (36 ft. long trench) is shown in Figure 7-32 (a through f). Each transverse scan in Figure 7-31 was performed over all the three trenches, starting from the 3 ft. deep trench and ending over the 2 ft. deep trench (or from the top line of pipes to the bottom line of pipes according to the layout given in Figure 6-12 in Chapter 6). Subsequent scans (from a through k) were conducted starting from the left side to the right side of the layout in Figure 6-12 in Chapter 6.

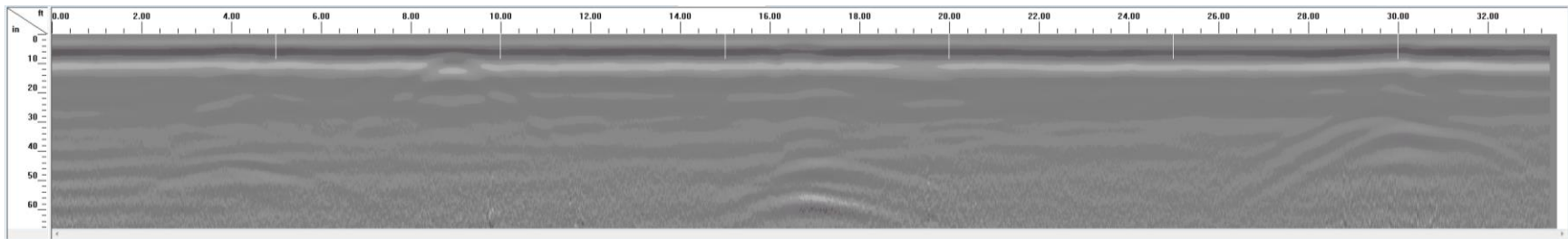
Looking at Figure 7-31 (g through k), it is evident that, the PVC pipes (6", 12", and 3" diameters from left to right on each figure) without any wrap (Unwrapped PVC in Figure 7-31g) produced the weakest radar reflections among all the scans from g through k. Contrary to the unwrapped PVC pipes, the PVC pipes with aluminum foil or CFRP strips (Figures 7-31 i and k) produce the strongest radar reflections among all the scans from g through k. The PVC pipes with CFRP strips also produced reflections with higher amplitudes at the apex of the hyperbola reflection (Figure 7-31k) compared to the PVC pipes with aluminum foil strips (Figure 7-31i). Radar reflections from the PVC pipes with aluminum foil or CFRP rings produced mixed results (Figure 7-31 h and j), with some of the reflections having higher amplitudes compared to those obtained from the unwrapped PVC while amplitudes of the remaining reflections are comparable in magnitude to the ones obtained from the unwrapped PVC pipes.

The mixed results from pipes with aluminum foil or CFRP rings can be attributed to the fact that, the path of the radar antenna axis might have been between two rings for some of the pipes. Hence the radar hyperbolas for such pipes were produced from reflections off the bare PVC or GFRP pipe rather than off the CFRP/aluminum rings. Using spiral wraps around the pipes instead of parallel rings will ensure there is always part of the wrap at every section along the length of the pipe, this could help address the problem associated with parallel rings.

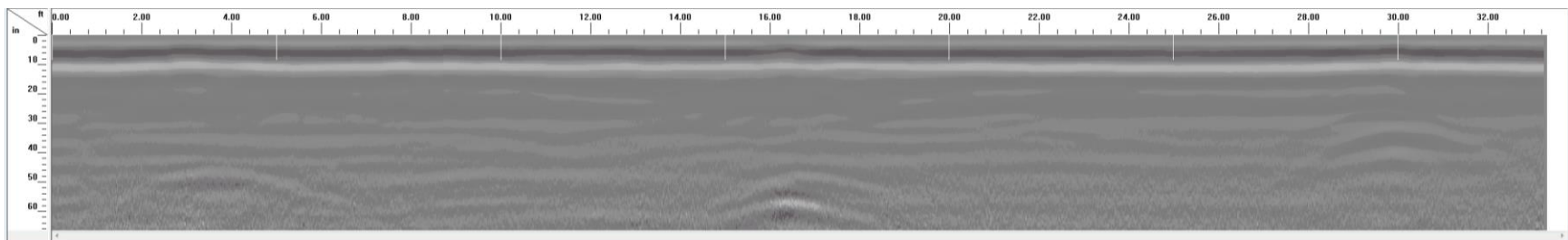
The same observation made for Figure 7-31 (g through k) also applies to Figure 7-31 (a through f), though this is less obvious since the surface configurations of the pipes in each scan shown in Figure 7-31 (a through f) are not the same. Thus, pipe sections with the same surface configuration have to be identified from multiple scans before the comparisons can be made.



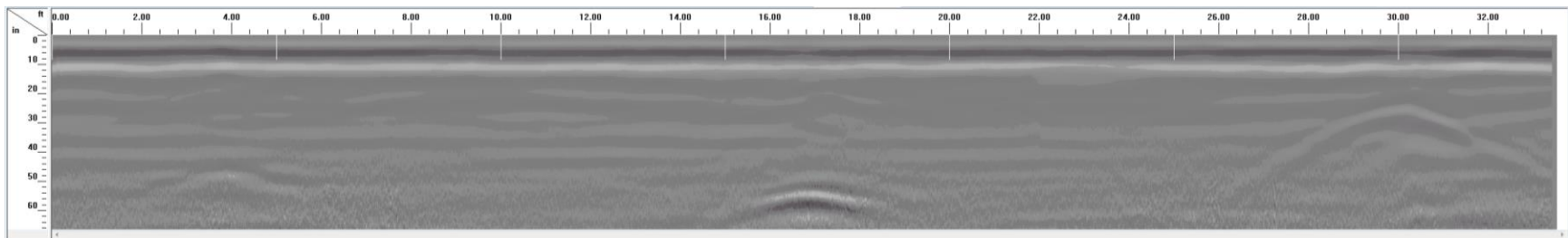
(a) 12" dia. Unwrapped GFRP at 3', 12" dia. CFRP at 4', and 3" dia. CFRP at 2'



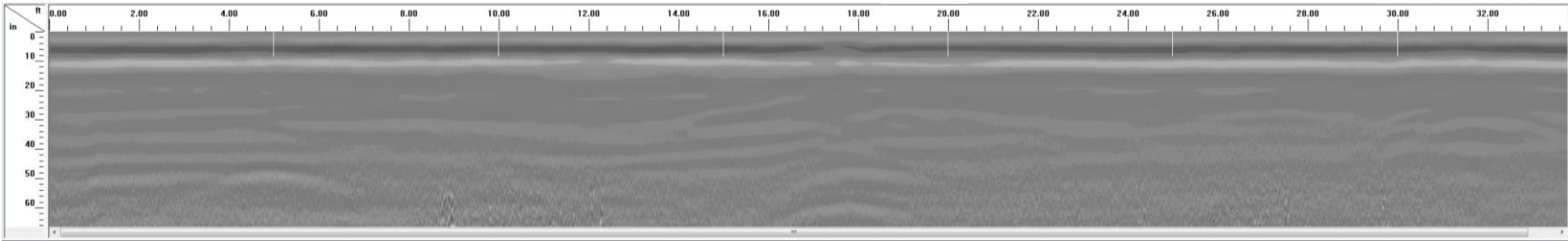
(b) 12" dia. CFRP Ring GFRP at 3', 12" dia. Unwrapped GFRP at 4', and 3" dia. Unwrapped GFRP at 2'



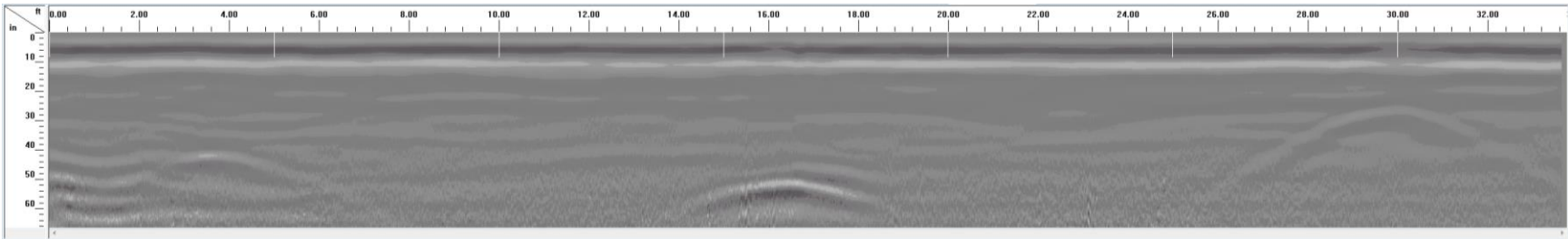
(c) 12" dia. CFRP Strip GFRP at 3', 12" dia. Al. Foil Ring GFRP at 4', and 3" dia. Al. Foil Ring GFRP at 2'



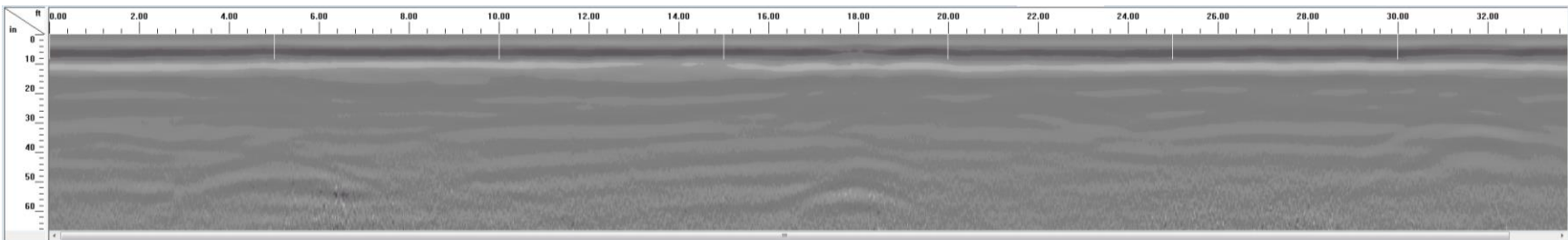
(d) 12" dia. Unwrapped PVC at 3', 12" dia. Al. Foil Strip GFRP at 4', and 3" dia. Al. Foil Strip GFRP at 2'



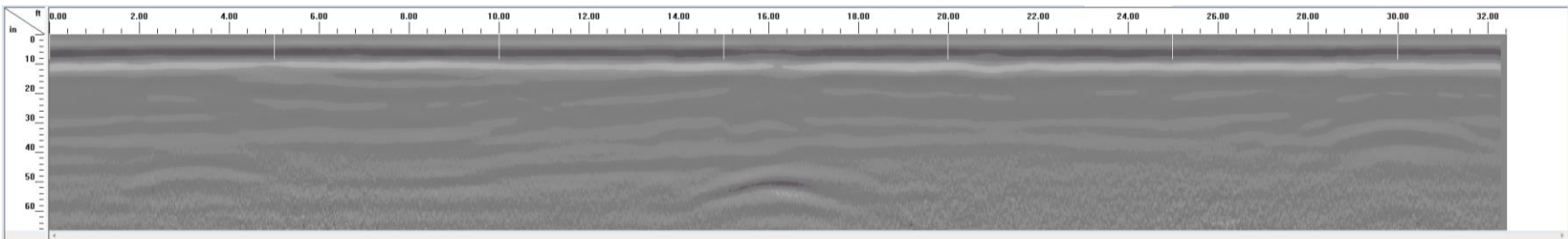
(e) 12" dia. Al. Foil Ring PVC at 3', 12" dia. CFRP Ring GFRP at 4', and 3" dia. CFRP Ring GFRP at 2'



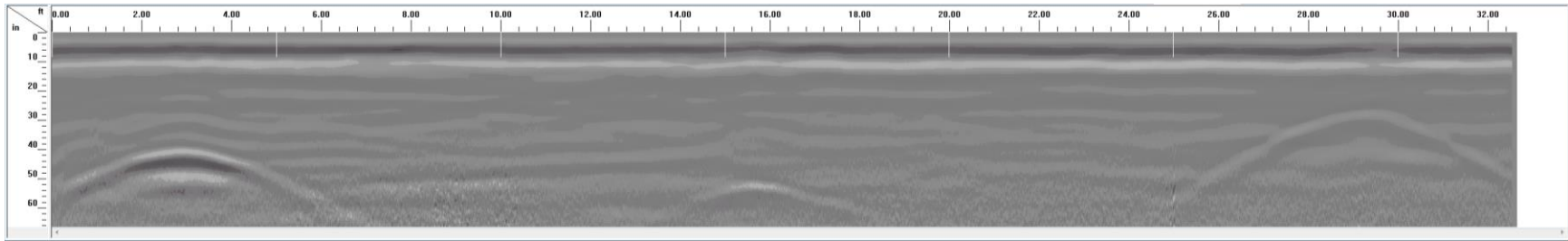
(f) 12" dia. Al. Foil Strip PVC at 3', 12" dia. CFRP Strip GFRP at 4', and 3" dia. CFRP Strip GFRP at 2'



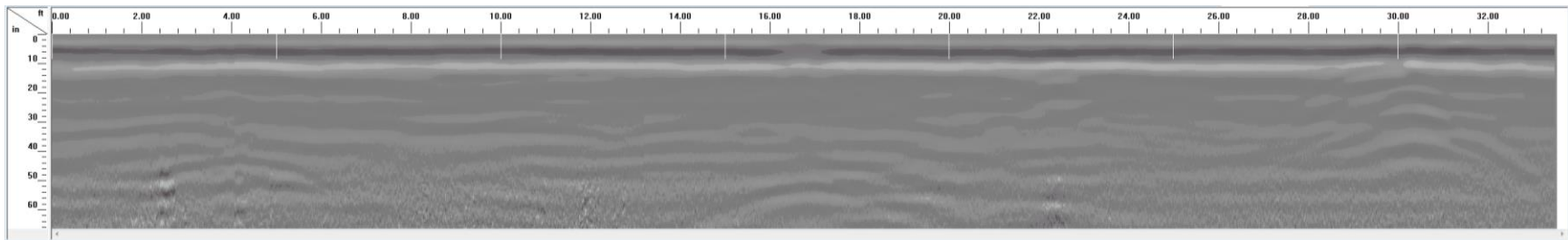
(g) 6" dia. Unwrapped PVC at 3', 12" dia. Unwrapped PVC at 4', and 3" dia. Unwrapped PVC at 2'



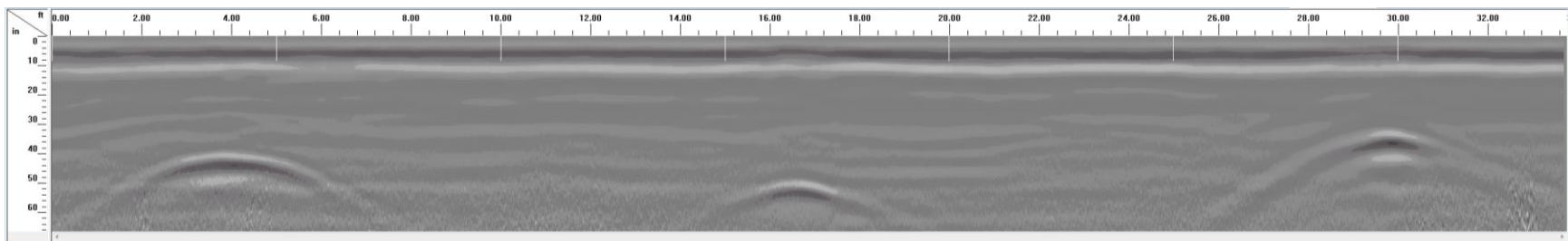
(h) 6" dia. Al. Foil Ring PVC at 3', 12" dia. Al. Foil Ring PVC at 4', and 3" dia. Al. Foil Ring PVC at 2'



(i) 6" dia. Al. Foil Strip PVC at 3', 12" dia. Al. Foil Strip PVC at 4', and 3" dia. Al. Foil Strip PVC at 2'

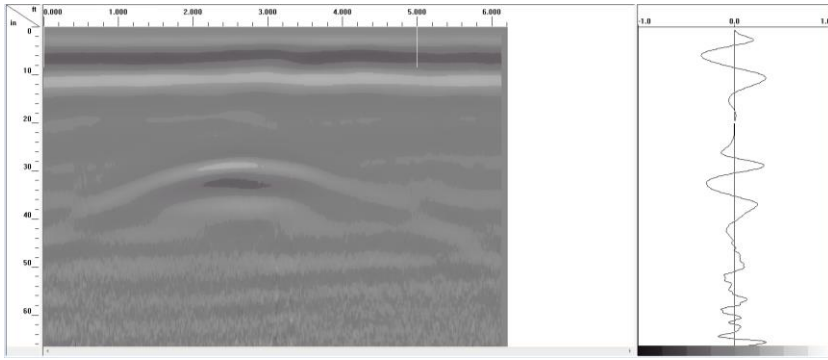


(j) 6" dia. CFRP Ring PVC at 3', 12" dia. CFRP Ring PVC at 4', and 3" dia. CFRP Ring PVC at 2'

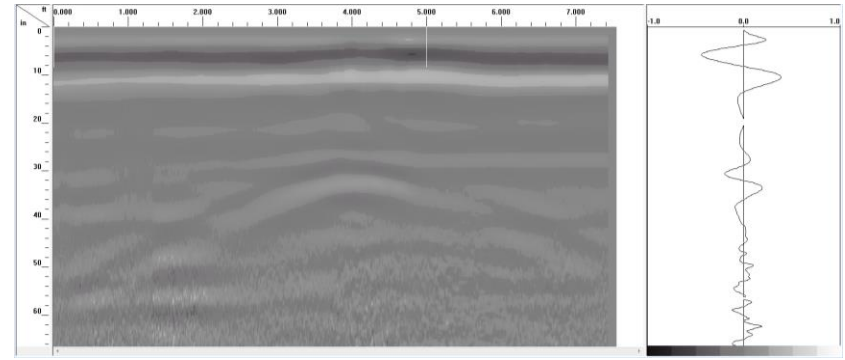


(k) 6" dia. CFRP Strip PVC at 3', 12" dia. CFRP Strip PVC at 4', and 3" dia. CFRP Strip PVC at 2'

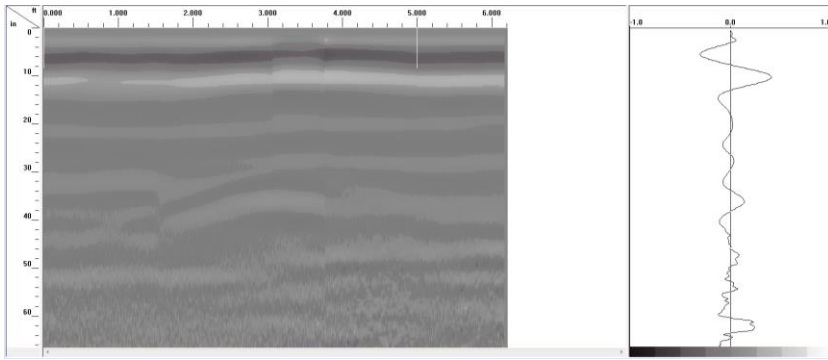
Figure 7-31: *Transverse scans over the pipes in 65 ft. long trenches using 200 MHz antenna for Dataset III*



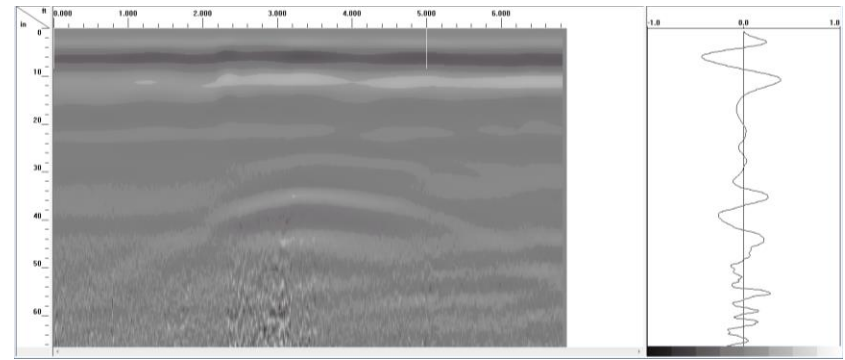
(a) GFRP pipe wrapped CFRP fabric



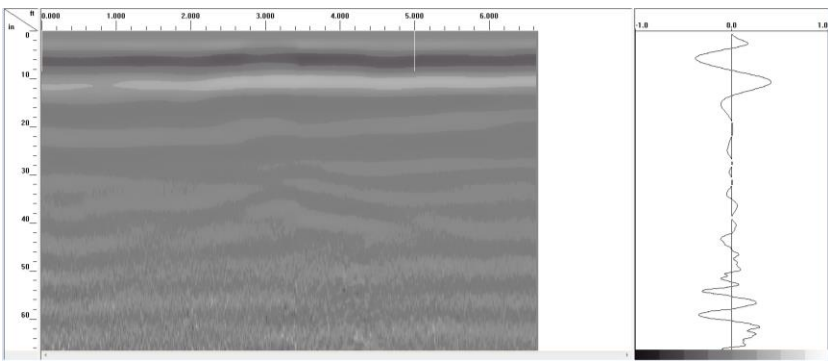
(b) Unwrapped GFRP pipe



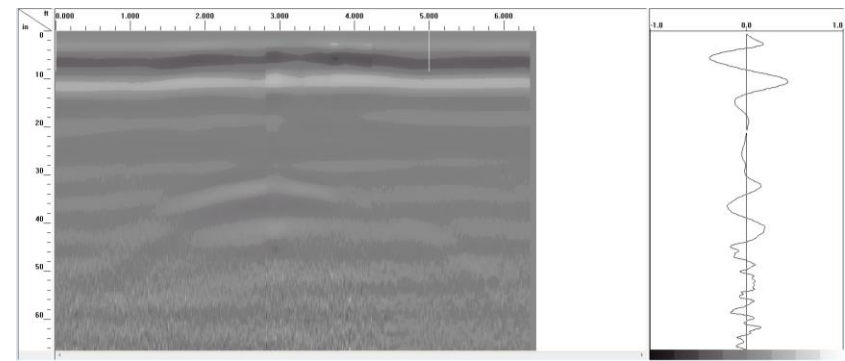
(c) GFRP pipe with carbon nanoparticle overlay



(d) PVC pipe wrapped with Aluminum foil strip



(e) Unwrapped GFRP pipe (10" diameter)



(f) Steel pipe

Figure 7-32: Transverse scans over the pipes in 36 ft. long trench using 200 MHz antenna for Dataset III

Figure 7-32 shows transverse scans (using 200 MHz antenna) over the 12" and 10" diameter pipes buried with 2 ft. of soil cover. Similar to the other GPR scans already discussed, pipe sections with CFRP/aluminum foil strip at the top (Figure 7-32 a and d) produced GPR reflections with high amplitudes. The pipe with CFRP strip produced the highest amplitude radar reflection, followed by the one with aluminum foil strip. The GFRP pipe with no surface wrap and the steel pipe (Figure 7-32 b and f) also produced good radar reflections, with the amplitude of reflection from the steel pipe being higher. The GFRP pipe with carbon nanoparticle coating produced a very weak reflection, while no noticeable reflection was recorded from the 10" diameter GFRP pipe with no surface wrap. Transverse scans for these 12" and 10" diameter pipes buried with 2 ft. of soil cover recorded from Datasets I and II are shown in Appendix B.3.

7.2.5 Performance of Surface Configurations

From the discussion of GPR test results presented in the three datasets above, the performance of the various pipe surface configurations investigated in this study can be summarized as follows:

- i. Carbon fabric and aluminum foil overlays improved detectability of buried non-metallic pipes by GPR.
- ii. Carbon fabric and aluminum foil strips along the full length of the pipe performs better than carbon fabric and aluminum foil ring at regular spacing around the pipes.
- iii. Carbon fabric overlays on pipes generally perform better than aluminum overlays.

Performance of carbon fabric and aluminum foil in improving the detectability of the buried non-metallic pipes can be attributed to the fact that, carbon fabric and aluminum are good electrical conductors, hence they reflect the incident radar waves significantly better than the non-conducting pipe material and the surrounding soil. These higher amplitude reflections from the overlays are recorded by the receiving antenna, and hence making it possible to locate the buried pipes.

The performance of strips versus rings can be evaluated in two parts and explained by the following observations. For GPR scans conducted along the length of the pipe (longitudinal scans), significant portion of the antenna's electromagnetic beam will fall on the long strips (about 4.5 ft. long strips, excluding pipe caps) and be reflected, as opposed to the 3 inch wide rings which only cover small portion of the antenna beam. For scans conducted perpendicular to the pipe direction (transverse scans), the rings produced very good results when the antenna is centered over a ring.

Results produced by pipes with rings around them when the survey antenna is centered over a ring are comparable to the results obtained from pipes with strips along the full. For situations when the antenna is centered between two rings during a transverse scan, the results were very poor (comparable to results from non-metallic pipes without any wraps) because reflections or non-thereof were produced by the non-metallic pipe materials rather than by the overlays.

Carbon fabric overlays on buried pipes performed better in terms of detectability with GPR compared to aluminum foil overlays because the carbon fabrics used were far thicker than the aluminum foil. Increasing the thickness of aluminum overlay around the pipes (or wrapping pipes with aluminum sheets) can improve their detectability when buried, as well as increase the durability of the overlay. However, this approach is not practically feasible for buried pipe detection.

The above observations (i through iii) are illustrated by comparing the returned radar signal amplitude from five different 6" diameter PVC pipes buried with 3 ft. of soil cover as shown in Figure 7-33 (GPR results in Dataset I were used for this plot). Peak amplitude of reflected radar signal from all the other pipe sections investigated were plotted and shown in Figures 7-34 and 7-35. In Figures 7-34 and 7-35, 3"@2' means 3 inch diameter pipes buried with 2 ft. of soil cover. Similar naming schemes are used for all the other pipes shown in these plots. It is seen in Figures 7-34 and 7-35 that, data points for pipes without any surface configuration (shown in red) are always lower than data points for all the pipes with CFRP or aluminum foil overlays (with the exception of 12" diameter GFRP pipes buried with 3 ft. of soil cover, where signal from the unwrapped pipe is slightly higher than that from GFRP pipe wrapped with CFRP strip). It is also observed that, signals from the GFRP pipe with carbon nanoparticle overlay and the steel pipe buried at 2 ft. depth are the lowest. The addition of carbon fabric or aluminum foil overlays was found to increase the reflected signal amplitude by up to 4.52 times, and 2.02 times on average across all the pipe sections tested.

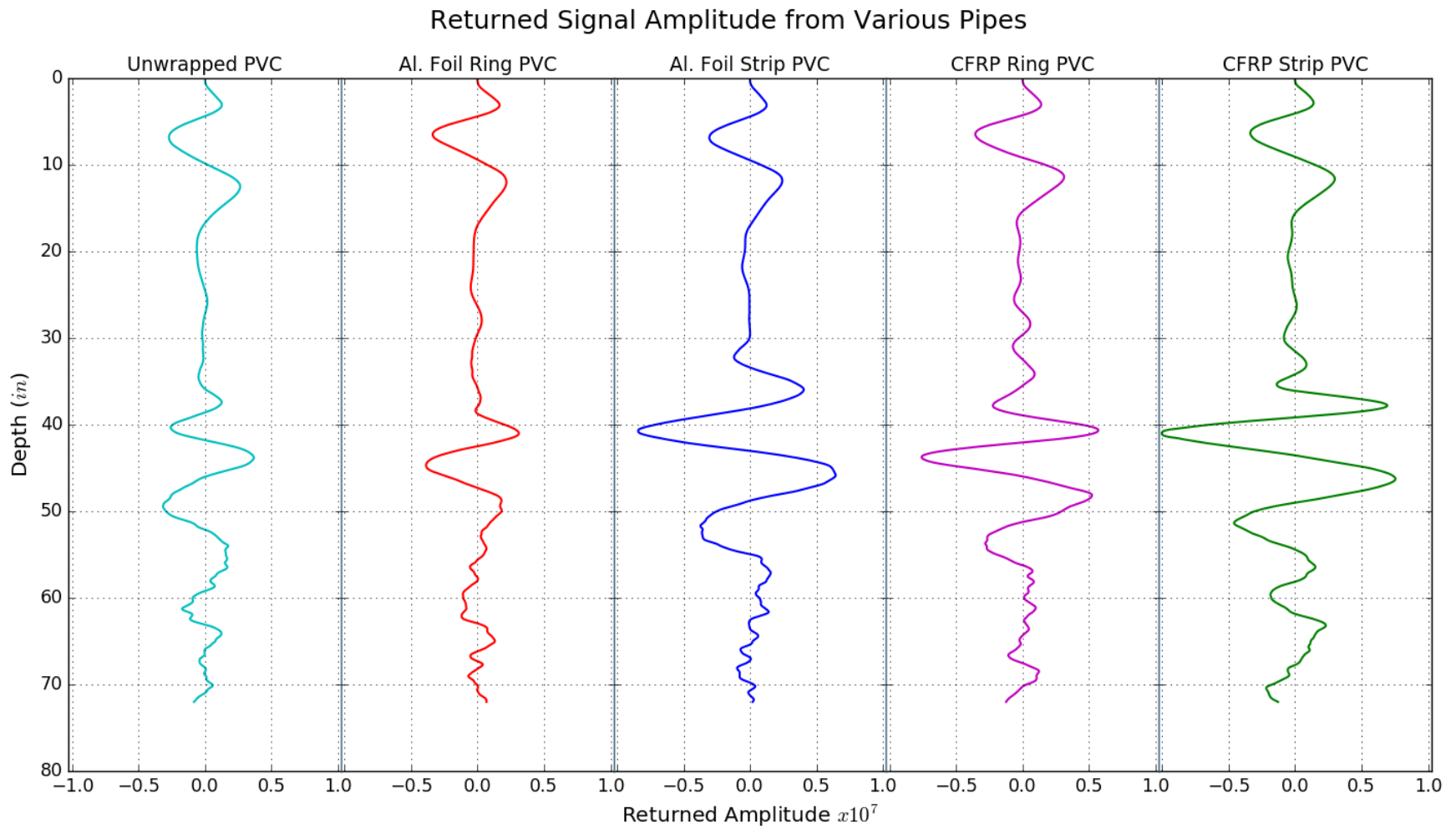


Figure 7-33: Comparison of returned radar signal amplitude from different pipe configurations

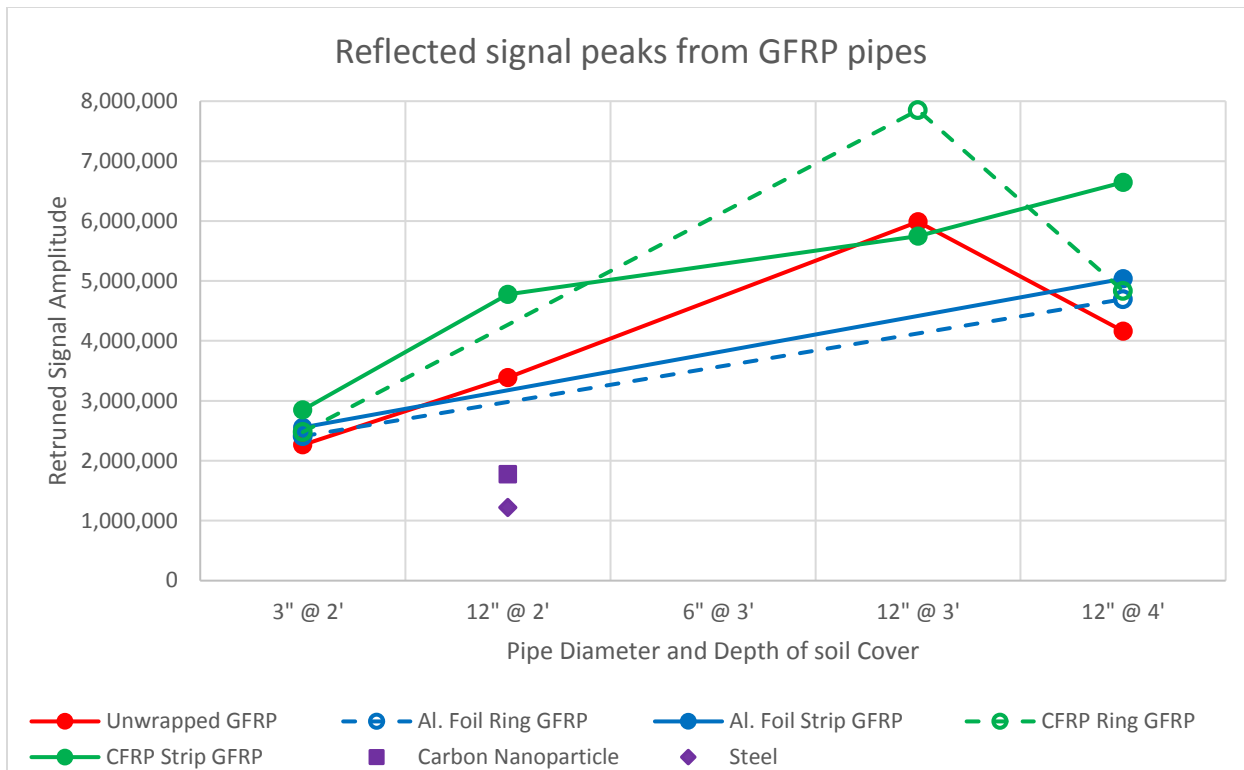


Figure 7-34: Comparison of returned radar signal amplitude from GFRP pipe configurations

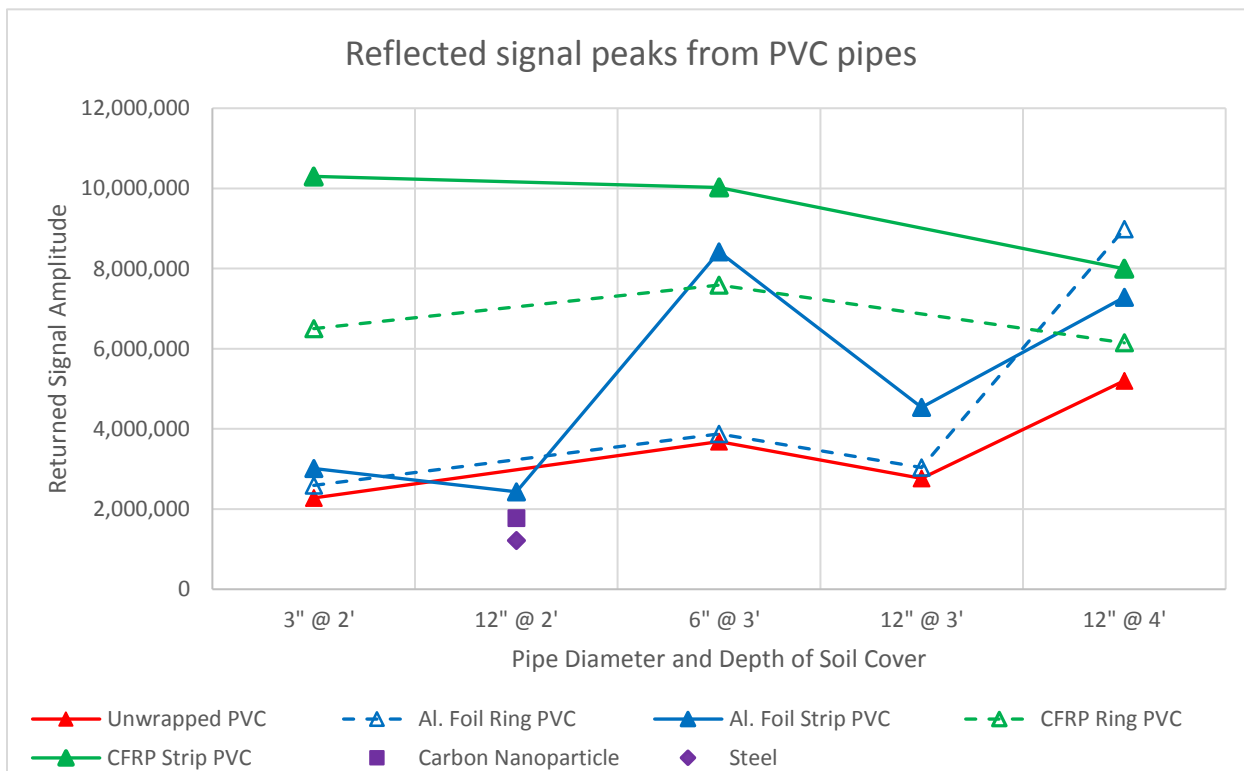


Figure 7-35: Comparison of returned radar signal amplitude from PVC pipe configurations

7.3 DETERMINATION OF DEPTH

In addition to finding the locations of buried pipes, another parameter that is of importance to pipeline asset managers, operators, or construction crews is the depth at which the pipeline is buried. Thus accurate estimation of the burial depth is essential in GPR surveys. Depth to a buried target can be estimated by multiplying half of the two way travel time (two way travel time from GPR antenna to buried object and back to the antenna) by the GPR wave velocity. A number of methods can be employed in estimating the wave velocity, and hence pipe depth, from GPR data, three of such methods are described below.

7.3.1 Depth Estimation Using Soil Dielectric Constant

During GPR surveys, the amplitudes of reflected waves are recorded as a function of the elapsed time between the transmission and receiving of the reflected waves. While the amplitude of the reflected waves are used to determine the presence of buried objects, the travel time can be used to estimate the depth to that buried object by means of the velocity of the radar wave. As discussed in Chapter 4, velocity (v) of radar waves can be estimated using the dielectric constants of the medium being investigated. Thus, if the dielectric constant of the soil (or medium under investigation) is known, the signal velocity can be calculated using Equation 4-2 provided in Chapter 4. The velocity and signal travel time (two way travel time) can then be combined to obtain the depth, d , of subsurface of objects (Equation 7-1).

$$d = \frac{vt}{2} = \frac{ct}{2\sqrt{\epsilon_r'}} \quad (7-1)$$

where $c \approx 3 \times 10^8$ m/s is the velocity of electromagnetic waves in vacuum (speed of light).

t = two way travel time of radar signal (s)

ϵ_r' = dielectric constant of the soil/medium

Most GPR survey systems have applications that can automatically calculate the depth to buried objects if the correct dielectric constant is provided by the user. In this research, dielectric constant of the soil was measured using GS3 soil sensors. This was then used in estimating the depth to the buried pipes as presented in Section 7.2.

7.3.2 Depth Estimation Using GPR Hyperbolic Fitting

Reflections from buried circular objects appear as hyperbolas in GPR data/radargram when the survey is conducted perpendicular to the length of the object. Distance from the antenna to the buried object becomes increasingly longer when the antenna is moved away from the pipeline, compared to when the antenna is directly above the pipe. The longer path of the radar wave from the antenna to the buried pipe and back to the antenna is indicated by the longer travel time ($t_1 > t_0$) as shown in Figure 7-36. This is because the GPR signal spreads out from the antenna into the medium under investigation with a conical footprint. This results in producing a reflection hyperbola with the apex directly at the location of the buried pipe. The shape of this hyperbola is dependent on the soil dielectric constant and the depth at which the object is located. The radar wave velocity can be estimated from the hyperbola using Equation 7-2.

$$v = \frac{2(x)}{\sqrt{t_1^2 - t_0^2}}, \quad x = x_0 - x_1 \quad (7-2)$$

And the depth to target will be:

$$d = \frac{vt}{2} = \frac{2(x_0 - x_1)(t_0 - t_g)}{\sqrt{(t_1 - t_g)^2 - (t_0 - t_g)^2}} \quad (7-3)$$

For data with time-zero correction already applied, t_g will be 0.

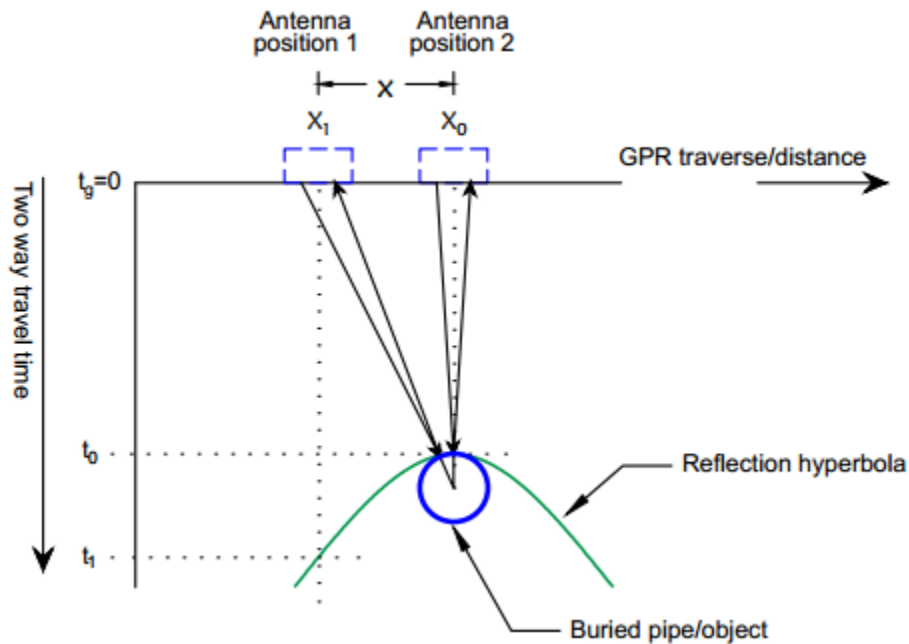


Figure 7-36: Circular reflector and associated hyperbolic feature

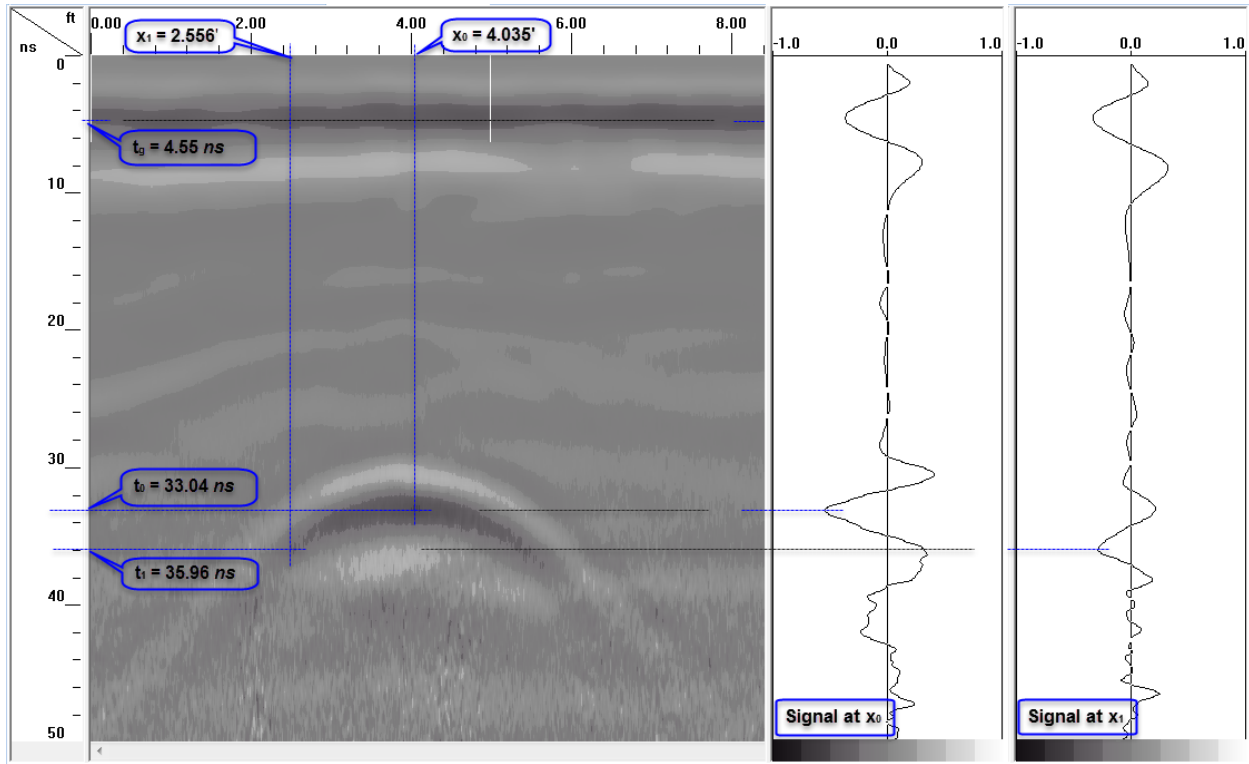


Figure 7-37: Velocity estimation using hyperbolic feature in GPR data (pipe 6"@3')

Table 7-3: Target depth estimated using hyperbolic fitting

Pipe Label	Nominal Depth (ft)	Distance, x (ft)		Time, t (ns)			Velocity, v (ft/ns)	Estimated Depth (in.)	% Error
		x_0	x_1	t_0	t_1	t_g			
6"@3'	3	4.035	2.556	33.04	35.96	4.55	0.22366	38.23	6.20
12"@4'	4	16.660	15.785	40.58	41.40	4.06	0.22487	49.27	2.65
12"@2'	2	29.854	28.535	27.44	31.25	4.55	0.19192	26.36	9.82
3"@2'	2	2.604	1.625	24.51	26.38	4.95	0.22364	26.25	9.36

Figure 7-37 and Table 7-3 show sample velocity and depth determination from experimental GPR data in Figures 7-31(k) and 7-32(a) using the hyperbolic fitting method.

This method of estimating GPR wave velocity is sometimes likely to result in errors since inaccuracies in picking the travel times could have high effects on the estimated velocity. Thus, care must be taken to minimize errors associated with picking the travel time from the GPR hyperbola. For the sample velocity and depth calculations shown above, errors associated with the estimated depths are all less than 10%.

7.3.3 Depth Estimation Using Common Mid-Point (CMP) Method

Another method that can be used to estimate the velocity of radar waves and depth of subsurface object is the Common Mid-Point (CMP) method. Two separate antenna to serve as transmitter and receiver are required for this method (as opposed to a monostatic antenna). During CMP survey, the transmitting and receiving antennae are placed at equal distances away from a common mid-point and the GPR data is recorded. The antennae are then moved out at equal distances from the common mid-point in each step (Figure 7-38), with GPR data recorded and the process repeated until the survey is complete.

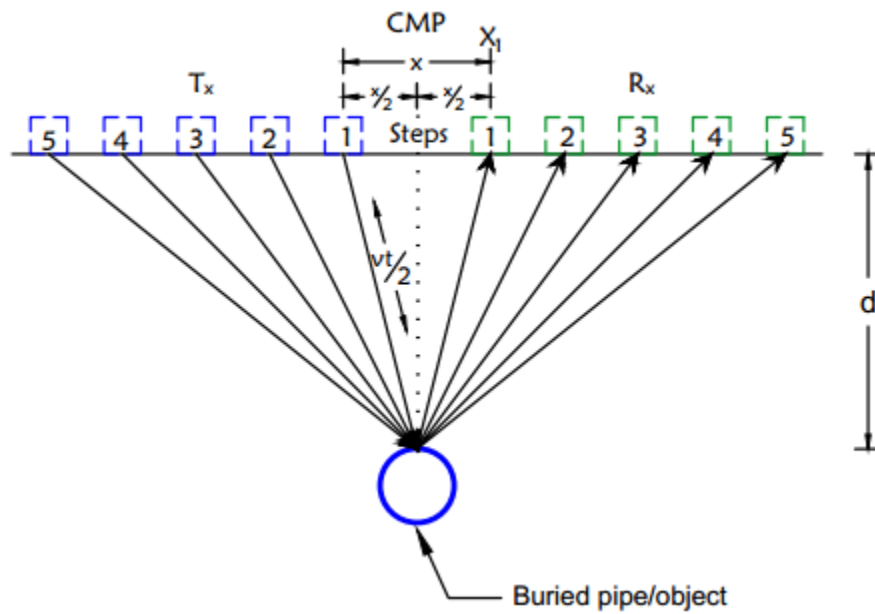


Figure 7-38: Common Mid-Point (CMP) technique

From Figure 7-38;

$$\left(\frac{x}{2}\right)^2 + d^2 = \left(\frac{vt}{2}\right)^2 \rightarrow t^2 = \left(\frac{1}{v^2}\right)x^2 + \left(\frac{2d}{v}\right)^2 \quad (7-4)$$

Thus the slope of a t^2 against x^2 plot (Figure 7-39) can be used to obtain the wave velocity.

$$slope = \frac{1}{v^2} \rightarrow v = \sqrt{\frac{1}{slope}} \quad (7-5)$$

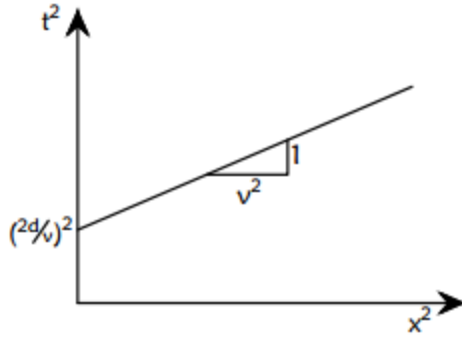


Figure 7-39: Plot for estimating velocity from CMP survey

A simplified variant of the CMP method involves taking only two data points as shown in Figure 7-40. The transmitter and receiver are first placed at the common mid-point and the GPR data is recorded, the antennae are then moved apart at equal distances from the mid-point as before and the GPR data is recorded again.

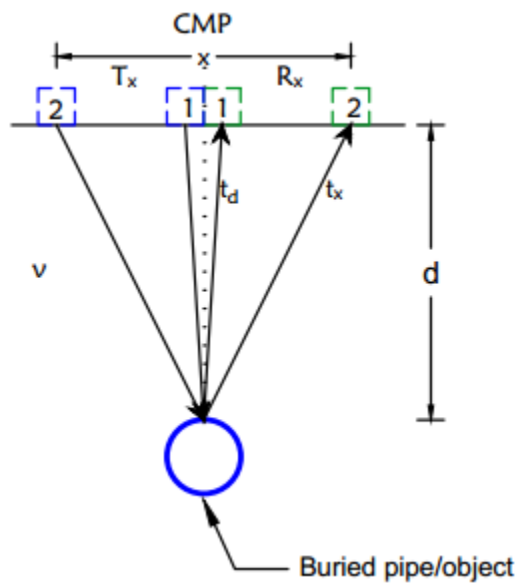


Figure 7-40: The simplified Common Mid-Point (CMP) technique

It can be shown from Figure 7-40 that (GSSI 2017);

$$v = \frac{x}{\sqrt{t_x^2 - t_d^2}} \quad (7-6)$$

With the GPR wave velocity estimated, the depth to the buried/subsurface object can now be calculated using the two way travel time as before.

7.4 CONCLUSIONS

From the GPR test data presented in this chapter, it is evident that, the use of CFRP and aluminum foil/tape overlays (in the form of rings and strips) improve the detectability of buried non-metallic pipe sections such as GFRP and PVC. In cases where the buried unwrapped GFRP and PVC pipes were detectable (albeit with faint and difficult to interpret signals), the addition of carbon or aluminum foil overlays significantly increased the strength/amplitude of the reflected GPR signal and made it easier to identify the pipe sections. CFRP and aluminum foil overlays performed significantly better in making the buried non-metallic pipes detectable because these overlays are electrical conductors, hence they reflect the incident radar waves much better than the non-conducting pipe material and the surrounding soil.

Production of stronger and easier to interpret signals from buried non-metallic pipes with carbon fabric or aluminum foil overlays also implies that, the depth of pipe burial can be increased beyond the 4 ft. maximum depth evaluated in this research and still obtain adequate signal strength using GPR. Maximum penetration depths for GPR surveys in different types of soils and different soil moisture contents are evaluated in the next chapter.

Carbon fabric overlays (strips/rings) were observed to produce stronger radar signal reflections from buried pipes compared to aluminum foil overlays. It was observed that carbon fabric and aluminum foil strips bonded to the top of the pipes generally produce better/stronger signals compared to carbon fabric and aluminum foil rings around the non-metallic pipe sections. The performance of strips versus rings can be explained by the following observations. For GPR scans conducted along the length of the pipe, significant portion of the antenna's electromagnetic beam will fall on the long strips (about 4.5 ft. long strips, excluding pipe caps) and be reflected, as opposed to the 3 inch wide rings which only cover small portion of the antenna beam. For scans conducted perpendicular to the pipe direction, the rings produced good results comparable to the strips when the antenna is centered over a ring. For situations when the antenna is centered between two rings, the results were very poor (comparable to results from non-metallic pipes without any wraps) because reflections or non-reflections were produced by the non-metallic pipe materials.

The addition of carbon nanoparticle coating on a GFRP pipe was however not found to provide any noticeable benefit in making the non-metallic pipe detectable using GPR. This can be

attributed to the lack of interconnection between the individual nanoparticles to form a continuous conductor in the overlay.

Furthermore, it was found from the GPR testing that, snow cover on the ground surface does not hinder the performance of GPR in detecting the buried pipes. This can be attributed to the fact that, the dielectric constant and electrical conductivity of snow are very low, hence the GPR signal travels through the snow cover without much attenuation.

Finally, it was observed that, 200 MHz GPR antenna performed significantly better in locating the buried pipes compared to the 400 MHz and 900 MHz antennae. This is because signal from the higher frequency antennae attenuates significantly more with respect to travel distance compared to the lower frequency antenna. The attenuation characteristics of these antennae will be evaluated in the next chapter. The 400 MHz antenna performed well in locating the pipes buried with 2 ft. of soil cover, especially when scanned in the transverse direction (which is the primary mode/direction of scanning during utility locating surveys).

CHAPTER 8

NUMERICAL COMPUTATIONS

8.1 INTRODUCTION

Successful GPR surveys and accurate interpretation of GPR data requires adequate knowledge/estimation of the soil dielectric properties. This also requires adequate estimation of the effect of soil properties on the radar wave propagation. Thus, in addition to soil dielectric properties, parameters such as phase coefficient (k_R), attenuation coefficient (k_I), skin depth (d_p), and wavelength (λ) are important in GPR surveys and data interpretation. This chapter provides numerical modelling of soil dielectric constant (ϵ') from volumetric water content, VWC (θ), and vice versa. Computation of phase and attenuation coefficients, wavelength, skin depth, among other parameters that provides extra information and interpretation of the experimental GPR data is also provided.

8.2 SOIL DIELECTRIC MODELLING

Dielectric constant is one of the most important material properties in GPR surveys. It is the primary parameter used in estimation wave propagation velocity and the depth at which objects are buried. The dielectric constant is also used, together with other material properties in estimating other GPR survey parameters such as attenuation and penetration depth. Accurate determination of dielectric properties of materials is therefore important in GPR survey applications.

Decagon GS3 soil moisture sensors were used to measure volumetric moisture content, electrical conductivity, dielectric constant, and temperature of the soil at 0, 2, and 4 ft. depths in the field during this experiment. For dielectric constant measurements, the GS3 sensors use a capacitance/frequency domain technology, with a measurement frequency of 70 MHz. Data was collected occasionally between September 2016 and September 2018, some of the data are summarized in Table 8-1. Prolonged rainy spells were experienced during the testing period, thus most of the test was conducted in wet soil conditions. Data for soil VWC below 0.208 was therefore obtained by taking a block of soil from the field and allowing it dry under normal

laboratory conditions while the dielectric properties were continuously measured. A plot of the soil dielectric constant versus the volumetric water content is shown in Figure 8-1. A third order polynomial function (Equation 8-1) was fitted to the experimental $\varepsilon - \theta$ data in this study. This function modelled the data accurately (passing through all the field data points and overlapping the original line connecting the data points) with an R^2 value of 1.000. Though Equation 8-1 fitted the data accurately, it should be noted that, this model was developed based on volumetric water content values between 0.119 and 0.489; thus the model might not work properly for data outside this range. This limitation is evident in the slightly negative ε' that will be produced by this model if the θ value is 0.

$$\varepsilon'_r = -0.0267 + 61.576\theta - 127.88\theta^2 + 247.25\theta^3 \quad (8-1)$$

The field data (and Equation 8-1) was compared to the dielectric models presented in Section 4.6.1 in Chapter 4 as shown in Figure 8-2. Equation 4-33, which is the Topp et al. (1980) model for organic soils is the closest to the data, especially at higher VWC, while Equations 4-32, 4-37, and 4-41 are closer to the data at lower VWC.

Equation 4-34, which is the Roth et al. model for mineral soils, under-predicts by an average of 9.4% (minimum 0.7% and maximum 16.7%) when volumetric water content is below 0.185 and over-predicts by an average of 18.8% (minimum 0.5% and maximum 27.8%) when volumetric water content is above 0.185. Equations 4-32, 4-37, and 4-41 over-predict by an average of 18 – 22%, while the remaining models (Equations 4-33, 4-35, and 4-39) under-predict by an average of 14 – 34%.

Table 8-1: Measured soil dielectric properties

Test Date	Depth (ft.)	Volumetric Water Content, θ (m^3/m^3)	Conductivity (mS/m)	Dielectric Constant, ϵ'
27-Sep-16	0	0.339	14.88	15.9
2-Nov-16		0.399	10.91	19.84
26-Apr-17		0.394	18.41	19.52
17-May-17		0.346	15.24	16.28
31-May-17		0.388	18.10	19.04
29-Jun-17		0.297	9.89	13.56
4-Aug-17		0.285	7.82	12.92
1-Sep-17		0.308	12.26	14.13
11-Sep-17		0.307	9.63	14.08
6-Oct-17		0.235	10.33	10.58
20-Jan-18		0.465	15.35	25.74
2-May-18		0.275	8.80	12.46
30-Jul-18		0.382	19.96	18.79
18-Sep-18		0.479	25.19	27.56
27-Sep-16		2	0.366	15.00
2-Nov-16	0.396		17.36	19.67
26-Apr-17	0.41		16.37	20.72
17-May-17	0.419		16.02	21.39
31-May-17	0.416		15.76	21.16
29-Jun-17	0.406		14.55	20.39
4-Aug-17	0.417		16.37	21.29
1-Sep-17	0.395		14.24	19.57
11-Sep-17	0.388		14.33	19.05
6-Oct-17	0.345		11.56	16.25
20-Jan-18	0.482		18.82	27.79
2-May-18	0.411		16.13	20.74
30-Jul-18	0.361		12.23	17.28
18-Sep-18	0.489		21.54	28.86
27-Sep-16	4		0.458	21.39
2-Nov-16		0.463	20.28	25.50
26-Apr-17		0.476	22.33	27.06
17-May-17		0.47	20.28	26.35
31-May-17		0.474	21.16	26.75
29-Jun-17		0.461	19.01	25.28
4-Aug-17		0.464	18.81	25.62
1-Sep-17		0.456	17.45	24.75
11-Sep-17		0.456	17.64	24.77
6-Oct-17		0.442	16.02	23.44
20-Jan-18		0.473	18.81	26.66
2-May-18		0.465	16.72	25.74
30-Jul-18		0.456	13.10	24.79
18-Sep-18		0.479	14.76	27.36

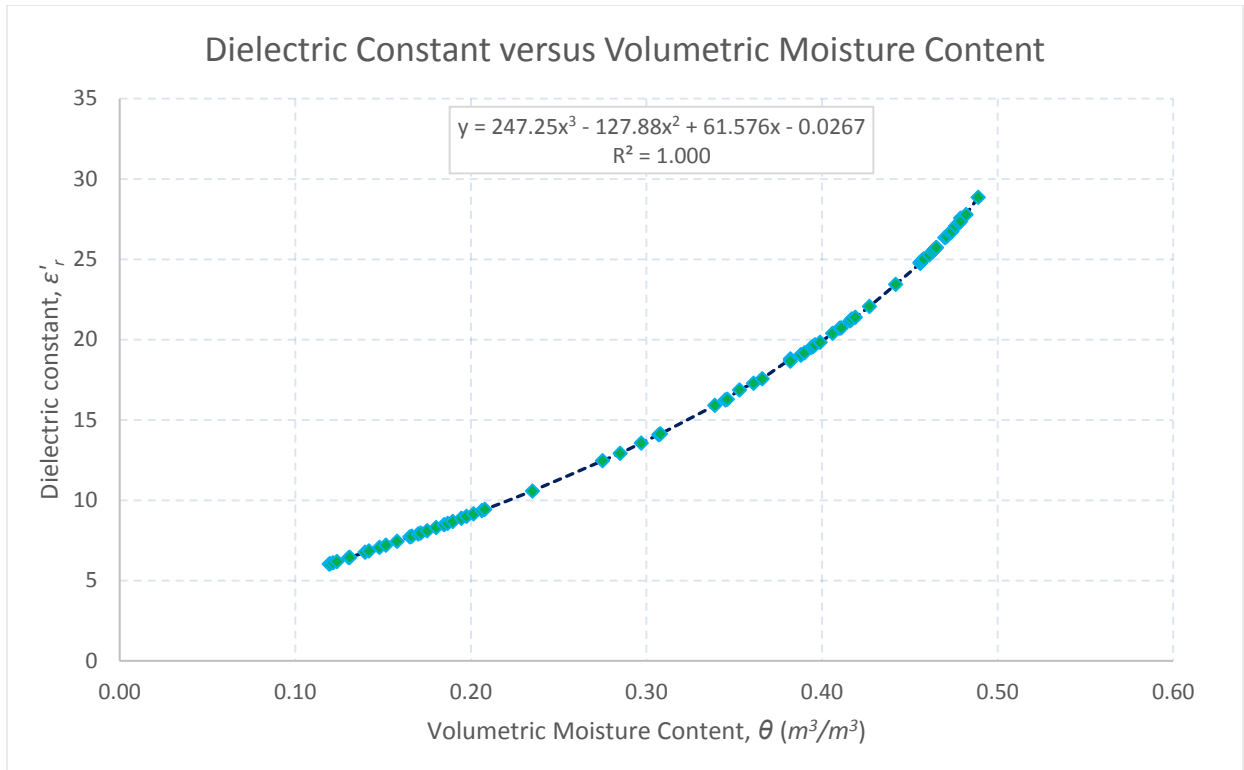


Figure 8-1: Experimental dielectric constant versus VWC

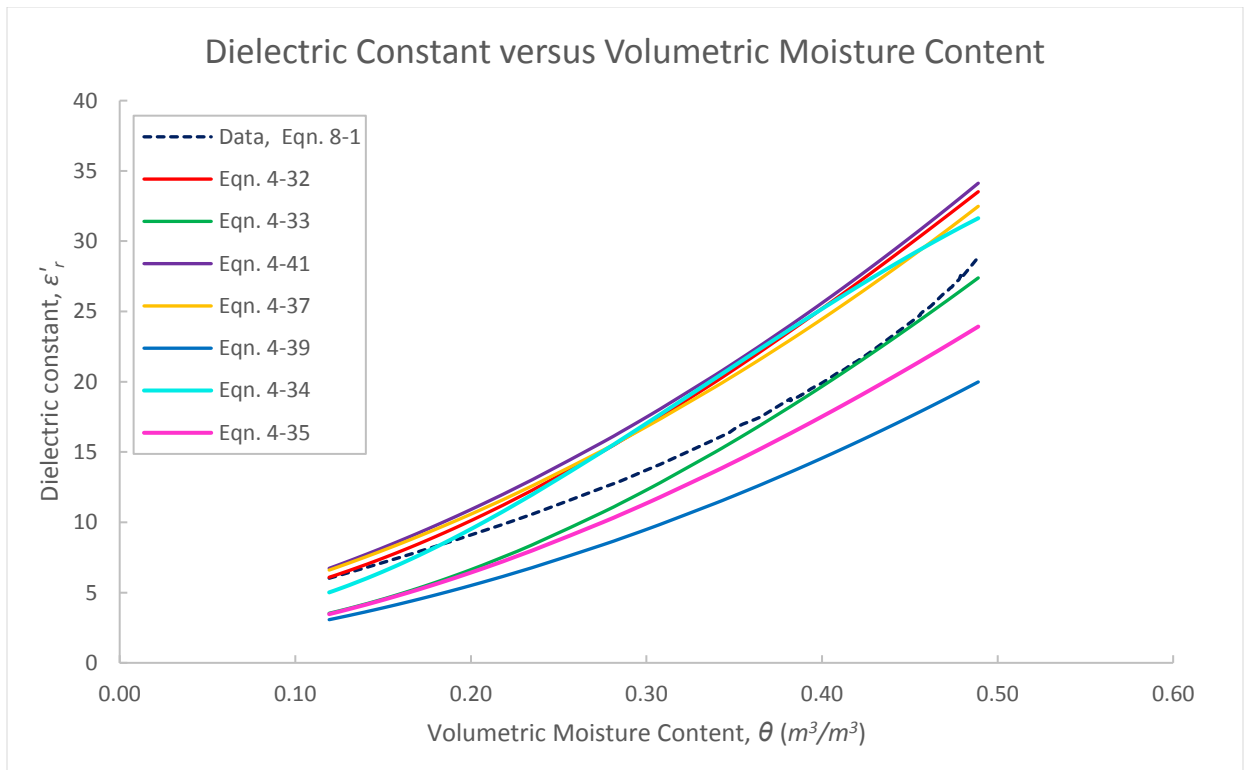


Figure 8-2: Comparison between dielectric models and experimental data

For the purpose of making it easier to quickly estimate dielectric constant from volumetric water content measurements in the field, two other functions that are simpler than Equation 8-1 were fitted to the data. These are a quadratic and a linear function (Equations 8-2 and 8-3), with R^2 values of 0.996 and 0.979 respectively. These two equations proposed in this study are slightly less accurate, but are convenient for quick computations in the field. In addition, all three models/functions presented in this section are only applicable for VWC between 0.119 and 0.489. The three models are summarized in Table 8-2 and plotted in Figure 8-3

$$\varepsilon_r' = \left(\frac{\theta + 0.1953}{0.1312} \right)^2 \quad (8-2)$$

$$\varepsilon_r' = 58.482\theta - 2.332 \quad (8-3)$$

Table 8-2: Dielectric models derived from experimental data

Dielectric Models			
No.	Model	R ²	Equation Number
1	$\varepsilon_r' = -0.0267 + 61.576\theta - 127.88\theta^2 + 247.25\theta^3$	1.000	8-1
2	$\varepsilon_r' = \left(\frac{\theta + 0.1953}{0.1312} \right)^2$	0.996	8-2
3	$\varepsilon_r' = 58.482\theta - 2.332$	0.979	8-3

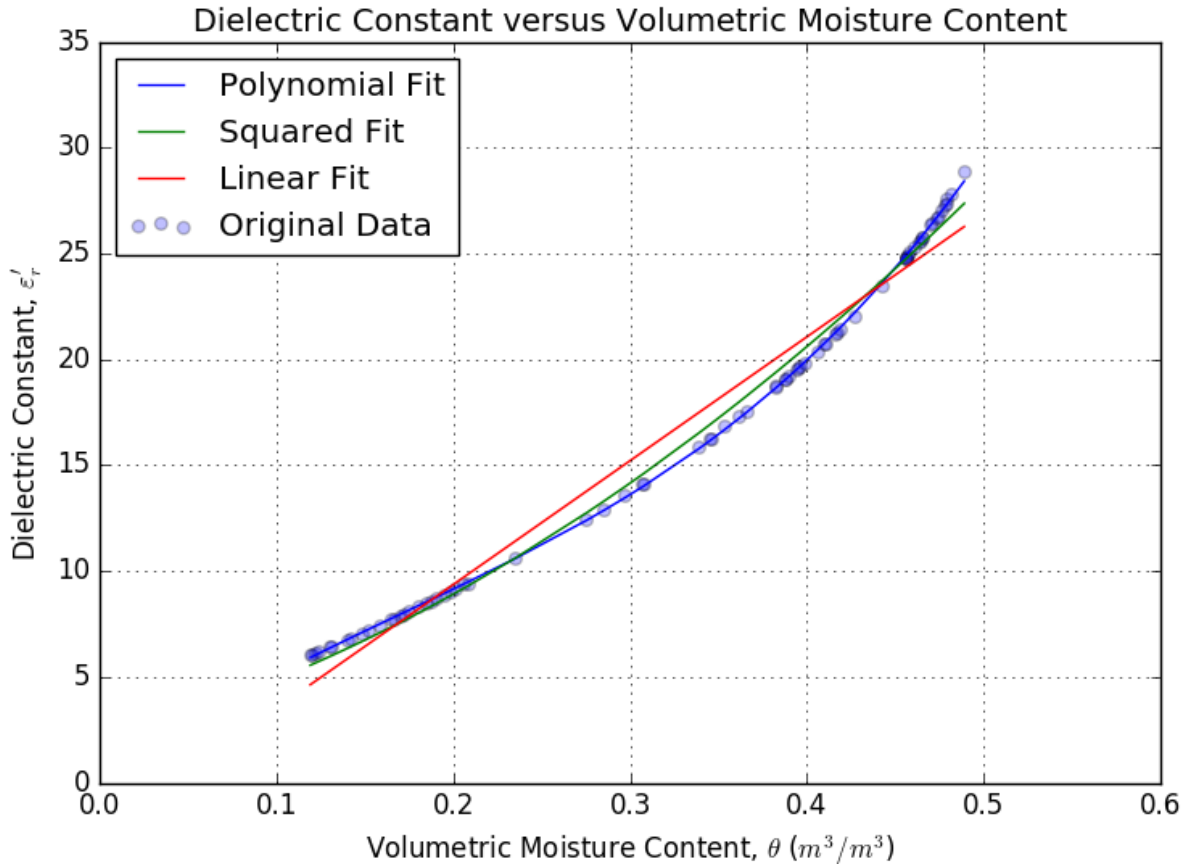


Figure 8-3: Comparison between the three dielectric models and experimental data

8.3 INVERSE DIELECTRIC MODELLING

While accurate estimation of dielectric constant is very important for GPR surveys, there are times when there is the need to estimate other soil properties such as volumetric water content from GPR data or dielectric constant measurements. Dielectric constant can be estimated from GPR data if the depth to the target object is known, or it can be determined using the Common Mid-Point (CMP) survey approach. The depth to buried objects can also be estimated using any of the methods discussed in Section 7.3 of Chapter 7.

The experimental volumetric water content measurement data is plotted against the dielectric constant as shown in Figure 8-4.

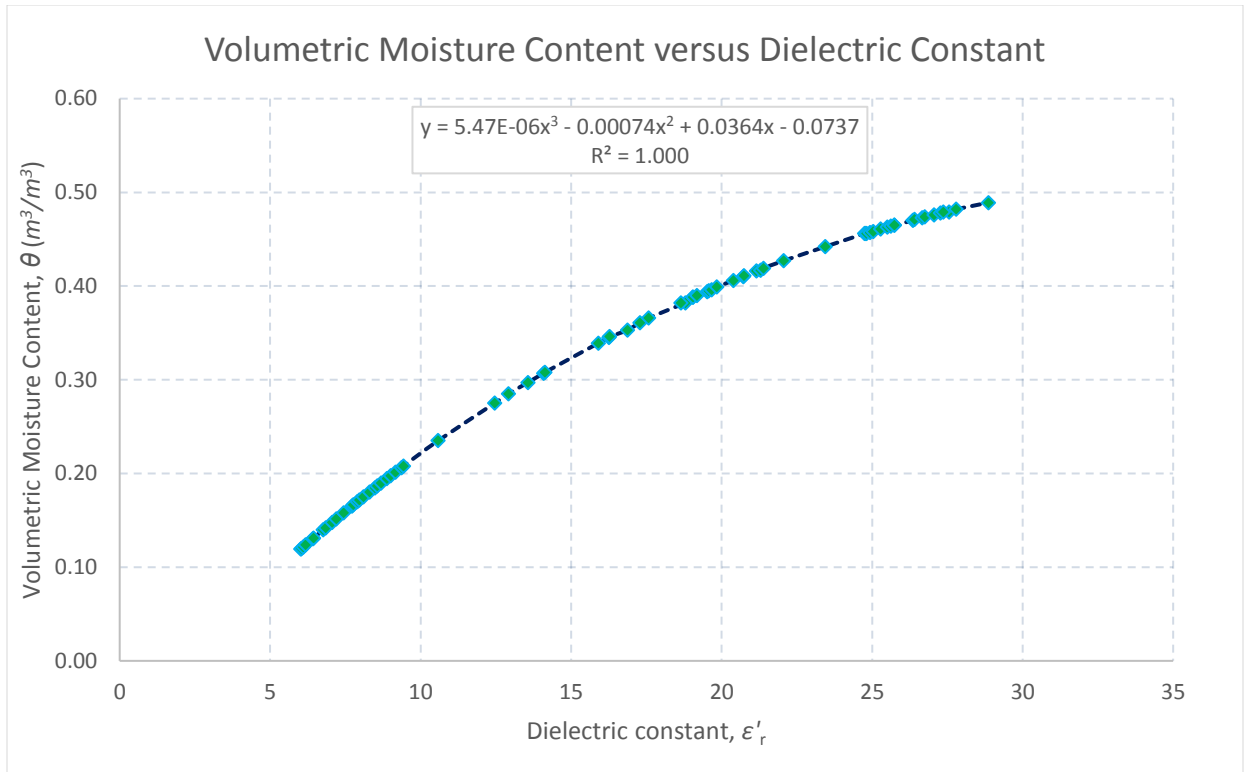


Figure 8-4: Experimental VWC versus dielectric constant

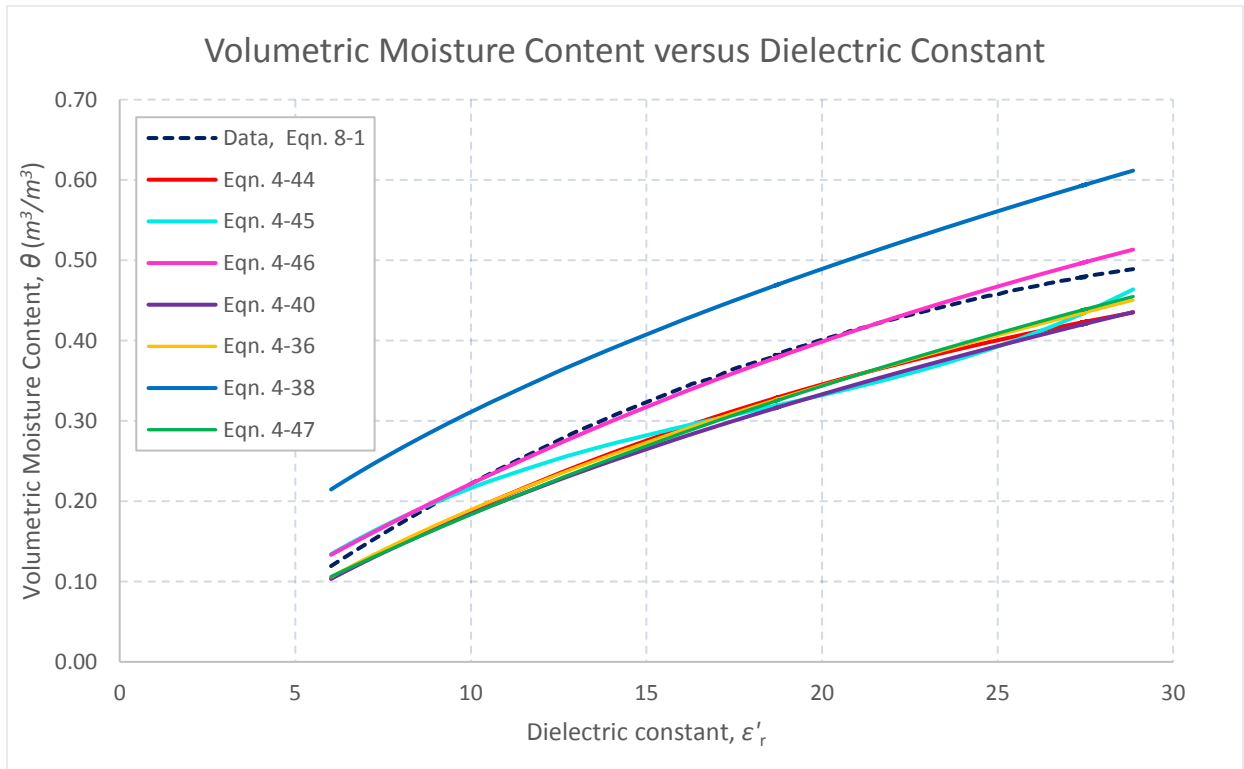


Figure 8-5: Comparison between inverse dielectric models and experimental data

As with the dielectric model in the previous section, a third order polynomial function (Equation 8-4) was fitted to the inverse ε'_r - θ data. This function also modelled the data accurately (passing through all the field data points and overlapping the original line connecting the data points) with an R^2 value of 1.000. Though Equation 8-4 fitted the data accurately, it should be noted that, this model was also developed based on dielectric constant values between 6.02 and 28.86, and volumetric water content values between 0.119 and 0.489; thus the model might not work properly for data outside this range.

$$\theta = -0.0737 + 0.0364\varepsilon'_r - 0.00074\varepsilon_r'^2 + 0.00000547\varepsilon_r'^3 \quad (8-4)$$

The field data (and Equation 8-4) was compared to the inverse dielectric models presented in Section 4.6.2 in Chapter 4 as shown in Figure 8-5. Equation 4-46, which is the Roth et al. (1992) model for organic soils is the closest to the data. This equation only over-predicts by an average of 2.2%, with maximum over-prediction of 11.7% and maximum under-prediction of 1.97% compared to the field data. Equation 4-38 over-predicts by an average of 36% (maximum of 80%), while Equation 4-40 under-predicts by an average of 15%. All the other remaining models under-predict by an average of 13%.

For the purpose of making it easier to quickly estimate volumetric water content (VWC) from dielectric constant measurements in the field, two other functions that are simpler than Equation 8-4 were fitted to the data. These are a radical and a linear function (Equations 8-5 and 8-6), with R^2 values of 0.996 and 0.979 respectively. Similar to Equations 8-2 and 8-3 from the forward model, the two other equations proposed in this study (Equations 8-5 and 8-6) are slightly less accurate, but are convenient for quick computations in the field. In addition, all three models/functions presented in this section may only be applicable for dielectric constant values between 6.02 and 28.86, and VWC between 0.119 and 0.489. The three models are summarized in Table 8-3 and plotted in Figure 8-6

$$\theta = 0.1312\sqrt{\varepsilon'_r} - 0.1953 \quad (8-5)$$

$$\theta = 0.0167\varepsilon'_r + 0.0460 \quad (8-6)$$

Table 8-3: Inverse dielectric models derived from experimental data

Inverse Dielectric Models			
No.	Model	R ²	Equation Number
1	$\theta = -0.0737 + 0.0364\varepsilon_r' - 0.00074\varepsilon_r'^2 + 0.00000547\varepsilon_r'^3$	1.000	8-4
2	$\theta = 0.1312\sqrt{\varepsilon_r'} - 0.1953$	0.996	8-5
3	$\theta = 0.0167\varepsilon_r' + 0.0460$	0.979	8-6

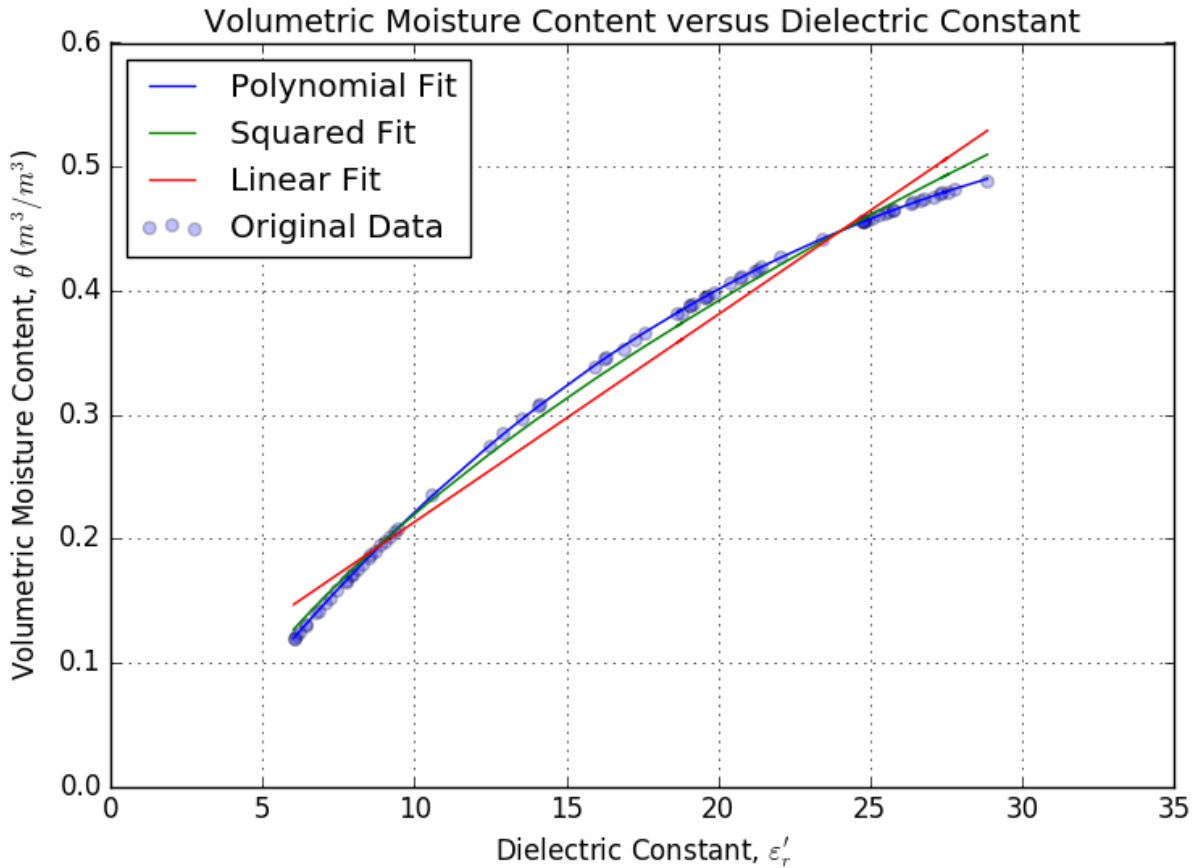


Figure 8-6: Comparison between the three inverse dielectric models and experimental data

Finally, the ε - θ data and model from this experiment (Equation 8-1) was compared to secondary data from previous researches, as compiled by Muklisin and Saputra (2013). The plot provided by Muklisin and Saputra (2013) is overlaid with the model from this experiment, represented by the thick red curve at the center of the plot as shown in Figure 8-7. Equation numbers in parentheses represent equations found in Muklisin and Saputra (2013), while the members in square brackets represent equations as they appear in this document. The closest models to the data from this research are Equations 4-33 and 4-46, which are models for organic soils presented by Topp et al. (1980) and Roth et al. (1992) respectively.

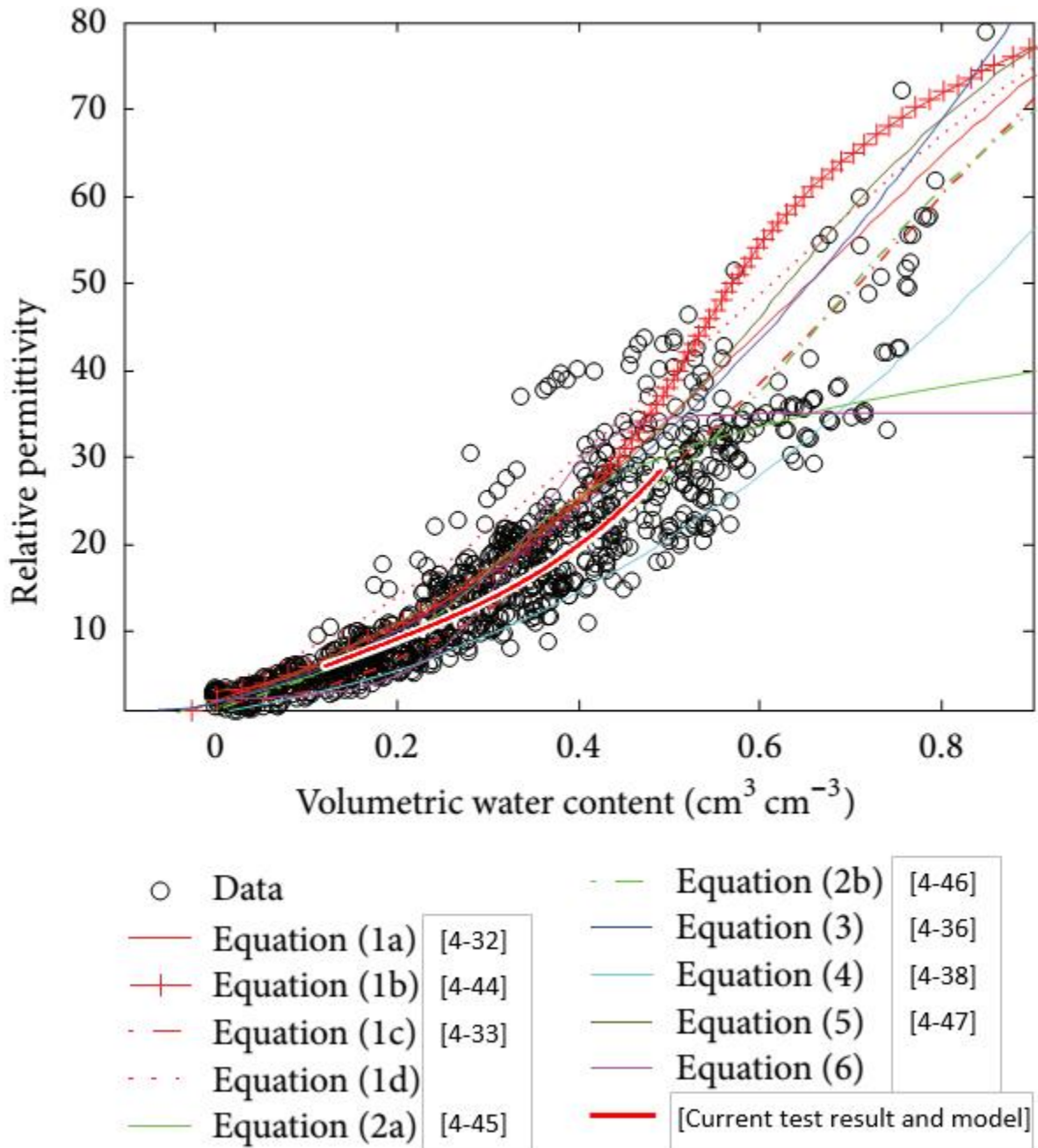


Figure 8-7: Comparison between experimental data/model and secondary data and models

8.4 SIGNAL AMPLITUDE AND ATTENUATION

The amplitude of an electromagnetic wave at a distance x and time t as it travels through a medium has been explained with Equation 4-18 in Chapter 4. The signal amplitude and phase depends on the attenuation coefficient, k_I , and the phase coefficient, k_R . For all data produced through this study, $\varepsilon''/\varepsilon'$ (or $\varepsilon_m''/\varepsilon_m'$) was found to be much less than 1 for antenna frequencies 50 MHz and

above (or 20 MHz and above for most of the test), that is, the soil medium was slightly conducting. This implies the simplified equations for k_I and k_R , that is Equations 4-23 and 4-24, can be used in place of their full form if frequency of the survey antenna is 50 MHz and above. It can be seen from Equations 4-24 that, the material/ohmic attenuation coefficient does not depend on the frequency of GPR antennae used for the survey. However, both the full and simplified forms of the equation will be used for computations in this chapter to show their similarities. Figures 8-8 and 8-9 show comparisons of material attenuation variations between the full and simplified attenuation equations for GPR antenna frequencies from 1 to 2500 MHz. Material attenuation coefficients plotted in Figures 8-8 and 8-9 were computed from average soil properties up to 4 ft. depth recorded for Dataset II (dielectric constant is 26.73, conductivity is 16.85 mS/m). As shown in the figures, the simplified equation gives a constant attenuation coefficient, which is equal to that of the full form for all antenna frequencies above 50 MHz.

Table 8-4 shows material attenuation values for the three antenna frequencies used for field testing in this study. The table shows material attenuation coefficients associated with the soil properties recorded for the GPR datasets presented in Chapter 7. As shown in the table, using the simplified/constant attenuation expression is accurate, with average errors of only 0.050%, 0.013%, and 0.002% for the 200 MHz, 400 MHz, and 900 MHz antennae respectively. An error of less than 5% in the estimation of k_I is acceptable for field computations.

Table 8-4: Material attenuation values for the GPR datasets

Depth up to (ft.)	Dataset Number	Cond. (mS/m)	Diel. ϵ	Material Attenuation, k_I (rad/m)				Percentage Error (%)		
				Full Equation			Simplified (For all Frequencies)	[(Simplified-Full)/Full]x100		
				200 MHz	400 MHz	900 MHz		200 MHz	400 MHz	900 MHz
2	I	10.94	13.42	0.5622	0.5624	0.5625	0.5625	0.067	0.017	0.003
	II	17.08	26.77	0.6216	0.6218	0.6218	0.6218	0.041	0.010	0.002
	III	12.47	16.60	0.5762	0.5764	0.5765	0.5765	0.057	0.014	0.003
3	I	11.43	15.09	0.5539	0.5542	0.5542	0.5543	0.058	0.014	0.003
	II	16.97	26.75	0.6178	0.6180	0.6180	0.6181	0.041	0.010	0.002
	III	12.86	18.12	0.5688	0.5690	0.5691	0.5691	0.051	0.013	0.003
4	I	11.92	16.76	0.5482	0.5484	0.5484	0.5485	0.051	0.013	0.003
	II	16.85	26.73	0.6137	0.6138	0.6139	0.6139	0.040	0.010	0.002
	III	13.25	19.69	0.5622	0.5624	0.5625	0.5625	0.046	0.011	0.002

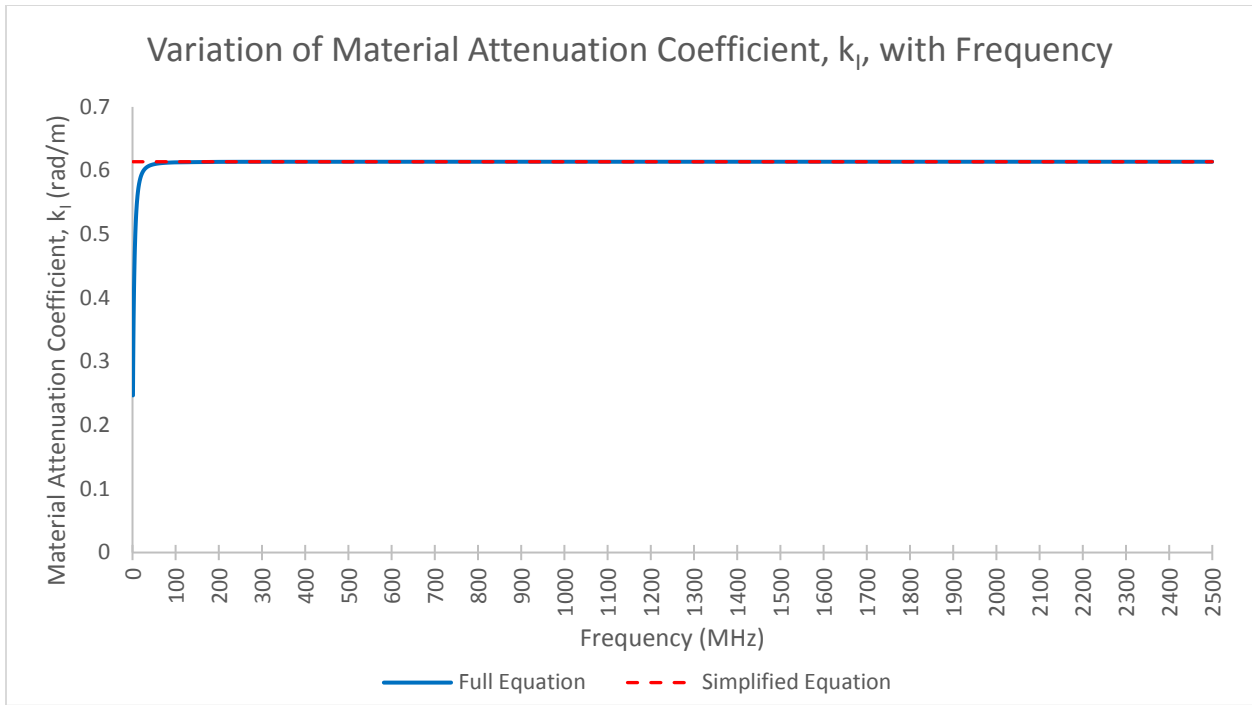


Figure 8-8: Variation of material attenuation coefficient with antenna frequency

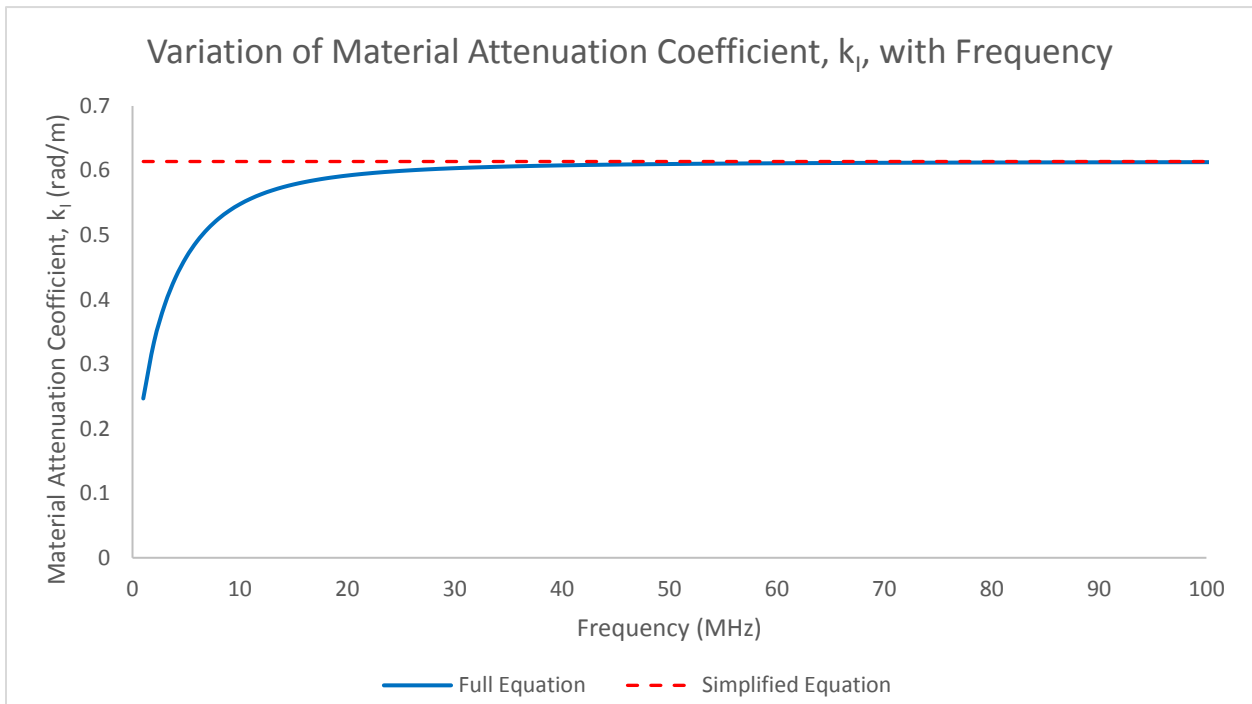


Figure 8-9: Variation of material attenuation coefficient with lower antenna frequencies

The results in Figures 8-8, 8-9, and Table 8-4 indicates that material/ohmic attenuation genially does not increase with antenna frequency in most GPR applications as commonly implied in literature.

Contrary to ohmic attenuation (k_I), scattering attenuation (k_{sca}) associated with inhomogeneity in the soil medium or clutter from subsurface objects such as gravels was found to increase with increasing antenna frequency. This means increase of total attenuation (k_T) with antenna frequency is controlled by scattering attenuation of the medium. Table 8-6 shows detailed attenuation components (including scattering due to air pockets and gravels, as well as material/ohmic attenuation) associated with the three antennae used for GPR testing in this study. The GPR signal attenuations shown in Table 8-5 were based on the average soil properties up to 4 ft. depth recorded for Dataset II. These soil properties, together with the dielectric properties of gravel and air used in this computation are summarized in Table 8-5. Scattering attenuation due to presence of air pockets and gravels in the soil were computed using “PyMieScatt” (Sumlin et al. 2018), an implementation of Equations 8-1 through 8-7 (Bohren and Huffmanin 1940, Annan 2009, Frezza et al. 2017), in an open source Python Mie Scattering module.

Figure 8-10 shows a plot of the variation of the different components of total attenuation computed in this study for antenna frequencies 1 MHz to 2.5 GHz.

Table 8-5: Material properties for scattering attenuation computation

Material Name	Dielectric Constant, ϵ	Conductivity (mS/m)	Particle Diameter (mm)
Air	1.00	0.00	8
Gravels	5.25	0.0001	20
Soil Medium	26.73	16.85	NA

Table 8-6: Components of total signal attenuation

Antenna Frequency	Scattering Attenuation			Material Attenuation, k_I or (M)	Total Attenuation, $k_T = k_I + k_{sca}$
	Air Pockets, (A)	Gravels, (G)	Combined, $k_{sca} = (A+G)$		
200 MHz	0.040318	0.125452	0.165770	0.613665	0.779436
400 MHz	0.288914	0.396081	0.684996	0.613850	1.298846
900 MHz	1.099720	0.453330	1.553050	0.613899	2.166949

$$k_{sca} = \frac{NC_{sca}}{2} \quad (8-1)$$

where k_{sca} is the scattering attenuation

N is the number of particles per unit volume

C_{sca} is the scattering cross section of scatter particles

$$C_{sca} = Ca^6 f^4 = \frac{2\pi}{k^2} \sum_{n=1}^{\infty} (2n+1)(|a_n|^2 + |b_n|^2) \quad (8-2)$$

$$= \pi a^2 \frac{2}{x^2} \sum_{n=1}^{\infty} (2n+1)(|a_n|^2 + |b_n|^2) \quad (8-3)$$

$$x = ka = \frac{2\pi Na}{\lambda_v} = \frac{2\pi a}{\lambda} \quad (8-4)$$

$$a_n = \frac{\mu m^2 j_n(mx) [x j_n(x)]' - \mu_1 j_n(x) [mx j_n(mx)]'}{\mu m^2 j_n(mx) [x h_n^{(1)}(x)]' - \mu_1 h_n^{(1)}(x) [mx j_n(mx)]'} \quad (8-5)$$

$$b_n = \frac{\mu_1 j_n(mx) [x j_n(x)]' - \mu j_n(x) [mx j_n(mx)]'}{\mu_1 j_n(mx) [x h_n^{(1)}(x)]' - \mu h_n^{(1)}(x) [mx j_n(mx)]'} \quad (8-6)$$

$$m = \frac{k_1}{k} = \frac{N_1}{N} \quad (8-7)$$

where

C is a constant

a is the radius of the scattering particle

f is the frequency of the electromagnetic wave

k is the wave number

N, N_1 are the refractive indices of the soil medium and particle respectively

λ_v, λ is the wavelength of the electromagnetic wave in vacuum and in the soil medium respectively

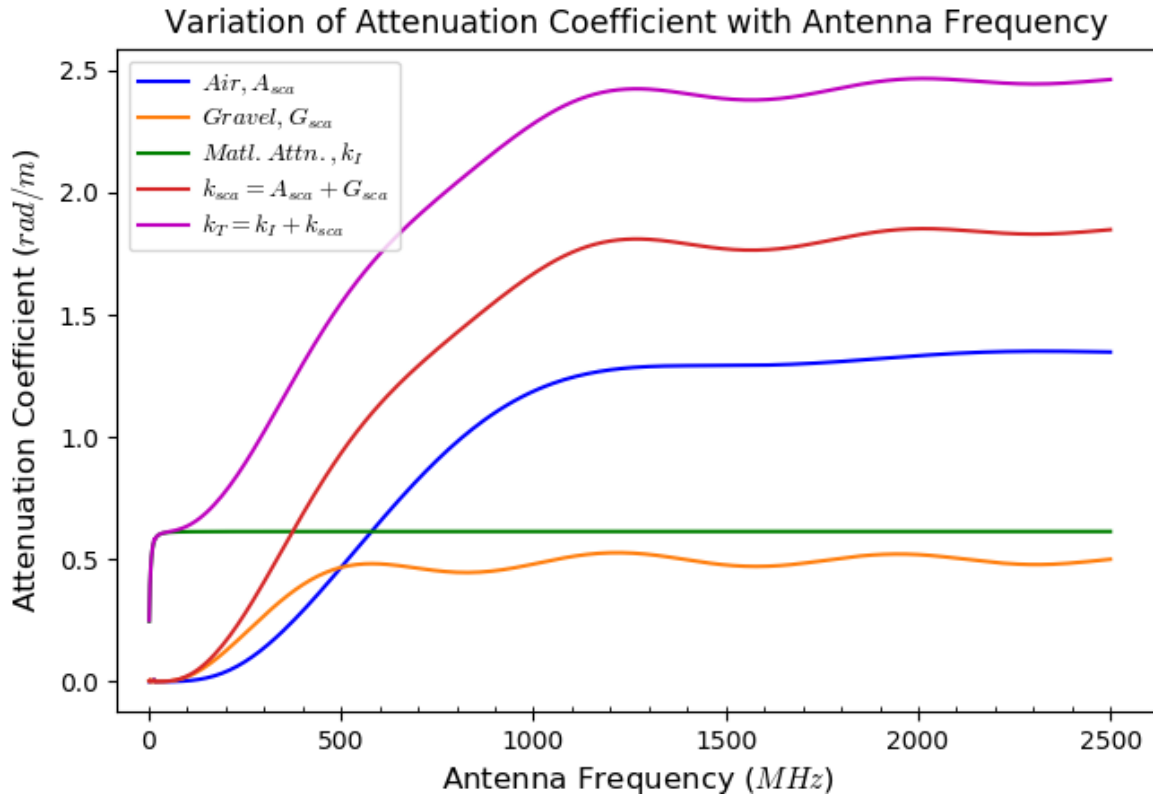


Figure 8-10: Variation of components of attenuation with antenna frequency

As shown in Table 8-6, the total GPR signal attenuation increases with antenna frequency, which will result in less returned signal amplitude from subsurface objects for higher frequency antennae. A plot of the remaining signal amplitude (%) as the wave travels through the soil is shown in Figure 8-11 for the three antenna frequencies used for the experimental work in this study (200, 400, and 900 MHz). The total attenuation coefficients in Table 8-6 and Equation 4-18 were used in computing the remaining signal amplitude. For two way travel of radar wave to the buried pipe and back, the reflection coefficient on top of the pipe is assumed to be 1.0 in this computation. Table 8-7 summarized the remaining signal amplitude for a two way travel to and from a pipe buried at 4 ft. depth in this study based on the total attenuation coefficients in Table 8-6. For some of the other field tests, the soil properties will result in higher attenuation coefficients and hence lower remaining signal amplitude after the two way travel.

The results in Figure 8-11 and Table 8-7 (together with different power output of the different antennae) explains why the 200 MHz radar antenna was able to detect the buried pipes at all the

depths studied while the 400 MHz and 900 MHz antennae were not successful in locating the buried pipes.

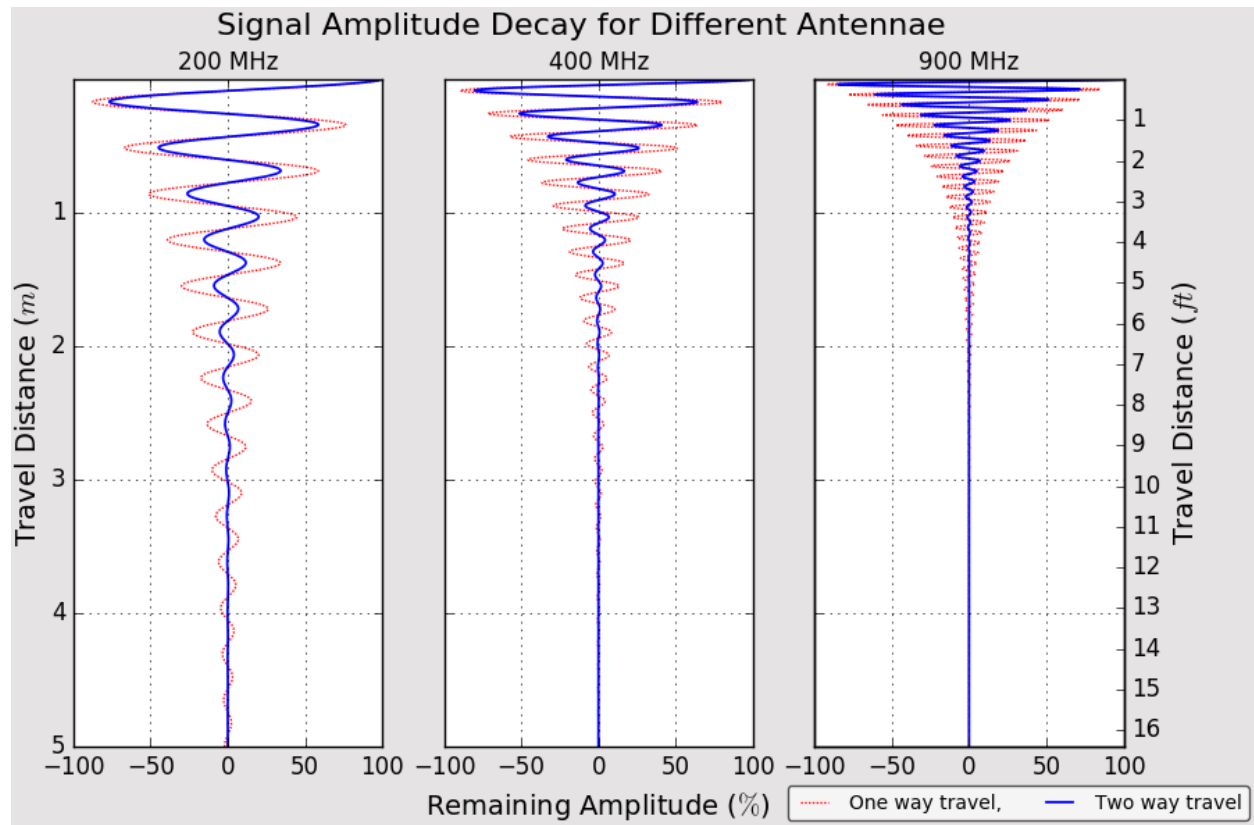


Figure 8-11: Decay of signal amplitude with travel distance

Table 8-7: Remaining signal amplitude after two way travel to 4 ft. depth

Antenna Frequency	Remaining Signal Amplitude for Two Way Travel to 4' (%)
200 MHz	14.96
400 MHz	1.21
900 MHz	0.51

8.5 ANTENNA PERFORMANCE AND PENETRATION DEPTH

To help evaluate the performance of the different antennae used for this study in different soil properties, the total attenuation coefficient (k_T) was computed for five different soil types (based on soil moisture content and composition). The attenuation coefficients will also help estimate the penetration depths of the various antennae. Total attenuation coefficients were computed for the

three datasets presented in Chapter 7, together with coefficients for dry clay soil and dry sandy soil. The dry clay soil is the same soil in which the pipes were buried; the soil dielectric properties were measured after a block of the soil was allowed to dry in normal laboratory atmosphere. The dry clay and dry sand represent the type of soil medium in which the maximum penetration depths stated for each antenna are expected to be achieved. Variation of attenuation coefficient, k_T , for the different soil types is presented in Figure 8-12. As evident in Figure 8-12, the dry clay soil and dry sand have very little attenuation coefficients compared to the wet clay soils (Datasets I through III).

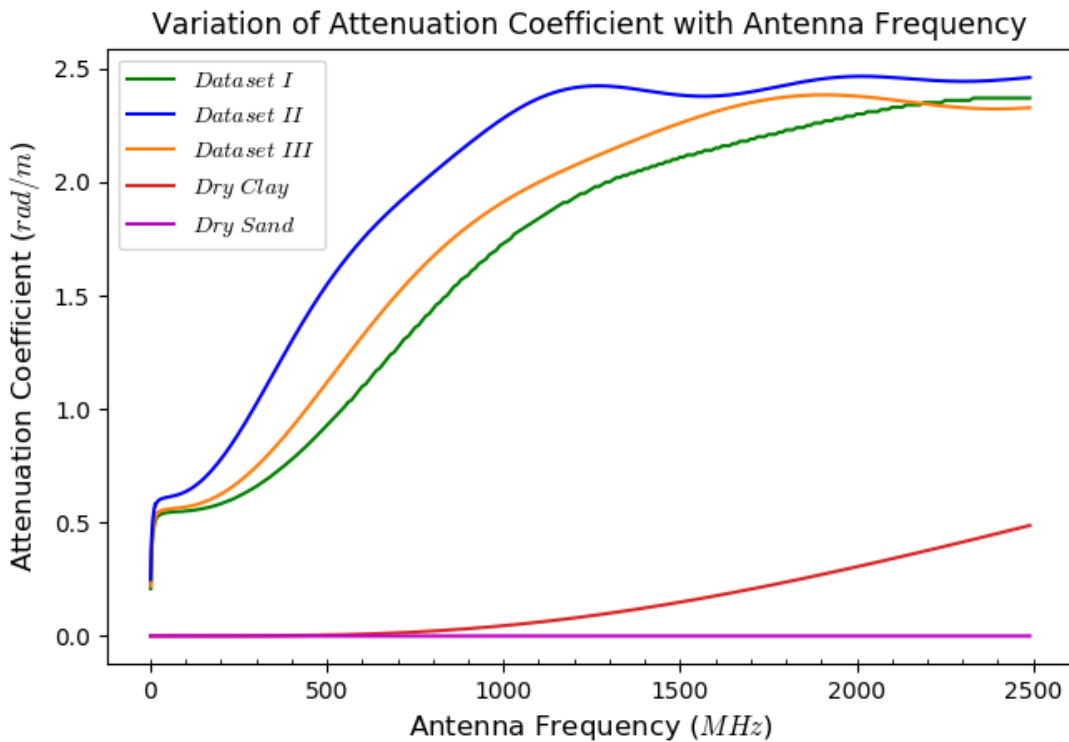


Figure 8-12: Variation of attenuation coefficient for different soil types

Variation of skin depth, d_p , across antenna frequencies for soils in the three datasets presented is shown in Figure 8-13. The skin depth, which is the distance a plane wave has to travel (one way travel) for its amplitude to reduce to 37%, decreases with increasing antenna frequency, and gives an indication of how each antenna performs with respect to depth. The skin depths shown in Figure 8-13 are based on the total signal attenuation, k_T .

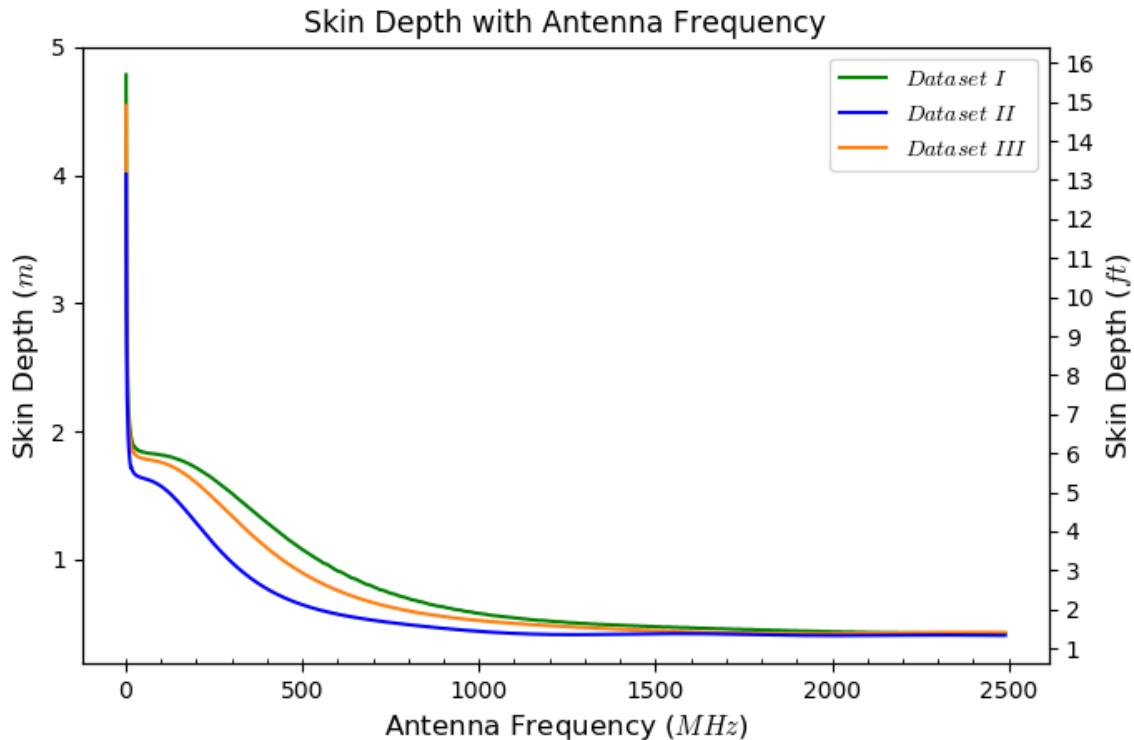


Figure 8-13: Variation of skin depth with antenna frequency for different soil types

The maximum penetration depths for the three antenna frequencies used in this study were estimated for four different soil types and plotted as shown in Figure 8-14. The soil types evaluated in the penetration depth estimation include the wet clay soils in Datasets II and I (Clay soil A and Clay soil B), dry clay soil (Clay soil C) and dry sandy soil (Sandy Soil). To estimate the maximum penetration depths for antennae in different soil types, the attenuation coefficients in Figure 8-12 and Equation 4-18 in Chapter 4 were used. The estimated penetration depth takes into consideration the two way travel time/distance of radar waves from the transmitting antenna to a target and be reflected back to the receiving antenna. This estimation of depth also considered geometric spreading losses (also called geometric attenuation) of the radar wave as it travel from the transmitter into the subsurface.

The maximum penetration depths shown in Figure 8-14 are also the maximum depths at which buried pipes wrapped with carbon fabric (strips or full wraps) are expected to be detectable using GPR. As shown in Figure 8-14, the maximum penetration depth for each antenna decreases with increasing electrical conductivity and dielectric constant of the soil (or decreases with increasing soil moisture content).

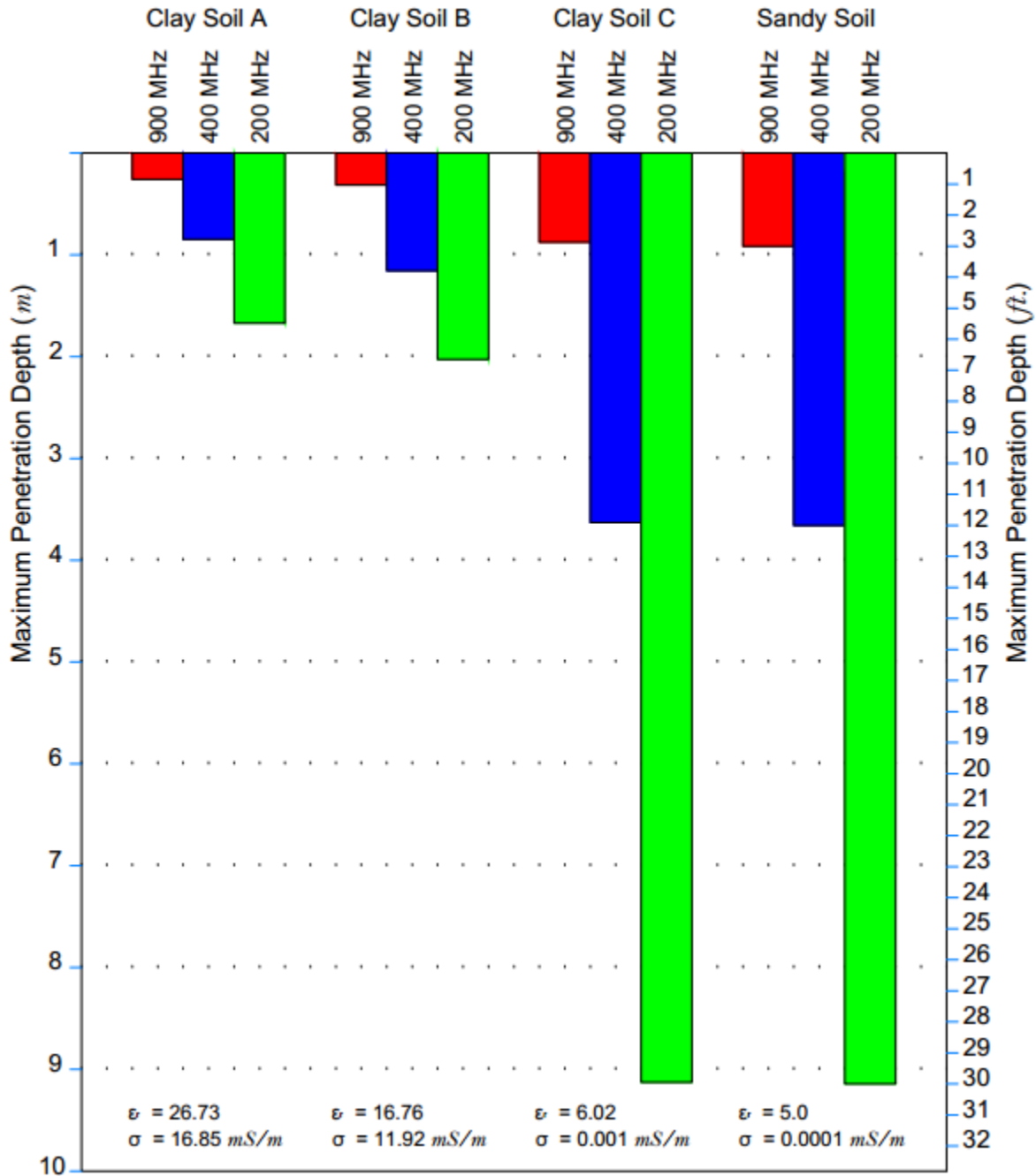


Figure 8-14: Estimated penetration depths for antennae in different soil types

From Figure 8-14, the 200 MHz antenna is expected to penetrate up to 5.5 ft. while the 400 MHz one can only penetrate up to 2.8 ft., with the 900 MHz antenna penetrating even lower at just 0.8 ft. in Clay soil A (or Dataset II with electrical conductivity and dielectric constant of 16.85 mS/m and 26.73 respectively). The penetration depths increase for Clay Soil B (Dataset I) when the soil electrical conductivity and dielectric constant decrease to 11.92 mS/m and 16.76 respectively. In

Clay soil B, penetration depths for the 200 MHz and 900 MHz antenna increase to 6.7 ft. and 1.0 ft. respectively. The penetration depths for dry clay soil and dry sand (Clay Soil C and Sandy Soil) are about the same, and the depth for each of the three antennae frequencies used in this study is equal to the maximum penetration depth specified for that antenna.

These estimated penetration depths for different soil types further explains why the 200 MHz radar antenna was able to detect the buried pipes in different soil moisture contents at all the depths studied while the 400 MHz and 900 MHz antennae were not successful in locating the buried pipes. Considering Clay Soil A and Clay Soil B (which represents soil properties for datasets in Chapter 7), penetration depths for 200 MHz antenna are all more than 4 ft.; making it possible for this antenna to detect the buried pipes at all the depths investigated. Penetration depths for the 400 MHz antenna in the same soils are more than 2 ft. but less than 4 ft., while that for the 900 MHz antenna are 1 ft. and below. Hence the 400 MHz antenna was able to locate some of the pipes buried at 2 ft. depth (though with weak reflected signal amplitude), but the 900 MHz antenna could not detect buried pipes at any of the depths.

8.6 WAVE VELOCITY AND WAVELENGTH

Unlike the ohmic attenuation which is almost constant for antenna frequencies above 50 MHz, the phase coefficient and wavelength are dependent on frequency. Higher phase coefficients and lower wavelengths are associated with high frequency antennae and vice versa. Thus, though high frequency antennae are not able to penetrate deep in soil mediums because of signal attenuation, their smaller wavelengths make them better at detecting smaller objects at reasonable depths. Lower frequency antennae on the other hand can penetrate deeper but might not be able to locate smaller subsurface objects. The resolution of an antenna is generally approximated as $\lambda/4$, meaning objects smaller than a quarter of a wavelength might not be detected by an antenna. Table 8-8 shows the phase coefficient for the three antennae used for GPR testing in this study, together with the wavelength in air and in the soil. Wavelength for the 200 MHz antenna is (which is the antenna predominantly used in this study) about 1 ft. on average for the three datasets presented, a quarter of this wavelength is 3 inches. This explains why the 200 MHz antenna did not perform well on the 3 inch diameter pipes buried at 2 ft. depths as compared to the bigger diameter pipes at different depths.

Table 8-8: Phase coefficient and wavelength of the antennae used for GPR test

Dataset Number	Antenna Frequency	Phase Coefficient, k_R (Np/m)		Wavelength, λ (m)		Wavelength, λ (ft.)	
		In Air	In Soil	In Air	In Soil	In Air	In Soil
I	200 MHz	4.19	17.17	1.499	0.366	4.918	1.201
	400 MHz	8.38	34.32	0.749	0.183	2.459	0.601
	900 MHz	18.86	77.22	0.333	0.081	1.093	0.267
II	200 MHz	4.19	21.68	1.499	0.290	4.918	0.951
	400 MHz	8.38	43.35	0.749	0.145	2.459	0.476
	900 MHz	18.86	97.52	0.333	0.064	1.093	0.211
III	200 MHz	4.19	18.61	1.499	0.338	4.918	1.108
	400 MHz	8.38	37.20	0.749	0.169	2.459	0.554
	900 MHz	18.86	83.70	0.333	0.075	1.093	0.246

8.7 CONCLUSIONS

Dielectric models for estimating soil dielectric constant from volumetric water content measurements and vice versa have been presented in this chapter. Some of the popular models have been evaluated with respect to the experimental data. From all the models evaluated, the Topp et al. (1980) model for organic soils and Roth et al. (1992) model for organic soils were found to be the closest to the experimental data for the forward and inverse dielectric models respectively. Other models that fit the experimental data better were generated in this study.

Numerical computations in this chapter also shows that, material/ohmic attenuation of GPR signal is constant for antenna frequencies above 50 MHz. and antenna frequencies below 50 MHz experience a sharp vertical drop in the material attenuation. Scattering attenuation due to inhomogeneity and subsurface clutter was however found to be increasing with antenna frequency, accounting for the increase of total signal attenuation with increase in antenna frequency.

CHAPTER 9

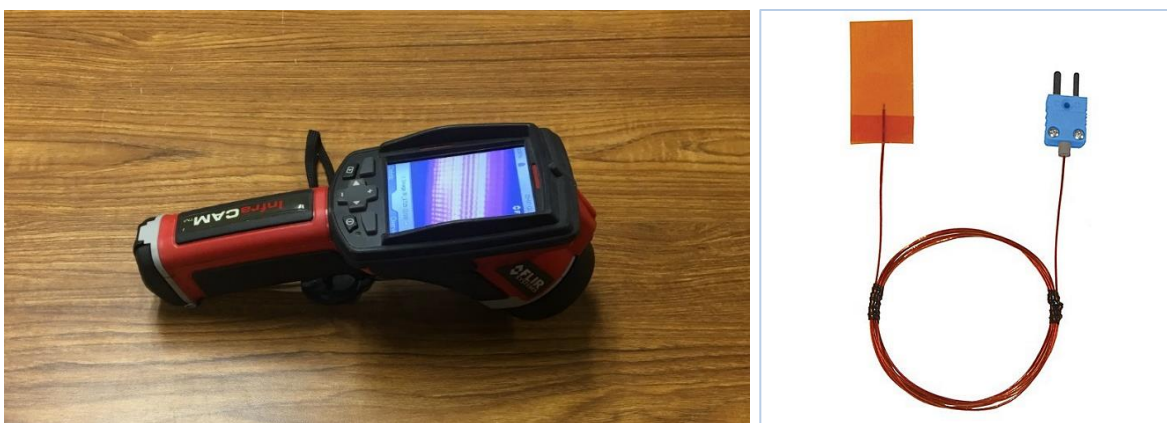
INFRARED THERMOGRAPHY TESTING AND RESULTS

9.1 INTRODUCTION

The feasibility of detecting subsurface pipelines transporting hot fluid using Infrared Thermography (IRT) was explored in this research. Since petroleum products are hot in the initial part of the pipeline (within about 5 miles from the source of production wells), the IRT technique offers some promise for detecting such pipeline sections. Furthermore, there is the potential for detecting pipelines carrying other hot fluids such as hot water or steam. This chapter provides the test set up, testing and results from laboratory tests in addition to field testing results.

9.2 IRT TEST EQUIPMENT (CAMERA AND THERMOCOUPLES)

InfraCAM SD thermal imager (Figure 9-1a) manufactured by FLIR Systems, Inc. was used for the IRT testing. This is a portable handheld infrared camera with a spectral range of 7.5 to 13 μ m, a 0.12°C thermal sensitivity at 25°C, and $\pm 2^\circ\text{C}$ accuracy.



(a) FLIR InfraCAM SD camera

(b) Digi-Sense type-T thermocouple
(Source: Novatech USA)

Figure 9-1: FLIR InfraCAM SD camera and type-T thermocouple

The Digi-Sense type-T thermocouple probe (WD-08519-54, shown in Figure 9-1b) was used for contact temperature measurements. A 1"x2" high temperature self-adhesive tape was used to attach the thermocouple to the pipe surface during testing. The thermocouple has a temperature range of -200°C to 260°C and a $\pm 1.0^\circ\text{C}$ accuracy for readings above 0°C. The thermocouples were read

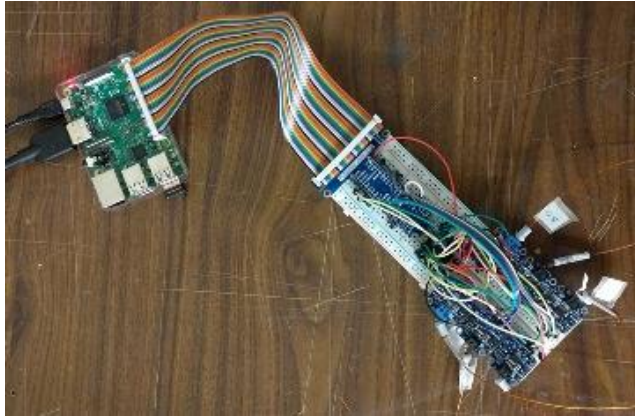
using an automated reader/recorder (Figure 9-2a) that was built to enable continuous collection of temperature data on the buried pipe throughout the IRT testing period. Ambient temperature during the test was recorded using Thermo Recorder TR-72Ui (Figure 9-2b).

9.3 EXPERIMENTAL SET-UP FOR IRT TESTING

An insulated wooden box with an internal dimension of 24"x24"x22" (after insulation) was built for the IRT testing of buried CFRP pipe carrying hot liquid. The insulation in the box (with R-Value of 10) will ensure that heat detection (if any) will only be as a result of heat propagation from the hot pipe through the soil to the soil surface. Also, the insulation ensures no heat leakage out of the box, which will help in heat transfer computations to extrapolate the surface temperature for different soil depths. Figures 9-3 and 9-4 show the wooden box and capped 3" diameter CFRP pipe respectively. The CFRP pipe, fitted with aluminum caps was buried in the insulated box with hot water circulated through the pipe.

The pipe was buried in the box filled with a mixture of gravel, sand, and organic soil in the ratio of 1:1:2, and having a moisture content of 14%. Three inch (3") depth of the soil mixture was placed at the bottom of the insulated box before the pipe was inserted. Soil cover above the pipe was 14", and 2" space was left at the top of the box as shown in Figure 9-5. The box was left open at the top during the experiments to simulate field conditions where the soil surface is exposed.

Five thermocouples were installed on the surface of the CFRP pipe before burying (3 thermocouples at the top and 2 at the bottom surface of the pipe as shown in Figure 9-4). Another thermocouple was placed at the surface of soil in the box to measure soil surface temperature. The 6 thermocouples were connected to the automated recorder to enable continuous data collection. Hot water (at a temperature of 95°C) was circulated through the buried pipe, while the temperature changes at the surface of the buried pipe and the soil surface were recorded over a period of 10 days. Soil surface temperature was also recorded using infrared thermography (IRT) throughout the testing period. It should be noted that, water circulation was started with the water initially at room temperature (21.6°C), and it took 3 hours for the water temperature to rise to the 95°C level. Also, the hot water did not fully fill the pipe to the top due to entrapped air pocket, hence top portion of the pipe was colder than the bottom portion by about 4.5°C because of the trapped air. The IRT test setup is shown in Figure 9-5.



(a)



(b)

Figure 9-2: (a) Automated thermocouple reader and (b) Thermo Recorder



(a)



(b)

Figure 9-3: Insulated wooden box used for IRT testing

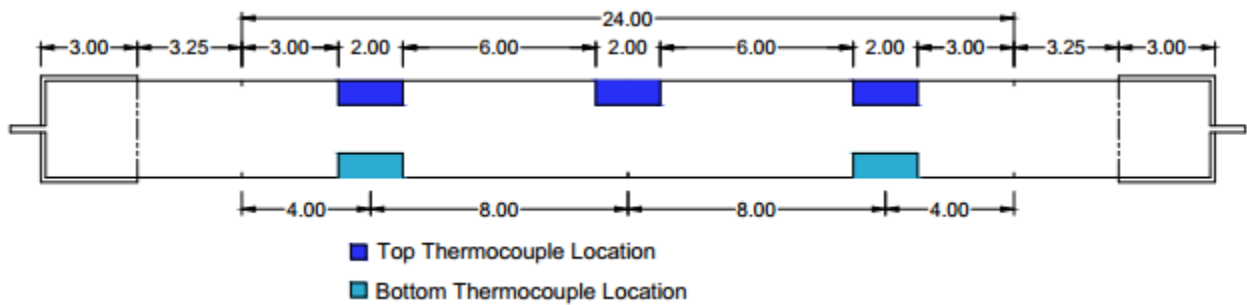


Figure 9-4: CFRP pipe for IRT testing (top), sketch showing thermocouple locations (bottom)

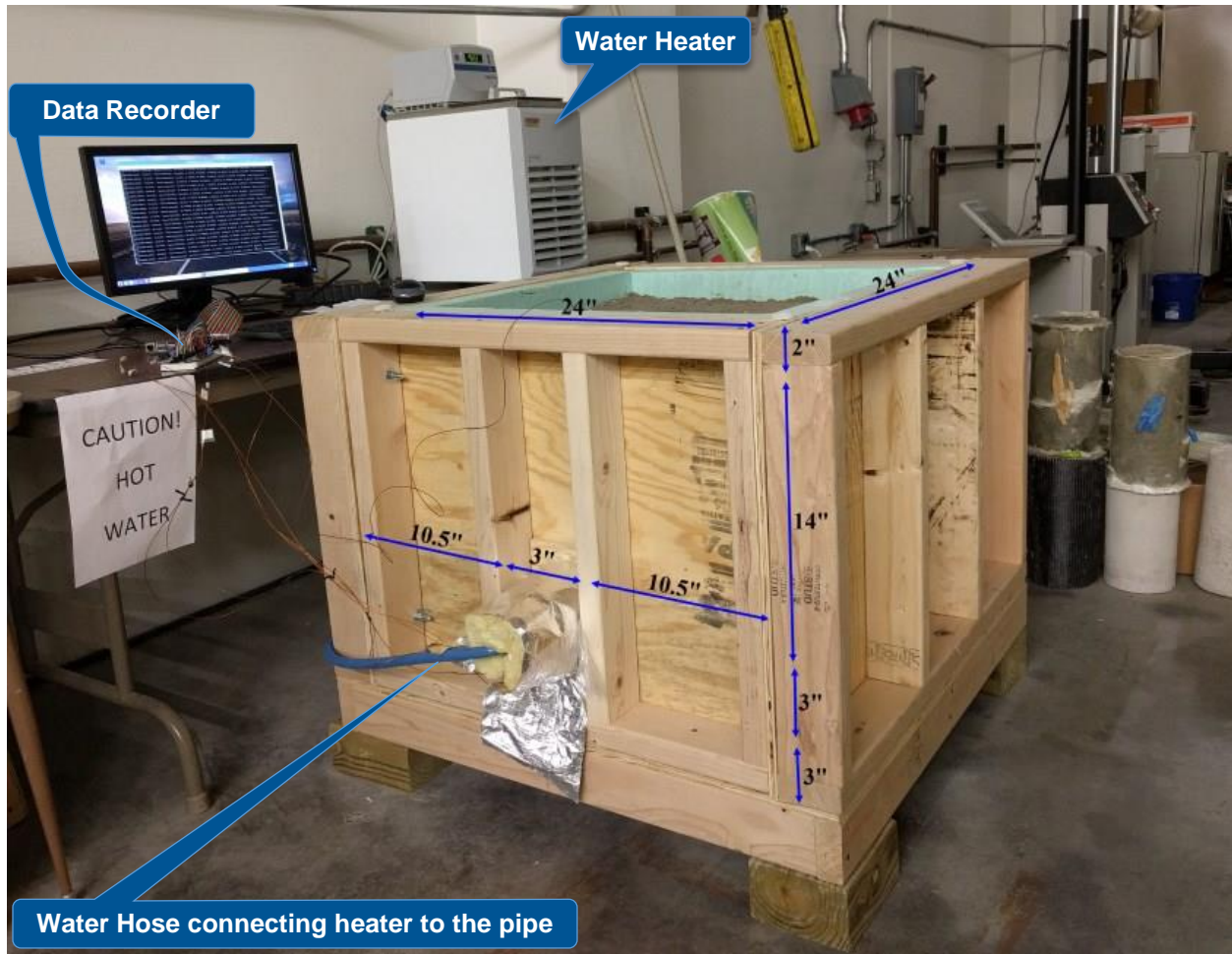


Figure 9-5: IRT test set-up

9.4 IRT TEST RESULTS

IRT testing was carried out to illustrate both the period when the pipeline is in operation and transporting hot fluids, and the period immediately following pipeline shut down or ceasing of pumping operations. Results from both testing phases are presented below.

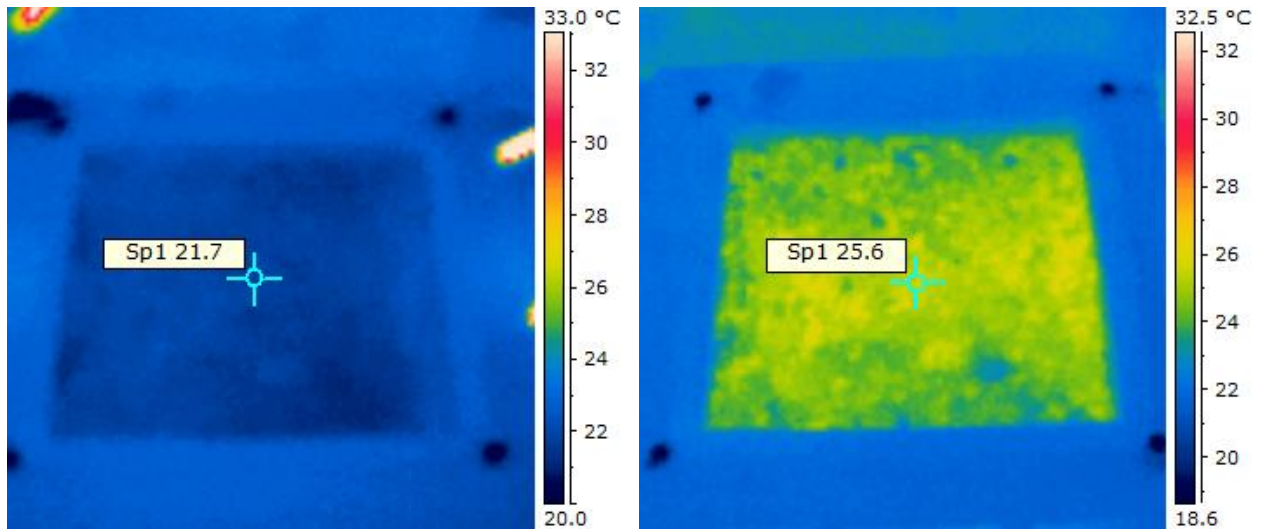
9.4.1 Pipe Operating /Heating Cycle

As stated previously, the IRT test was carried out over a period of 10 days where hot water at a temperature of 95°C was circulated through the buried 3" CFRP pipe. The temperature at the pipe and soil surfaces, and room/ambient temperatures were recorded over the testing period. Temperature at the soil surface had a sharper increase during the first 48 hours of testing, followed by a gradual increase up to the sixth day of testing. There was not much temperature increase

between the sixth and tenth days of testing. Figure 9-6 shows some of the IRT data at various stages of testing. Figures 9-7 and 9-8 show plots of temperature changes during the test period. Each test day starts at 8:00 am and ends at 7:59 am the following day. The regular fluctuations (jitter) in temperatures shown in Figures 9-7 and 9-8 are due to diurnal temperature changes between day and night. These diurnal changes are present in the laboratory data since the laboratory temperature was not regulated. Maximum daily temperatures recorded during the test occurred between 3:00 pm and 5:15 pm. The results (IRT curve in Figure 9-7) show approximately 14°C increase in surface temperature of the soil for this pipe carrying hot liquid, thus making it possible to detect such buried pipes using infrared thermography measurements at the soil surface. Infrared thermography readings at the soil surface were found to be about 2-3°C higher than the thermocouple readings at the same location. The difference in surface temperature readings can be attributed to the accuracies of the infrared camera and the thermocouple, which are $\pm 2^{\circ}\text{C}$ and $\pm 1.0^{\circ}\text{C}$ respectively.

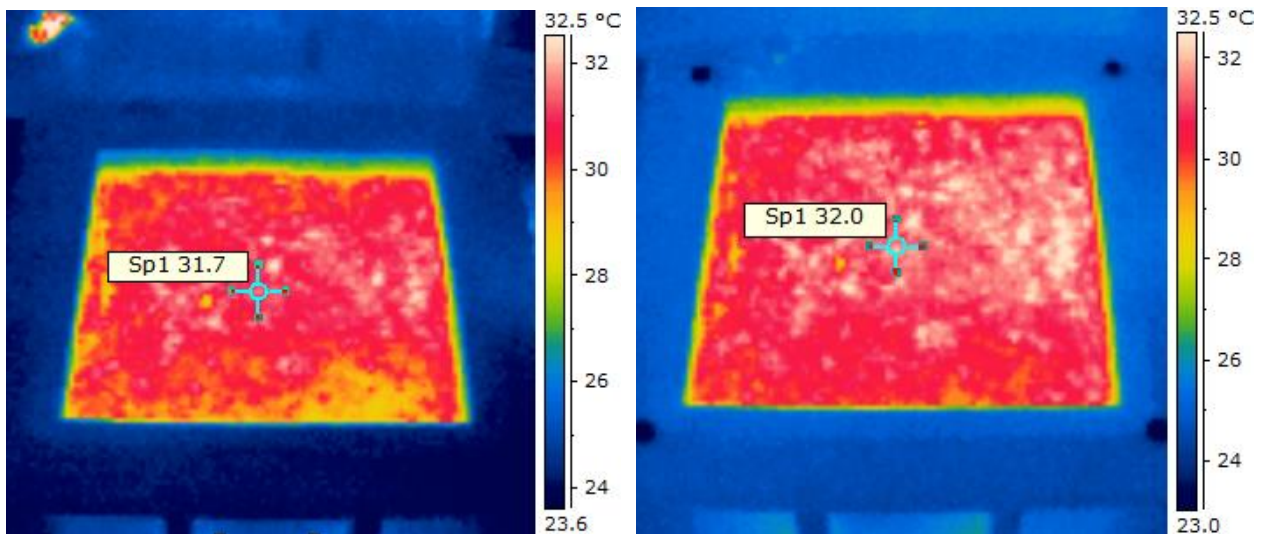
The following nomenclature is adopted to explain the IRT data in Figures 9-6 through 9-8:

- IRT** – Infrared thermography image/data/temperature reading at soil surface
- TSC** – Thermocouple reading taken at the center of the soil surface
- Amb** – Ambient/room temperature
- TSC-Amb** – Difference between TSC and Amb
- IRT-Amb** – Difference between IRT and Amb



(a) After 2.75 hours of heating

(b) After 24 hours of heating



(c) After 6 days of heating

(d) After 10 days of heating

Figure 9-6: Infrared thermography data at the soil surface at various stages of testing

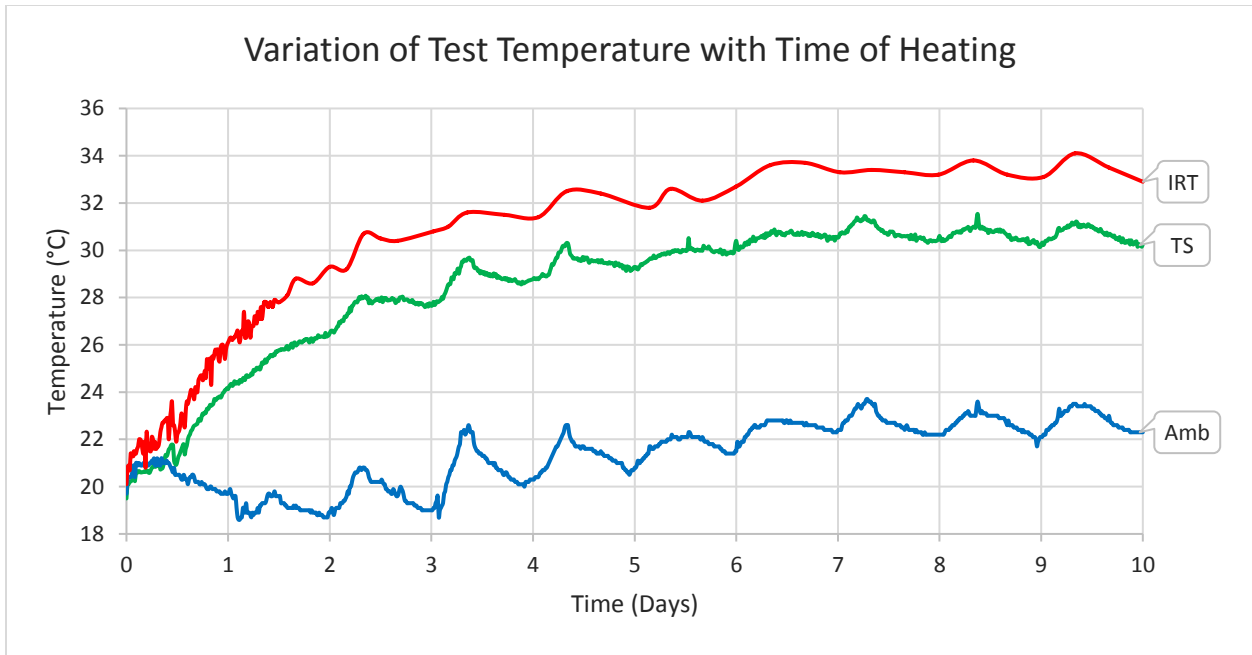


Figure 9-7: Variation of soil surface (TSC, IRT) and room (Amb) temperatures with time

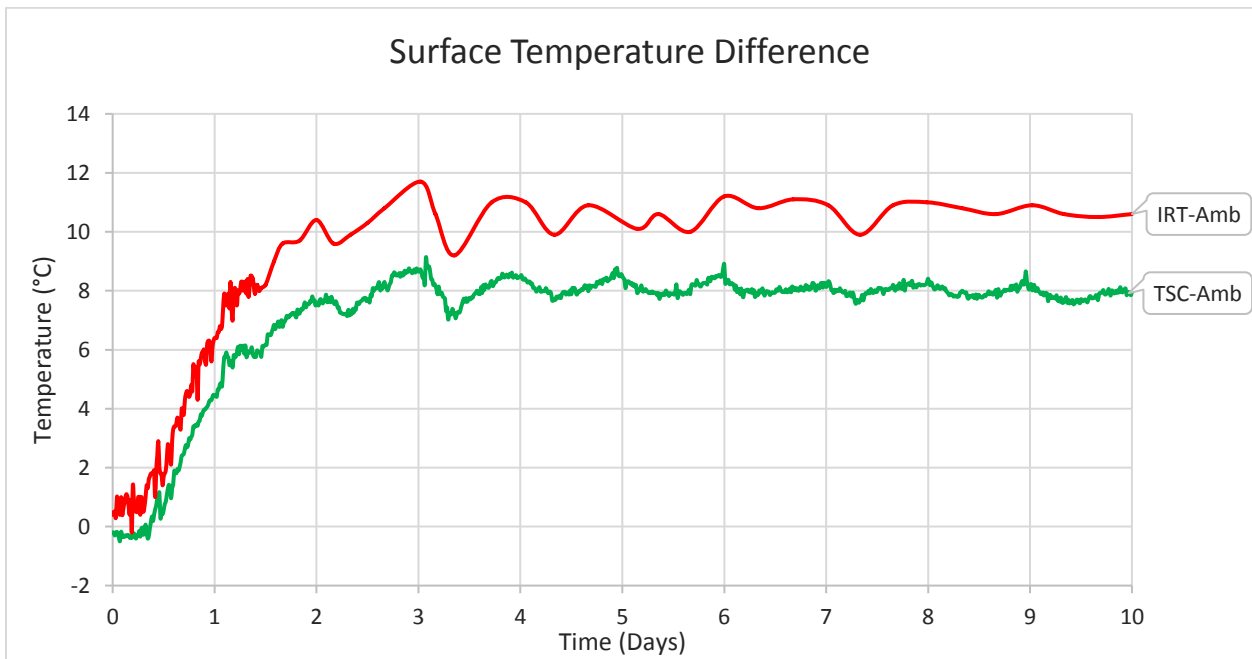


Figure 9-8: Soil surface temperature difference with time

The results show that, the 3" diameter CFRP pipe buried with 14" of soil cover and carrying 95°C of liquid can be detected at the ground surface using infrared thermography.

The experimental results were extrapolated using a one-dimensional heat transfer (conduction) formulation to estimate the depth at which the pipe will no longer be detectable using IRT. The heat transfer equation for one-dimensional heat conduction is given by Equation 9-1.

$$q_{net} = \frac{k}{d}(T_h - T_c) \quad (9-1)$$

where,

q_{net} = net heat flow through a unit area of a material per unit time (W/m²)

k = thermal conductivity of the medium (W/m/°C)

T_h = temperature of the hotter side (°C)

T_c = temperature of the colder side (°C)

d = thickness/depth of the medium (m)

$$q_{net} = \frac{k}{d}(\Delta T) \quad (9-2)$$

$$\Delta T = T_h - T_c$$

$$\Delta T = \frac{q_{net}}{k}(d) \quad (9-3)$$

Assuming q_{net}/k is constant, that is

$$\frac{q_{net}}{k} = \frac{\Delta T}{d} = \text{constant} \quad (9-4)$$

Thus given the same soil material with varying depths d_1 and d_2 ,

$$\Delta T_1 = \frac{q_{net}}{k}(d_1) \rightarrow \frac{q_{net}}{k} = \frac{\Delta T_1}{d_1}$$

$$\Delta T_2 = \frac{q_{net}}{k}(d_2) \rightarrow \frac{q_{net}}{k} = \frac{\Delta T_2}{d_2}$$

$$\frac{\Delta T_1}{d_1} = \frac{\Delta T_2}{d_2} \rightarrow \Delta T_2 = \frac{d_2 \cdot \Delta T_1}{d_1} \quad (9-5)$$

Thus, using d_1 and ΔT_1 from the experiment, ΔT_i can be estimated for any given depth, d_i , of soil cover over a buried pipe if thermal properties of the soil are the same as used in the experiment. The ratio q_{net}/k was assumed to be constant for the soil mixture during the computation. The experimental data at day 6 was used as a baseline for this computation because the system had reached a steady state by that time as illustrated by the almost constant temperature difference in Figure 9-8. All temperatures in this computation are from thermocouples readings:

$$q_{net}/k = \Delta T/d = \Delta T_1/d_1, \text{ assumed constant (and computed using the following data)}$$

T_h = Temperature at the surface of the buried pipe at day 6, measured to be 85.47°C

T_c = Temperature at the surface of the soil at day 6, measured to be 30.40°C

d = depth of soil cover over the pipe, 14"

Soil surface temperature difference (difference between soil surface temperature and room temperature or TSC-Amb) for different depths of soil cover were computed, sample computation results are shown in Table 9-1 and the result is plotted in Figure 9-9. Table 9-1 and Figure 9-9 also show the projected temperature difference using IRT (IRT-Amb), which is higher than TSC-Amb by 2.5°C at each data point. The plot in Figure 9-9 shows that, the same 3" CFRP pipe buried in the same soil medium and carrying a liquid at 95°C will be detectable using IRT, up to a depth of about 16.5"; with a temperature increase of about 1.6°C.

Table 9-1: Estimated variation of soil surface temperature with depth

Depth, d (in.)	ΔT (°C)	TSC (°C)	Amb (°C)	TSC-Amb (°C)	IRT (°C)	IRT-Amb (°C)
12.00	47.2	38.3	21.5	16.8	40.8	19.3
14.00	55.1	30.4	21.5	8.9	32.9	11.4
16.00	62.9	22.5	21.5	1.0	25.0	3.5
16.50	64.9	21.5	21.5	0.0	23.1	1.6
16.75	65.9	21.5	21.5	0.0	22.1	0.6
17.00	66.9	21.5	21.5	0.0	21.5	0.0
18.00	70.8	21.5	21.5	0.0	21.5	0.0

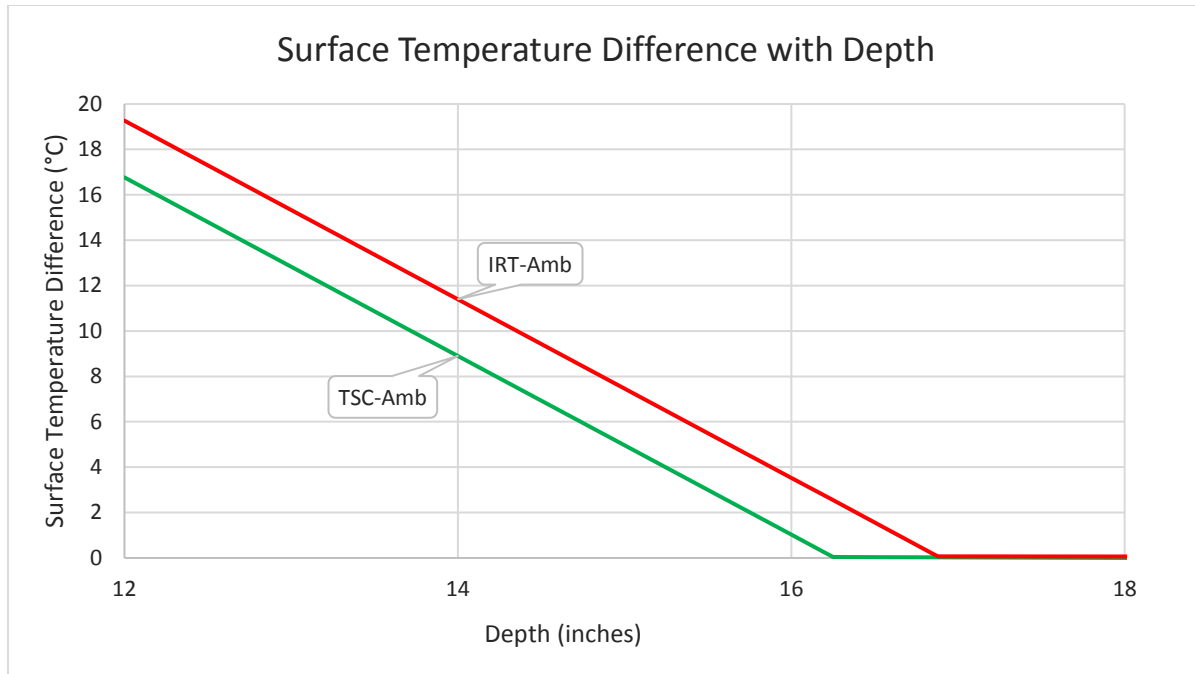


Figure 9-9: Difference between soil surface temperature and room temperature with depth

9.4.2 Pipe Cooling Cycle

There is a potential for a pipe transporting hot fluid to be located using IRT even after the pipe has been shut down, either for maintenance or to identify a problem. Thus determining how long it takes after the pipe has been shut down for the heat to dissipate and make the pipeline undetectable with IRT is important for inspection decision making. Cooling cycle for the 3" diameter CFRP pipe was monitored after pumping of hot water through it has been stopped.

Soil surface temperature (IRT and TSC) had a sharper decrease during the first four days of cooling (from day 10 to 14) as illustrated in Figure 9-10, with almost uniform daily room/ambient temperature. From the fourth to the eighth day (day 14 to 18), soil surface temperature remained constant with slight increase in ambient temperature, indicating a net decrease in soil temperature as shown in Figure 1-11. Both the soil surface temperature and ambient temperature decreased between the eighth and eleventh days of cooling (day 18 to 21), indicating a net uniform soil temperature. A plot of the soil surface temperature difference is given in Figure 9-11, showing a sharp temperature drop during first four days, a gently drop for the next four days of cooling, after which the soil temperature became almost constant/achieved steady state. Similar to the heating cycle, regular fluctuations in Figures 9-10 and 9-11 are due to diurnal temperature changes.

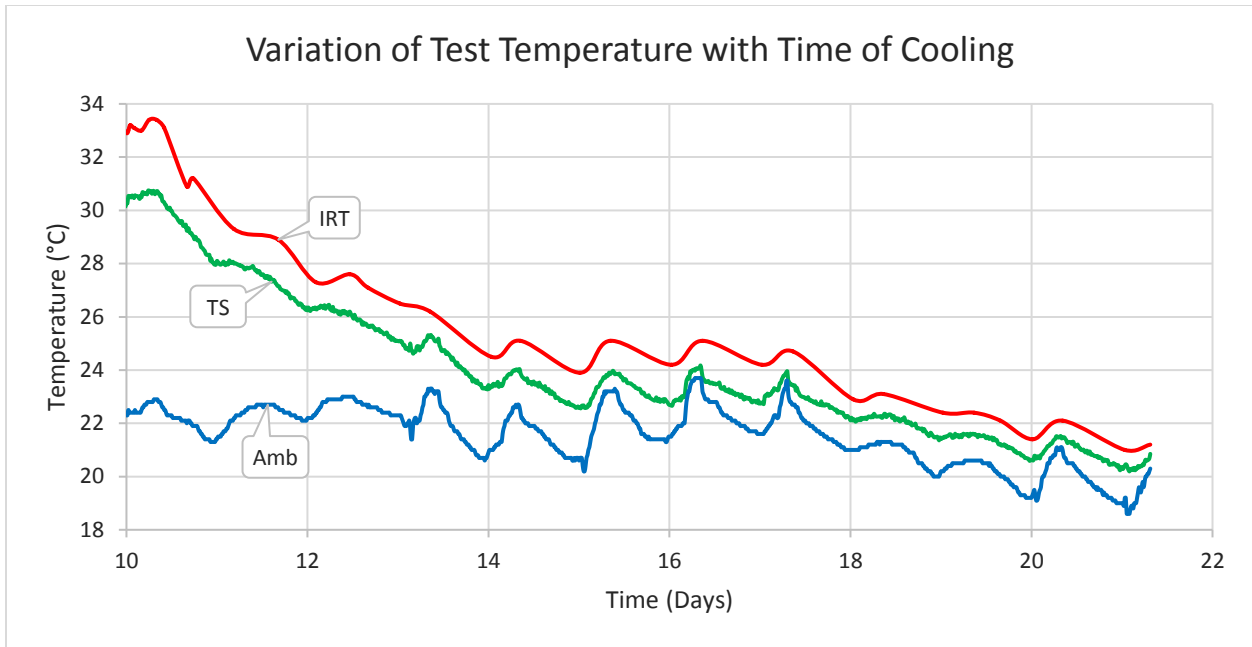


Figure 9-10: Variation of soil surface (TSC, IRT) and room (Amb) temperatures during cooling

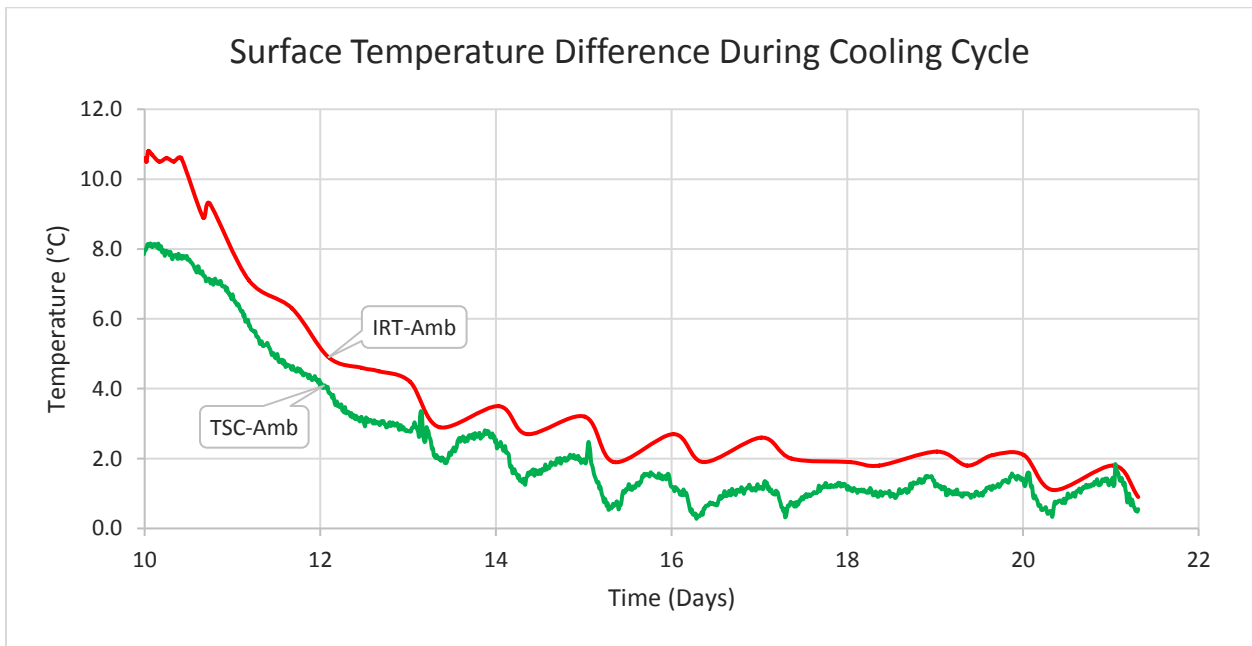


Figure 9-11: Soil surface temperature difference with time during cooling

The results in Figures 9-10 and 9-11 indicate that, the same 3" CFRP pipe in the same environmental conditions will be detectable using IRT during the first eight days after pumping of

hot fluid has been stopped. The heat will dissipate into the surrounding soil and the system will achieve a steady state after eight days, and the pipe will not be detectable using IRT.

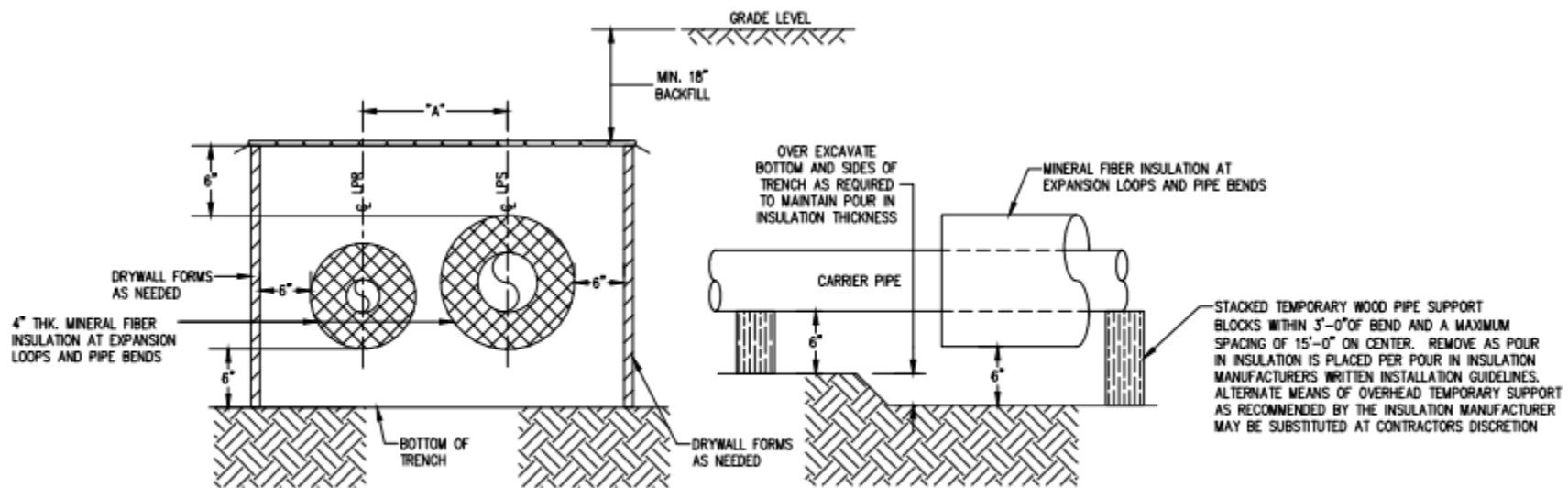
Additional plots from the laboratory IRT test, including variations in pipe inlet and outlet temperatures, variations in pipe top and bottom temperatures, and soil temperature changes for both the heating and cooling cycles are given in Appendix C.

9.5 TESTING OF FIELD PIPES

After investigating the potential for IRT detection of buried pipe transporting hot water in the laboratory, testing of buried pipe operating in the field and transporting steam was carried out to study how the technique performs in the field environment. This buried pipe is used by WVU Facilities Management for transporting high pressure steam for on campus heating. The field pipe to be tested is located near the Mineral Resources Building (MRB) on WVU campus (location shown in Figure 9-12). The pipe system consists of a 6" diameter high pressure steam (HPS) line and a 3" diameter condensate pumped (CP) line buried side-by-side in the same trench. The pipes had a minimum of 6" poured in insulation around them (4" mineral fiber insulation at bends and expansion loops, and additional 6" poured in insulation through the entire pipe length). Details of the piping system are shown in Figure 9-13 and Table 9-2.



Figure 9-12: Location of field IRT test pipe



DETAIL 3

NO SCALE

DRITHERM INSULATION SYSTEM EXPANSION LOOP AND BEND CUSHION INSULATION AND TEMPORARY PIPE SUPPORT

Figure 9-13: Field IRT test pipe installation details (CJD 2015)

Table 9-2: Field IRT test pipe parameters

Parameter	Value
Pipe Location/Test Site	MRB-PRT Track
Type of Fluid (e.g. water, steam, heated air, etc.)	Steam, Condensate
Water/Fluid Temperature	105 °C (221 °F)
Depth of Soil Cover over the Pipe	2.5' - 3'
Pipe Diameter ⁷	6", 3"
Pipe Material	Steel
Pipe Wall Thickness	0.280", 0.300"
Is the Pipe Insulated?	Yes ⁸ , Min 6" around pipes
Number of Pipes	Two pipes: 6" and 3" diameters
Date of Installation	2015

IRT testing on the buried steam pipe was carried out in three different weather conditions (tests were done in winter, spring, and summer seasons). Results from these tests are summarized in Figures 9-14 through 9-17. Figure 9-14 shows a comparison between a visible image and IRT image taken at the site, with the identified features labelled. Figure 9-15 show IRT images of the pipe taken from a distance of about 50 ft. from the pipe location in different weather conditions. For all IRT images in Figure 9-15, the buried pipe is the first horizontal linear feature from the bottom of the image (first horizontal hot path from the bottom) as illustrated in Figure 9-14. The buried pipe was easily detected using IRT in all weather conditions as shown in Figure 9-15. During IRT testing in the winter, the ground was covered with snow up to a depth of 3.75". The snow cover however did not hinder the performance of this technique for buried pipe detection since the buried hot pipe increased temperature of the snow over the pipe to 0.5°C compared to the surrounding snow covered soil which had a temperature of -8.7°C as shown in Figure 9-15(c). Soil surface temperature over the pipe during summer testing was measured to be 39°C, while temperature of the surrounding soil was measured to be 26°C.

⁷ 6" diameter schedule 40 steel pipe for steam and 3" diameter schedule 80 steel pipe for condensate

⁸ Pour in insulation with minimum thickness of 6" on all sides of the pipes

Figure 9-16 shows IRT image of the pipe taken from close distance (about 5 ft. from the pipe) in different weather conditions. Plots of temperature distribution across the buried pipe (from the bottom to the top of each IRT scan in Figure 9-16) in each season are shown in Figure 9-17. It can be observed from Figure 9-17 that, the buried pipe increased the soil surface temperature by 9.5°C to 20°C compared to the surrounding soil, thereby making it possible to detect this buried insulated pipe transporting high pressure steam.

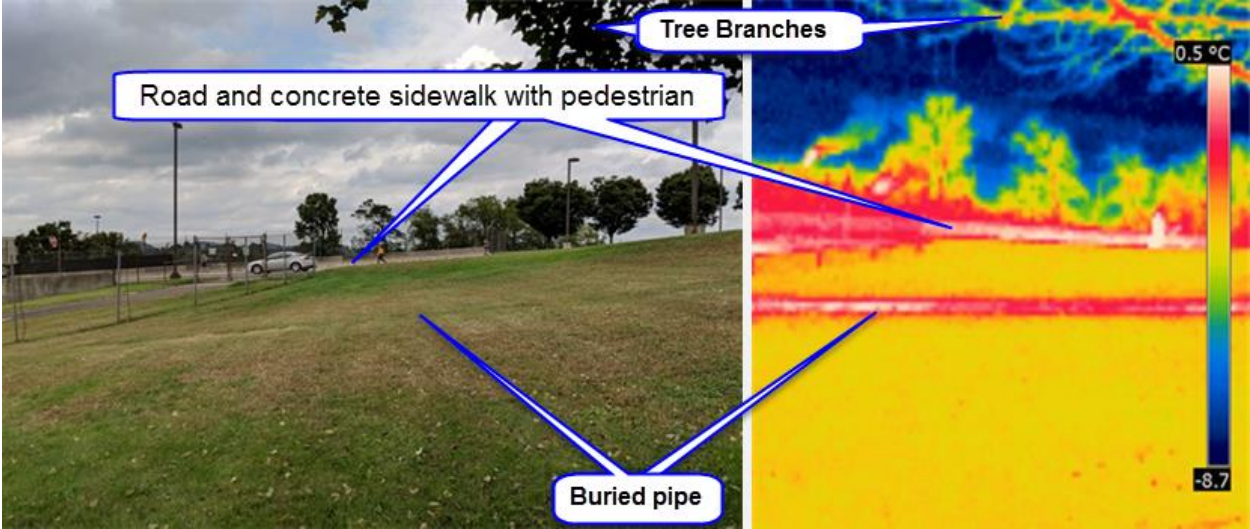
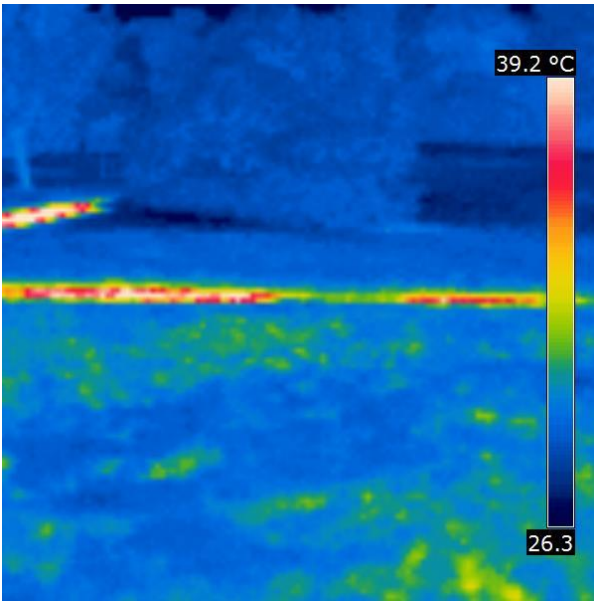
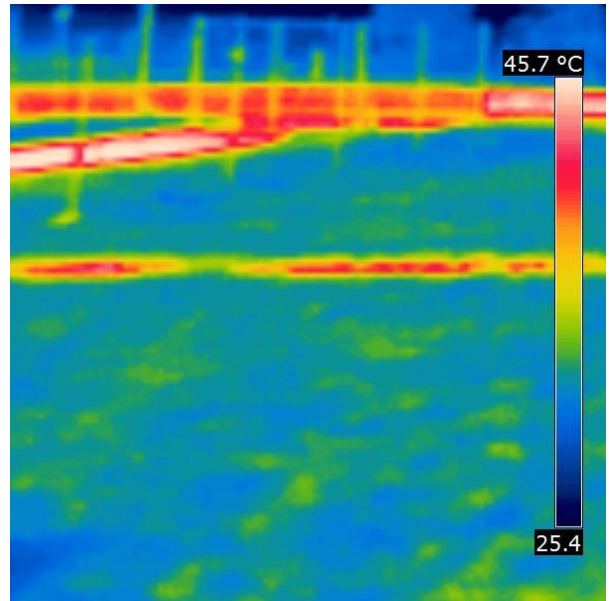


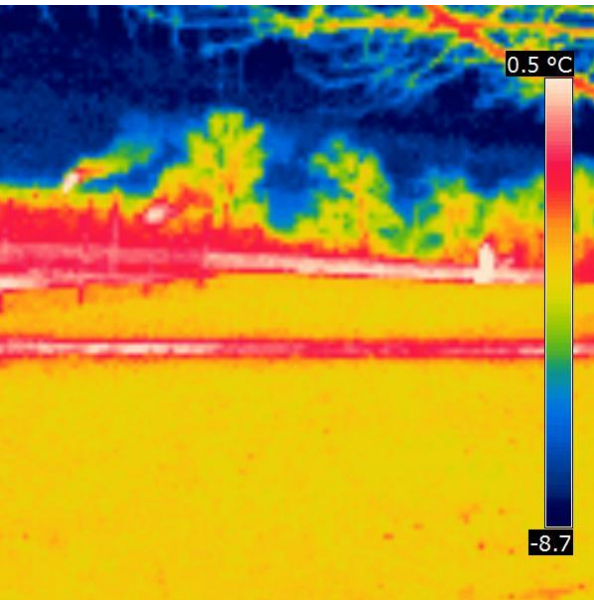
Figure 9-14: Comparison of IRT and visible image results



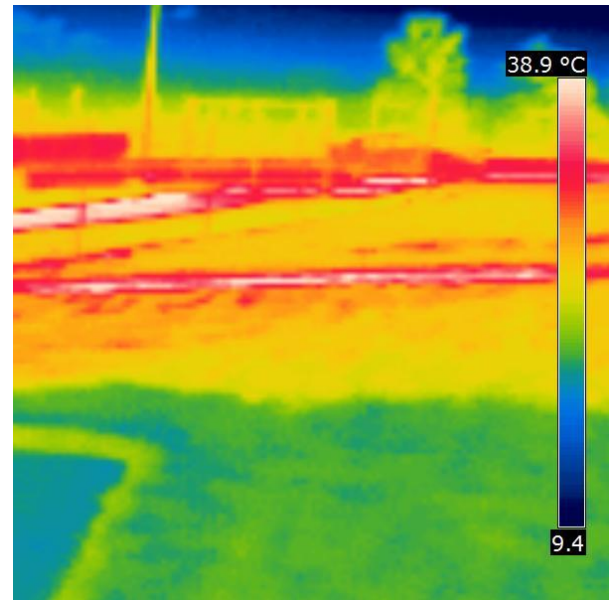
(a) Summer test result



(b) Summer test from another angle

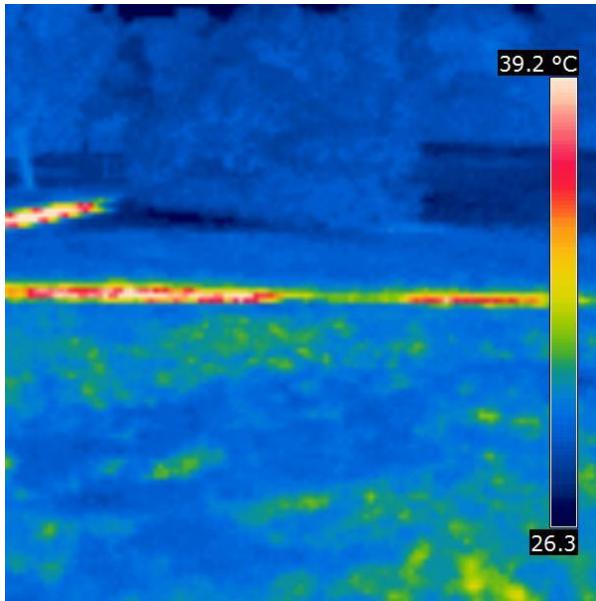


(c) Winter test result

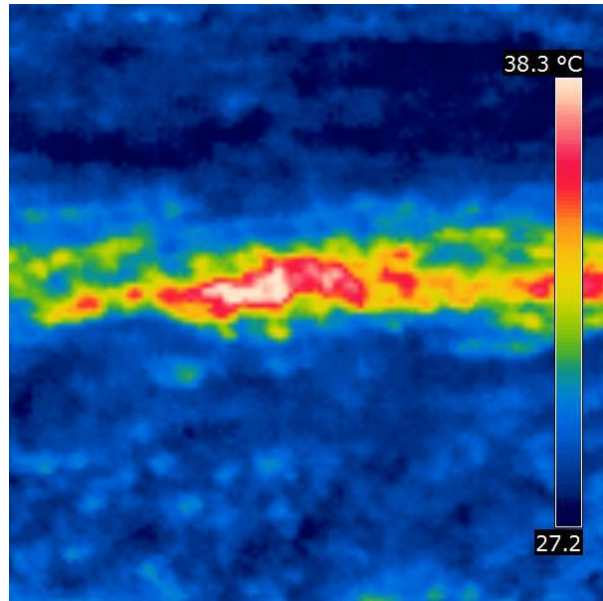


(d) Spring test result

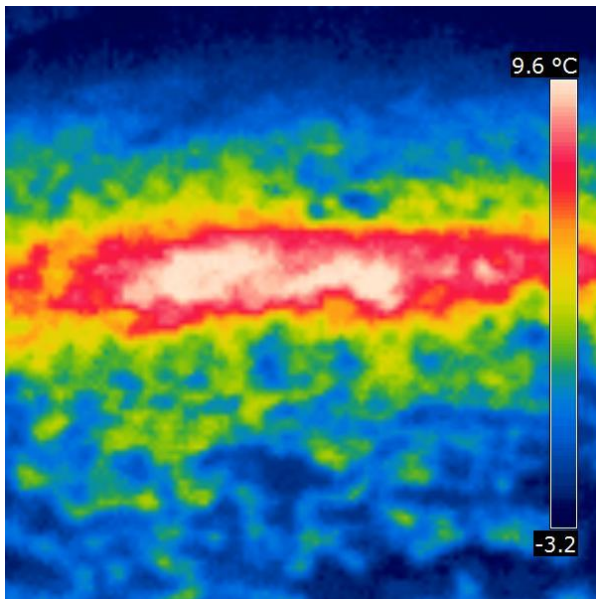
Figure 9-15: Infrared thermography data at the soil surface in different seasons



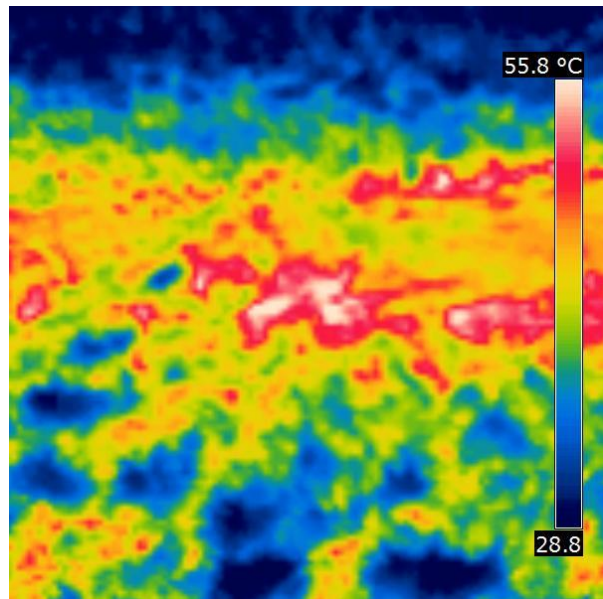
(a) Summer test result (longer distance)



(b) Summer test result



(c) Winter test result



(d) Spring test result

Figure 9-16: IRT data at the soil surface taken from close range in different seasons

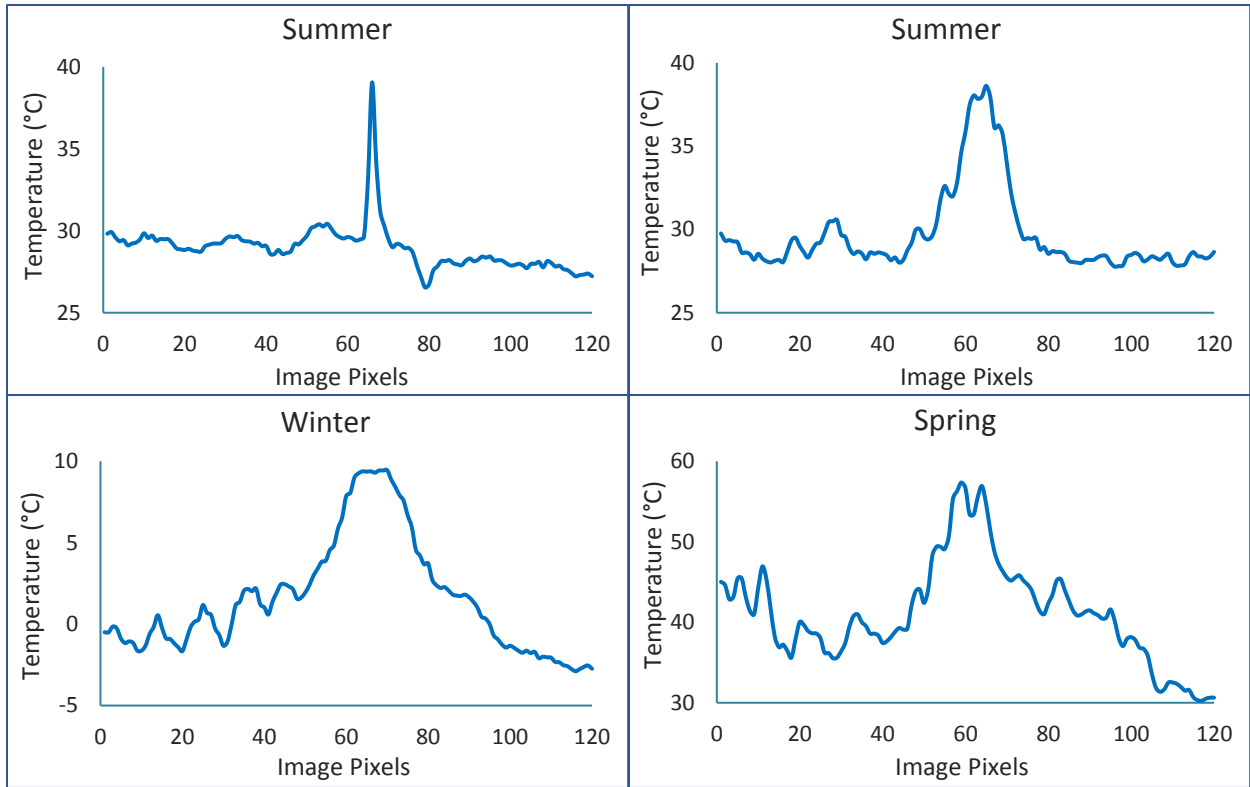


Figure 9-17: Temperature distribution across each IRT data in Figure 9-16

9.6 CONCLUSIONS

The IRT test conducted in this research demonstrate that, buried pipe transporting hot fluid such as steam or petroleum products from production wells or refinery plants have the potential of being detectable using IRT. The results from laboratory tests show that, IRT can be used to detect the 3" CFRP pipe up to a depth of 16.5" in the test medium when 95°C water is pumped through the pipe.

Test conducted on a buried pipe operating in the real world and transporting steam showed that, the IRT technique for detecting buried pipes transporting hot fluids has a higher performance than the laboratory test suggested. Though the field pipe was buried at a much deeper depth (2.5 – 3 ft.) and was insulated to prevent loss of heat to the surrounding soil, the IRT technique performed remarkably well. This can be attributed to higher moisture content of the soil and higher compaction of the backfill material (leading to higher thermal conductivity) in the field compared to the laboratory work. The performance of the IRT technique is expected to be even better for pipes with less or no insulation at all (compared to the field pipe tested in this study). Performance of the IRT technique is also expected to be better for bigger diameter pipes.

Computations on the laboratory test data assumed a one-dimensional heat conduction equation to arrive at the depth of possible pipe detection. Heat transfer in the field environment will not be one-dimensional, but rather three-dimensional. Also, bigger diameter pipes (much bigger than 3") are used in the field to transport petroleum products at temperatures less than or equal to 200°F (93°C). This temperature is about equal to what was used in the laboratory test (water temperature was 95°C, but trapped air pocket above the water in the pipe reduced the pipe surface temperature at the top of the pipe by 4.5°C compared to the pipe surface temperature at the bottom of the pipe). The three-dimensional heat transfer in the field environment will reduce the depth of pipe detection to an extent, but the use of bigger diameter pipes, coupled with higher moisture content and better compaction of backfill material is expected to have a bigger effect in increasing the depth of possible detection using IRT.

Thus, IRT has the potential of being used in detecting pipelines transporting hot fluids, but the maximum depth at which the pipe can be detected will depend on the diameter of the pipe and the temperature of liquid being transported.

CHAPTER 10

CONCLUSIONS AND RECOMMENDATIONS

10.1 RESEARCH SUMMARY

High strength plastics and advanced non-metallic composite pipe materials such as Glass Fiber Reinforced Polymer (GFRP) have desirable engineering and mechanical properties that can help address some of the challenges encountered in the pipeline transportation industry. However, difficulties in locating buried GFRP and plastic pipes are among the challenges limiting the adoption of such materials in the pipeline industry. This study sought to develop and investigate strategies for easily locating buried non-metallic pipelines in a bid to help address corrosion and excavation damage incidents, which are major challenges affecting the pipeline infrastructure (especially in the oil and gas industry). The non-metallic pipe materials investigated include CFRP and GFRP for high pressure applications, and PVC (plastic) for low pressure applications. The following research tasks were undertaken to achieve the study objectives:

1. Carbon fabric and aluminum foil/tape overlays (in the form of strips and rings) were used on GFRP and PVC pipes for easier detection using Ground Penetrating Radar (GPR).
2. Carbon nanoparticle coating was applied on a GFRP pipe to improve detection during GPR survey.
3. Thirty-nine pipe segments of different diameters were produced from the three non-metallic materials (CFRP, GFRP, and PVC), with various surface configuration, and buried at different depth from 2 ft. to 4 ft. of soil cover. One metallic pipe segment was also buried alongside the non-metallic pipes for comparison.
4. GPR equipment with different frequency antennae were used for investigating the detectability of the buried pipes in different soil moisture conditions.
5. Infrared thermography was used to investigate and locate buried pipes transporting hot fluids in a laboratory setting and in the field environment to ascertain the potential of this technique in locating buried pipes carrying hot contents.

10.2 CONCLUSIONS

Alternative strategies for locating buried non-metallic pipes using available ground sensory technologies such as GPR and IRT has been developed and investigated in this study. The following conclusions can be drawn from the findings of the study:

1. From the GPR test results presented in this study, it is evident that, the use of CFRP and aluminum foil overlays (in the form of rings and strips) improve the detectability of buried non-metallic pipe sections such as GFRP and PVC. The addition of carbon fabric or aluminum foil overlays makes the otherwise undetectable non-metallic pipes detectable, producing significantly stronger GPR reflection signals during testing. This is due to the high conductive nature of the overlays compared to the pipe material.
2. In cases where the buried unwrapped GFRP and PVC pipes are detectable (albeit with weak and difficult to interpret reflected signals), the addition of carbon or aluminum foil overlays significantly increases the strength/amplitude of the reflected GPR signal and makes it easier to identify the pipe sections. This is because carbon fabric and aluminum are good electrical conductors, hence they reflect the incident radar waves much better than non-conducting pipe materials and the surrounding soil.
3. The production of strong and easier to interpret signals from buried non-metallic pipes with carbon fabric or aluminum foil overlays also implies that, the depth of pipe burial can be increased beyond the 4 ft. maximum depth used in this research and still obtain adequate signal strength using GPR. The maximum depths at which these pipes can be detected for different soil types have been evaluated in Section 8.5.
4. By comparing GPR signal reflections from the buried pipes, carbon fabric overlays (strips/rings) were observed to produce stronger signals compared to aluminum foil overlays. This is because the aluminum foils used for the overlays were very thin, compared to the thickness of the carbon fabric overlays. Increasing the thickness of the aluminum overlay around the pipes (or wrapping pipes with aluminum sheets) can improve their detectability when buried. However, this approach is not practically feasible for buried pipe detection.

5. Additionally, it was observed that carbon fabric and aluminum foil strips bonded to the top of the pipes generally produce better/stronger signals compared to carbon fabric and aluminum foil rings around the non-metallic pipe sections. This is explained by the fact that, for scans conducted along the length of the pipe, only a small portion of the antenna beam is covered by a ring compared to a strip. For scans conducted perpendicular to the pipe direction, the rings only produced good results when the antenna is centered over a ring, as opposed to being centered between two rings.
6. The addition of carbon nanoparticle coating on a GFRP pipe in this study did not provide any noticeable benefit in making the buried non-metallic pipe detectable by GPR. The possible explanation for this is that, there is no interconnection between the individual nanoparticles, hence the coating did not act as a conductor as was expected. This is evident in the A-Scans shown in Figure 7-32; where pipes with conductive overlays/surfaces such as the GFRP pipe with CFRP strip, the PVC pipe with aluminum foil strip, and the steel pipe (Figure 7-32a, d, and f) produced signal reflections with reversed polarity (negative reflection peak resulting from negative reflection coefficient) while reflections from non-conductive pipes (Figure 7-32b, c, and e) did not experience any reversal in polarity. The GFRP pipe with carbon nanoparticle coating (Figure 7-32c) did not experience reversal in signal polarity, indicating that it is not acting as a conductor.
7. Furthermore, it was found from the GPR testing that, snow cover on the ground surface does not hinder the performance of GPR in detecting the buried pipes. This can be attributed to the fact that, the dielectric constant and electrical conductivity of snow are very low, hence the GPR signal travels through the snow cover without much attenuation, and at higher signal velocity compared to the underlying soil medium.
8. It was also observed that, 200 MHz GPR antenna is ideal for buried pipe detection. This antenna performed significantly better in locating the buried pipes at all the depths investigated compared to the 400 MHz and 900 MHz antennae, which were much less effective in locating the buried pipes even at 2 ft. depth. This is because signal from the higher frequency antennae attenuates significantly more with respect to travel distance compared to the lower frequency one. The 200 MHz antenna is also expected to penetrate deeper than the maximum 4 ft. depth investigated in this study, even in very wet clay soils

as estimated in Section 8.5. The 400 MHz antenna however performed well in locating the pipes buried at 2 ft. depth, especially when scanned in the transverse direction.

9. The 200 MHz antenna is however bigger and heavier than the 400 MHz and 900 MHz ones (antenna specifications are given in Table 5-1). With dimensions of 24"Lx24"Wx12"D and 45 lb. weight, this antenna is four times the weight and occupies four times the area of the 400 MHz antenna. The bigger size and higher weight makes this antenna more difficult to use in the field. Thus field crews tend to use the higher frequency antennae with manageable physical dimension; this makes it difficult for them to locate buried objects since the higher frequency antennae are less effective in locating these objects in most soils and soil moisture conditions.
10. Though GPR signal attenuation is generally regarded to increase with antenna frequency, this behavior is usually attributed to material/ohmic attenuation while scattering attenuation is hardly mentioned in literature. It has been found in this study that material attenuation is generally constant for antenna frequencies of 50 MHz and above (based on soil dielectric constant and electrical conductivity), while frequencies below 50 MHz experience a vertical drop in ohmic attenuation coefficient. Scattering attenuation on the other hand was observed to increase with antenna frequency, which explains the difference in performance between the different antennae used in the study.
11. Results from this study have shown that IRT have the potential to be used in locating buried pipes transporting hot fluids such as steam or petroleum products from production wells or refinery plants. A 3 inch diameter CFRP pipe buried with 14 inches of soil cover and transporting hot water at a temperature of 95°C in a laboratory setting was detected using IRT. Additionally, a 6 inch diameter steam pipe with a minimum of 6 inch insulation and buried with 2.5 – 3 ft. of soil cover was easily detected in varying soil moisture conditions and seasons using IRT in the actual field environment.
12. Finally, the findings of the IRT tests performed in the field environment have showed that snow cover on the ground surface does not hinder the performance of this technique for buried hot pipe detection. Additionally, the technique works very well in both wet soil and relatively dry soils.

10.3 RECOMMENDATIONS FOR FIELD IMPLEMENTATION AND FUTURE STUDY

The following are recommended for field implementation of the findings of this study, and to aid in buried non-metallic pipe detection. This also includes recommendations for future works to expand these findings of the current study.

10.3.1 Recommendations for Field Implementation

1. Carbon fabric strips bonded to the top of buried pipes and spanning the entire length of the pipe is found to be the best surface configuration for GPR detection. Hence, this is the configuration recommended for field implementation on GFRP pipes. In addition to being the best configuration in making buried non-metallic pipes detectable, carbon fabric is also very durable (very high corrosion and abrasion resistance, and high strength to withstand various forms of mechanical damage) compared to aluminum foils which are very fragile and prone to environmental degradation. Also, the entire pipe can be wrapped with carbon fabric for strengthening; this will make the pipe stronger and be able to resist higher operating pressures in addition to being detectable using GPR. Finally, Carbon fabric overlays can also be incorporated into the manufacturing process for GFRP pipes, streamlining the production process.
2. If carbon fabric rings around the pipe must be used in any particular case, they should be wrapped in a spiral fashion. Using spiral wraps around the pipes instead of parallel rings will ensure there is always part of the wrap at every section along the length of the pipe. Spiral wraps will be easier to detect using GPR compared to rings if scans are performed perpendicular to the length of the pipe. Spiral wraps around the pipe will also be easier to incorporate into the manufacturing process of fiber composite (such as GFRP) pipes compared to rings around the pipe.
3. Since both PVC pipes and aluminum foils are readily available in hardware stores, it will be easier to use aluminum foil overlays on PVC pipes as opposed to using carbon fabric overlays. Additionally, the installation process of aluminum foil on pre-fabricated PVC pipes is simpler than installing carbon fabric overlays, which can further streamline the process of making buried PVC pipes intrinsically locatable using GPR.

4. For GPR field testing in dry as well as most wet soil conditions, the 200 MHz radar antenna is recommended. This antenna frequency performed very well in all soil moisture conditions and at all the depths investigated in this study.
5. If variation of attenuation coefficient with antenna frequency is required, then scattering attenuation should be considered in addition to material/ohmic attenuation. Scattering attenuation was found to be the primary component of attenuation that increases with antenna frequency, while ohmic attenuation was found to be constant across the antenna frequencies. This will be even more pronounced in very inhomogeneous materials such as soils with gravels or lots of clutter objects.

10.3.2 Recommendations for Future Study

1. Different pipe diameters buried at various depths and transporting contents of different temperatures should be investigated in different weather conditions for IRT detection. This can help establish which temperatures and pipe diameters will be detectable at different depths and in different soil/weather conditions.
2. Future studies should also include how long pipe content of a given temperature will travel in the pipe before it loses its temperature difference and becomes undetectable using IRT.

REFERENCES

- Al-Qadi, I. L., & Lahouar, S. (2005). Measuring layer thicknesses with GPR – Theory to practice. *Construction and Building Materials*, 19(10), 763-772.
- Alani, A. M., Aboutalebi, M., & Kilic, G. (2013). Applications of ground penetrating radar (GPR) in bridge deck monitoring and assessment. *Journal of Applied Geophysics*, 97, 45-54.
- Allred, B. J., Fausey, N. R., Peters, L. J., Chen, C., Daniels, J. J., & Youn, H. (2004). Detection of Buried Agricultural Drainage Pipe with Geophysical Methods. *Applied Engineering in Agriculture*, 20(3), 307-318.
- Annan, A. P. (2009). Electromagnetic Principles of Ground Penetrating Radar. In H. M. Jol (Ed.), *Ground Penetrating Radar Theory and Applications* (3-40). New York: Elsevier B.V.
- ASCE. (2017). *2017 Infrastructure Report Card: A Comprehensive Assessment of America's Infrastructure*. American Society of Civil Engineers (ASCE):
- Asry, Z., Samsudin, A. R., Yaacob, W. Z., & Yaakub, J. (2012). Groundwater investigation using electrical resistivity imaging technique at Sg. Udang, Melaka, Malaysia. *Bulletin of the Geological Society of Malaysia*, 58, 55-58.
- Baker (2008). *Pipeline Corrosion - FINAL REPORT*. Michael Baker Jr., Inc. Retrieved on March 7, 2018 from https://primis.phmsa.dot.gov/gasimp/docs/finalreport_pipelinecorrosion.pdf.
- Baker (2009). *Mechanical Damage - FINAL REPORT*. Michael Baker Jr., Inc. Retrieved on March 7, 2018 from https://primis.phmsa.dot.gov/gasimp/docs/Mechanical_Damage_Final_Report.pdf.
- Barone, P. M., Bellomo, T., Mattei, E., Lauro, S. E., & Pettinelli, E. (2011). Ground-penetrating Radar in the Regio III (Pompeii, Italy): Archaeological Evidence. *Archaeological Prospection*, 18(3), 187-194. doi:10.1002/arp.405
- Barone, P. M., Mattei, E., Lauro, S. E., & Pettinelli, E. (2010). Non-destructive technique to investigate an archaeological structure: A GPR survey in the Domus Aurea (Rome, Italy). *Proceedings of the XIII International Conference on Ground Penetrating Radar*, Lecce, Italy.

- Bohren, C. F., & Huffman, D. R. (1940). *Absorption and Scattering of Light by Small Particles*. New York: Wiley.
- Bowders, J. J., Koerner, R. M., & Lord, A. E. (1982). Buried container detection using ground-probing radar. *Journal of Hazardous Materials*, 7(1), 1-17.
- Butnor, J. R., Doolittle, J. A., Johnsen, K. H., Samuelson, L., Stokes, T., & Kress, L. (2003). Utility of Ground-Penetrating Radar as a Root Biomass Survey Tool in Forest Systems. *Soil Science Society of America Journal*, 67(5), 1607-1615.
- Butnor, J. R., Doolittle, J. A., Kress, L., Cohen, S., & Johnsen, K. H. (2001). Use of ground-penetrating radar to study tree roots in the southeastern United States. *Tree Physiology*, 21(17), 1269-1278.
- Carrière, S. D., Chalikakis, K., Sénéchal, G., Danquigny, C., & Emblanch, C. (2013). Combining Electrical Resistivity Tomography and Ground Penetrating Radar to study geological structuring of karst Unsaturated Zone. *Journal of Applied Geophysics*, 94, 31-41.
- Cassidy, N. J. (2009). Electrical and Magnetic Properties of Rocks, Soils and Fluids. In H. M. Jol (Ed.), *Ground Penetrating Radar Theory and Applications* (pp. 41-72). New York: Elsevier B.V.
- CIA. (n.d.). The World Factbook- Central Intelligence Agency. Retrieved on December 20, 2015 from <https://www.cia.gov/library/publications/the-world-factbook/fields/2117.html>
- Cist, D. B., & Schutz, A. E. (2001). *State of the Art for Pipe & Leak Detection*. Report No: DE-FC26-01NT41317, Geophysical Survey Systems, Inc.
- CJD (2015). Underground Steam Line Replacement at Mineral Resources Building, West Virginia University (WVU), Morgantown, West Virginia. Obtained from WVU Facilities Management.
- Costello, S. B., Chapman, D. N., Rogers, C. D. F., & Metje, N. (2007). Underground asset location and condition assessment technologies. *Tunnelling and Underground Space Technology*, 22(5), 524-542.

- Curtis, J. O. (2001). Moisture effects on the dielectric properties of soils. *IEEE Transactions on Geoscience and Remote Sensing*, 39(1), 125-128.
- Dalrymple, G. A. (2014). Forensic Evaluation Techniques for Masonry and Concrete Construction. *Information & Insight*.
- Daniels, D. J. (2004) Ground Penetrating Radar. *IEE Radar, Sonar, Navigation and Avionics Series 15* (2nd Ed.). London: The Institution of Electrical Engineers.
- Davis, J. L., & Annan, A. P. (1989). Ground Penetrating Radar for High Resolution Mapping of Soil and Rock Stratigraphy. *Geophysical Prospecting*, 37(5), 531-551.
- DOT (2011). Failure Investigation Report – Dixie Pipeline Company 8-inch Propane Pipeline Release. Retrieved on February 10, 2016 from https://www.phmsa.dot.gov/sites/phmsa.dot.gov/files/docs/Dixie_HL_GA_20100705.pdf
- EIA (2015). *Annual Energy Outlook 2015: with projections to 2040*. Washington, DC: U.S. Energy Information Administration (EIA). Retrieved on May 24, 2017 from [https://www.eia.gov/outlooks/aeo/pdf/0383\(2015\).pdf](https://www.eia.gov/outlooks/aeo/pdf/0383(2015).pdf)
- EIA (n.d.-a). Primary Energy Consumption by Source. Washington, DC: U.S. Energy Information Administration (EIA). Retrieved on August 3, 2017 from <https://www.eia.gov/totalenergy/data/browser/?tbl=T01.03#/?f=A&start=1949&end=2014&charted=1-2-3-5-12>
- EIA. (n.d.-b). Refinery Receipts of Crude Oil by Method of Transportation (Thousand Barrels). Washington, DC: U.S. Energy Information Administration (EIA). Retrieved on May 7, 20185 from https://www.eia.gov/dnav/pet/pet_pnp_caprec_dcu_nus_a.htm
- Ferré, P. A., Rudolph, D. L., & Kachanoski, R. G. (1996). Spatial Averaging of Water Content by Time Domain Reflectometry: Implications for Twin Rod Probes with and without Dielectric Coatings. *Water Resources Research*, 32(2), 271-279.
- Folkman, S. (2018). Water Main Break Rates in the USA and Canada: A Comprehensive Study. *Mechanical and Aerospace Engineering Faculty Publications, Paper 174*.

- Frezza, F., Mangini, F., & Tedeschi, N. (2017). Tutorial: Introduction to electromagnetic scattering. *Journal of the Optical Society of America A*, 1-11.
- Friedman, S. P. (1998). A saturation degree-dependent composite spheres model for describing the effective dielectric constant of unsaturated porous media. *Water Resources Research*, 34(11), 2949-2961.
- GangaRao, H. V. S., Taly, N., & Vijay, P. V. (2007). *Reinforced Concrete Design with FRP Composites*. London: CRC Press.
- Gavish, N., & Promislow, K. (2016). Dependence of the dielectric constant of electrolyte solutions on ionic concentration: A microfield approach. *Physical Review E*, 94(1).
- Ghosh, K. K., & Karbhari, V. M. (2011). Use of infrared thermography for quantitative non-destructive evaluation in FRP strengthened bridge systems. *Materials and Structures*, 44(1), 169-185.
- Goodman, D., & Piro, S. (2013). *GPR Remote Sensing in Archaeology*. New York: Springer.
- GSSI. (2017). *Antennas Manual*. In. Nashua NH, USA: Geophysical Survey Systems, Inc.
- Halabe, U. B., & Dutta, S. S. (2010). Quantitative Characterization of Debond Size in FRP Wrapped Concrete Cylindrical Columns using Infrared Thermography. *The Fourth Japan-US Symposium on Emerging NDE Capabilities for a Safer World*, Makena Beach & Resort Hotel, Maui Island, Hawaii, USA.
- Halabe, U. B., Petro, S. H., & GangaRao, H. V. S. (1995). *Nondestructive Evaluation Methods for Highway Bridge Superstructures* (CFC 95-215).
- Halabe, U. B., Sotoodehnia, A., Maser, K. R., & Kausel, E. A. (1993). Modeling of the Electromagnetic Properties of Concrete. *Materials Journal*, 90(6), 552-563.
- Hansen, G. P. (1982). Dowsing: A Review of Experimental Research. *Journal of the Society for Psychical Research*, 51(792), 343-367.
- Hing, C. L. C., & Halabe, U. B. (2010). Nondestructive Testing of GFRP Bridge Decks Using

- Ground Penetrating Radar and Infrared Thermography. *Journal of Bridge Engineering*, 15(4), 391-398.
- Hirano, Y., Dannoura, M., Aono, K., Igarashi, T., Ishii, M., Yamase, K., Makita, N., & Kanazawa, Y. (2009). Limiting factors in the detection of tree roots using ground-penetrating radar. *Plant and Soil*, 319(1), 15-24.
- Huang, H., & Won, I. J. (2003). Characterization of UXO-Like Targets Using Broadband Electromagnetic Induction Sensors. *IEEE Transactions on Geoscience and Remote Sensing*, 41(3), 652-663.
- Johnson, W. J. (2003). Applications of the Electrical Resistivity Method for Detection of Underground Mine Workings. *Paper presented at the Geophysical Technologies for Detecting Underground Coal Mine Voids, Lexington, KY.*
- Kavi, J. (2015). *Nondestructive evaluation of corrosion in reinforced concrete structures with or without FRP wraps*. (M.S. Thesis), Department of Civil and Environmental Engineering, West Virginia University, Morgantown WV.
- Koch, G. H., Brongers, M. P. H., Thompson, N. G., Virmani, Y. P., & Payer, J. H. (2002). *Corrosion Costs and Preventive Strategies in the United States*. Publication No. FHWA-RD-01-156, NACE International.
- Lamsters, K., Karušs, J., Rečs, A., & Bērziņš, D. (2016). Detailed subglacial topography and drumlins at the marginal zone of Múlajökull outlet glacier, central Iceland: Evidence from low frequency GPR data. *Polar Science*, 10(4), 470-475.
- Ledieu, J., De Ridder, P., De Clerck, P., & Dautrebande, S. (1986). A method of measuring soil moisture by time-domain reflectometry. *Journal of Hydrology*, 88(3), 319-328.
- Mallick, P. K. (2007). *Fiber-Reinforced Composites: Materials, Manufacturing, and Design* (3rd Ed.). London: CRC Press.
- Mariita, M. O. (2007). The Magnetic Method. *Paper presented at the Surface Exploration for Geothermal Resources, Lake Naivasha, Kenya.*

- Metwaly, M. (2007). Detection of metallic and plastic landmines using the GPR and 2-D resistivity techniques. *Natural Hazards and Earth System Science*, 7, 755-763.
- Mitani, K., & Matsumoto, M. (2012). *Innovative Bridge Assessment Methods Using Image Processing and Infrared Thermography Technology*. Paper presented at the 37th Conference on Our World in Concrete & Structures, Singapore.
- Mohamaden, M. I. I., & Ehab, D. (2017). Application of electrical resistivity for groundwater exploration in Wadi Rahaba, Shalateen, Egypt. *NRIAG Journal of Astronomy and Geophysics*, 6(1), 201-209.
- Mukhlisin, M., & Saputra, A. (2013). Performance Evaluation of Volumetric Water Content and Relative Permittivity Models. *The Scientific World Journal*, 2013, 7.
- Munk, J., & Sheets, R. A. (1997). *Detection of Underground Voids in Ohio by Use of Geophysical Methods* (FHWA/OH-97/010).
- Najafi, M. (2010). *Trenchless Technology Piping: Installation and Inspection*. New York: McGraw-Hill Education.
- Nicholson, L. (2015). 6,000 gallons of oil sopped up in California spill, but fraction of total. Aljazeera America Retrieved on February 10, 2016 from <http://america.aljazeera.com/articles/2015/5/21/daunting-california-oil-spill-cleanup-continues.html>
- NTSB (2011). *Pacific Gas and Electric Company Natural Gas Transmission Pipeline Rupture and Fire - San Bruno, California September 9, 2010: Accident Report* (NTSB/PAR-11/01, PB2011-916501).
- NTSB (2012). *Enbridge Incorporated Hazardous Liquid Pipeline Rupture and Release Marshall, Michigan, July 25, 2010* (NTSB/PAR-12/01, PB2012-916501).
- NTSB (2013). Pipeline Accident Brief: Natural gas transmission pipeline rupture and fire. Retrieved on February 10, 2016 from <https://www.nts.gov/investigations/AccidentReports/Reports/PAB1302.pdf>

- Pal, R. (2015). *Electromagnetic, Mechanical, and Transport Properties of Composite Materials*. New York: CRC Press.
- Paolo, F. D., Cosciotti, B., Lauro, S. E., Mattei, E., Callegari, M., Carturan, L., Seppi, R., Zucca, F., and Pettinelli, E. (2015). Combined GPR and TDR measurements for snow thickness and density estimation. *Paper presented at the 2015 8th International Workshop on Advanced Ground Penetrating Radar (IWAGPR)*.
- PHMSA (2014a). Pipeline Safety Stakeholder Communications - Fact Sheet: Excavation Damage. Retrieved on February 10, 2016 from <https://primis.phmsa.dot.gov/comm/FactSheets/FSExcavationDamage.htm>
- PHMSA (2014b). Incident Report Criteria History. Retrieved on February 10, 2016 from https://hip.phmsa.dot.gov/Hip_Help/pdmpublic_incident_page_allrpt.pdf
- PHMSA (2015). Funding Opportunity Announcement (FOA). In *Pipeline Safety Research Competitive Academic Agreement Program (CAAP)*.
- PHMSA (2016a). Pipeline Incident 20 Year Trends. Retrieved on February 10, 2016 from <https://www.phmsa.dot.gov/data-and-statistics/pipeline/pipeline-incident-20-year-trends>
- PHMSA (2016b). All Reported Incidents. Retrieved on February 10, 2016 from <https://hip.phmsa.dot.gov/analyticsSOAP/saw.dll?Portalpages>
- PHMSA (2016c). Serious Incidents. Retrieved on February 10, 2016 from https://opsweb.phmsa.dot.gov/primis_pdm/serious_inc_trend.asp
- PHMSA (2016d). Significant Incidents. Retrieved on February 10, 2016 from https://opsweb.phmsa.dot.gov/primis_pdm/significant_inc_trend.asp
- PHMSA (2016e). *Preliminary Factual Report - Plains Pipeline, LP, Failure on Line 901*.
- PHMSA (2016f). *Failure Investigation Report - Plains Pipeline, LP, Line 901*. Retrieved on February 10, 2016 from <https://www.phmsa.dot.gov/staticfiles/PHMSA/DownloadableFiles/Press%20Releases/Plains%20Preliminary%20Factual%20Report.pdf>

- PHMSA. (2017). Pipeline Safety Stakeholder Communications: Damage Prevention. Retrieved on March 2, 2018 from <https://primis.phmsa.dot.gov/comm/DamagePrevention.htm>
- Porretta, R., & Bianchi, F. (2016). Profiles of relative permittivity and electrical conductivity from unsaturated soil water content models. *Annals of Geophysics*, 59(3).
- Porsani, J. L., Ruy, Y. B., Ramos, F. P., & Yamanouth, G. R. B. (2012). GPR applied to mapping utilities along the route of the Line 4 (yellow) subway tunnel construction in São Paulo City, Brazil. *Journal of Applied Geophysics*, 80, 25-31.
- Prego, F. J., Solla, M., Puente, I., & Arias, P. (2017). Efficient GPR data acquisition to detect underground pipes. *NDT & E International*, 91, 22-31.
- PST. (2015) Pipeline Briefing Paper #7: Excavation Damage Prevention. In: Pipeline Safety Trust.
- Rawls, G. (2015). *Fiber Reinforced Composite Pipelines*. Retrieved on March 1, 2018 from https://www.hydrogen.energy.gov/pdfs/review15/pd022_rawls_2015_o.pdf
- Razinger, J. (2017). *Utilization of Ground Penetrating Radar (GPR) to Detect Shear Bolts in Bridges -- Colchester Bridges 77 & 76 – US I-89 (U2017-02)*.
- Reynolds, J. M. (2011). *An Introduction to Applied and Environmental Geophysics*. (2nd Ed.). Bognor Regis: Wiley.
- Roth, C. H., Malicki, M. A., & Plagge, R. (1992). Empirical evaluation of the relationship between soil dielectric constant and volumetric water content as the basis for calibrating soil moisture measurements by TDR. *Journal of Soil Science*, 43, 1-13.
- SacBee. (2010). Explosion levels San Bruno neighborhood. The Sacramento Bee (SacBee). Retrieved on February 8, 2016 from <http://blogs.sacbee.com/photos/2010/09/explosion-levels-san-bruno-nei.html>
- Sagnard, F., Norgeot, C., Derobert, X., Baltazart, V., Merliot, E., Derkx, F., & Lebental, B. (2016). Utility detection and positioning on the urban site Sense-City using Ground-Penetrating Radar systems. *Measurement*, 88, 318-330.

- Sakagami, T., Izumi, Y., Kobayashi, Y., Mizokami, Y., & Kawabata, S. (2014). Applications of infrared thermography for nondestructive testing of fatigue cracks in steel bridges. Paper presented at the Thermosense: Thermal Infrared Applications XXXVI.
- Satterfield, Z. (2006). Locating Distribution Lines. *Tech Brief 06*, 5(4).
- Schaap, M. G., de Lange, L., & Heimovaara, T. J. (1996). TDR calibration of organic forest floor media. *Soil Technology*, 11(2), 205-217.
- Sheets, R. A. (2002). *Use of Electrical Resistivity to Detect Underground Mine Voids in Ohio*. Water-Resources Investigations Report 02-4041. United States Geological Survey (USGS), Columbus, Ohio. Retrieved on February 8, 2018 from <http://eot.us.archive.org/eot/20111018041028/http://oh.water.usgs.gov/reports/wrir/wrir02-4041.pdf>
- Spring, R., Huff, R., & Schwoegler, M. (2011). Infrared Thermography: A Versatile Nondestructive Testing Technique. *Materials Evaluation*, 69(8), 934-942.
- Sumlin, B. J., Heinson, W. R., & Chakrabarty, R. K. (2018). Retrieving the aerosol complex refractive index using PyMieScatt: A Mie computational package with visualization capabilities. *Journal of Quantitative Spectroscopy and Radiative Transfer*, 205, 127-134.
- Taillade, F., Quiertant, M., Benzarti, K., Dumoulin, J., & Aubagnac, C. (2012). Nondestructive Evaluation of FRP Strengthening Systems Bonded on RC Structures Using Pulsed Stimulated Infrared Thermography. In R. V. Prakash (Ed.), *Infrared Thermography: InTech*.
- Takahashi, K., Igel, J., Preetz, H., & Kuroda, S. (2012a). Basics and Application of Ground-Penetrating Radar as a Tool for Monitoring Irrigation Process. In M. Kumar (Ed.), *Problems, Perspectives and Challenges of Agricultural Water Management: InTech*.
- Topp, G. C., Davis, J. L., & Annan, A. P. (1980). Electromagnetic Determination of Soil Water Content: Measurements in Coaxial Transmission Lines. *Water Resources Research*, 16(3), 574-582.

- Trela, C., Kind, T., & Günther, M. (2015). Ground penetrating Radar reflection vs transmission mode for void detection in concrete structure. Paper presented at the *International Symposium on Non-Destructive Testing in Civil Engineering (NDT-CE 2015)*, Berlin, Germany.
- USDOT (2017). Table 1-61: Crude Oil and Petroleum Products Transported in the United States by Mode, Bureau of Transportation Statistics. Retrieved on October 8, 2018 from https://www.bts.gov/archive/publications/national_transportation_statistics/table_01_61
- Vealey, R. (2016). Put that in your pipeline: Building gas infrastructure must look beyond economy, Editorial. *The Dominion Post*, 03/27/2016, pp. 1-C.
- Wijewardana, Y. G. N. S., & Galagedara, L. W. (2010). Estimation of spatio-temporal variability of soil water content in agricultural fields with ground penetrating radar. *Journal of Hydrology*, 391(1), 24-33.
- Won, I. J., Keiswetter, D. A., & Bell, T. H. (2001). Electromagnetic induction spectroscopy for clearing landmines. *IEEE Transactions on Geoscience and Remote Sensing*, 39(4), 703-709. doi:doi:10.1109/36.917876
- Zegelin, S. J., White, I., & Russell, G. F. (1992). A Critique of the Time Domain Reflectometry Technique for Determining Field Soil-Water Content. In G. C. Topp, W. D. Reynolds, & R. E. Green (Eds.), *Advances in Measurement of Soil Physical Properties: Bringing Theory into Practice* (pp. 187-208). Madison, WI: Soil Science Society of America.
- Zhu, J., Currens, J. C., & Dinger, J. S. (2011). Challenges of using electrical resistivity method to locate karst conduits—A field case in the Inner Bluegrass Region, Kentucky. *Journal of Applied Geophysics*, 75(3), 523-530.
- Ékes, C., Neduczka, B., & Henrich, G. R. (2011). *GPR goes underground: Pipe Penetrating Radar on Environmental*. Paper presented at the NASTT No-Dig Show, Washington, DC.

**APPENDIX A: PHMSA INCIDENT DEFINITION AND CRITERIA
HISTORY**

PIPELINE INCIDENTS

According to the PHMSA, pipeline incident reports have been collected since 1970. “The reporting regulations and incident report formats have changed several times over the years” (PHMSA 2016a). “PHMSA merged the various report formats to create pipeline incident trend lines going back 20 years” (PHMSA 2016a). The following are the definitions of the different incident categories according to PHMSA (PHMSA 2016a).

SERIOUS INCIDENTS

Serious Incidents include a fatality or injury requiring in-patient hospitalization. From 2004 forward, gas distribution incidents caused by a nearby fire or explosion that impact the pipeline system are excluded.

SIGNIFICANT INCIDENTS

Significant Incidents are those including any of the following conditions, but gas distribution incidents caused by a nearby fire or explosion that impacted the pipeline system are excluded:

1. Fatality or injury requiring in-patient hospitalization
2. \$50,000 or more in total costs, measured in 1984 dollars
3. Highly volatile liquid releases of 5 barrels or more or other liquid releases of 50 barrels or more
4. Liquid releases resulting in an unintentional fire or explosion

ALL-REPORTED INCIDENTS

Includes all reports submitted to PHMSA. Changes to PHMSA reporting regulations have caused large shifts in the trend line.

PHMSA INCIDENT REPORT CRITERIA HISTORY

https://hip.phmsa.dot.gov/Hip_Help/pdmpublic_incident_page_allrpt.pdf

APPENDIX B: SUPPLEMENTARY GPR DATA

B.1 DETAILS OF PIPES IDENTIFIED IN THE 36 FT. LONG TRENCH USING 400 MHZ ANTENNA

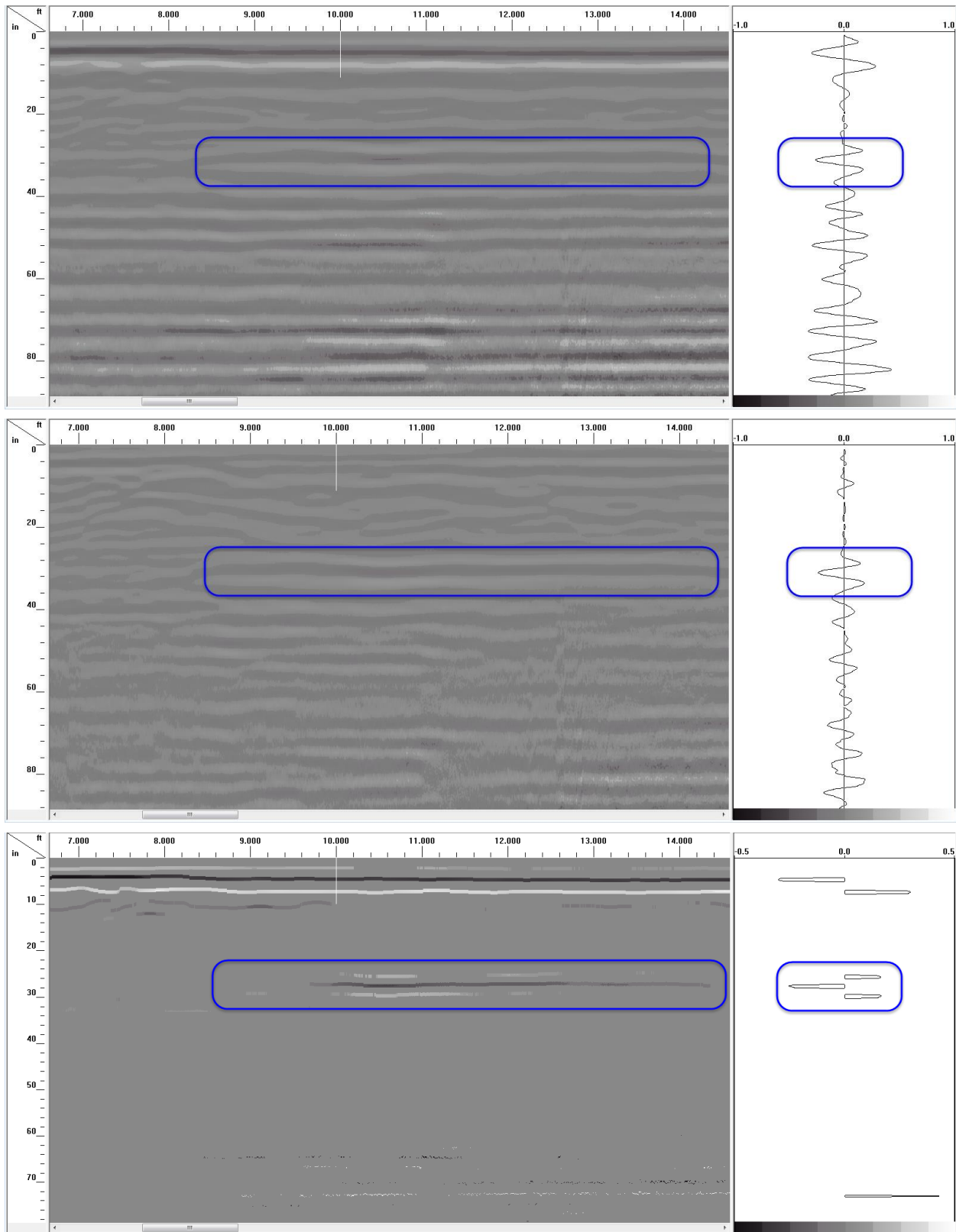


Figure B-1: Longitudinal scan over 12" CFRP Strip GFRP pipe: raw data (top), data with background noise removed (middle), and reflection peaks extracted from the data (bottom)

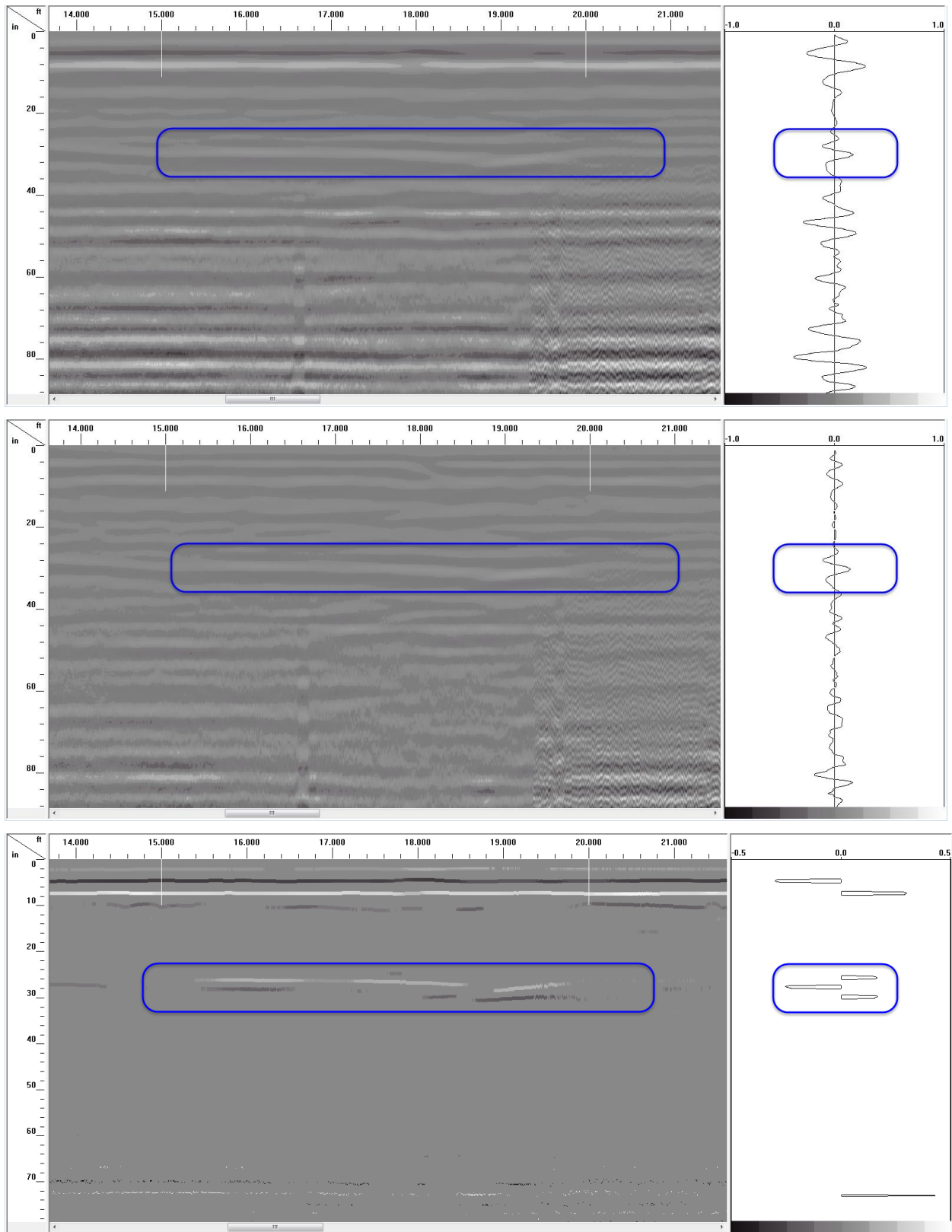


Figure B-2: Longitudinal scan over 12" Unwrapped GFRP pipe: raw data (top), data with background noise removed (middle), and reflection peaks extracted from the data (bottom)

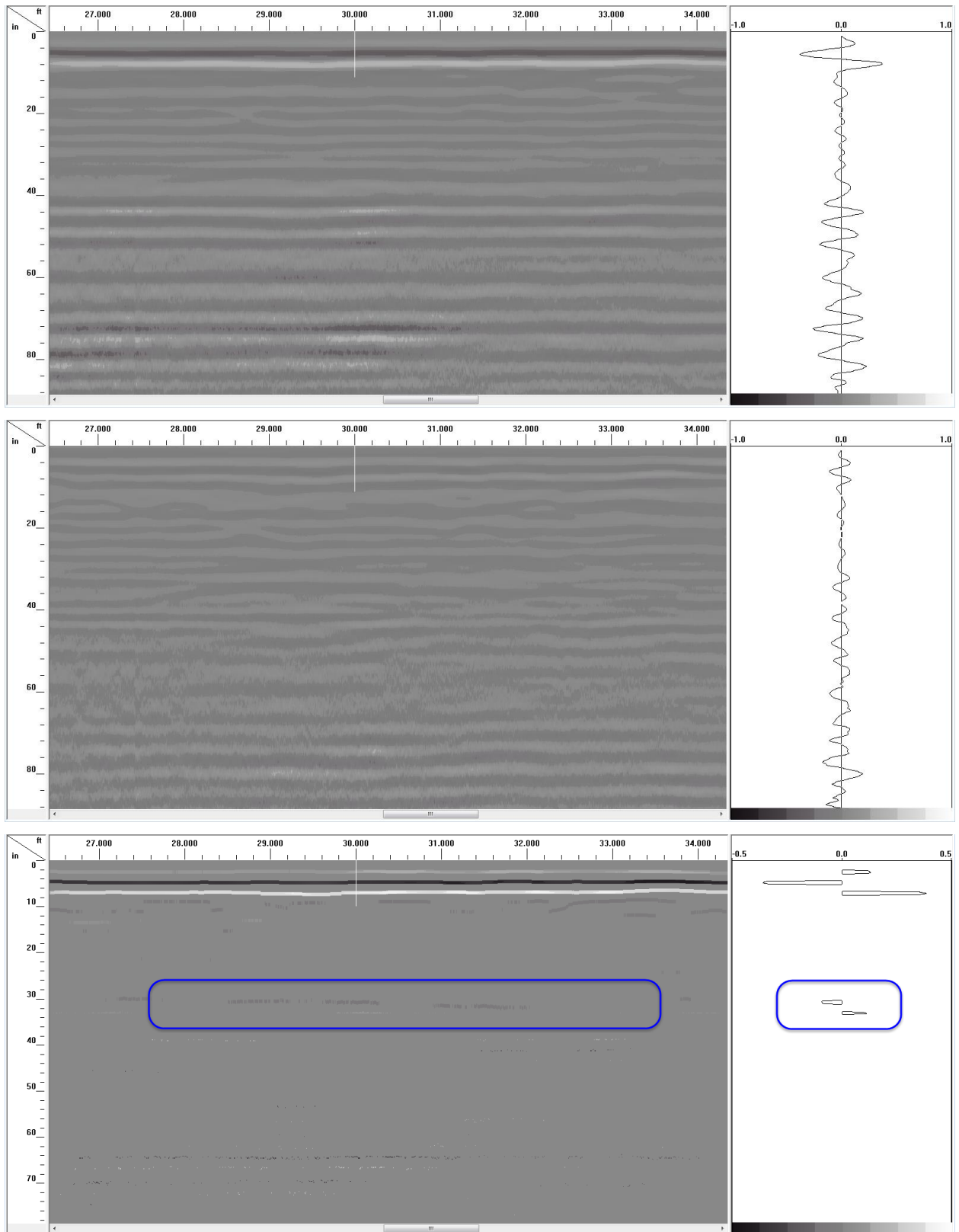


Figure B-3: Longitudinal scan over 12" Al. Foil Strip PVC pipe: raw data (top), data with background noise removed (middle), and reflection peaks extracted from the data (bottom)

B.2 DETAILED RADAR PROFILE FOR FEATURES MARKED IN FIGURE 7-29(B) FOR DATASET II

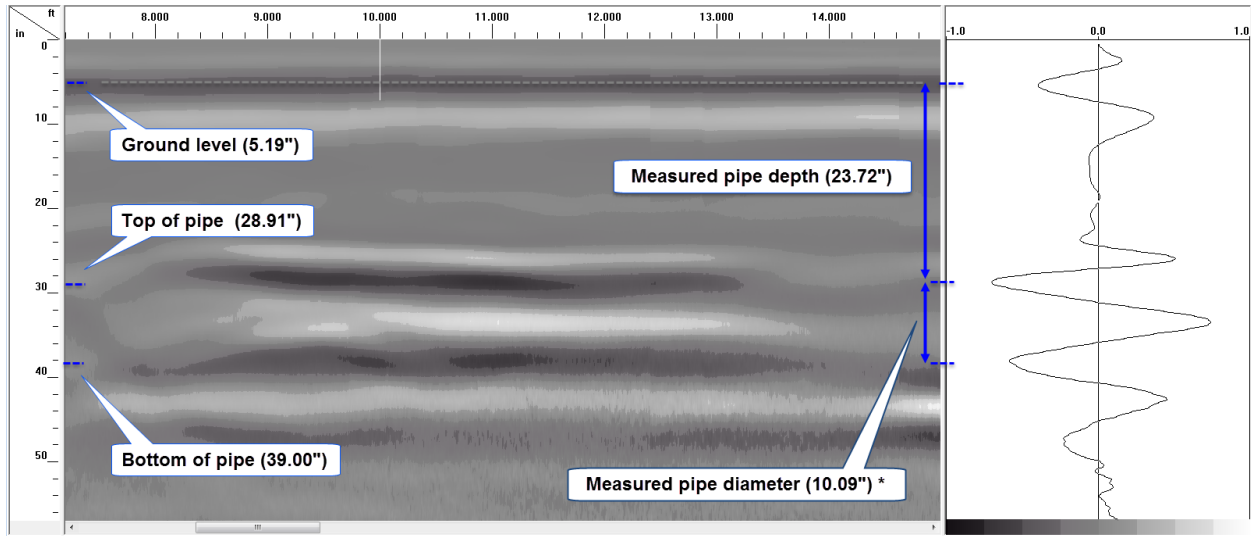


Figure B-4: Features A and A1

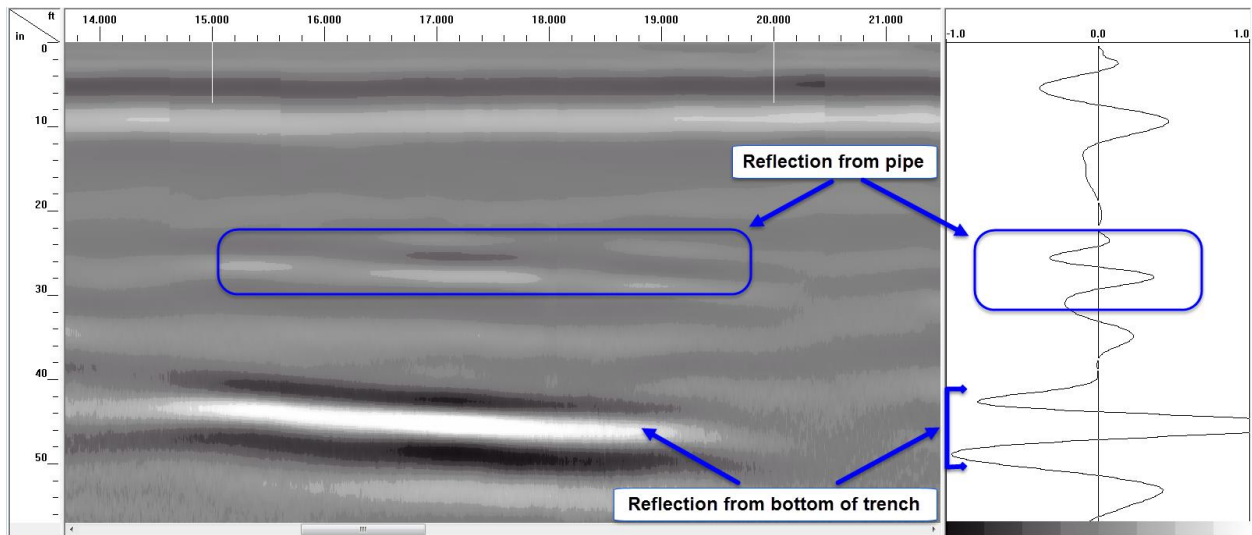


Figure B-5: Features B and B1

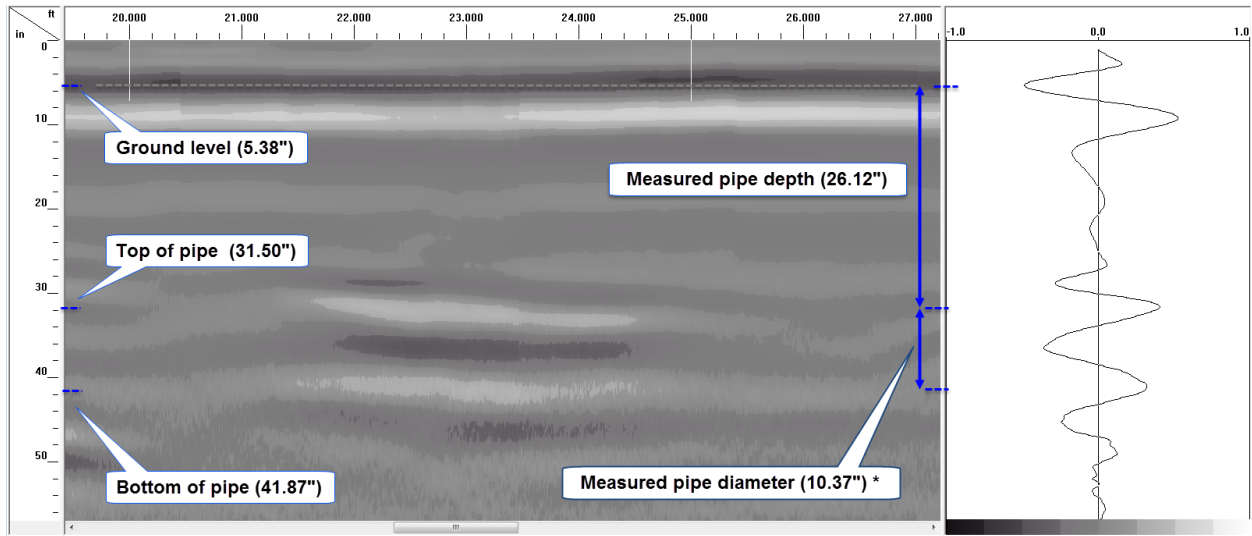


Figure B-6: Features C and C1

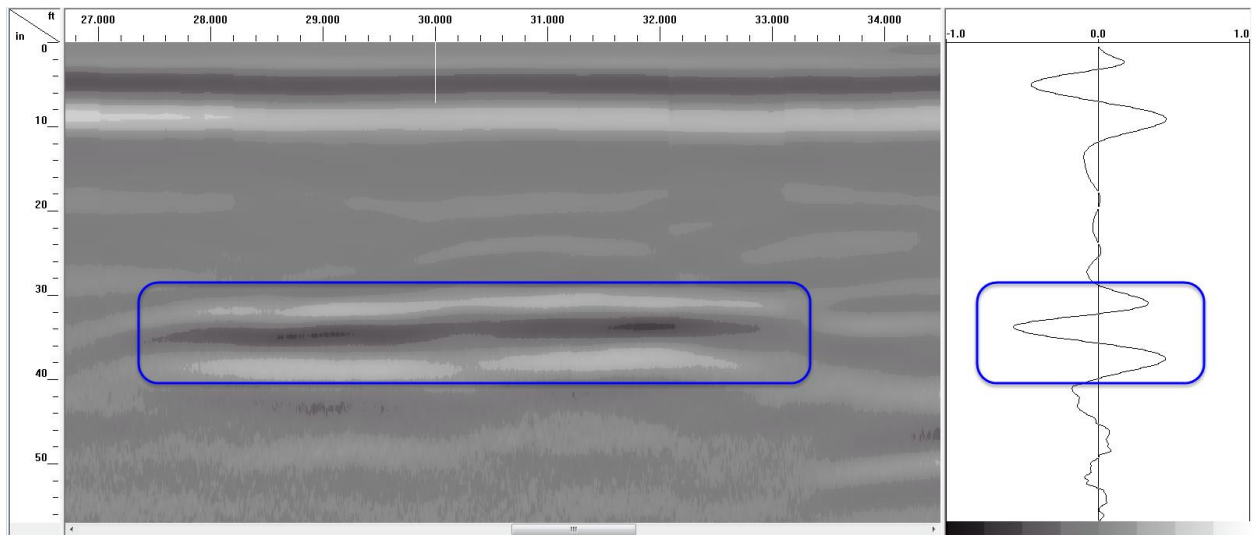


Figure B-7: Feature D

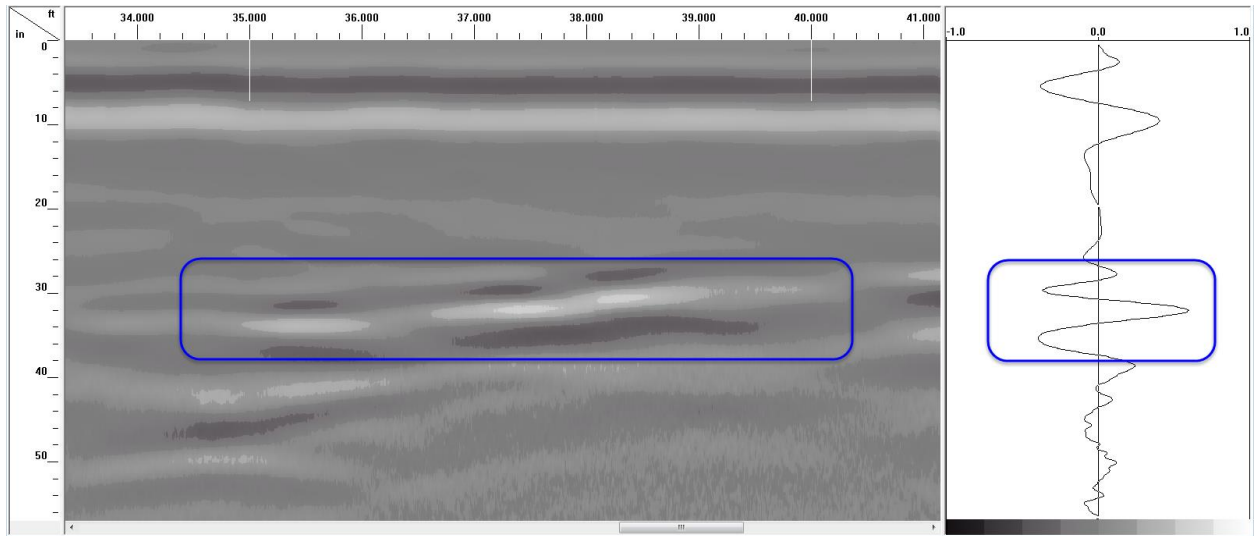


Figure B-8: Feature E

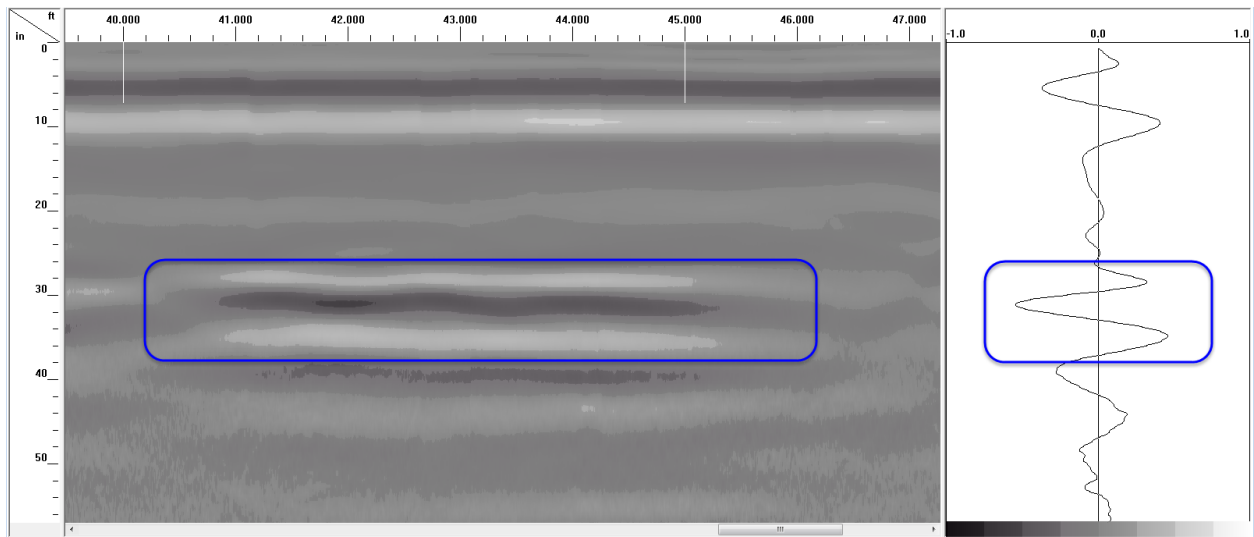
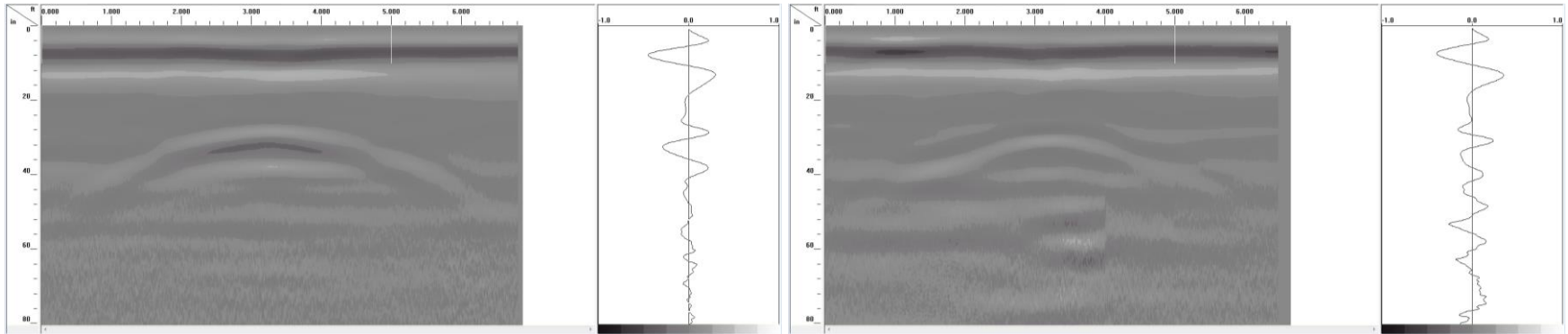


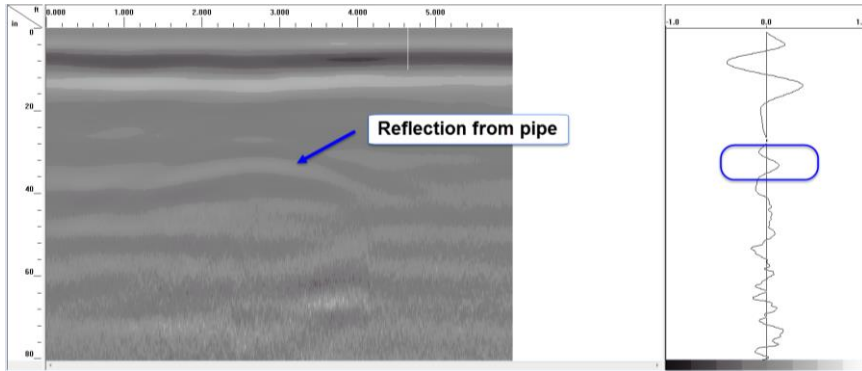
Figure B-9: Feature F

B.3 TRANSVERSE GPR SCANS OVER 36 FT. LONG TRENCH USING 200 MHz ANTENNA

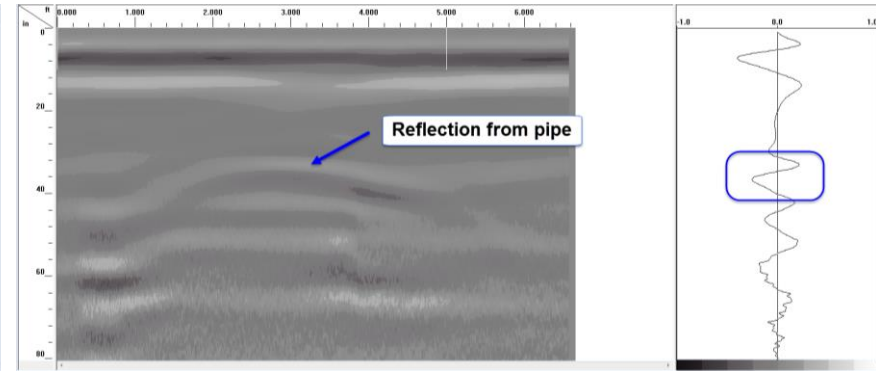


(a) GFRP pipe wrapped CFRP fabric

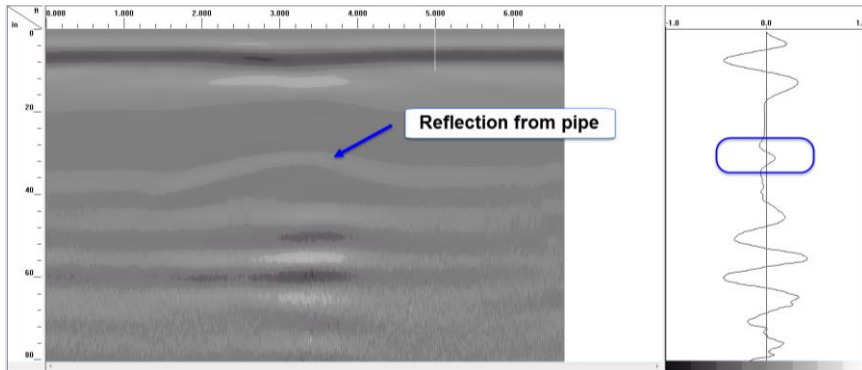
(b) Unwrapped GFRP pipe



(c) GFRP pipe with carbon nanoparticle overlay

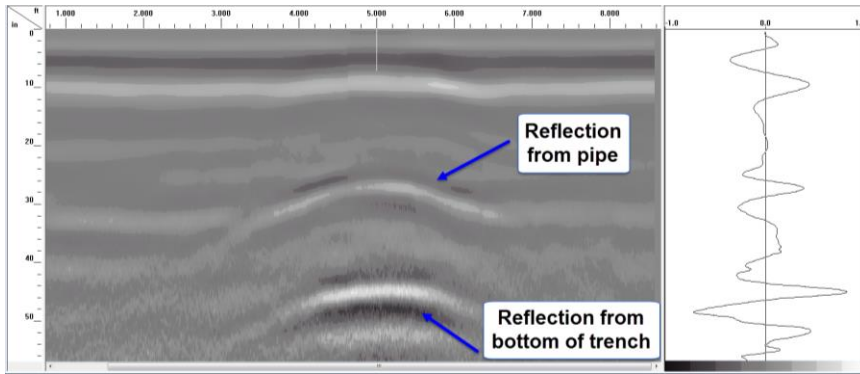


(d) PVC pipe wrapped with Aluminum foil strip

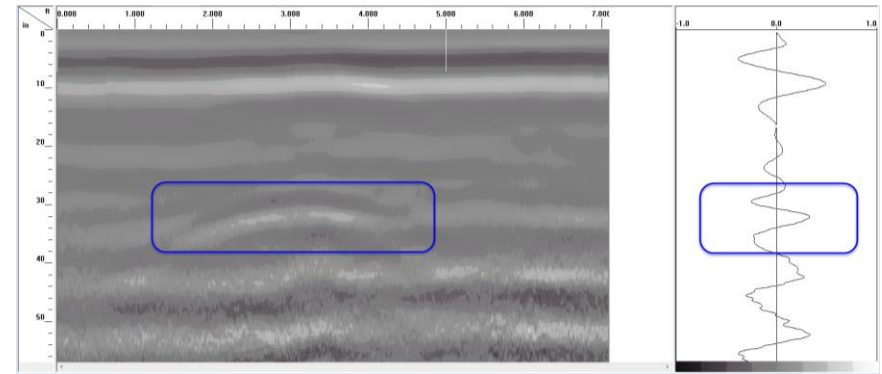


(e) Unwrapped GFRP pipe (10" diameter)

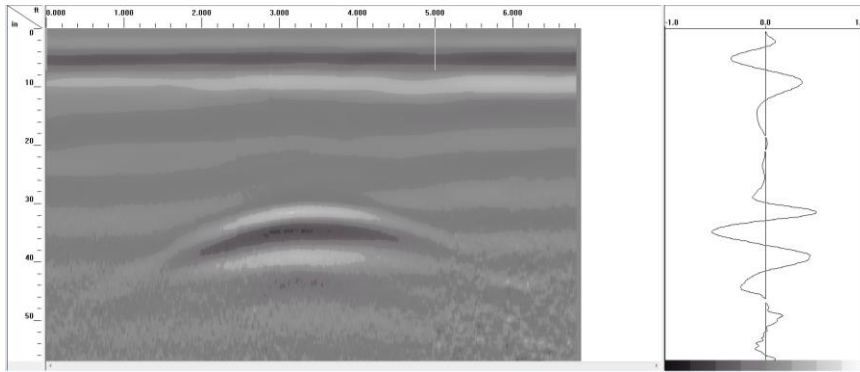
Figure B-10: Transverse scan over some of the pipes in 36 ft. long trench using 200 MHz GPR antenna for Dataset I



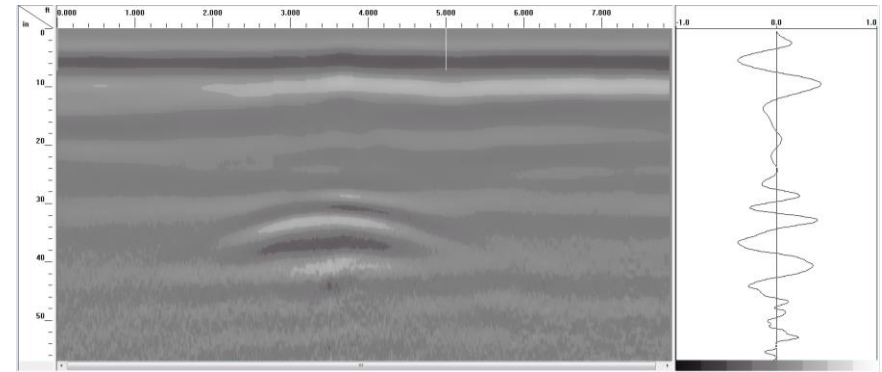
(a) Unwrapped GFRP pipe



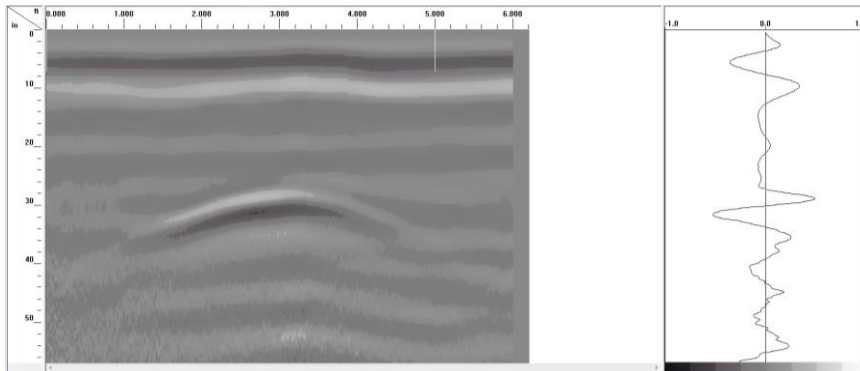
(b) GFRP pipe with carbon nanoparticle overlay



(c) PVC pipe wrapped with Aluminum foil strip



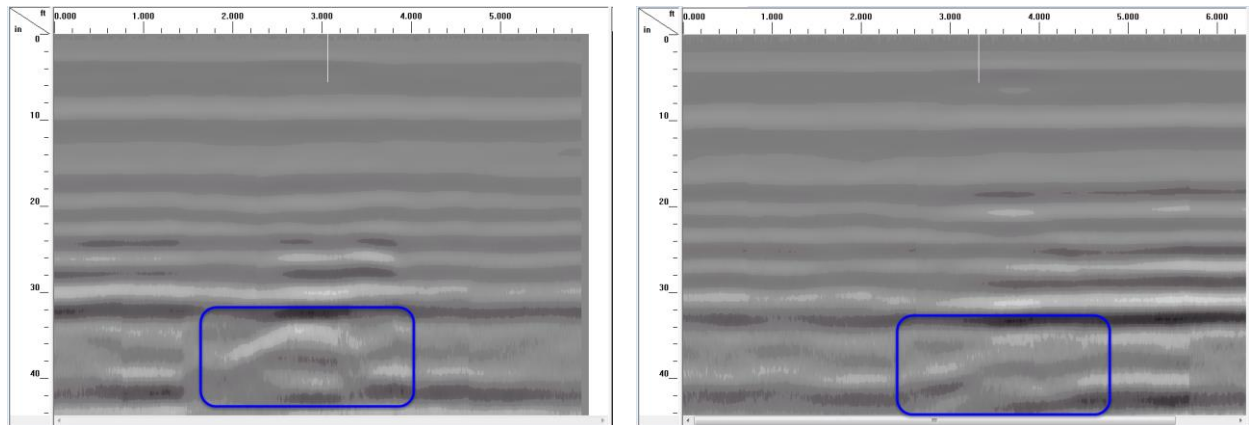
(d) Unwrapped GFRP pipe (10" diameter)



(e) Steel pipe

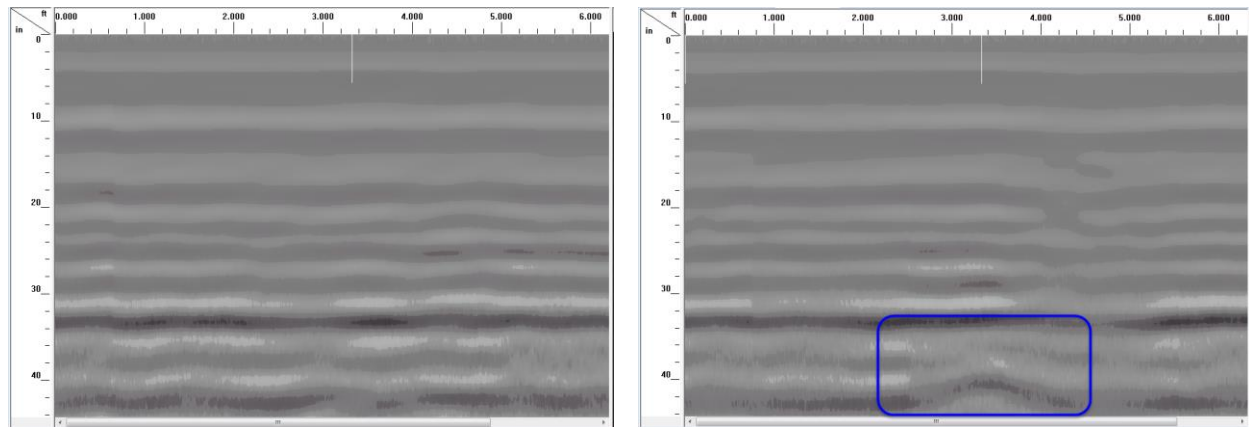
Figure B-11: Transverse scan over some of the pipes in 36 ft. long trench using 200 MHz GPR antenna for Dataset II

B.4 TRANSVERSE GPR SCANS OVER 36 FT. LONG TRENCH USING 400 MHz ANTENNA



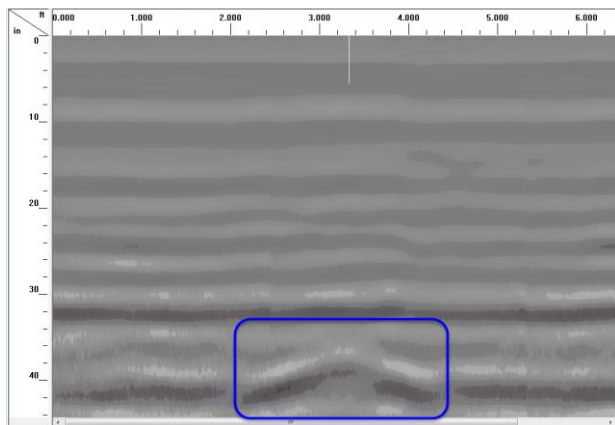
(a) GFRP pipe wrapped CFRP fabric

(b) Unwrapped GFRP pipe



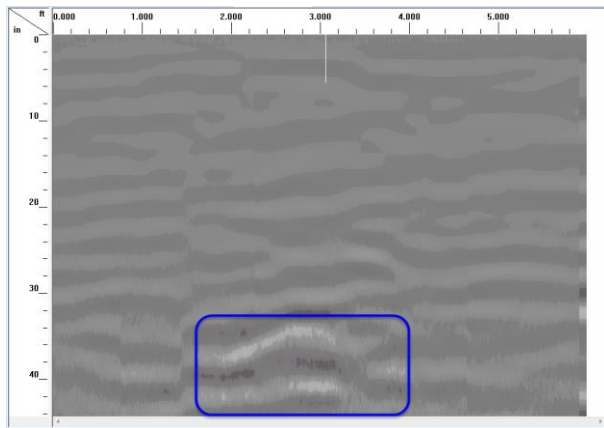
(c) GFRP pipe with carbon nanoparticle overlay

(d) PVC pipe wrapped with Aluminum foil strip

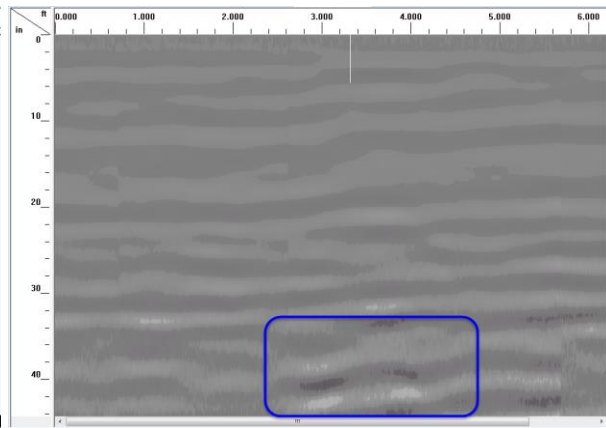


(e) Steel pipe

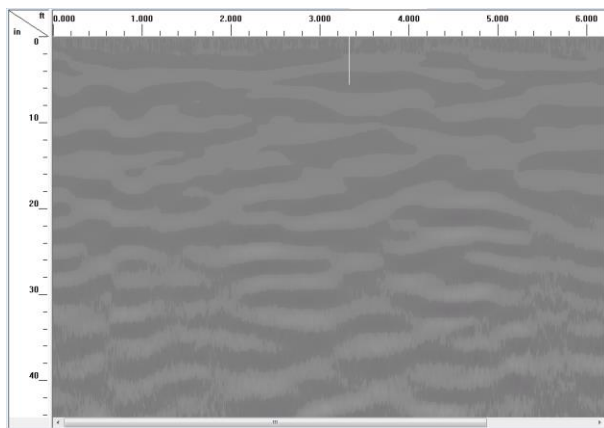
Figure B-12: Transverse scan over some of the pipes in 36 ft. long trench using 400 MHz GPR antenna for Dataset II (raw data)



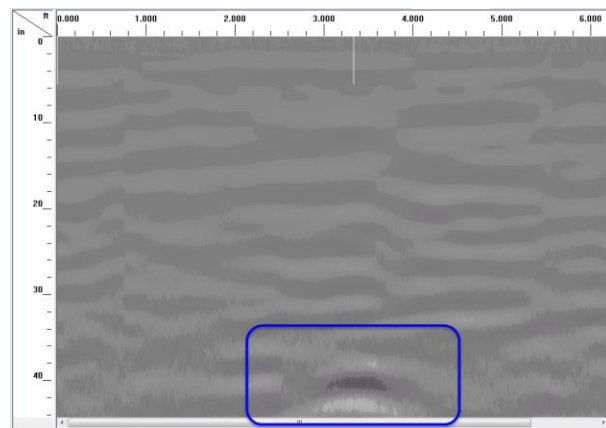
(a) *GFRP pipe wrapped CFRP fabric*



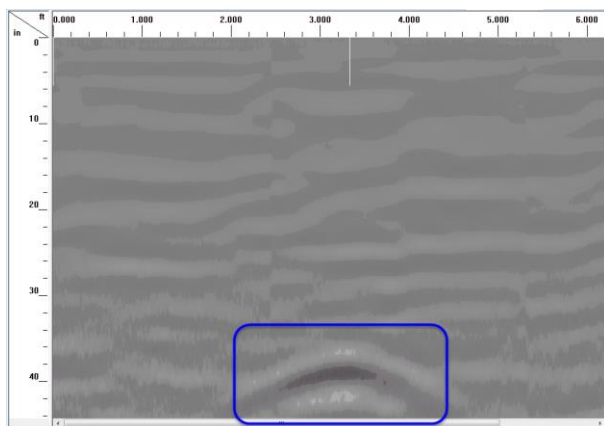
(b) *Unwrapped GFRP pipe*



(c) *GFRP pipe with carbon nanoparticle overlay*



(d) *PVC pipe wrapped with Aluminum foil strip*



(e) *Steel pipe*

Figure B-13: *Transverse scan over some of the pipes in 36 ft. long trench using 400 MHz GPR antenna for Dataset II (data with background noise removed)*

APPENDIX C: SUPPLEMENTARY IRT PLOTS

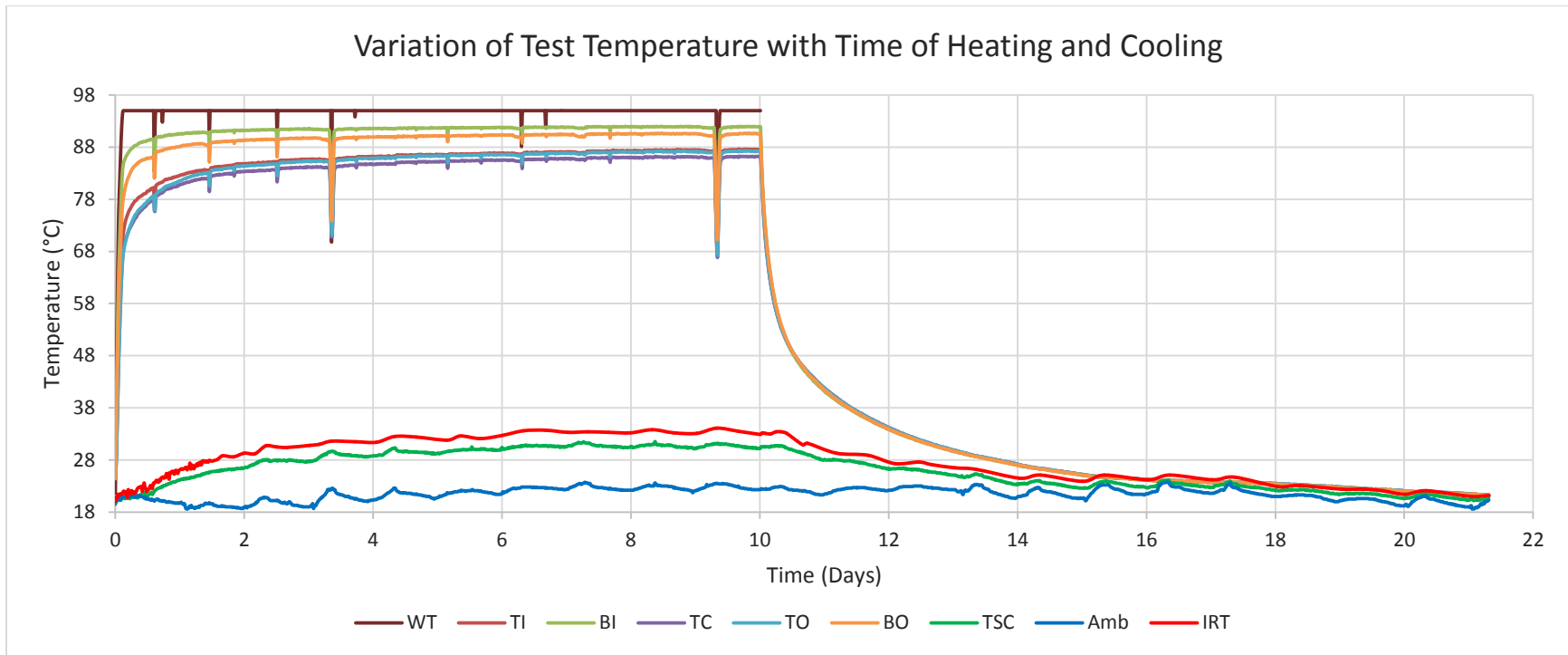


Figure C-1: Variation of test temperature with time of heating and cooling

- Hot water was pumped through the pipe from day 1 to 10 after which heating and pumping was stopped and the pipe was allowed to cool under ambient laboratory temperature.

WT: Water Temperature

TI: Top Inlet temperature (inlet temperature measured at the top of the pipe)

BI: Bottom Inlet temperature (inlet temperature measured at the bottom of the pipe)

TC: Top Center temperature (temperature measured at the top of the pipe, midway between the inlet and the outlet)

TO: Top Outlet temperature (outlet temperature measured at the top of the pipe)

BO: Bottom Outlet temperature (outlet temperature measured at the bottom of the pipe)

TSC: Top Soil Center temperature (temperature at top of the soil over mid portion of the pipe)

Amb: Ambient temperature

IRT: Infrared Thermography temperature reading

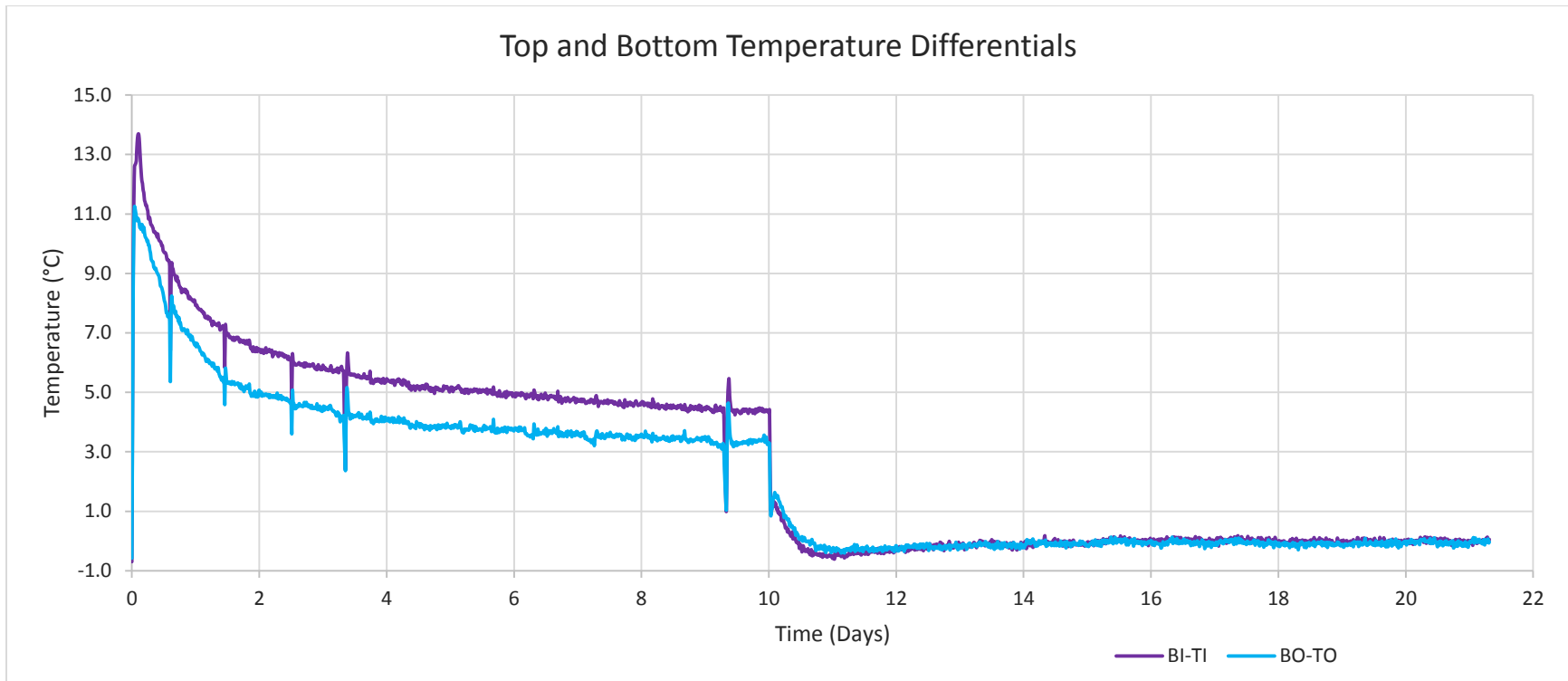


Figure C-2: Top and bottom temperature difference of the pipe during heating and cooling

- Hot water was pumped through the pipe from day 1 to 10 after which heating and pumping was stopped and the pipe was allowed to cool under ambient laboratory temperature.

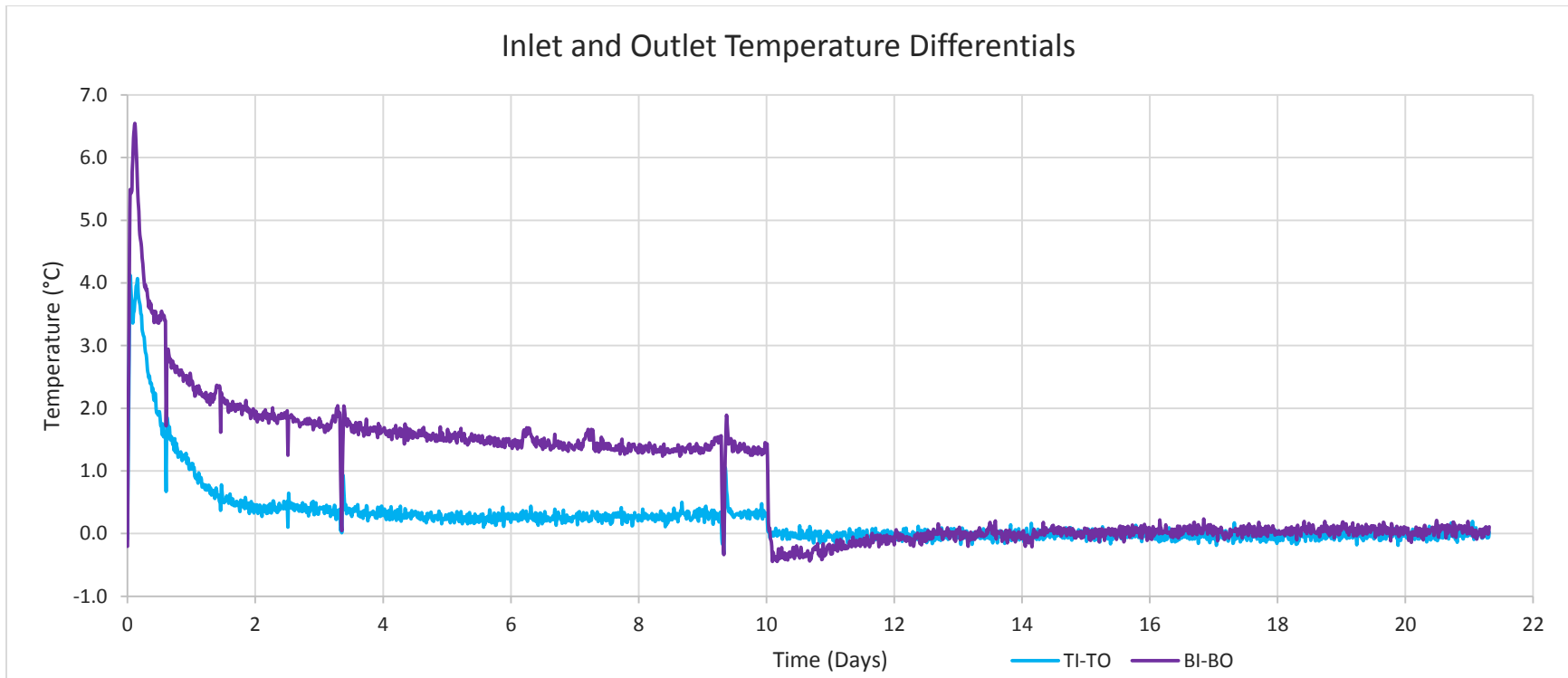


Figure C-3: Inlet and outlet temperature difference of the pipe during heating and cooling

- Hot water was pumped through the pipe from day 1 to 10 after which heating and pumping was stopped and the pipe was allowed to cool under ambient laboratory temperature.

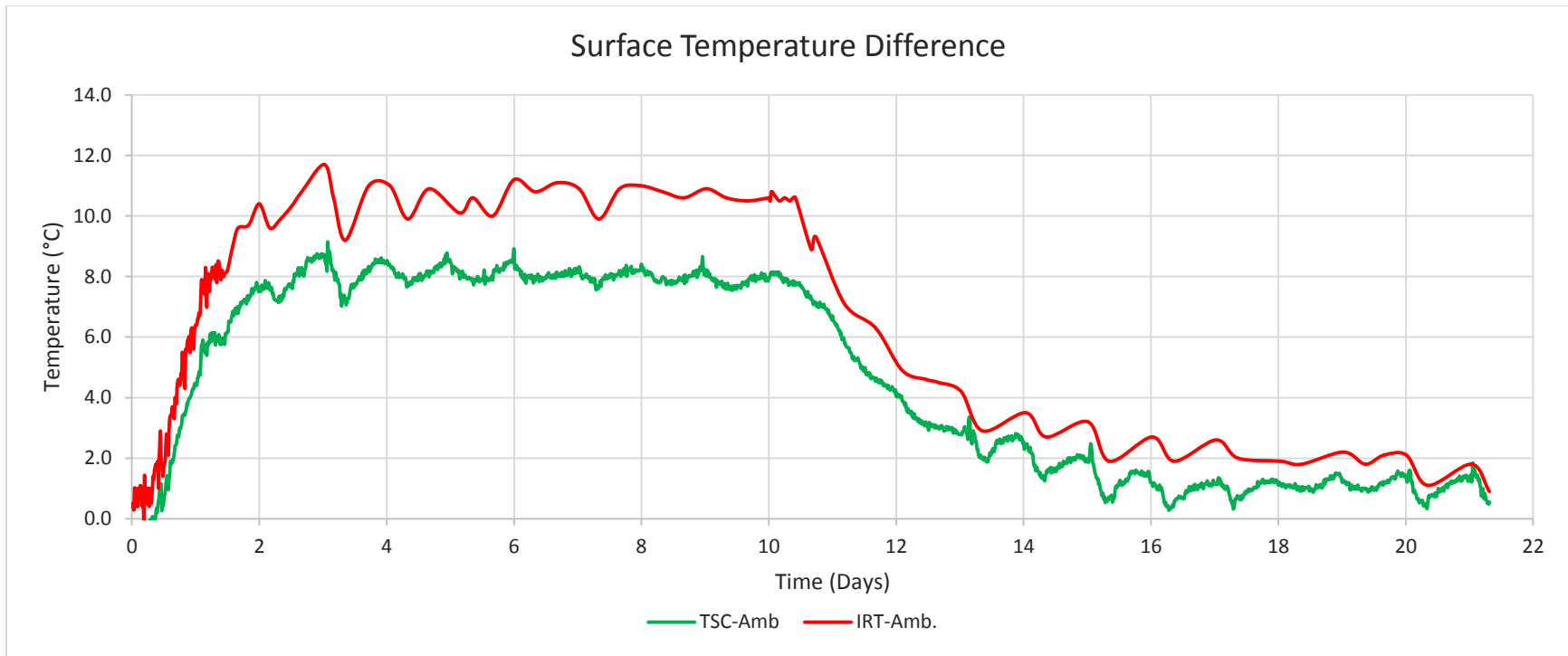


Figure C-4: Soil surface temperature difference during heating and cooling

- Hot water was pumped through the pipe from day 1 to 10 after which heating and pumping was stopped and the pipe was allowed to cool under ambient laboratory temperature.